Investigation of structure-property relationship in some low dimensional nickelates

A thesis

Submitted in partial fulfilment of the requirements of the degree of

Doctor of Philosophy

by

Dibyata Rout

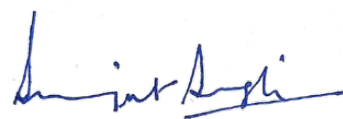Registration ID-20163493

Department of Physics

INDIAN INSTITUTE OF SCIENCE EDUCATION AND RESEARCH

PUNE-411008, India

Certificate

Certified that the work incorporated in the thesis entitled **"Investigation of structure-property relationship in some low dimensional nickelates"** submitted by **Dibyata Rout** was carried out by the candidate, under my supervision. The work presented here or any part of it has not been included in any other thesis submitted previously for the award of any degree or diploma from any other university or institution.

Date: April 28, 2023

Dr. Surjeet Singh

(Supervisor)

Declaration

I declare that this written submission entitled **"Investigation of structure-property relationship in some low dimensional nickelates"** represents my ideas in my own words and where others ideas have been included, I have adequately cited and referenced the original sources. I also declare that I have adhered to all principles of academic honesty and integrity and have not misrepresented or fabricated or falsified any idea/data/fact/source in my submission. I understand that violation of the above will be cause for disciplinary action by the Institute and can also evoke penal action from the sources which have thus not been properly cited or from whom proper permission has not been taken when needed.

Date: April 28, 2023

Dibyata Rout

(20163493)

It always seems impossible until it's done

- Nirmal Purja

Dedicated to Gita Mausi

Acknowledgements

Abstract

The realm of spin 1 quantum systems remains relatively uncharted compared to their spin $\frac{1}{2}$ counterparts. They exist at the delicate borderland between quantum and classical physics, displaying moderate quantum fluctuations that influence the behaviour of the systems in unexpected ways. This thesis delves into the experimental study of spin 1 quantum systems comprising two principal low-dimensional lattices, namely, the square and the triangular. The thesis deals with an exhaustive investigation of structure-property relationship in the Ruddlesden-Popper (RP) nickelates $R_4Ni_3O_{10}$ (R = La, Pr, and Nd) where Ni ion is located in an octahedral environment, the infinite layered T' nickelates $R_4Ni_3O_8$ where Ni ions form a square-planar lattice, and the triple perovskite $Ca_3NiNb_2O_9$ where the Ni ions form well-isolated triangular layers resulting in a triangular lattice antiferromagnet. The n = 3 members of the Ruddlesden-Popper nickelates ($R_4Ni_3O_{10}$) with mixed-valent Ni^{2+}/Ni^{3+} states are scrutinized for their structural, transport, magnetic, and thermodynamic properties, with a focus on understanding the metal-to-metal transition (MMT) associated with the Ni 3d electrons. This MMT was earlier said to arise from a charge density wave (CDW) driven instability, we therefore used high resolution, low temperature synchrotron powder x-ray diffraction to study any subtle change in structural parameters or crystalline symmetry across this transition. The magnetic ground state of the rare-earth sublattice is also thoroughly examined, revealing novel insights not explored in detail in previous literature.

Further, we focus our attention on the oxygen reduced counterparts of these RP nickelates commonly referred to as the infinite layered T' nickelates, $R_4Ni_3O_8$. These T' nickelates are known to be structurally and electronically analogues of the high T_C superconducting cuprates. But owing to the difficulty involved in their synthesis, not much progress has been made in understanding their ground state properties. In this thesis, the mixed-valent triple layer T' nickelates, having Ni^{1+} and Ni^{2+} in the ratio of 2:1, are investigated. The evolution of the ground state from a charge/spin stripe insulator in $La_4Ni_3O_8$ to a correlated metal in $(Pr/Nd)_4Ni_3O_8$ is probed systematically across these trilayer nickelates using transport, magnetization, low temperature synchrotron x-ray diffraction and specific heat probes. This study elucidates the effect of chemical pressure on the metal-insulator transition (MIT) seen for the $La_4Ni_3O_8$ com-

pound at 105 K. In the last part of the thesis, we study the triangular lattice antiferromagnet $Ca_3NiNb_2O_9$ and its non-magnetic counterpart $Ca_3MgNb_2O_9$. Here, the $S = 1$ Ni^{2+} ions are arranged on a triangular motif that are well separated from each other by non-magnetic buffer layers, which renders the system as quasi two dimensional. We show that this compound exhibits a $120°$ ordered ground state that gives way to field-induced quantum phase transitions in the form of magnetization plateaux. We grew single crystals of $Ca_3NiNb_2O_9$ using the optical floating-zone method. Depending on the growth condition, we obtained two structural variants of $Ca_3NiNb_2O_9$ - a low-symmetry 1:2 ordered (Ni/Nb order) phase, and a high-symmetry, disordered $CaMO_3$-type perovskite structure with M-site occupied randomly by Ni and Nb. The ground state properties of these two variants are studied in detail. The ordered specimen is shown to undergo a two-step transition to the $120°$ spin structure, confirmed using the neutron scattering experiments. On the other hand, the disordered sample $Ca(Nb,Ni)O_3$ exhibit a complex glassy ground state with no long-range order.

Synopsis

In this thesis, we have focussed on the structure-property relationship in three different classes of compounds with Ni ion as the common building block. These three distinct families of compounds are, namely, the n = 3 members of the Ruddlesden Popper nickelate family (where Ni atom sits within an octahedral environment), the n = 3 member of the T' nickelate family (where Ni atom is stabilized on a square planar geometry) and the triangular lattice antiferromagnet, $Ca_3NiNb_2O_9$ (where Ni atoms sit on the vertices of a triangular motif).

In **Chapter 1**, we discuss the diverse facets of how a material's structure impacts its physical properties. We provide a succinct overview of the captivating properties exhibited by transition metal oxides (TMOs) and briefly explain the various energy scales that are germane to comprehending the physics of TMOs. Subsequently, we explain in brief the perovskite building block and how the Ruddlesden Popper structure is derived from it. Additionally, we elucidate on the methodology of synthesizing the T' nickelates from the Ruddlesden Popper phases and establish the motivation behind the significant renewed interest in understanding the ground state of nickelates that are structurally and electronically analogous to the to that of high T_C superconducting cuprates. We then move on to the nickelates based on the triple perovskite structure $A_3BB'_2O_9$, which constitute the remaining part of this thesis and expound on how the degree of B-site ordering affects their physical properties. Since B-atoms in this structure form a triangular lattice, we explain geometrical frustration in a triangular lattice antiferromagnet and how quantum fluctuations help in stabilizing novel quantum states as a function of applied magnetic field in these systems.

Chapter 2 of the thesis provides a comprehensive account of the experimental tools employed to investigate the three material classes that are a part of this thesis.

Chapter 3 focuses on the crystal growth technique, specifically the use of a four-mirror-optical floating zone furnace, and delves into the intricacies of the growth process.

In **Chapter 4** we investigate in detail the low temperature structural and physical properties of the trilayer nickelates $R_4Ni_3O_{10}$ (R = La, Pr and Nd) using resistivity, thermopower, thermal conductivity, specific heat, high-resolution synchrotron powder x-ray diffraction, and thermal expansion experiments. We try to investigate the presence/absence of change in structural

symmetry below the metal-to-metal transition (MMT) which was theoretically predicted in a previous study by Puggioni *et al.*. Besides understanding the physics of the nickel sublattice that drives the MMT, we also look closely at the behavior of the rare-earth sublattice and report new features in the magnetization and specific heat of these materials that were not previously reported to the best of our knowledge.

In **Chapter 5** we investigate the n = 3 members of the infinite layered T' series, $R_4Ni_3O_8$ (R = La, Pr and Nd) and at the same time, to understand the role of R-site ionic radius in giving rise to concomitant spin/charge-stripe ordering, which is also accompanied by a metal-insulator transition (MIT), we studied solid solutions of the form $(R, La)_4Ni_3O_8$ (R = Pr, Nd) where the lattice parameters are tuned gradually. We observed a crossover from charge/spin stripe insulator in $La_4Ni_3O_8$ to a correlated metal in $(Pr/Nd)_4Ni_3O_8$ via various low-temperature probes such as synchrotron powder x-ray diffraction, specific heat, and magnetization measurements.

In **Chapter 6** we discuss the details of the crystal growth of the triangular lattice antiferromagnetic system - $Ca_3NiNb_2O_9$ and its non-magnetic analog $Ca_3MgNb_2O_9$ using a four-mirror optical floating zone furnace. We study in great detail the effect of growth atmosphere and pulling rate on the grown crystalâs quality and phase homogeneity. We also investigate the effects of annealing (in various atmospheres) on the ground state properties of $Ca_3NiNb_2O_9$. Thereafter, we make use of room temperature synchrotron powder x-ray diffraction, low temperature specific heat, magnetization and single crystal neutron diffraction measurements to elucidate the ground state properties of the as-grown and annealed crystals.

In the concluding chapter of this thesis (**Chapter 7**), we present a summary of the important new results obtained during this thesis with future perspective and outlook.

List of Publications

1. *Structural and physical properties of trilayer nickelates $R_4Ni_3O_{10}$ (R = La, Pr and Nd)*; **Dibyata Rout**, Sanchayeta Ranajit Mudi, Marco Hoffmann, Sven Spachmann, Ruediger Klingeler, and Surjeet Singh, Phys. Rev. B, 102, 195144 (2020).

2. *Ordered and disordered variants of the triangular lattice antiferromagnet $Ca_3NiNb_2O_9$ crystal growth and magnetic properties*; **Dibyata Rout**, Ran Tang, Markos Skoulatos, Bachir Ouladdiaf, Yuto Kinoshita, Atsushi Miyake, Masashi Tokunaga, Sagar Mahapatra and Surjeet Singh, Phys. Rev. Materials 7, 024419 (2023)

3. *Crossover from a charge/spin stripe ordered phase to that of a correlated metal in n = 3 member of the T' nickelate series*; **Dibyata Rout**, Sanchayeta Ranajit Mudi and Surjeet Singh, (to be submitted)

4. *Crystal growth of quantum materials: a review of selective materials and techniques*;, Nashra Pistawala, **Dibyata Rout**, Kumar Saurabh, Rabindranath Bag, Koushik Karmakar, Luminita Harnagea and Surjeet Singh, Bull Mater Sci, 45, 10 (2022)

5. *X-ray photoemission and absorption study of the pyrochlore iridates $(Eu_{1−x}Bi_x)_2Ir_2O_7$, $0 \leq x \leq$*; Prachi Telang, Abhisek Bandyopadhyay, Kshiti Mishra, **Dibyata Rout**, Rabindranath Bag, A Gloskovskii, Yu Matveyev and Surjeet Singh, Journal of Physics: Condensed Matter, Volume 34, Number 39 (2022)

6. *Giant orbital polarization of Ni^{2+} in a square planar environment*; Prithwijit Mandal, Ranjan Kumar Patel, **Dibyata Rout**, Rajdeep Banerjee, Rabindranath Bag, Koushik Karmakar, Awadhesh Narayan, John W. Freeland, Surjeet Singh, and Srimanta Middey, Phys. Rev. B 103, L060504 (2021)

7. *Growth, Properties, and Applications of Pulsed Laser Deposited Nanolaminate Ti_3AlC_2 Thin Films*; Abhijit Biswas, Arundhati Sengupta, Umashankar Rajput, Sachin Kumar Singh, Vivek Antad, Sk Mujaffar Hossain, Swati Parmar, **Dibyata Rout**, Aparna Deshpande, Sunil Nair, and Satishchandra Ogale, Phys. Rev. Applied 13, 044075 (2020)

8. *Laser-diode-heated floating-zone crystal growth of ErVO$_3$; Prachi Telang, Andrey Maljuk,* **Dibyata Rout**, Markos Skoulatos, Koushik Karmakar, Silvia Seiro, Bertrand Roessli, Uwe Stuhr, Bernd Buchner, Sang-Wook Cheong and Surjeet Singh, Journal of crystal growth, 507, 406-412 (2019)

9. *Anomalous pressure dependence of phonon linewidths in metallic pyrochlore iridates* *(Eu$_{1-x}$Bi$_x$)$_2$Ir$_2$O$_7$: Crossover from incoherent to coherent metal*; Anoop Thomas, Prachi Telang, **Dibyata Rout**, Kshiti Mishra, Anand Pal, D V S Muthu, P S Anil Kumar, Surjeet Singh, and A. K. Sood, (accepted in Pramana)

10. *Formation of the Γ_1 phase and the mechanism underlying the spin reorientation in* *the rare-earth orthoferrites: The case of Mn-doped SmFeO$_3$*; R. Nickel, S. Babu, R. Hissariya, **Dibyata Rout**, R. Abrudan, F. Radu, S. Singh, J. van Lierop, and S.K. Mishra, (under review)

11. *Evidence of Charge-Phonon coupling in van der Waals materials Ni$_{1-x}$Zn$_x$PS$_3$*; Nashra Pistawala, Ankit Kumar, Devesh Negi, **Dibyata Rout**, Luminita Harnagea, Surajit Saha and Surjeet Singh, (to be submitted)

12. *Optically induced symmetry breaking due to nonequilibrium steady state formation in* *charge density wave material 1T-TiSe$_2$*; Harshvardhan Jog, Luminita Harnagea, **Dibyata Rout**, Takashi Taniguchi, Kenji Watanabe, Eugene J. Mele, Ritesh Agarwal, (submitted to Nature Physics)

Contents

Chapter 1

Introduction

For decades, structure-property relationships have fascinated condensed matter physicists. The underlying crystal structure and the coordination symmetry of the ions in a material play a crucial role in determining its physical properties. For example, metals possessing a crystalline structure generally exhibit greater strength and ductility compared to those with an amorphous structure. [1, 2]. Another example is the high thermal conductivity of diamond (24 - 25 W cm^{-1}K^{-1} at 300 K) [3] due to the efficient transfer of thermal energy through the ordered lattice structure. In contrast, materials with a disordered structure, such as glasses, exhibit lower thermal conductivity due to the scattering of phonons [4, 5]. In addition to the arrangement of atoms, the presence of impurities [6], defects [7–9], and grain boundaries [10, 11] can also influence the physical properties of a material. For example, by intentionally introducing and controlling defects in the semiconductor material [12], the semiconductor industry can tailor the properties of the material to meet specific performance requirements. This approach is widely used in the manufacture of various electronic devices such as transistors, diodes, solar cells, and LEDs.

Changes made to crystal structure can have a profound impact on a material's electrical conductivity by altering its band structure and electronic density of states. By changing the crystal structure, it is possible to obtain a suitable band engineering [13] that enhances the thermoelectric properties of the material. Another example is the effect of chemical pressure [14–16] that alters the interatomic distances and angles, which in turn affects the electronic properties of the material. Piezoelectricity is another phenomenon that illustrates the

1

effect of structure-property relationship. Here a material produces an electric charge when subjected to stress or strain. Piezoelectric materials such as quartz [17, 18], $BaTiO_3$ [19], and lead zirconium titanate (PZT) [20] serve as prime examples. Apart from this, the optical properties of a material such as the refractive index, absorption, and transmission efficiency are also affected by the underlying structure [21]. This is evident in materials with a highly ordered structure, such as single-crystal silicon, which exhibit high transparency and low absorption in the visible range. In contrast, materials with a disordered structure, such as amorphous silicon, exhibit low transparency and high absorption due to the presence of defects and disorder in the material. In summary, the structure-property relationship is a crucial aspect of materials science research. By examining the organization of atoms, presence of impurities and defects, particle size, and other factors, scientists can design materials with specific physical properties for various applications in industries such as electronics [22, 23], aerospace [24], and biotechnology [25, 26].

From a fundamental physics perspective, the study of the interplay between various degrees of freedom, such as spin, charge, lattice, and orbital degrees of freedom, in highly correlated electron systems is a burgeoning field of research [27, 28]. For decades, fundamental research aimed at elucidating the correlation between crystal structure and magnetic properties has taken center stage. For example, people have extensively studied the role of dilute impurities on the ground state properties of low dimensional spin systems such as spin chains [29, 30] and spin ladders [31] and have experimentally validated the theoretical constructs. Another interesting aspect of low dimensional magnetism is seen in layered Van der Waal's materials where the magnetic order parameter evolves as a function of layer thickness of the material [32, 33]. Recent studies have also focused on the role of dimensionality and topology in the magnetic properties of low dimensional quantum magnets. For example, the introduction of topological defects in the two-dimensional lattice structure can give rise to new topologically protected magnetic states, such as skyrmions [34–36], which have potential applications in spintronics and data storage. Thus, it is evident that the magnetic ground state of a material can be profoundly intertwined with the arrangement of the magnetic ions in a specific crystal lattice, and this aspect constitutes the essence of this thesis.

1.1 Transition metal oxides

Transition metal compounds constitute a distinctive category of solids that exhibit a wide range of intriguing physical properties [37]. These materials encompass both excellent conductors (e.g. $LaNiO_3$, ReO_3) and robust, high-gap insulators (e.g. $BaTiO_3$), in addition to systems which undergo metal-insulator transition, as for example in manganites [38, 39]. Furthermore, their magnetic characteristics are highly varied, ranging from a Pauli paramagnetism to a local moment systems. The ground state properties of these materials can also be tuned nicely by use of external parameters like temperature, pressure, doping or magnetic field. These compounds exhibit numerous fascinating phenomena, including multiferroicity [40, 41], colossal magnetoresistance [42], charge and spin density waves [43, 44], spin switching [45, 46], charge ordering [47–49] and high-Tc superconductivity [50–52] as a result of complex interplay of various electronic interactions. Hence, in the upcoming sections, a brief introduction will be given to the energy scales relevant to the physics of the transition metal oxides (TMOs) and how their interplay decides the ground state of these systems.

1.1.1 Crystal field splitting energy

In TMOs, the central metal ion can be coordinated with the anions in various possible ways viz octahedral, trigonal bipyramidal, tetrahedral, square planar, square pyramidal, pentagonal bipyramidal, etc. The specific geometry of the anion cage around the transition metal ion governs the behaviour of the d orbitals of the transition metal and is explicitly explained by the crystal field theory. The crystal field theory describes the lifting of the orbital degeneracy in transition metal complexes due to an electrostatic field produced by the surrounding ligands. This theory was developed by Hans Bethe and J.H. van Vleck [53] in the 1930s. According to this theory, the negatively charged ligands surrounding a positively charged metal ion in a complex create a crystal field that affects the energy levels of the metal's d orbitals. The d orbitals that lie along the line of approach of the ligands face the maximum repulsion and are lifted in energy while those orbitals that are further away from the ligands get lowered in energy. This splitting of d orbitals (also known as crystal field splitting (CFS)) results in the breaking of orbital degeneracy. The CFS depends primarily on the ligand coordination symmetry and the distance between the metal ion and the ligand and so on. The CFS is
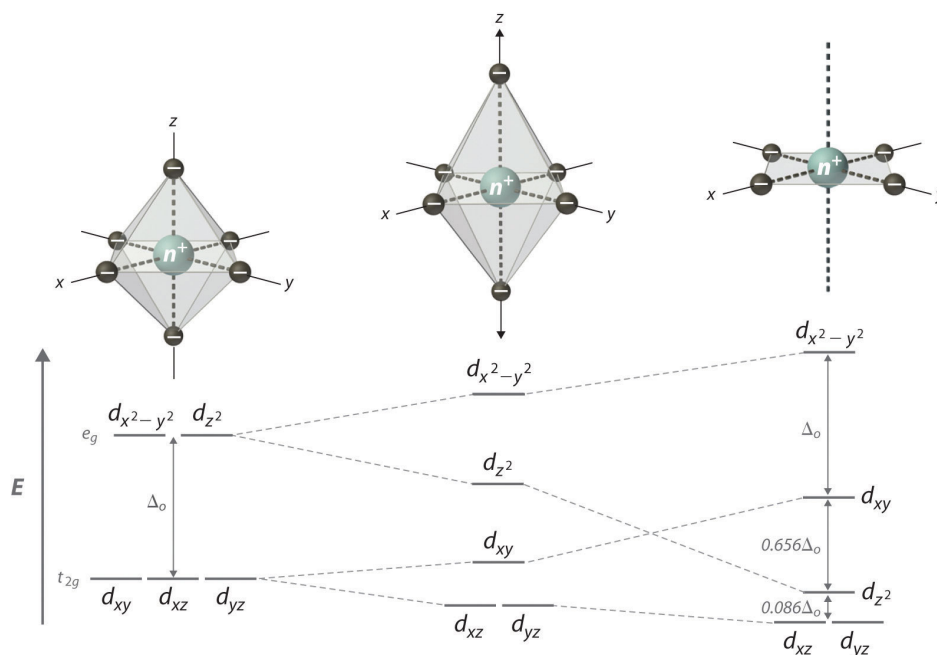
Figure 1.1: (a) Graphical representation of the crystal field splitting scheme in an octahedral complex. (b) represents the change in energy of the d orbitals as the ligands along the z-axis move further away from the basal plane. (c) represents the energetic arrangement of the d orbitals in a square planar complex. This figure is taken from Ref. [54].

responsible for determining the color, magnetism, and other properties of the transition metal complex.

Consider the case of an octahedral transition metal complex. When the ligands approach the transition metal ion from the x, y and z direction, the d_{z^2} and $d_{x^2-y^2}$ orbitals feel greater repulsion (as they lie along these axes) and their overall energy is increased. On the other hand, the energy of the d_{xy}, d_{yz} and d_{zx} orbitals is lowered as they are not in the direct line of approach of the ligands. This results in crystal field splitting of the d orbitals into the t_{2g} and e_g sets, where the e_g orbitals have higher energy than the t_{2g} orbitals. A schematic representation of the CFS in octahedral complexes in shown in Fig. 1.1 (a). Now if we consider the case of square planar complexes, the crystal field splitting scheme will be slightly different as the ligands are absent along the z-direction. The orbitals that lie along the xy plane will feel a greater force of repulsion as compared to those along the z direction. Hence the $d_{x^2-y^2}$ orbital has the highest energy followed by the d_{xy} and d_{z^2} orbitals. The d_{xz} and the d_{yz} orbitals are lowest in energy and remain degenerate as shown in Fig. 1.1 (c). Now depending on the competition between the crystal field splitting energy and the pairing energy, these transition

metal complexes can either give rise to low spin (less number of unpaired electrons) or high spin (more number of unpaired electrons) complex.
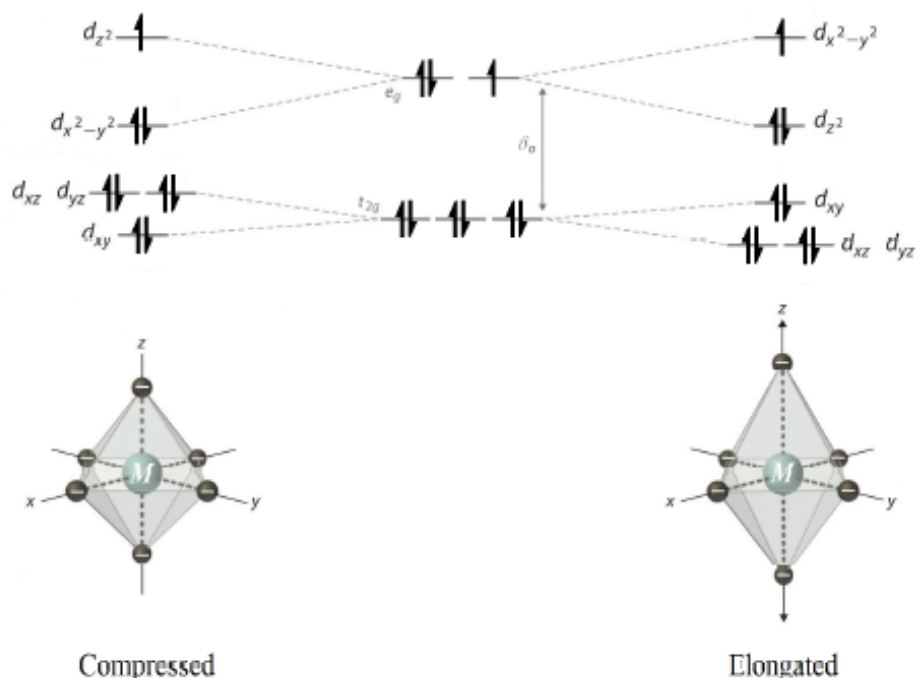
Figure 1.2: (a) Graphical representation of Jahn-Teller distortion in an octahedral complex. When the unpaired electron resides in the d_{z^2} orbital (left), the octahedra is compressed along the z-direction. Alternatively, an unpaired electron in the $d_{x^2-y^2}$ orbital (right) elongates the octahedra. The figure is taken from Ref. [55].

1.1.2 Jahn Teller distortion

The Jahn-Teller theorem was postulated by Hermann Jahn and Edward Teller in the year 1937 [56] and it stated that the electronic degeneracy in a non-linear molecule is unstable and the system will undergo structural distortion to reach a state of lower degeneracy and symmetry, which is energetically more stable. Jahn-Teller (JT) distortion is nothing but a geometrical distortion typically observed among octahedral complexes where the two axial bonds can be shorter or longer than those of the equatorial bonds as shown in Fig. 1.2. The JT distortion basically breaks the orbital degeneracy of the t_{2g} and e_g orbitals.

1.1.3 Hubbard Model

In order to explain the effect of electron-electron interactions in transition metal oxide (TMO) systems, John Hubbard proposed the famous Hubbard model [57] in the 1960s. It is to be noted that at the same time, this model was independently introduced by Martin Gutzwiller [58] and Junjiro Kanamori [59]. This model was devised to deal with the shortcomings of the band theory of solids in explaining the insulating ground state observed in TMOs like CoO, NiO, etc. The Hubbard Hamiltonian for a one-dimensional lattice of N sites, with one orbital per site, can be described by an equation of the form:

$$\hat{H} = -t\sum_{i,\sigma}(\hat{c}_{i,\sigma}^{\dagger}\hat{c}_{i+1,\sigma} + \hat{c}_{i+1,\sigma}^{\dagger}\hat{c}_{i,\sigma}) + U\sum_{i}\hat{n}_{i\uparrow}\hat{n}_{i\downarrow} \tag{1.1}$$

where i and $i+1$ represent the spatial lattice sites, $\hat{c}_{i,\sigma}^{\dagger}$ and $\hat{c}_{i+1,\sigma}$ denote the creation and annihilation operators respectively associated with an electron with spin σ at site i, $\hat{n}_{i\sigma} = \hat{c}_{i,\sigma}^{\dagger}\hat{c}_{i,\sigma}$ is the spin density operator and the density is given as $\hat{n}_{i\uparrow} = \hat{n}_{i\uparrow} + \hat{n}_{i\downarrow}$. As is evident from the equation, this model is primarily governed by two terms i.e.,

(a) the hopping integral (t): it quantifies the ease with which an electron can hop from site i to its nearest neighbor site $i+1$. It is associated with the kinetic energy of the electrons.

(b) the Coulomb repulsion term (U): it represents the penalty or price the electron has to pay in units of energy to doubly occupy a given orbital, in accordance with the Pauli's exclusion principle.

In the absence of the second term in the above equation, the Hubbard model reduces to the tight-binding model for a single orbital. It is this inclusion of the second term that empowers the Hubbard model to predict a metal to insulator transition as the $\frac{U}{t}$ ratio is varied. Depending on the values of U and t, we can have the following scenarios:

(i) $U = 0$ and t is finite

Here the Hubbard model reduces to the tight-binding model, which predicts a metallic ground state for the system unless the total number of electrons is twice the total number of sites available i.e., n = $2N$ and the system then becomes a band insulator.

(ii) $t = 0$ and U is finite

Here the electrons are stuck to their lattice sites and they are no longer free to hop from one
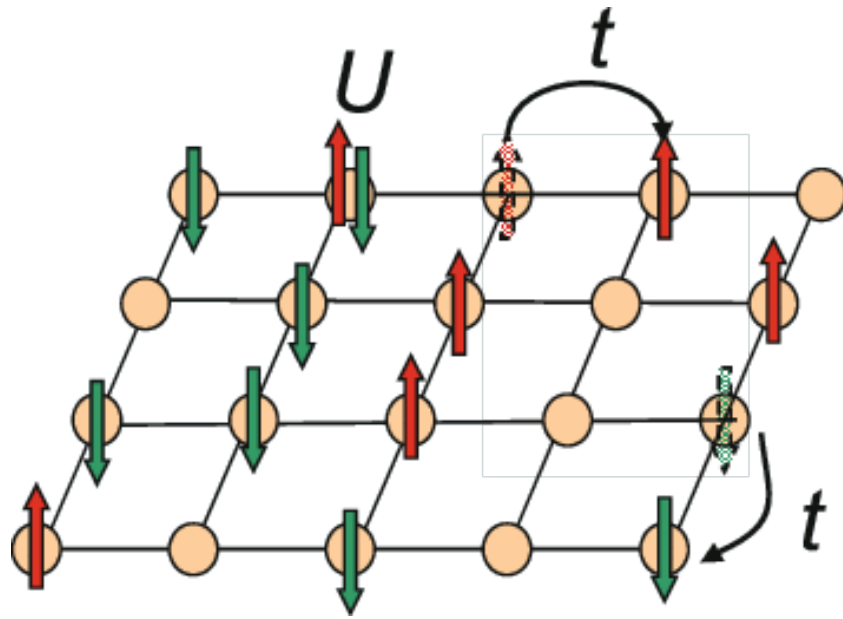
Figure 1.3: Graphical representation of a two dimensional Hubbard model taken from Ref. [60]. Here the up and down arrows represent the up and down spin of the electron respectively.

site to the other. The different lattice sites basically become independent of each other.

(iii) $t >> U$

In this case, the hopping integral is much larger than the Coulomb repulsion term, hence, the bandwidth (W) will be substantially large. This will facilitate the hopping of electrons and the system will exhibit metallic conductivity. Now since U $\neq 0$, the band will split into a Lower Hubbard Band (LHB) and a Upper Hubbard Band (UHB) with U as the splitting energy separating the two bands. This energy gap is also known as a Mott gap. This system will, however, exhibit insulating behaviour if the total number of electrons becomes equal to twice the number of lattice sites as in this case both the LHB and the UHB will be completely filled. Also, there won't be any preferential alignment of spins and so the system should behave like a Pauli paramagnet.

(iv) $t << U$

This is the scenario that explains the insulating ground state in TMOs like CoO, NiO, etc. Since $t << U$, the LHB and UHB will be very narrow as shown in the right panel of Fig. 1.4. The ground state will be a metallic Pauli paramagnet for both $n > N$ (UHB is partially filled) and $n < N$ (LHB is partially filled). But for the special case of half-filling, the ground state will be an antiferromagnetic insulator. This is because for the case of half-filling, the
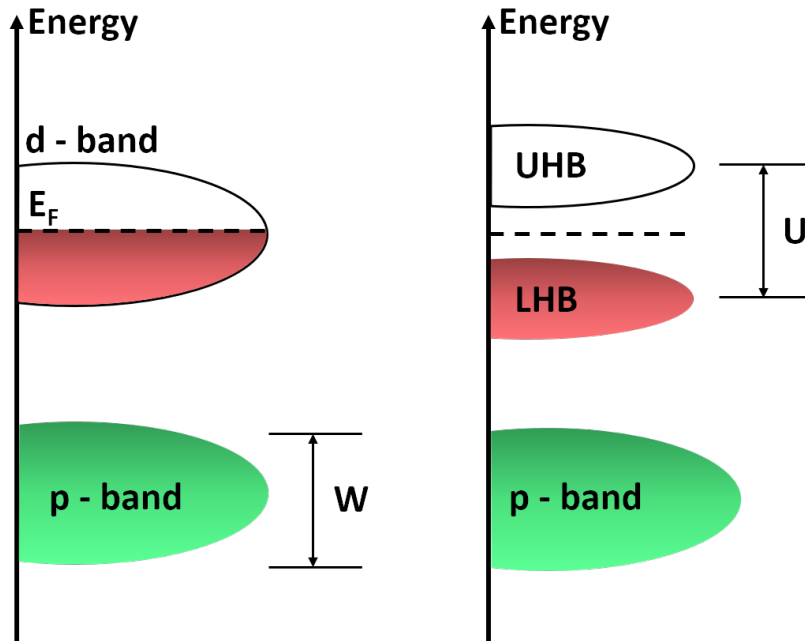
Figure 1.4: Graphical representation of the Hubbard model for the case of half filled d band. The panel on the left shows the unsplit d band in the absence of Coulomb interaction term U and the panel on the right shows the splitting of the d band into lower and upper Hubbard band in the presence of U. Here W and E_F denote the bandwidth and the Fermi energy respectively.

LHB will be completely filled and the UHB will be completely empty and both of them will be separated from each other with a large value of U. Hence, the electron do not have any empty states accessible to them and the ground state thus, turns out to be insulating. On the other hand, the alternating up/down configuration of the spins allows for virtual hopping of electrons (superexchange), which helps in lowering the kinetic energy of the system. Hence, the system prefers to choose the antiferromagnetic configuration of spins as its ground state.

Thus, we see that the Hubbard model is a remarkable theoretical model in condensed matter physics that has provided valuable insights into the behavior of strongly correlated electron systems. Despite its simplistic approach, the Hubbard model has been shown to exhibit a rich variety of electronic phases, including metal-insulator transitions, magnetic ordering, and superconductivity. Later, a more general and versatile model was developed, which is known as the Zaanen-Sawatzky-Allen phase diagram. This model can be applied to a wider range of materials and phenomena, as is discussed next.

1.1.4 Zaanen Sawatzky Allen (ZSA) phase diagram

The Zaanen Sawatzky Allen (ZSA) phase diagram is a theoretical phase diagram that describes the electronic behaviour of transition metal oxides, particularly those with a perovskite crystal structure. It was developed by Jan Zaanen, George Sawatsky, and James Allen in 1985 [61] as a way to explain the fundamental difference between Mott Hubbard insulators and Charge-transfer insulators. The various regions of the phase diagram are discussed as follows:
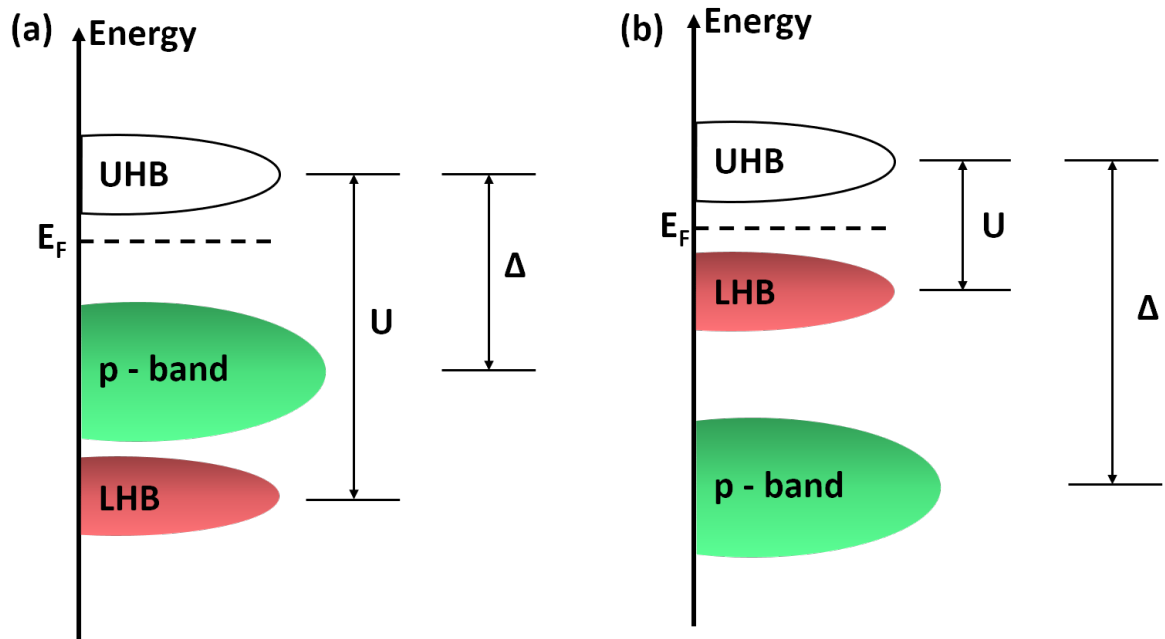
Figure 1.5: Schematic diagram showing (a) the Charge transfer type insulators and (b) the Mott-Hubbard type insulators

(a) $U < \Delta$

In this case, the p-band of the ligand is lower in energy than the LHB as shown in Fig. 1.5 (b). This case corresponds to the region to the right hand side in Fig. 1.6. Here the band gap (E_g) is proportional to U and the Coulomb repulsion term U is less than the charge transfer energy (Δ). Now Δ is defined as the energy required to transfer an electron/hole from the d band of the transition metal to the p band of the ligand. Now if the bandwidth (W) exceeds U, the resultant ground state will be metallic, while, if $W < U$, the resultant ground state will be insulating. These type of insulating TMOs are known as Mott-Hubbard type insulators, for, example, $LaCrO_3$, $LaTiO_3$, TiO, Cr_2O_3, etc.

(b) $U > \Delta$
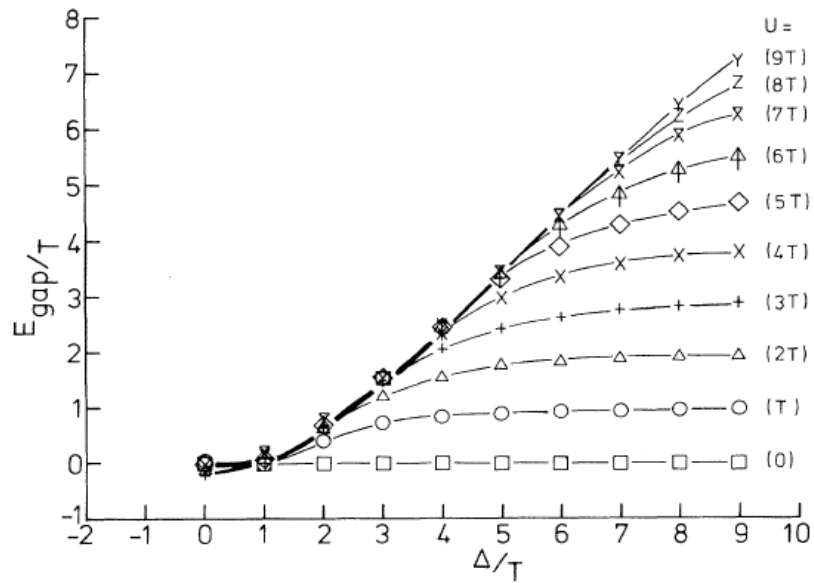
Figure 1.6: The calculated band gap as a function of Δ for various values of U all in units of T (hybridization interaction). For the materials considered 1.0 eV $< T <$ 1.5 eV and W = 3 T. The figure is taken from Ref. [61]
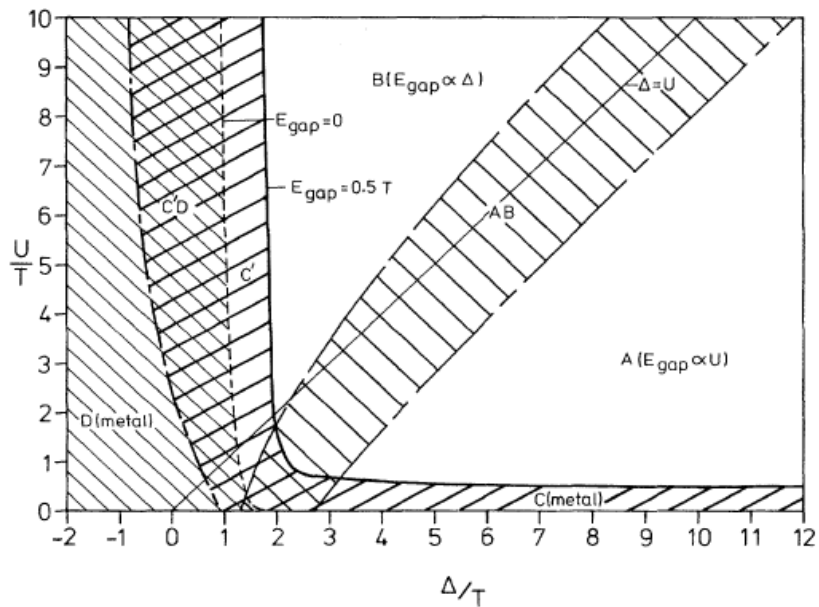
Figure 1.7: The ZSA phase diagram taken from Ref. [61]. Here the heavy solid line represents the separation between semiconducting and metallic ground state.

This is the scenario where the anion p-band is positioned between the LHB and the UHB as shown in Fig. 1.5 (a). This case corresponds to the "converging lines" shown in Fig. 1.6 and the band gap (E_g) is proportional to Δ. Here $U > \Delta$ and hence a transition of electron from the p band to the d band is preferred instead of a $d - d$ transition between the LHB and the UHB. This type of excitation can be represented by the following expression:

$$d_i^n \rightarrow d_i^{n+1}\underline{L} \tag{1.2}$$

where $\underline{L}$ denotes a hole in the anion valence band. The strong hybridization between the transition metal d and anion p orbitals results in strong covalency that raises the p orbital of the anion closer to the Fermi level (see Fig. 1.5 (a)). These type of insulators are called Charge transfer insulators and the late TMOs generally exhibit this type of ground state, for example, NiO, CuO, La_2CuO_4, etc.

For the case of $U = 0$, $E_g = 0$ for all values of Δ and the system is metallic. On the other hand for large U and $\Delta < W/2$, the system results in a metallic ground state. The results discussed above have been pictorially represented in Fig. 1.7 where the different regions are marked as **A, B, C, D, AB, C' and C'D**. Here the Mott-Hubbard insulating phase and the charge transfer phase correspond to the regions **A** and **B** respectively in the ZSA phase diagram. Now that we have discussed the relevant energy scales that govern the physics of the TMOs, we shall now look at the structural aspect of the various systems that we will be discussing in this thesis.

Since the two main systems studied in this thesis have an underlying perovskite structure, it is essential to study the basics of the perovskite structure as is discussed next.

1.1.5 The perovskite structure

A conventional perovskite structure is represented by the general formula of ABX_3, where A and B are two positively charged cations and X is a negatively charged anion (usually oxygen). In an ideal cubic structure, the ABX_3 compound has the B-cation sitting in a 6-fold octahedral coordination while the A-cation exhibits a 12-fold cubooctahedral coordination. Any slight change in the ionic radii of the A and B-site cations leads to distortion from the ideal cubic structure. The degree of distortion from the ideal cubic structure is quantified by the Goldschmidt tolerance ratio (t) [62], given by:

(a) Perovskite Structure

(b) Cubic Perovskite

(c) Tilted & Distorted Perovskite

B-site

A-site

Oxygen

Oxygen vacancy
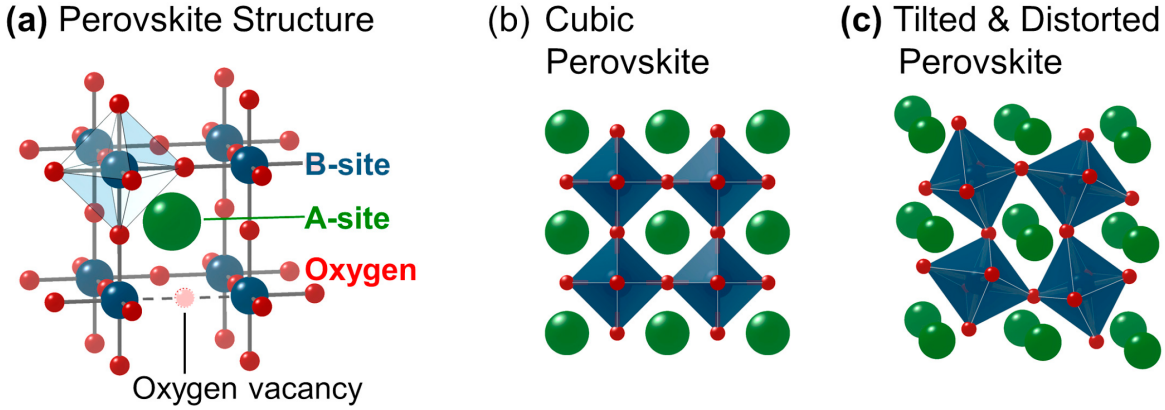
Figure 1.8: (a) Represents the unit cell of a perovskite structure (b) denotes the perovskite in a cubic symmetry and (c) a perovskite with tilted and distorted octahedra. The image is taken from Ref. [63].

$$t = \frac{(r_A + r_X)}{\sqrt{2}(r_B + r_X)} \tag{1.3}$$

where r_A, r_B and r_X denote the ionic radius of the A, B and X-site ion respectively. As the value of t decreases from unity, the distortion from the ideal cubic structure increases. The most common reason behind this distortion is the tilting of the BO_6 octahedra, which can lead to lowering of lattice symmetry (e.g., to orthorhombic or tetragonal), which in turn reduces the coordination number of the A and B cations as shown in Fig. 1.8(b).

When the perovskite structure is layered, it can result in three types of phases, namely, the Aurivillius phase [64], the Dion-Jacobson phase [65] and the Ruddlesden Popper phase [66, 67], which exhibit interesting physical properties. We have extensively studied the n = 3 member of the Ruddlesden Popper phase in the Chapter 4 of the thesis.

1.1.6 The Ruddlesden Popper phase

Over the last few years research activities in the area of Ruddlesden Popper (RP) nickelates has intensified owing to their similarities with high Tc superconducting cuprates [68, 69]. The Ruddlesden-Popper series with the general formula of $A_{n+1}M_nO_{3n+1}$, where A is usually an alkaline earth or rare earth metal ion and M is a transition metal ion and n = 1,2,3,.....,∞; were first reported in the year 1958 [70]. The crystal structure of the various members of the RP series is shown in Fig. 1.9. The structure comprises of n consecutive perovskite layers $(AMO_3)_n$ alternating with rock salt layers (AO), along the crystallographic c direction. The
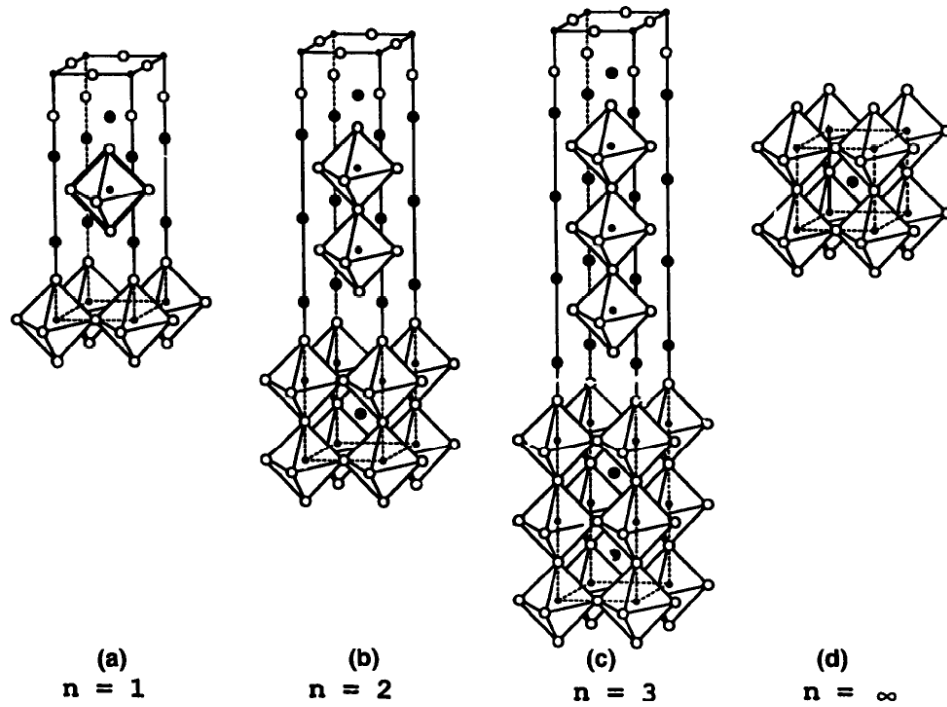
Figure 1.9: Schematic representation of the Ruddlesden-Popper series as a function of "n", taken from Ref. [71].

average oxidation state of the transition metal ion increases with the value of n i.e., for n = 1,2,3,....,∞, the corresponding oxidation state of M ion is +2, +2.5, +2.67 and +3 respectively. The physical properties of the various members within a given series is typically governed by the width of the perovskite slab or the number of layers (n), the nature of the A ion, the M–O bond distance, the M–O–M bond angle and the oxygen stoichiometry [71]. As the number of layers in the perovskite slab increases, the electrical conductivity increases accordingly. For example, the n = 1 member in the rare-earth nickelate series i.e., R_2NiO_4 is an insulator [72] and the n = 3 member i.e, $R_4Ni_3O_{10}$ is metallic [68, 73, 74].

In this thesis, we have explicitly explored the low temperature crystal structure and physical properties of the trilayer nickelates $R_4Ni_3O_{10}$ where R = La, Pr and Nd. These compounds exhibit a metal-to-metal transition (MMT) in the temperature range of 135 to 160 K [75], which was commonly attributed to instabilities driven by charge density waves (CDWs) [76]. We not only look at the physics of the Ni sublattice in this system but also shed light on some new anomalies associated with the rare-earth sublattice.
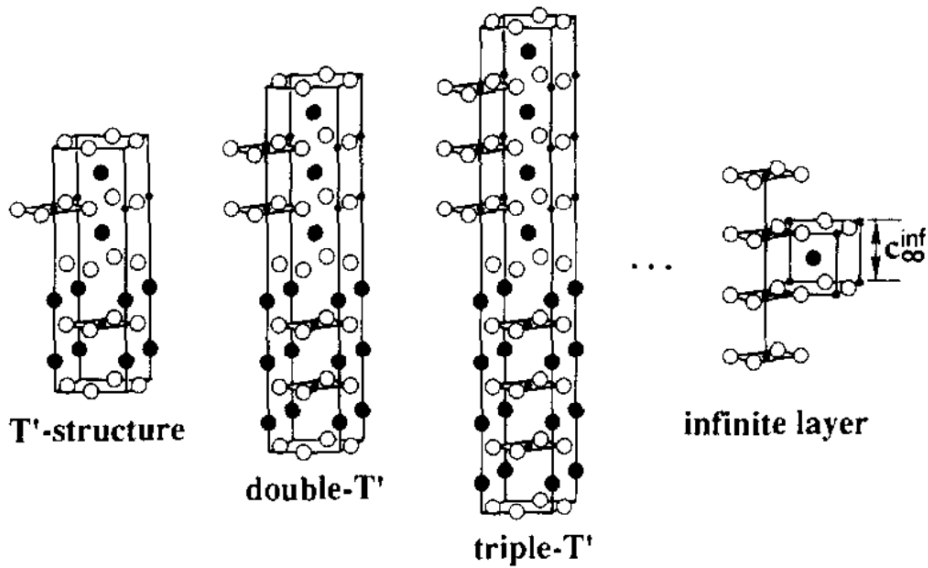
Figure 1.10: Schematic representation of the T' structural arrangement as a function of "n", taken from Ref. [77].

1.1.7 The T' nickelates

The T' mixed valent structure was first stabilized in nickelates by Lacorre in the year 1992 [77]. The general formula of the T' nickelates is given by $A_{n+1}Ni_nO_{2n+2}$ where n can take up values from = 1,2,3,....., ∞. In this structure there are n NiO_2 planes, separated by an intervening fluorite layer of R/O$_2$/R along the crystallographic c direction. These layered nickelates are very similar in structural arrangement to that of high-T$_C$ cuprates. The T' nickelates are obtained from their parent RP phases by the method of reduction [78, 79]. The conversion of the parent RP phase to the T' phase is a reversible reaction under moderate temperature conditions. The details pertaining to this conversion for a specific case of n = 3 are described in section 5.3 of Chapter 5. The mixed valent state of Ni^{1+}/Ni^{2+} in these nickelates is akin to the $3d^9/3d^8$ electronic configuration of Cu^{2+}/Cu^{3+} in the high-T$_C$ cuprates and provides an ideal test bed to test the commonalities and differences between cuprates and nickelates.

1.1.8 Nickelates vs Cuprates

Since the groundbreaking discovery of high temperature superconductivity in copper oxide materials (cuprates) by George Bednorz and Karl Muller in 1986 [50], there have been tremendous efforts by both theoretical and experimental condensed matter physicists to understand the underlying mechanism of this unconventional superconductivity. In fact, the excitement
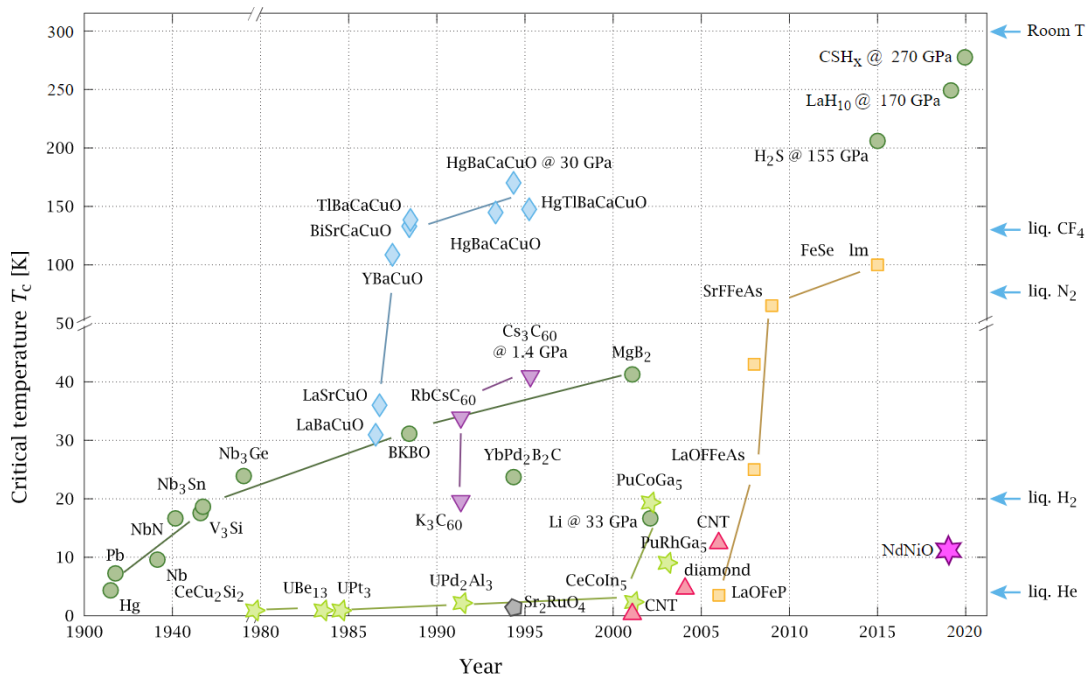
Figure 1.11: Superconducting transition temperatures plotted as a function of year of discovery for various classes of superconductors, taken from Ref. [81].

related to this new class of "high-T_c" materials was so enormous that it resulted in the famous marathon superconductivity session at the 1987 APS March Meeting and came to be known as the "Woodstock of Physics" [80]. Later in 1987, the famous duo of Bednorz and Muller was awarded the prestigious Nobel Prize in Physics for their break-through in the discovery of high-T_c superconductivity in Ba doped La_2CuO_4. Efforts have been underway ever since to discover new materials with similar properties. This led to the discovery of numerous superconducting cuprates as well as other families of superconducting TMOs with the T_C climbing up the ladder with every single discovery as shown in Fig. 1.11.

Physicists are still seeking a proper consensus on the underlying mechanism of high-temperature superconductivity, which has led them to search for other cuprate analogs that can imitate the crystal and electronic structure of these HTSCs. This search is aimed at gaining insight into the unconventional superconductivity phenomena. The so called common ingredients that one looks for in these cuprate analogs are namely, (a) large orbital polarization of the e_g states (b) a small value of charge transfer energy gap (Δ) and (c) strong hybridisation between the O $2p$ and transition metal's $3d$ states.

Ni is the most apparent transition metal option to replace Cu due to its proximity to Cu in

the periodic table and ability to attain a stable d^9 electronic configuration, which is similar to that of Cu^{2+}, meeting the aforementioned criteria. In fact, in 1999, Vladimir Anisimov [82] and colleagues predicted that $LaNiO_2$ (which is the n $= \infty$ member of the T' series) can prove to be a strong cuprate analog and may host superconductivity upon suitable doping. However, Lee and Pickett did not agree well with this hypothesis and claimed that "Ni^{1+} is not Cu^{2+}" [83]. However, the long wait of three decades finally came to an end when Hwang *et al.* [84] finally achieved superconductivity in thin films of $Nd_{0.8}Sr_{0.2}NiO_2$ with a T_C of $\sim$ 10-15 K. Later superconductivity was also confirmed in Sr doped thin films of $PrNiO_2$ [85] and in Ca doped thin films of $LaNiO_2$ by Ariando *et al.* [86] in 2021, with the T_C staying more or less in the same ballpark of 9 to 15 K. These results indicated that the superconductivity in the n $= \infty$ member of the T' nickelates was independent of the contribution of $4f$ electrons of the rare-earth member. Further in 2022, superconductivity was also established in the thin films n $= 5$ member of the T' series, which was grown using the sophisticated technique of molecular beam epitaxy (MBE) [87]. These experimental observations further validated the analogy that was drawn between the cuprate and nickelate phase diagram [88–90]. However, till date no experimental signature of superconductivity has been seen in the bulk [91] samples of hole doped $RNiO_2$ members, which further raises questions regarding the intrinsic nature of superconductivity seen in thin films.

The emergence of superconductivity in nickelates marks the beginning of a new era, showcasing the remarkable mastery and control of material scientists in synthesizing these compounds with exact precision. This discovery motivates the possibility of superconductivity in other higher members of the nickelate series as stated by Antia Botana [92] and Warren E. Pickett [93]. Furthermore, DFT studies on the n $= 3$ member of the T' nickelate series, based on the $t - J$ model, reveal possibility of attaining a T_C as high as 90 K upon electron doping [94]. However, recent O K-edge resonant inelastic x-ray scattering (RIXS) measurements carried out on single crystals of $La_4Ni_3O_8$ sample [95] reveal that this member shows mixed Mott-Hubbard and charge transfer character. The values of U and Δ are comparable and hence the doped holes are spread among both the transition metal and oxygen sites in $La_4Ni_3O_8$. Therefore, it is very important to pay close attention to understanding the physics of these higher members of the T' nickelate series.

1.2 Triple perovskites

Since Chapter 6 of this thesis deals with the study of triple perovskites, it is essential to understand the structural aspects of the triple perovskite that govern its physical properties. Triple perovskites are represented by the general formual of $A_3B_3X_9$, where the A and B sites can be occupied by more than one type of ion.
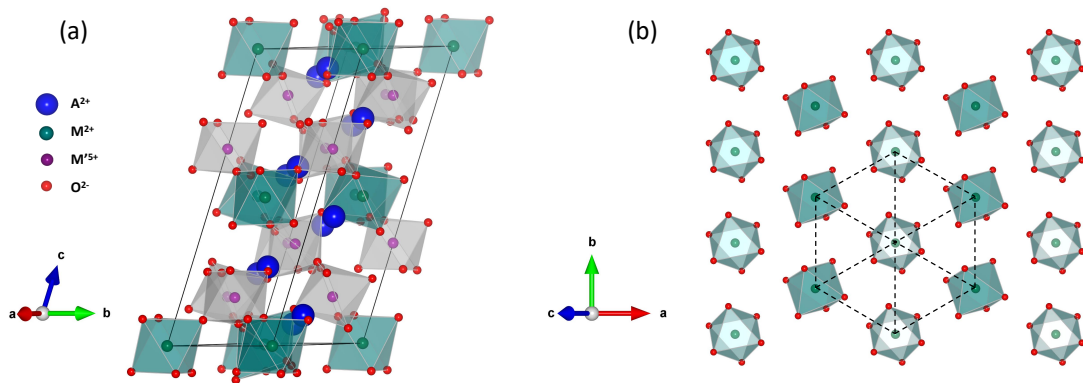
Figure 1.12: (a) Shows the crystal structure of a triple perovskite compound $A_3MM'_2O_9$, stabilizing in the monoclinic symmetry of $P12_1/c_1$. (b) shows the underlying triangular motif formed by the magnetic M ions that gives rise to geometrical frustration.

The typical crystal structure of a triple perovskite compound $A_3B_3X_9$ is shown in Fig. 1.12 (a). Here the B-site is occupied by two types of ions, namely M and M'. Generally, these structures exhibit corner sharing MO_6 octahedra, where the magnetic M-ion forms a triangular lattice in the *ab* plane, as shown in Fig. 1.12 (b). These triangular layers are well separated from each other by either corner-sharing or face-sharing double octahedra formed by M' ions. It is this underlying triangular motif that gives rise to geometrical frustration in these compounds, which will be discussed in section 1.2.1. These compounds are highly flexible in terms of the elements that can be accommodated at the A and B sites. This chemical tunability allows one to use triple perovskites as excellent multiferroics [96–98], photocatalysts [99], dielectrics [100, 101], relaxor ferroelectrics [102], and so on. For a given A or A-site occupied only by one type of atom and B-site by two types of atoms, say B and B' (as in $A_3BB'_2O_9$), the degree of B-site ordering [103, 104] governs the physical properties of the system. The presence/absence of B-site ordering can be ascertained by the presence/absence of superlattice

peaks [105–107], which arise because this ordering imparts a new periodicity in the lattice. The existence of layered arrangement and the possibility of stabilising various types of ions at the B-site provides a wonderful playground to tune the magnetic properties of these systems. In some cases, disordered structures of the type A(BB')X$_3$ can result when the charge difference between the B and B' sites is less than 2 or the ionic radii of B and B' are comparable. Apart from charge and ionic radii difference, the temperature of synthesis also has a deciding role to play in the degree of B-site ordering. In fact, Gallaso and Pyle carried out a detailed study of the effect of sintering temperature on the degree of B-site ordering [108, 109]. For example, Mg^{2+} and Ta^{5+} in Ba(Mg$_{1/3}$Ta$_{2/3}$)O$_3$ calcined at 1600°C, are completely ordered in 1:2 arrangement, while synthesis at a lower temperature of 1300°C results in a disordered arrangement [110].

In fact, in Chapter 6 of the thesis, we discuss in great detail the ordered and disordered variants of the triple perovskite compound Ca$_3$NiNb$_2$O$_9$ and how annealing experiments at higher temperatures in air resulted in the transformation from a disordered phase to an ordered phase.

1.2.1 Geometrical frustration

In the context of magnetic materials, the term "frustration" was first coined by Gerard Toulouse in 1977 [111]. Geometrical frustration is a phenomenon that occurs in magnetic materials when the arrangement of magnetic spins is incompatible with their tendency to minimize their energy. The simplest case of geometrical frustration in 2D is seen in systems with triangular lattice motifs, where the nearest neighbour Ising spins are coupled antiferromagnetically. Here the two spins sitting at the vertices of the triangle can align antiparallel to each other but the third spin cannot satisfy its antiparallel arrangement with either of the remaining spins (see Fig. 1.13(a)). This gives rise to a sixfold degenerate ground state as shown in Fig. 1.13(b). Frustration usually tends to suppress (conventional) magnetic order and is quantified using a parameter known as the "frustration index", first introduced by Arthur Ramirez [112] and is given by:

$$f = \frac{|\theta_{CW}|}{T_N} \tag{1.4}$$
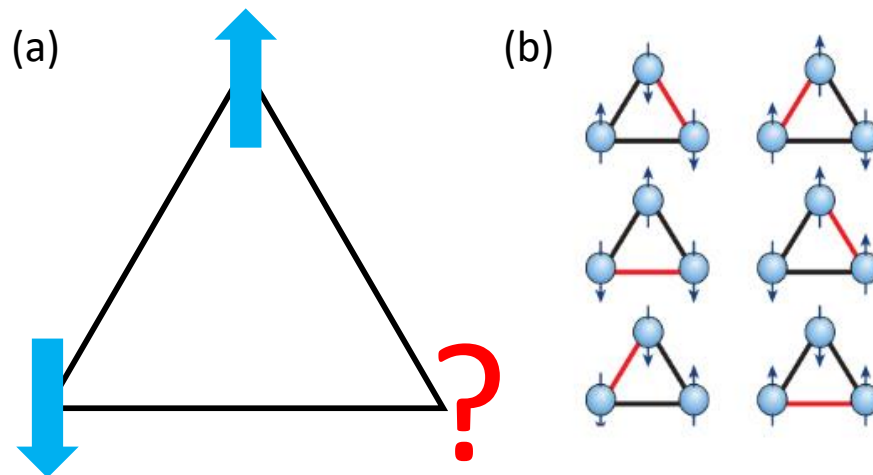
Figure 1.13: (a) Graphical representation of geometrical frustration on a trianglular lattice of Ising spins that are coupled antiferromagnetically. (b) Shows the 6-fold degenerate ground state that arises due to geometrical frustration on a triangular lattice. Here red color of the bond indicates that it is frustrated.

where θ_{CW} is the Curie-Weiss temperature that measures the magnitude of exchange interaction between moments and T_N is the magnetic ordering temperature. Values of $f > 10$ indicate the presence of high frustration in the system that inhibits long range magnetic ordering in the system. Such a scenario may give rise to exotic quantum states of matter like the spin liquid [113], spin ice [114], spin glass [115], etc. In Chapter 6, we extensively study the effects of geometrical frustration in a triangular lattice. We look at the effects of lattice distortion on the ground state of a triple perovskite system and see how frustration and quantum fluctuations can lead to a cooperative effect that stabilizes the 120° ordered ground state.

1.2.2 120° ground state and Magnetization plateaux

The triangular lattice antiferromagnet (TLAF) is one of the simplest geometrically frustrated spin system that exhibits two distinct ground states: a disordered ground state (i.e., spin liquid state) stabilized by strong zero-point vibrations [116–118], and a long range ordered ground state characterized by a 120° spin structure [98,119,120] at zero magnetic field. For small spins (S = $\frac{1}{2}$ or 1) sitting on such triangular lattice, strong quantum spin fluctuations emerge at low temperatures, resulting in the formation of exotic ground states [119,121–125,125–129]. One such phenomenon is the evolution of the ordered 120° ordered ground state into the novel up-

up-down (uud) state and oblique phase at non-zero magnetic fields [98,120,123,128,130,131]. This colinear uud state is unique in the sense that it has a total moment that is precisely equal to one-third of the saturation magnetization (M_S) and is stabilized over a broad range of applied fields, resulting in a magnetization plateau. In classical Heisenberg TLAF, thermal fluctuations are responsible for stabilizing the uud state, while for systems having small values of spin (S $= \frac{1}{2}$), quantum fluctuations stabilize the uud state [119]. The uud state becomes energetically unstable at higher magnetic fields, yielding to the oblique phase. Experimentally, both the quantum spin liquid (QSL) and the 120° ordered ground state have been stabilized in triple perovskite systems [98,119,132,133].
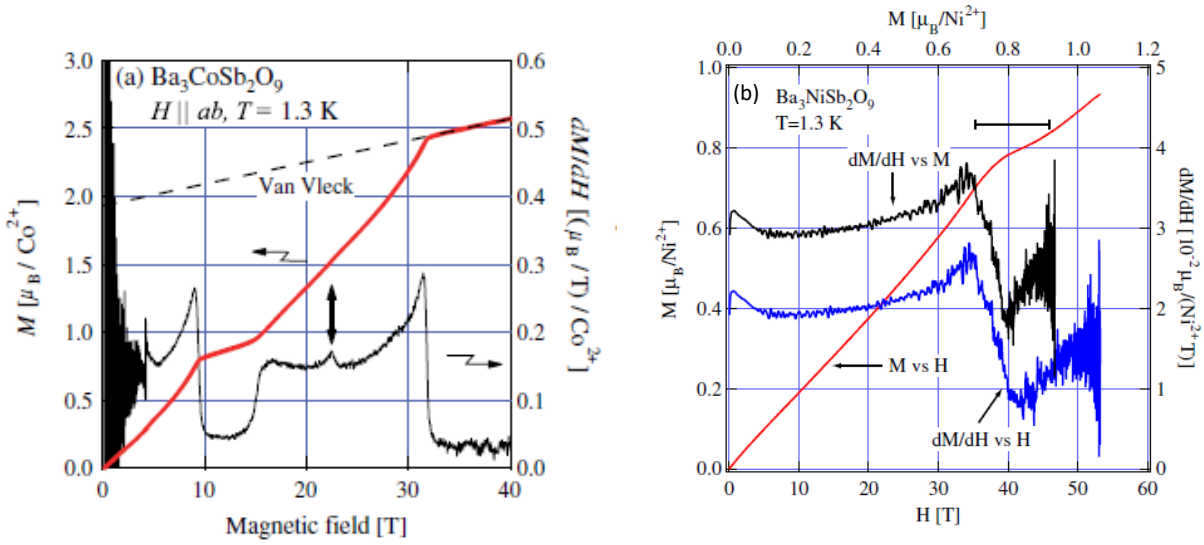
Figure 1.14: (a) and (b) show the experimental observation of magnetization plateau in single crystals of $Ba_3CoSb_2O_9$ and polycrystalline sample of $Ba_3NiSb_2O_9$; (a) and (b) are taken from Ref. [124] and Ref. [119] respectively.

Magnetization plateaus [134–137] refer to a phenomenon in which the magnetization of a magnetic material remains constant over a range of applied magnetic fields, instead of increasing linearly with the field strength. These plateaus are hallmarks of frustrated magnetic systems, where the crystal lattice structure and the interactions between the magnetic moments of the atoms create an energetically stable configuration that prevents the magnetization from changing. This results in plateaus that occur when the magnetization is pinned at a fraction of its saturation value, in agreement with the predictions made in some pioneering papers [136,138–142] of the field.

Magnetization plateaus have been observed in frustrated magnetic systems like the kagome lattice [143, 144], the spin-1/2 Heisenberg antiferromagnet on a Shastry-Sutherland lattice [145, 146], triangular lattice antiferromagnets with both spin-1/2 [127, 128] and spin-1 [98], and the spin-3/2 antiferromagnet on a breathing pyrochlore lattice [147], among others. These plateaus can be understood in terms of the competition between the magnetic interactions and the applied field, and they provide insights into the complex behavior of frustrated magnetic systems.

In Chapter 6 of this thesis we discuss about the possible experimental evidence of one-third magnetization plateau associated with the uud state in triangular lattice antiferromagnetic system. We establish the need of high quality single crystals for unambigious observation of these magnetization plateaux.

Chapter 2

Experimental Methods

One of the biggest challenges of experimental condensed matter physics is the need for suitable model materials that satisfy the stringent conditions set by theoretical contructs. Robust experimental verification of these theoretical models need synthesis of high quality samples, whose physical properties are accurately measured and are reproducible. This chapter discusses the various experimental techniques used to characterize low-dimensional quantum magnets. Some of the experimental techniques include probes that are used to establish the phase purity of the samples, like x-ray powder diffraction (XRPD), Scanning Electron Microscopy (SEM), polarized optical microscopy and Laue diffractometer. Other experimental techniques involve low-temperature characterization of the samples with instruments such as the Physical Properties Measurement System (PPMS), Single crystal neutron diffraction, zero field capacitive dilatometry and pulsed high field magnetization measurement. In this chapter, we shall briefly discuss the working principle of the techniques involved in establishing the structure-property relationship in the studied quantum materials.

2.1 Synthesis

The term "synthesis" refers to the act of forming a new chemical entity by carefully combining stoichiometric ratio of requisite precursors and subjecting them to favourable formation conditions. The samples studied in this thesis are mainly transition metal oxide (TMO) based systems. The polycrystalline form of these TMOs are typically synthesized using the method of solid state synthesis. Conventional solid state synthesis route involves the following cru-

cial steps: thorough mixing and grinding of carefully weighed amount of precursors using an agate mortar and pestle. This process helps reduce the particle size of the reactants and in turn maximizes their surface area that is in contact with each other. Thereafter pelletization of the powder uisng a KBr or hydraulic press at pressures ranging from 50 to 70 MPa, speeds up the reaction kinetics by reducing the distance or separation between the crystallites. Eventually these polycrystalline pellets are then placed in alumina crucibles and subjected to heat treatment at high temperatures. This process is called as "sintering" and can last from several hours to days to months, (with intermediate grinding and repelletizing), depending on the reaction speed. After each such cycle, the pellets are ground and their phase is checked using lab based x-ray source. If the precursors are found to be unreacted, the entire process is repeated. Once the reaction between the precursors is complete and the required phase has been stabilised, the sintering process is brought to an end.

In this thesis, we have worked on three main classes of compounds that required their own specialized synthesis protocol, i.e.,

(a) The Ruddlesden Popper (RP) nickelates: In Chapter 4 we mainly focussed on the n = 3 members of the RP nickelate family. These compounds were synthesized using the sol-gel method, followed by solid state synthesis.

(b) The infinite layer nickelates: In Chapter 5 we study the reduced variants of these RP nickelates, i.e., the infinite layer nickelates with the T' structure. These compounds are derived from the parent RP phases using the method of topotactic reduction or reduction under a stream of H_2 or Ar - 10% H_2 gas.

(c) Triangular lattice AFM: In Chapter 6, we study the triangular lattice antiferromagnet - $Ca_3NiNb_2O_9$. The polycrystalline samples of this compound was first prepared using solid state synthesis and then single crystals were grown using the four mirror optical floating zone technique.

2.2 Structural and compositional characterization

For confirming the structural and compositional homogeneity of the synthesized samples, lab based PXRD and scanning electron microscopy (SEM) was used. For the case of single crys-

tals, small circular discs were cut from the grown crystal boule at various lengths and examined using optical microscopy, SEM, energy dispersive x-ray (EDX) analysis and powder XRD. To confirm the local structure, High Resolution Transmission Electron Microscopy (HRTEM) and selected area electron diffraction (SAED) was also carried out. The vivid details of these characterization techniques are given in the upcoming section.

2.2.1 Powder x-ray diffraction

Powder x-ray diffraction is a simple yet powerful bulk sensitive technique used to verify the phase purity of the synthesized samples. Diffraction of light occurs when it is scattered off of a periodic array of atoms that exhibit long range order. X-rays are most commonly used to obtain the diffraction pattern as their wavelength is often of the same order of magnitude as the lattice spacing d between two crystallographic planes. Bragg's law [148], formulated by William Henry Bragg and William Lawrence Bragg in the year 1913, forms the basis of x-ray diffraction technique and is given as:

$$2d \sin \theta = n\lambda \tag{2.1}$$

Here, d represents the interplanar spacing between the lattice planes, λ represents the wavelength of the incident x-ray beam, θ represents the angle of incidence of the beam and n is the order of the reflection. Bragg's law basically specifies the condition for constructive interference between the x-rays that get diffracted from a given crystal lattice.

The x-rays are typically generated in a cathode ray tube where electrons are accelerated using a potential difference and are then bombarded on an anode material that is used as a target. When these electrons suffer collision at the target material, they are suddenly decelerated and give rise to electromagnetic radiation in the form of x-rays. This is also known as "breaking radiation" or "Bremsstrahlung", which gives rise to a continuous spectrum in the diffraction pattern. When the incoming electrons have sufficient energy to dislodge inner shell electrons of the target material, a vacancy is created. Another electron may fill the vacancy and in doing so releases an x-ray photon of a specific energy, known as characteristic x-rays. These spectra consist of several components, the most common being K_α and K_β. K_α consists, in part, of $K_{\alpha 1}$ and $K_{\alpha 2}$. $K_{\alpha 1}$ has a slightly shorter wavelength and twice the intensity as $K_{\alpha 2}$.
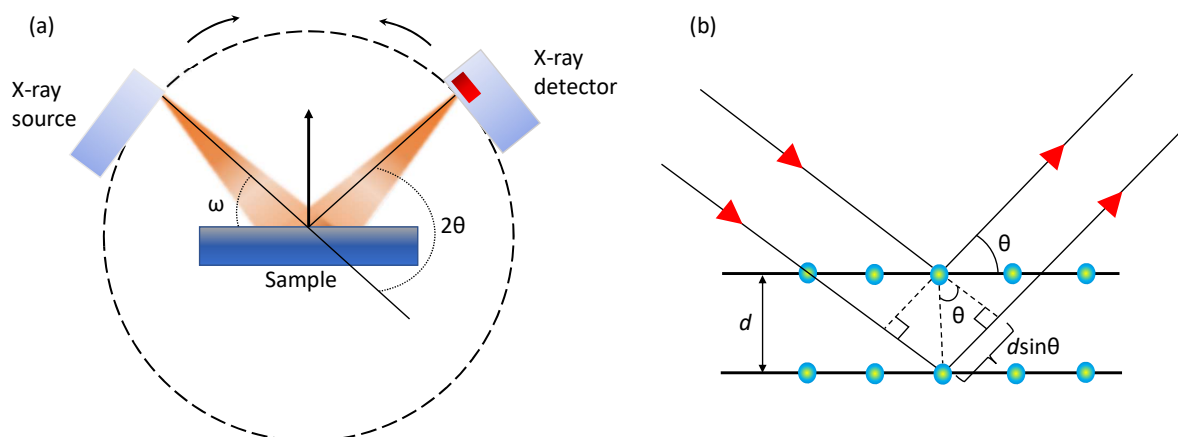
Figure 2.1: (a) Represents the Bragg-Brentano geometry where the incident and diffracted beams are focussed at a fixed radius from the sample position; (b) shows the schematic representation of diffraction of x-rays by a periodic array of atoms in a crystal.

The most commonly used geometry for conducting x-ray diffraction is the Bragg-Brentano geometry as shown in Fig. 2.1(a). This geometrical arrangement offers high-resolution and high beam-intensity analysis at the cost of very precise alignment requirements and carefully prepared samples. Here, both the x-ray source and the detector move synchronously and a diffraction pattern is recorded electronically where the peak intensities are plotted as a function of the diffraction angle 2θ. In this thesis, lab-based XRPD experiments were carried out using a Bruker D8 Advance diffractometer with a Cu- $K\alpha$ source ($\lambda_1 = 1.54060$ Å and $\lambda_2 = 1.54442$ Å), equipped with a Lynxeye detector. The samples were prepared in the form of finely ground powder and then sprinkled on a glass slide with a thin layer of paraffin oil as adhesive. Amorphous material like glass and oil, do not showcase any long range order and hence they do not produce any diffraction peak. Then this glass slide is placed onto the sample holder and x-ray diffractograms are collected as per the desired 2θ range. The duration of data collection can be increased to several hours in order to improve the intensity count and the signal to noise ratio. The resultant diffraction pattern was then compared with the simulated pattern present in the standard ICDD PDF-2 database to confirm the phase purity of the sample.

2.2.2 Rietveld refinement

Rietveld refinement [149], named after Hugo Rietveld [150], is a method of non-linear least square fitting where we fit a model to our experimental data. It is a method for estimating the intensities of the Bragg peaks in a diffraction pattern within the constraints imposed by the crystallographic space group. Since it is a refinement procedure and does not solve the crystal structure, one must already have a pre-defined knowledge of the space group symmetry in which the sample is stabilising. For a typical structural refinement process using the Rietveld method, first the correct space group symmetry is input into the FullProf program [151]. Then one refines the scale factor followed by the background, which results in the scaling of the experimental data w.r.t. the simulated pattern. Thereafter the lattice parameters and zero point correction are refined to locate the Bragg reflections. Subsequently the peak shape is refined based on the peak profile choosen (e.g. Pseudo Voigt, Thomson Cox Hastings, etc). This is followed by refinement of atomic positions and atomic occupancies that affects the peak intensities. The isotropic thermal factor "B" can also be refined individually for each element depending on the data quality and it helps give an estimate of the thermal motion of the ions from their mean position. The Rietveld method is aimed at minimizing the function S, where S is given as:

$$S = \sum_{i}^{n} w_i (y_{io} - y_{ic})^2 \tag{2.2}$$

Here y_{io} and y_{ic} are the observed and the calculated peak intensities at the ith step of diffraction pattern i.e., at each 2θ value and w_i is a weighing factor given by $w_i = \frac{1}{y_{io}}$. The calculated intensities in this fitting model are given as:

$$y_{ic} = s \sum_{k} L_K |F_K|^2 \phi(2\theta_i - 2\theta_K) P_K A + y_{ib} \tag{2.3}$$

where s is the scale factor, K is a given Bragg reflection, L_K contains Lorentz polarisation and multiplicity factors, ϕ is a reflection profile function, F_K is the structure factor for the Kth Bragg reflection, P_K is the preferred orientation function, A is an absorption factor and y_{ib} is the background intensity at the ith step. For all the refinements carried out in this thesis, Pseudo-Voigt peak shape was used, which is given by the following expression:

$$\eta L + (1 - \eta)G \tag{2.4}$$

where L and G denote the Lorenztian and Gaussian contribution to the peak shape and η is the mixing parameter, which can be refined as a linear function of 2θ. The mathematical form of L and G is given as:

$$G = \frac{(4 \ln 2)^{1/2}}{H_k \sqrt{\pi}} \exp[-4 \ln 2 (2\theta_i - 2\theta_k)^2] \tag{2.5}$$

and

$$L = \frac{2}{\pi H_k} \frac{1}{[1 + 4 \frac{(2\theta_i - 2\theta_k)^2}{H_k^2}]} \tag{2.6}$$

Here $2\theta_k$ is the calculated position for the kth Bragg reflection corrected for the counter zero-point and H_k is the FWHM of the kth Bragg reflection and is given by the Caglioti formula:

$$H_k^2 = U \tan^2 \theta + V \tan \theta + W \tag{2.7}$$

where U, V and W are free parameters and depend on the sample and the instrument used for the diffraction experiment. Refinement of U, V and W affects the peak shape of the diffraction pattern. Since refinement depends on finding the best fit between the calculated model and the experimental data, it is important to have a numerical figure of merit quantifying the quality of the fit. Below are the figures of merit generally used to characterize the quality of a refinement. They provide a quantitative assessment on how well the model fits the observed data:

Profile residual (reliability factor):

$$R_p = 100 \left[\frac{\sum_i |y_i^{obs} - y_i^{calc}|}{\sum_i y_i^{obs}} \right] \tag{2.8}$$

Weighted profile residual:

$$R_{wp} = 100 \left[\frac{\sum_i (y_i^{obs} - y_i^{calc})^2}{\sum_i w_i (y_i^{obs})^2} \right]^{1/2} \tag{2.9}$$

Bragg residual:

$$R_B = 100 \left[\frac{\sum_j |I_j^{obs} - I_j^{calc}|}{\sum_j I_j^{obs}} \right] \tag{2.10}$$

Expected profile residual:

$$R_{exp} = 100 \left[\frac{(N - P + C)}{\sum_i w_i (y_i^{obs})^2} \right]^{1/2} \tag{2.11}$$

Here N is the number of observations, P is the number of refinable parameters and C is the number of constraints.

Goodness of fit or χ^2:

$$\chi^2 = \sum_i \frac{(Y_i^{obs} - Y_i^{calc})^2}{n - p} = \left(\frac{R_{wp}}{R_{exp}} \right) \tag{2.12}$$

There are some concerns about the reliability of these R-factors, as there is no threshold or accepted value which dictates what represents a good fit. The most popular and conventional figure of merit used is the goodness of fit, given by equation 2.12, which should approach unity given a perfect fit, though this is rarely the case. In practice, the best way to assess the quality of a refinement is a visual analysis of the fit by plotting the difference between the observed and calculated data on the same scale. Once the refinement is satisfactory, the refined structure can be visualized using the VESTA software [152] and the bond lengths and bond angles can be evaluated as well.

2.2.3 Polarized optical microscopy

Optical microscopy under polarized light can be used as a quick visual inspection tool to check for phase segregation in a grown crystal boule as well as to identify the presence of differently oriented structural domains. For this purpose, thin slices of crystal discs were cut from different regions of the grown crystal using a low-speed diamond saw (Buehler, USA) and a wafering blade of thickness ~ 0.15 mm. During the cutting process, isopropyl alcohol was used as a coolant as the grown crystals were not sensitive to moisture. In order to remove undulations on the surface of the thin crystal discs, polishing was carried out using a silicon

carbide polishing paper. The grit size of these polishing papers was gradually varied from 1000 to 1200 in order to obtain a mirror - finish on the crystal surface. Then these polished crystal discs were examined under polarized light using the optical microscope as shown in Fig. 2.2. As is clear from the zoomed in region in panel (b), there is some phase segregation and the impurity phase has accumulated in the form of tiny triangular patches.
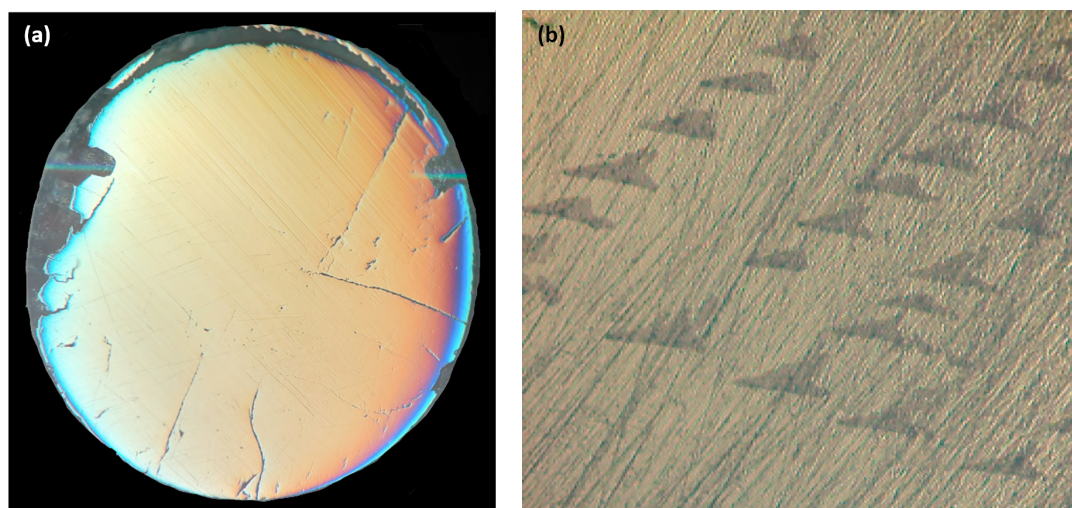
Figure 2.2: (a) shows the representative optical image under polarized light of a polished section of the crystal boule of $Ca_3MgNb_2O_9$ (b) shows a zoomed in region of the outer edge of the $Ca_3MgNb_2O_9$ crystal boule with signs of phase segregation.

2.2.4   Scanning electron microscopy (SEM) and Energy Dispersive X-ray spectroscopy (EDS)

Scanning electron microscopy (SEM) and Energy Dispersive x-ray Spectroscopy (EDS) are used as complementary techniques in addition to powder XRD to confirm the compositional homogeneity of the synthesized samples. A scanning electron microscope helps us image the sample by performing a raster scan over a small area of the specimen (ranging from few nm to hundreds of micron) using a highly energetic, focussed beam of electrons. The incident electron beam then interacts with the sample and produces multiple types of electrons (secondary, backscattered and Auger electrons) and photons. The secondary electrons provide information about the sample morphology and topography while the backscattered electrons are valuable in depicting contrasts in composition in multiphase samples. Apart from this, when secondary electrons are emitted from the inner shells of the atom, the electrons from the outer shell lose

energy and fill these vacancies. The energy thus released is seen in the form of x-ray photons and the wavelength of these emitted x-rays is characteristic of the atom. Hence, by detecting the energies of these x-ray photons, the elemental composition of the sample can be accurately determined. However, care must be taken to choose a proper value of incident beam energy to accurately determine the elemental composition of the sample. One may choose a higher excitation voltage for better penetration of electrons deep into the sample and obtain more data from the interior of the sample. But it may so happen that these electrons might suffer collisions and may not reach the detector. This gives rise to the error in carrying out qualitative analysis. An empirical rule to select the excitation voltage for EDS analysis is to choose the incident energy to be twice that of the energy of the highest excitation line for the elements present in the sample.

For the SEM analysis of the samples described in this thesis, a field emission secondary electron microscope (FESEM) from Zeiss Ultra Plus, Germany was used. This FESEM setup was equipped with an EDS analysis probe that had a 20 mm^2 detector from Oxford Inca that offers an energy resolution of 129 eV. A schematic of the FESEM setup is shown in Fig. 2.3.
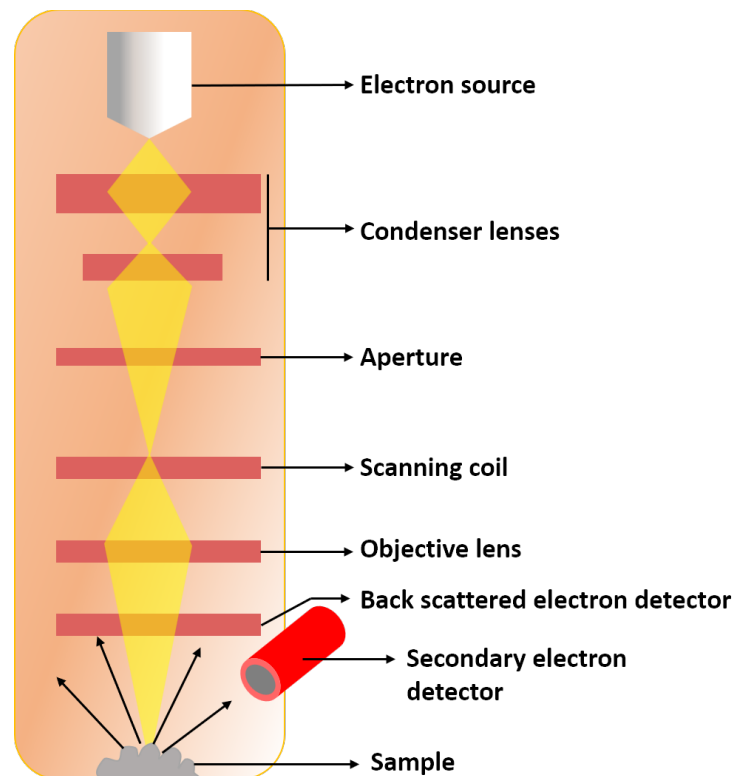
Figure 2.3: Schematic representation of a scanning electron microscope

Freshly broken, relatively flat sections of the sintered pellets were stuck to a double sided carbon tape and loaded onto a SEM stub. For each sample, multiple areas were randomly selected for examining their morphology and composition. In the case of single crystals, a thin disc was cut from the grown crystal boule and then polished to a mirror finish. Thereafter, the side opposite to the polished surface was stuck to the double sided carbon tape and then the sample was examined using SEM. It should be noted that before conducting FESEM imaging, the specimen should be rendered electrically conducting; otherwise a sharp image cannot be obtained and this also generates error in the quantitative determination of elemental composition. Hence, for insulating samples, a thin film of metal (such as gold) is deposited on the sample to make it conducting. The thickness of this deposited film can be of the order of few angstroms and it doesn't affect the resolution of the surface details. Another factor to keep in mind is that EDS detectors are not very sensitive to the presence of lighter elements in the sample such as hydrogen, oxygen, etc. Hence, for the purpose of compositional analysis, only the relative atomic weight percentage of heavier atoms is considered.
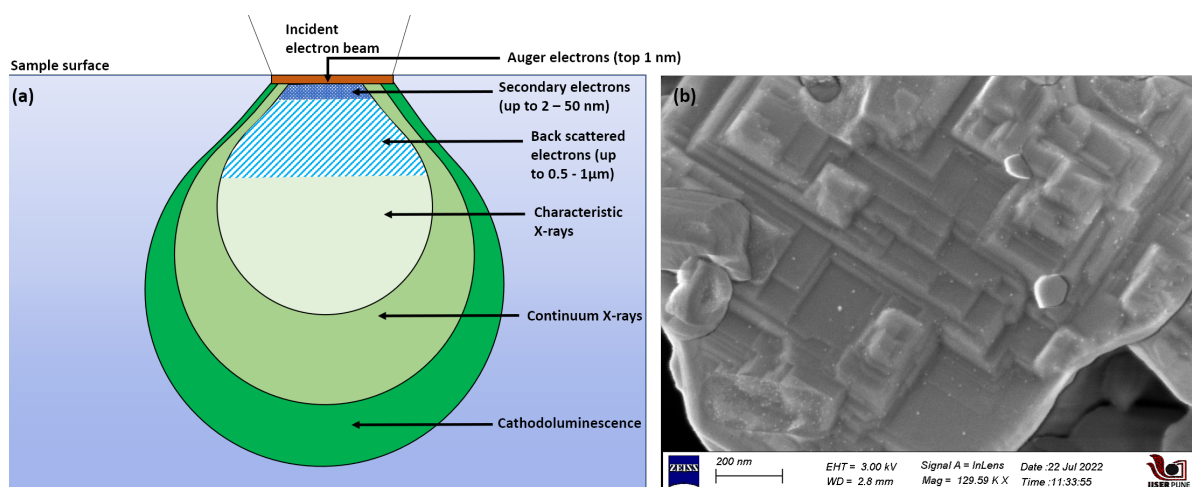
Figure 2.4: (a) Schematic representation of the various signals that are obtained after the incident electrons interact with a specimen during scanning electron microscopy. (b) Shows a typical FESEM image of $La_{0.4}Nd_{3.6}Ni_3O_8$ sample showcasing layered morphology.

2.2.5 Laue diffractometer

The Laue diffraction technique, developed by Max von Laue, is one of the easiest methods used to check the monocrystallinity of a grown crystal. In this method, white radiation (produced by a cathodic source) is incident on a crystalline sample and the diffracted rays are recorded on

a 2D scintillator detector in the form of a symmetric Laue pattern. The obtained laue pattern is then analyzed using the ORIENT EXPRESS software [153], which enables us to estimate the direction of the incident beam w.r.t. the mounted crystal. It also contains simulations that generates the rotation matrix elements that guide you to obtain the desired orientation of the crystal. Crystals oriented along the principal crystallographic directions are very essential if one needs to check for anisotropy in physical properties of the system under study.
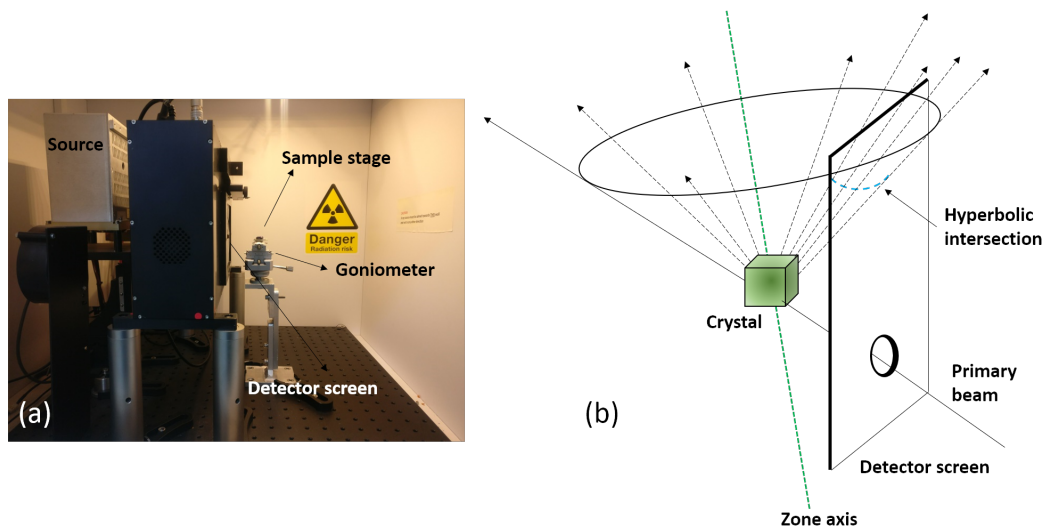
Figure 2.5: (a) Representative image of the Laue diffractometer setup. (b) Schematic showing the principle of a back-scattering Laue experiment.

Parameters	Details
Model	Photonic Science Laue diffractometer, UK and France
Target	Tungsten (Model)
X-ray wavelength	0.35 Å to 2.5 Å (Power = 15 W)
Collimater	Microfocal brush collimator (spot size = 0.5, 1, 1.5 mm)
Detector	GdOS (Gadolinium oxysulphate) scintillator film
Sample to screen distance	4.5 cm

Table 2.1: Specifications of the laue diffractometer instrument used at IISER Pune

The $Ca_3NiNb_2O_9$ crystals, described in this thesis, were oriented using a Laue diffractome-

ter from Photonic Science, UK. The Laue back reflection technique was used to orient the crystal along different crystallographic directions for various thermodynamic measurements. The specifications of the Laue diffractometer setup are given in Table 2.1 and the schematic representation of the Laue setup is shown in Fig. 2.5(a).

2.2.6 Transmission electron microscopy

Transmission electron microscopy (TEM) enables us to image the samples at a significantly higher resolution than typical light microscopes owing to the smaller de Broglie wavelength of electrons. Unlike SEM imaging where the electrons are scattered from the sample and collected at the detector, in TEM the electrons are allowed to pass through the sample to form the image and hence the name "transmission electron microscopy".

Magnified view of the drop casted sample present on the TEM grid
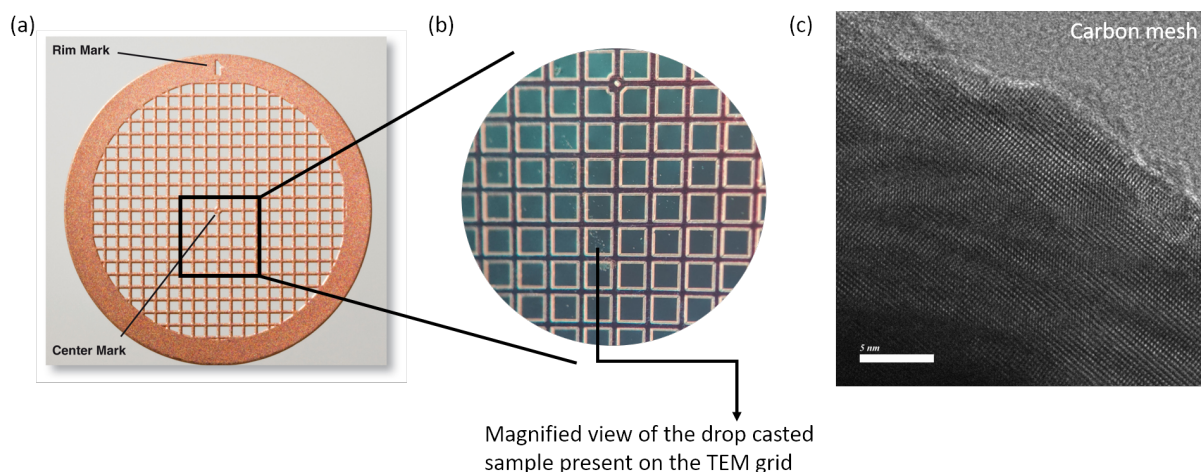
Figure 2.6: (a) Shows a typical Cu TEM grid of 200 mesh size; (b) Shows the magnified image of a section of the TEM grid containing the drop casted sample; (c) shows an HRTEM image obtained for $Pr_4Ni_3O_8$ sample.

For obtaining a clear high resolution transmission electron microscope (HRTEM) image with atomic resolution, proper sample thickness ($\leq$ 100 nm) needs to be ensured so that the electrons can pass through it. Usually the thicker regions of the sample produce a dark image and the thinner regions produce a bright contrast. The various conventional sample preparation techniques that can produce adequate sample thickness include mechanical milling, chemical etching, ion etching, ion milling, etc. However, the samples described in this thesis were prepared for TEM analysis using the method of liquid sonication. In this method, as a first step, less than few mg of the inorganic oxide sample was thoroughly ground in high purity ethanol,

using an agate mortar and pestle. Then the finely ground powder was dispersed in highly pure ethanol solution and sonicated in an ultrasonic bath for a period of 1 hr. The sonication process helps in removing the agglomeration of the sample particles. Thereafter, the solution was drop cast onto TEM copper grid (mesh size 200) that had a layer of amorphous carbon. The TEM grid was dried overnight in an evacuated dessicator and plasma cleaned before the experiment to remove the presence of organic impurities on the surface.

For the HRTEM analysis of the samples mentioned in this thesis, a high resolution transmission electron microscope JEOL JEM 2200FS from Japan was used. It is equipped with a 200KeV field emission gun (FEG) and an in-column energy filter (Omega filter), that allows for a zero-loss image. The collected HRTEM images and selected area electron diffraction (SAED) micrographs were analyzed using the GMS-3 software package. While the HRTEM images give us information about atomic arrangement in the sample, the SAED pattern provides us information about the sample's crystal structure and its orientation w.r.t. the beam direction. In brief, HRTEM imaging serves as a powerful tool to study material properties like particle size, presence of defects, stacking faults, atomic ordering and so on.

The TEM instrument can be operated in two basic modes i.e., imaging and diffraction mode as shown in Fig. 2.7(a) and (b) respectively. For both the modes, the sample is illuminated by a parallel beam of electrons that have been focussed using the system of condenser lenses and condenser aperture. In the imaging mode, the objective aperture is placed at the back focal plane of the objective lens (where diffraction spots are formed). Using this assembly, one can either obtain a bright or dark field image, as per the image requirement. If the objective aperture is positioned in such a way that all the transmitted electrons are allowed to pass through while the diffracted rays are blocked, then one obtains a bright field image. On the other hand, when the signal from the diffracted beam is allowed to pass through, a dark field image is obtained. The signal thus obtained is magnified and projected onto a screen with the help of intermediate and projector lenses. In Diffraction mode, a selected area aperture may be used to determine more precisely the specimen area from which the signal will be displayed. By changing the strength of current to the intermediate lens, the diffraction pattern is projected on a screen.

Imaging mode **Diffraction mode**

Electron Gun

System of condenser lenses
Condenser aperture

Specimen

Objective lens

In back focal plane of
Objective lens

Objective aperture

In image plane of
Objective lens

Selected area aperture
Intermediate lens
(strength changes between two regimes)

Projector lens

Screen

Image Diffraction pattern
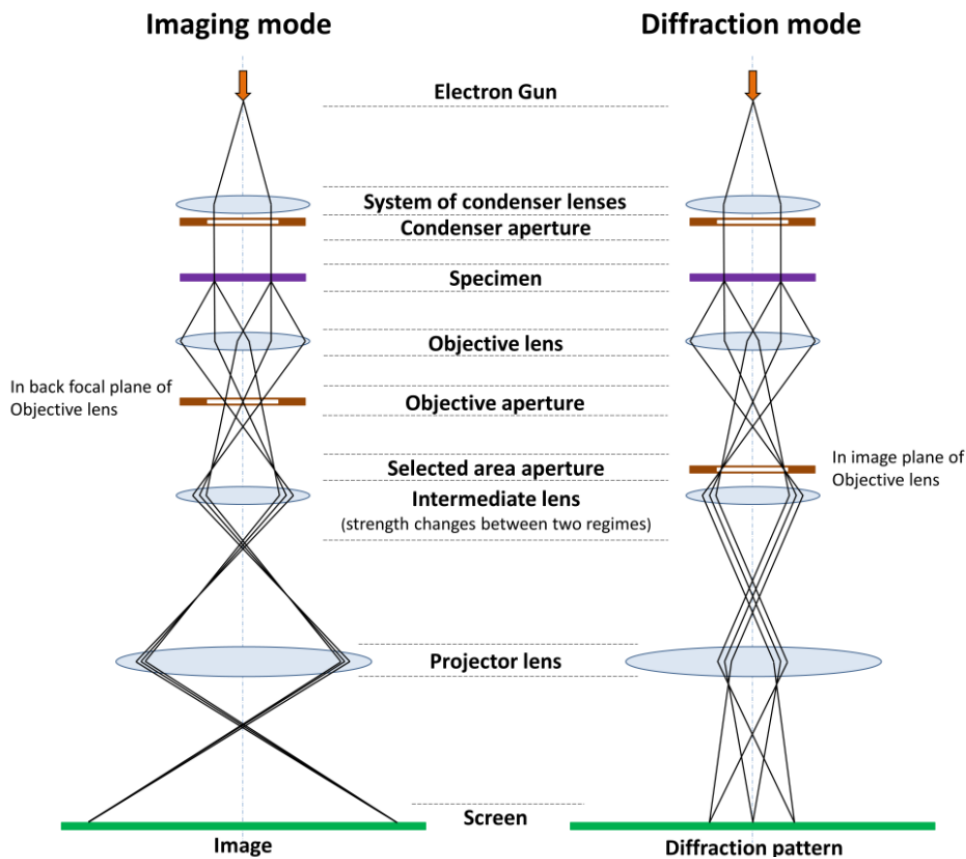
Figure 2.7: (a) and (b) show the schematic representation of TEM in imaging mode and diffraction mode respectively. This image was taken from wikipedia [154].

2.2.7 Synchrotron x-ray diffraction

A synchrotron source is an extremely powerful source of electromagnetic radiation that can be used to probe the physical characteristics of a given sample with great deal of accuracy and sensitivity. It works on the principle that when a charged particle is accelerated, it emits electromagnetic radiation. A synchrotron light source is basically a circular particle accelerator that makes use of bending magnets, wigglers and undulators to generate intense electromagnetic radiation of desired energy and coherence. As the electron's path undergoes a change with the help of magnets, it loses energy in the form of photons. This light can then be channeled out of the storage ring wall and into the experimental stations or hutches called beamlines.

Synchrotron radiation sources are prefered over conventional lab-based sources due to the various advantages associated with it, such as:
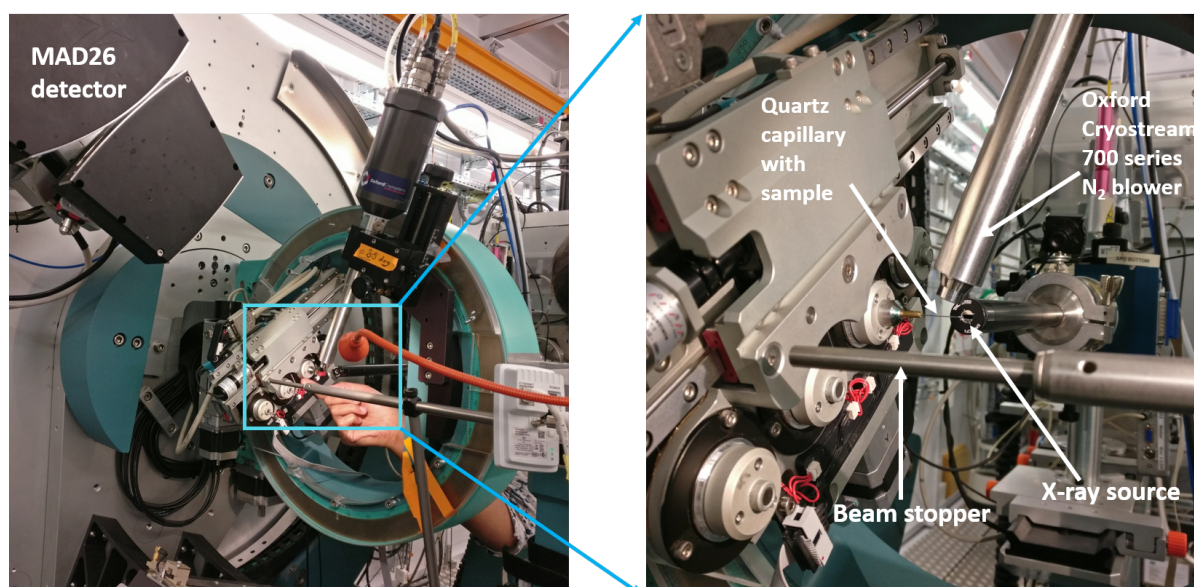
Figure 2.8: Shows the graphical representation of the low temperature synchrotron XRD setup at the MSPD-BLO4 beamline of ALBA synchrotron centre in Barcelona, Spain.

- **Brilliance**: The recent third generation synchrotron sources have enhanced the brilliance of radiation nearly 1000 times [155, 156] than that of lab based x-ray sources. Due to such high brilliance, synchrotron radiation is able to penetrate deep into the material sample under study.

- **Monochromatic beam**: Synchrotron sources can provide highly monochromatic beams depending on the requirement of the user by employing the appropriate single crystal monochromater that can choose from an array of available wavelengths.

- **Preferred orientation**: In conventional lab-based sources, the x-ray diffraction is carried out using flat plate geometry. This geometry can lead to focussing issues based on diffraction angle, area of sample illuminated based on slit width and so on. In synchrotron PXRD, the sample is filled in a capillary tube and hence the diffraction takes place in transmission geometry. This eliminates the problems associated with preferred orientation in the sample.

Parameters	Details
Photon energy range	8 to 50 keV
Flux at sample	$\sim 4 \times 10^{12}$ ph/sec
Energy resolution	2×10^{-4}
Geometry	Transmission geometry
Detectors	(i) Multi Analyzer Detector (MAD); used in the energy range of 8 - 30keV with and angular resolution of 0.02° FWHM (ii) Position Sensitive Detector (PSD) MYTHEN; used in the energy range of 8 - 50keV with and angular resolution of 0.005° FWHM;
Sample environment	(i) Oxford Cryostream 700 series (for 80 - 300 K) (ii) Dynaflow liquid He cryostat (for 10 - 300 K, to be used with samples in capillaries and MAD detection setup)

Table 2.2: Specifications of the MSPD - BLO4 beamline at ALBA synchrotron centre in Barcelona, Spain

When x-ray diffraction is carried out in transmission geometry, one needs to be careful about the sample's x-ray absorption (μR) values. For samples containing elements that have high-Z elements, x-rays can be highly absorbed and this leads to attenuation of diffraction peak intensities, especially at low 2θ angles. However, for samples with moderate absorption values, the peak intensities still remain attenuated but they are less dependent on the scattering angle. The available refinement software packages can correct for these effects and a sensible refinement result can be obtained. The absorption factor for a given sample can be calculated before conducting the experiment and is a function of sample composition, packed sample density, capillary diameter and the x-ray wavelength used. For samples with high absorption values, one can use capillaries with smaller diameter or the sample can be diluted with amorphous powder of silica or boron. For values of μR < 1 in a Debye-Scherrer geometry, no absorption correction is needed but for values of μR ≥ 5, the experiment is not feasible in

capillary geometry and corrections are inaccurate.

In the present thesis, synchrotron x-ray diffraction experiments were carried at MSPD-BLO4 beamline at ALBA synchrotron, Barcelona, Spain and Petra III, DESY (Deutsches elecktronen synkrotronen) beamline, Germany.

2.2.8 Thermogravimetric Analysis (TGA)/Differential Scanning Calorimetry (DSC)

Thermogravimetric analysis is a highly sensitive sample characterization tool that is used to monitor the change in mass of a sample as a function of time or temperature while the sample is subjected to a pre-determined temperature profile in a controlled atmosphere. Using TGA one can estimate the thermal stability of a sample, the oxygen content of a sample, the presence of metastable phases, melting behaviour and so on. Differential Scanning Calorimetry (DSC) is a thermal analysis technique that measures the heat flow into or out of the sample as a function of temperature and time. It is a very powerful technique to evaluate material properties such as glass transition temperature, melting, crystallization, specific heat capacity, oxidation behavior, and thermal stability. On the other hand, by using a simultaneous TGA/DSC setup, one can measure both the heat flow and weight changes in a material as a function of temperature and time in a controlled atmosphere. The complementary information obtained during the simultaneous measurement allows differentiation between endothermic and exothermic processes (e.g. melting, crystallization, etc) that have no associated weight loss and those which involve a weight loss (e.g. sample decomposition).

Before performing any TGA/DSC experiment, one has to choose the type of crucible (alumina, platinum, etc), type of thermocouple (E, K, S, W, etc) based on the temperature profile and sample environment (see Table 2.4), the heating and cooling profile and the gas flow in which one wants to carry out the experiment. The crucible is usually made up of an inert material like alumina or platinum so that the sample doesn't react with it in the programmed temperature range. Moreover, DSC crucibles are usually made with a flat bottom and are made up of a material with a high thermal conductivity. This ensures that there is optimum heat transfer and low temperature gradients between the sample, crucible and sensor.

In this thesis TGA/DSC experiments were mainly used to estimate the oxygen content of
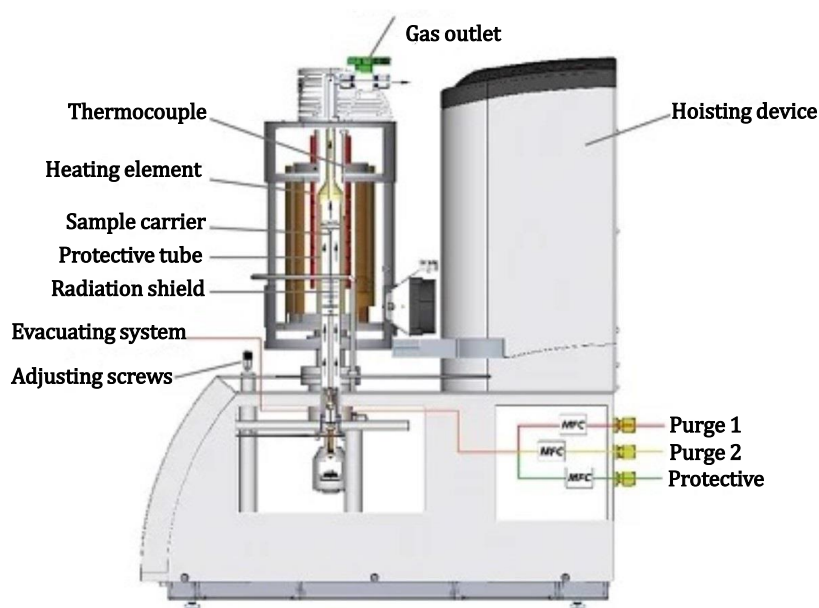
Figure 2.9: Shows the schematic representation of the Netzsch STA 449 F1 TGA setup. This image was taken from Netzsch website [157]

the as-synthesized samples. For this purpose, alumina crucibles were boiled in concentrated HNO_3 till all the acid evaporated. Then these crucibles were boiled in distilled water for few hours. Thereafter, the crucibles were air dried and glowed in a box furnace at a temperature of 1500°C for 12 hr. Then these crucibles were recovered from the box furnace at a temperature of 300°C and kept in a dessicator to prevent absorption of moisture. For estimating the oxygen content in the as-synthesized samples, TGA setup (Netzsch STA 449 F1) was used. A small amount of the sample with weight ranging from 15 - 20 mg was taken in a freshly glowed alumina crucible. The sample chamber was evacuated and purged 6 times to remove all traces of atmospheric oxygen as the W-type carrier is prone to oxidation in presence of trace amount of oxygen at higher temperatures. Then the sample was subjected to an isotherm run in a reducing atmosphere of Ar-H_2 10% that resulted in complete decomposition of the sample. From the observed weight loss in the TGA plot, the oxygen content of the samples was back calculated. PXRD was also carried out on the sample after the completion of the temperature profile to ensure complete decomposition of the sample.

To ensure accuracy of the measurements, regular calibration runs were done at intervals of 3-4 months using standard samples. Temperature calibration was carried out by measuring the melting point of few standard metals like zinc, tin, gold, etc. in a DSC run.

Parameters	Details
Model	Netzsch STA 449 F1 (Top loading)
Temperature range	SiC furnace, RT to 1600°C
Heating/cooling rate	0.001 K/min to 50 K/min (furnace dependent)
TGA resolution	0.025 μg
DSC resolution	$< 1\mu$W (dependent on sensor)
Atmospheres	inert, oxidizing, reducing, static, dynamic, vacuum
Integrated mass flow controller	Present for 2 purge gases and 1 protective gas
Cooling system	water based Julabo chiller

Table 2.3: Specifications of the TGA (Netzsch STA 449 F1) instrument

Sensor thermocouple	Operational temperature range	Atmosphere allowed
Type S (Pt-Pt10%Rh)	RT to 1650°C	oxidizing and inert
Type W (W3%Re-W25%Re)	RT to 2400°C	reducing, inert and vacuum
Type E (Chromel-Konstantan)	-150°C to 700°C	oxidizing and inert
Type K (Chromel-Alumel)	-150°C to 800°C	clean oxidizing and inert
Type P (Platinel)	-150°C to 1000°C	oxidizing and inert
Type B (Pt30%Rh-Pt6%Rh)	RT to 1700°C	oxidizing and inert

Table 2.4: Various types of thermocouples available with the Netzsch STA 449 F1 TGA setup and their corresponding operating protocol.

2.3 Physical properties

The samples described in this thesis were characterized using both lab-based instruments as well as advanced characterization techniques such as single crystal neutron diffraction and synchrotron XRD. But first, we would like to give a description of the lab-based techniques. The low temperature physical characterization was carried out using a physical properties measurement system (PPMS) from Quantum Design, Model 6000, USA. The instrument is equipped with an Evercool-II liquid helium refrigerator that allows the user to access temperatures rang-

ing from 1.9 to 400 K. The sample can be subjected to a magnetic field ranging from + 9 to - 9 T using a superconducting magnet, dipped in the liquid helium bath. For writing the sequence pertaining to the experiment and for controlling the various parameters of the PPMS, commands were relayed to the instrument via an interface called as MultiVu. Various measurement probes, such as specific heat, thermopower, resistivity, dc/ac susceptibility are available with the setup to probe the sample properties. The details pertaining to these setups are presented next.

2.3.1 Electrical transport

Electrical resistance of a sample is basically a measure of the opposition faced by the current flowing through the sample. While the resistance of a sample depends on the sample geometry, the resistivity is a characteristic property of the sample. The resistivity (ρ) of a sample is given by equation 2.13 where R is the resistance of the sample, A is the area of cross section of the sample through which the current flows and l is the distance of separation between the voltage probes.

$$\rho = \frac{RA}{l} \tag{2.13}$$

The resistivity of a regular sample can be measured either by using a two-probe method or a four-probe method. In a two-probe method, the current probes are the same as the voltage probes and hence the resistance measured using this method has a contribution coming from the contact resistance of the measuring leads. To overcome this issue, four probe method of measuring resistivity, introduced by Frank Wenner [158], is preferred. Here a constant current is passed through two outer probes and the voltage drop across the sample is measured across the two inner probes. Since the internal impedance associated with a voltmeter is of the order of 100 MΩ, all the current flows through the sample and the contact resistance does not come into picture.

It is to be noted that for highly resistive samples (where the sample resistance is larger than the contact resistance), the two-probe method can be safely employed. However, for metallic samples, it is ideal to use four-probe measurement geometry. In four-probe method the voltage probes are usually placed very close to the center of the sample as shown in Fig. 2.11. This is
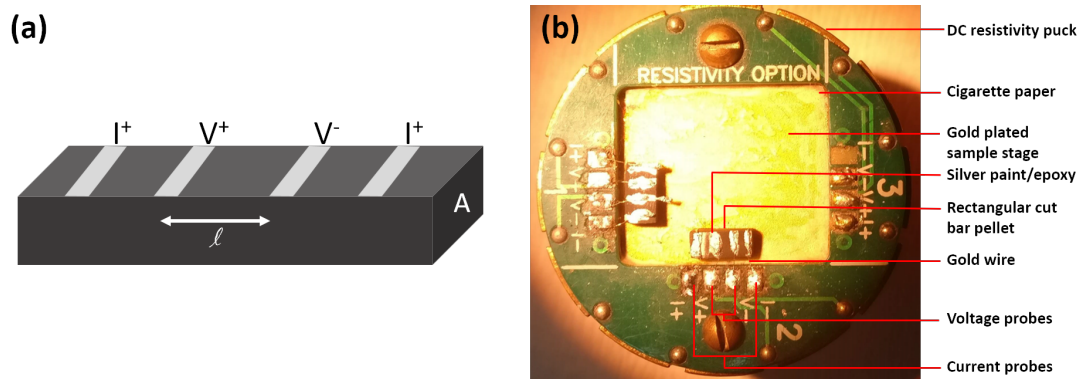
Figure 2.10: (a) Schematic showing the four probe method of measuring electrical resistivity. Here I^+ and I^- are the current probes and V^+ and V^- are the voltage probes. l denotes the distance between the voltage probes and A denotes the area of cross-section through which the current flows. (b) Shows a graphical representation of the DC puck used for four probe resistivity measurement using PPMS.

because, at the center of the sample, the electric lines of force are nearly uniform equidistant from each other. In case one has samples with irregular geometry, the Van-der-paw [159] method can be utilised.
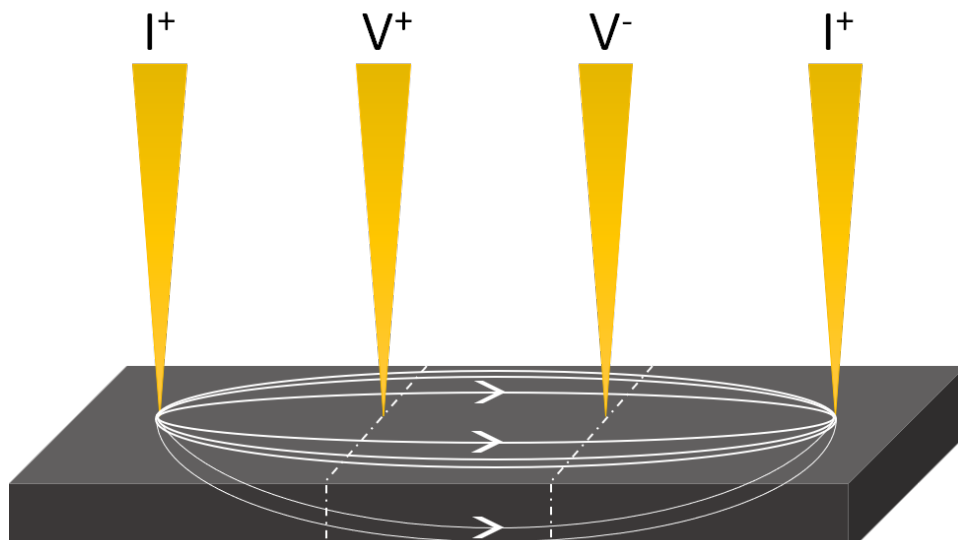
Figure 2.11: (a) Schematic showing the four probe method of measuring electrical resistivity with the electric lines of force marked by solid white lines.

For measuring resistivity using PPMS, the sintered samples were cut into rectangular bars, whose dimensions were precisely measured using vernier callipers. Then the rectangular bar pellet was attached to the DC puck sample stage using GE varnish. Before sticking the sample, the sample stage was covered with a thin layer of cigarette paper using GE varnish to prevent electrical shorting. Then four gold wires of thickness approximately 25 microns were soldered

to the voltage and current pads present on the DC resistivity puck. These wires were then gently laid on the rectangular bar pellet and colloidal silver paste from RS Pro company was used to make the contacts. The contacts were then allowed to cure for 30 min in a dry box before starting the measurement. The distance between the voltage probes was noted down using an optical microscope to convert the sample resistance into resistivity. For samples with metallic temperature dependence, higher currents ranging from 5 to 10 mA was used, while for resistive samples, lower current values was used.

2.3.2 Thermal and thermoelectric transport

Apart from measuring the electrical transport properties, one can also measure the thermal transport properties of a sample using the TT (thermal transport) option provided with PPMS. Using the TTO one can measure the thermal conductivity (κ), thermopower or Seebeck coefficient (α) and resistivity (ρ) of the sample simultaneously. Thermal conductivity measures the ability of a sample to conduct heat through it and hence provides information about the scattering of heat carrying phonons and electrons. On the other hand, Seebeck coefficient is a measure of the electrical voltage generated in a sample due to a thermal gradient present across it. Thermopower of a sample is very sensitive to the sign and density of the charge carriers and hence can act as a powerful tool to analyze the electronic structure of a material.

For performing thermal transport measurements, a rectangular bar shaped sample is mounted in a four-probe assembly onto the TTO puck as shown in Fig. 2.12. Here copper wires (whose enamel had been previously removed) are wound multiple times around the sample and then silver conducting paste is painted over it to ensure proper thermal contact between the sample and the wires. The length of these wire leads is kept around 2-3 mm so that the thermal diffusion time in the leads in minimized. Thereafter, three of these leads are screwed into the gold-coated shoes where two shoes serve as thermometers and one serves as a heater. The fourth lead goes into the cold foot that serves as a heat sink. A tiny amount of Apiezon H-grease is also added onto the part of the wire that goes into the cold sink to ensure proper thermal contact. The entire assembly is then covered with a copper isothermal radiation shield that minimizes the heat lost due to radiation between the sample and the environment. There is a removable cap at the top of this radiation shield that allows to user to visually inspect that none of the wires are touching the body of the radiation shield. Finally the entire assem-
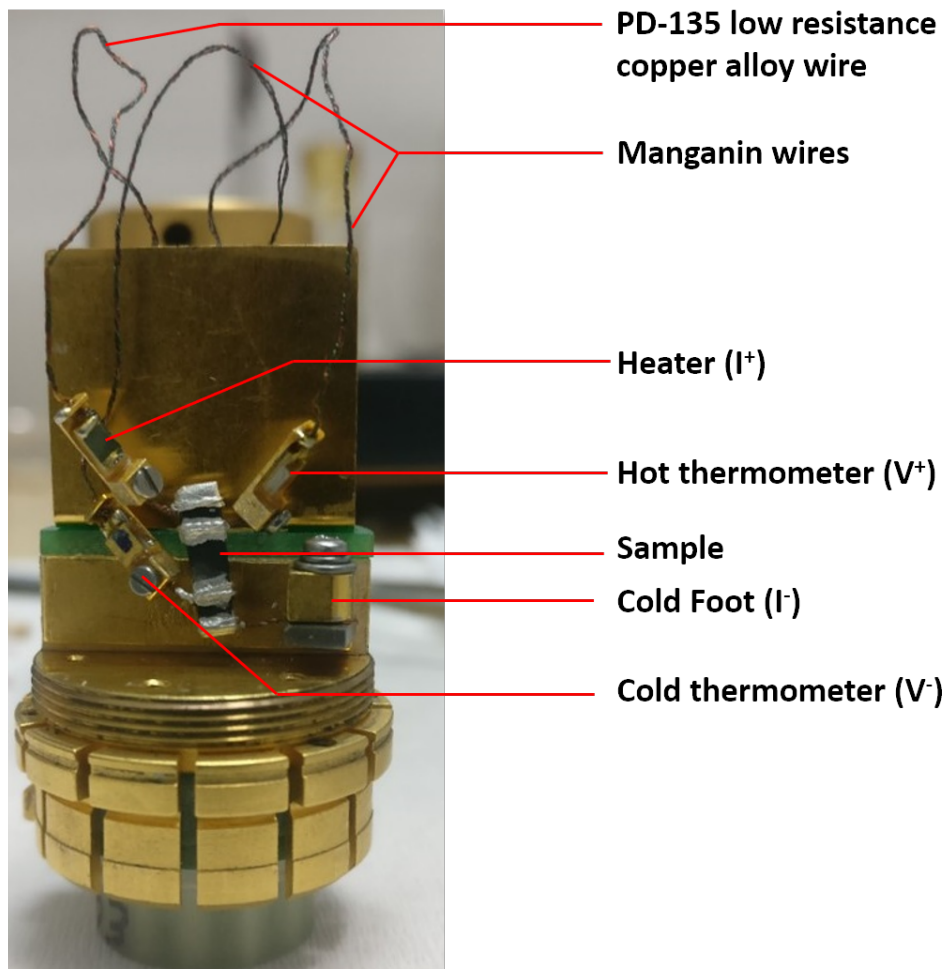
Figure 2.12: Graphical representation of the thermal transport option (TTO) available with the PPMS setup. Here a rectangular bar pellet of La$_4$Ni$_3$O$_{10}$ has been loaded for thermopower and thermal conductivity measurement.

bly is loaded into the PPMS sample chamber, which is then evacuated to a pressure of 10^{-5} Torr to begin the experiment. Such high vacuum conditions are necessary to avoid radiative heat losses during the measurement. The TTO offers two modes of measurement, namely, the "continuous measurement mode" and the "single measurement mode". For all the samples described in this thesis, the continuous measurement mode was used as it is a relatively less time consuming method as compared to the single mode measurement. It makes use of a sophisticated curve-fitting algorithm that determines the steady state thermal properties by extrapolating from the response of a relatively short heat pulse. For measuring κ and α, heat is applied to one end of the sample by supplying current to the heater. Then the temperatures at the hot and cold thermometers are recorded. The corresponding Seebeck voltage generated

due to the thermal gradient is also monitored. Then the supplied heat exits the sample through the cold foot. Electrical resistivity, on the other hand, is measured both before and after the heat pulse is applied.

2.3.3 Specific heat

The specific heat capacity of a material indicates its ability to store heat and is often used as a probe in magnetism to study phenomena like long-range magnetic ordering, phase transitions, structural transitions, etc. Apart from scanning tunneling microscopy, specific heat measurement helps one to directly probe the density of states in a sample. By measuring the specific heat capacity of a material as a function of temperature and magnetic field, it is possible to gain a deeper understanding of the underlying physics of the material. In this thesis, all the heat capacity measurements were carried out using the calorimeter probe attachment of PPMS. Fig. 2.13 shows a schematic representation of the specific heat assembly. It consists of a sample platform of dimension 3 X 3 mm^2, which is suspended by 8 connecting wires made up of Au-Pd alloy. These connecting wires not only provide electrical connectivity to the sensor and the heater but also allow a controlled thermal coupling between the puck and the platform. Typically a flat sample of thickness close to 1 mm and area less than 3 X 3 mm^2 is cut from a well sintered pellet for specific heat measurement. A smaller sample thickness ensures that there is no appreciable thermal gradient across the sample during the measurement. The sample mass can range from 2 to 200 mg but for the measurements mentioned in this thesis, the sample mass was kept below 30 mg. For obtaining adequate thermal coupling between the sample and the heat capacity platform, Apiezon grease was used. For measurements below 200 K, Apiezon-N grease is recommended while for those at higher temperatures, Apiezon-H grease is used. Apiezon-N grease is not used above room temperature as it begins to melt while Apiezon-H grease may pop off from the sample stage during rapid warming from low temperatures. The heat capacity measurement is then carried out under high vacuum ($\sim 10^{-5}$ mbar) to avoid thermal losses via radiation. Apart from this, a charcoal holder is used as a cryopump to help decrease the pressure at the bottom of the probe at temperatures below 10 K.

The specfic heat measurement for any given sample is carried out in two steps. First, the heat capacity of the Apiezon grease and the sample stage is measured. This is called addenda
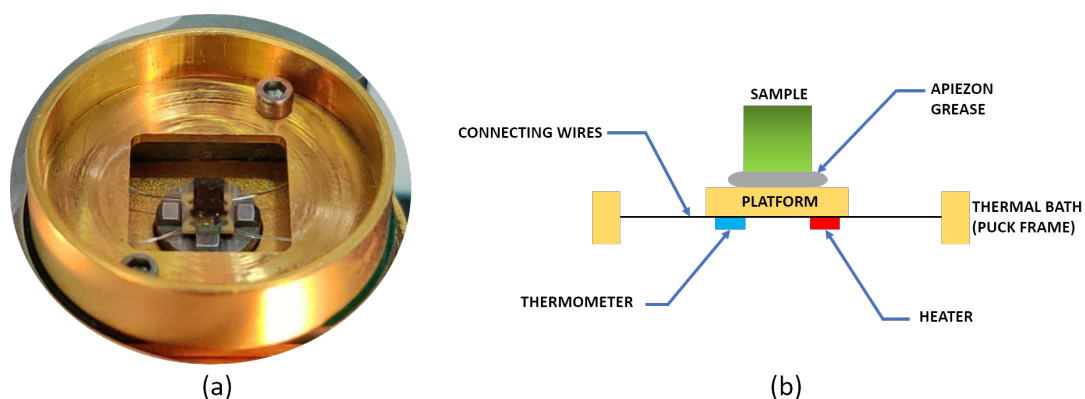
Figure 2.13: (a) Graphical representation of the PPMS calorimeter puck with a sample mounted on it using Apiezon-N grease. (b) Shows the schematic diagram of the calorimeter sample stage hanging from the calorimeter puck with the help of connecting wires.

measurement. Then the sample is gently placed on the same grease such that no grease is added or removed during the sample mounting process. Then the heat capacity of the sample, grease and the sample stage is measured together. The true heat capacity of the sample is then obtained by subtracting the heat capacity of addenda from the total heat capacity. In this thesis, specific heat was measured in the temperature range of 2 - 250 K using Apiezon-N grease and in some cases magnetic field as high as 9 T was applied to see the field dependence of specific heat.

2.3.4 DC susceptibility

The dc magnetization of the samples was carried out using a vibrating sample magnetometer (VSM) probe provided with the PPMS. Using the VSM probe the magnetization of the samples could be measured at a constant applied field from 2 K to 300 K. Moreover, field dependence of magnetization was also studied from - 9T to + 9T for some samples at different temperatures. The VSM functions by oscillating a sample near a detection coil and simultaneously detecting the induced voltage. By making use of a compact gradiometer pickup coil assembly, the VSM option can resolve magnetization changes as small as 10^{-6} emu with a data acquisition rate of 1 Hz. The gradiometer is designed in such a way that one can use large sample oscillation amplitude (1-3 mm peak) with frequencies as high as 40 Hz. The VSM option mainly consists of a linear motor transport (also known as VSM head) for vibrating the sample, a coilset puck for detection and electronics for driving the linear motor transport and detecting the response from the pickup coils. The sensitivity of the VSM coils is not significantly affected by large

magnetic fields, so it can perform sensitive measurements up to the maximum available field of 9 T in the PPMS. The working principle of the VSM is based on Faraday's law of induction i.e., a changing magnetic flux through the pickup coil will generate an e.m.f. in it. The time dependent induced e.m.f. is given by the following equation:

$$V_{coil} = \frac{d\phi}{dt} = \left(\frac{d\phi}{dz}\right)\left(\frac{dz}{dt}\right) \tag{2.14}$$

Here ϕ is the magnetic flux passing through the pickup coil due to the vibrating sample, z is the vertical position of the sample w.r.t. the coil and t denotes the time. For sinusoidal oscillation of the sample position, the voltage induced can be expressed as:

$$V_{coil} = 2\pi f C m A sin(2\pi f t) \tag{2.15}$$

where C is the coupling constant, m is the DC magnetic moment of the sample, A and f are the amplitude and frequency of oscillation respectively.
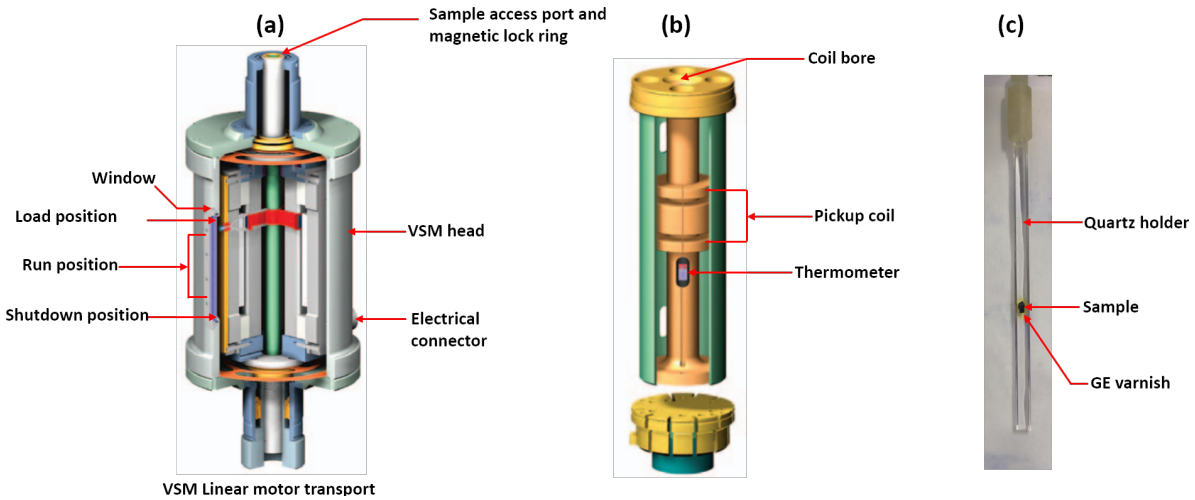
Figure 2.14: (a) Schematic representation of the VSM head that houses the linear motor transport assembly; (b) VSM pickup coil-set and (c) image of a VSM quartz holder with a polycrystalline sample glued to it using GE varnish. Images (a) and (b) are taken from Quantum Design, USA [160]

The center of oscillation of the sample is located at the vertical center of the gradiometer pickup coil and it is designed so that the induced voltage and the sample position is detected synchronously. The e.m.f. induced in the pickup coils is then amplified and measured using the lock-in technique. The voltage is then calibrated in electromagnetic (emu) units to give the magnetization of the sample. For the VSM measurements mentioned in this thesis, rectangular

sintered pellets were glued to a VSM quartz holder using GE varnish. The quartz holder provides a weak background signal as quartz is diamagnetic. The quartz holder was then attached to a sample rod, which was then installed inside the VSM head such that the sample position is at the centre of the pickup coils. Care must be taken such that the sample dimensions should not exceed the diameter of the quartz holder (4 mm), otherwise this can cause the sample to rub against the walls of the coil set bore and this can lead to significant heating effects at low temperatures and generation of noise at high magnetic fields.

2.3.5 AC susceptibility

AC susceptibility is a valuable tool that helps us study the spin dynamics and relaxation processes in a magnetic sample. It can be used to characterize spin glass behaviour, superparamagnetism, measuring critical temperature of superconductors and so on. During the AC measurement, an AC magnetic field is applied to the sample and the resultant AC moment is measured. Since the induced sample moment is time-dependent, these measurements yield valuable information about magnetization dynamics that are not obtained in DC measurements.

Parameters	Details
Drive Coil Frequency	10 Hz to 10 kHz
Temperature range	1.9 K to 350 K
Drive amplitude	2 mOe to 15 Oe
Sensitivity	5 X 10^{-8} emu (10 kHz)
AC harmonics measured	up to 10th
DC magnetization range	2.5 X 10^{-5} emu to 5 emu
DC extraction speed	1 m s^{-1}
Sample size	5.3 mm diameter; 12 mm length

Table 2.5: Specifications of the ACMS option in PPMS

In DC measurements, the sample moment is constant w.r.t. time. During AC susceptibility measurement, one has to deal with the magnitude of susceptibility i.e., χ and the phase shift ϕ of the measured signal w.r.t. the applied drive signal. The measured susceptibility has two components, namely, the in-phase, or real component (χ') and an out of phase or imaginary

component (χ"). These two components are related to each other via the following expressions:

$$\chi' = \chi cos\phi \tag{2.16}$$

$$\chi" = \chi sin\phi \tag{2.17}$$

$$\chi = \sqrt{\chi'^2 + \chi"^2} \tag{2.18}$$

$$\phi = arctan(\chi"/\chi') \tag{2.19}$$

In the low frequency regime, the AC measurement results are very similar to that of DC measurements and χ' is the slope of $M(H)$ curve. The imaginary part (χ") indicates the dissipative processes in the sample.
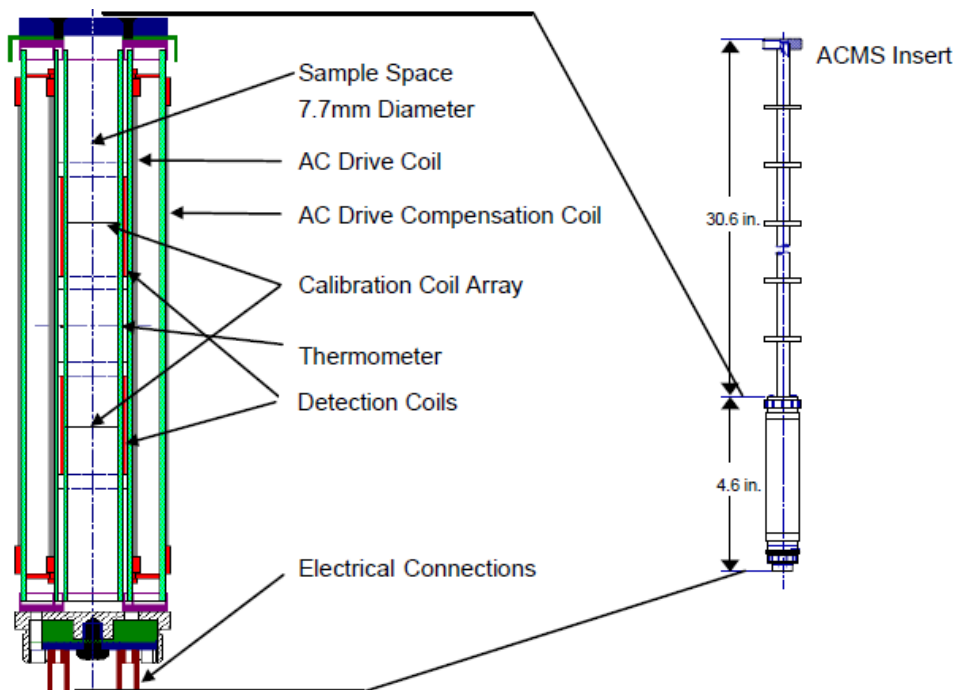
Figure 2.15: Schematic of the ACMS coilset and ACMS insert, adapted from Quantum Design PPMS manual, USA [161]

For measurement of AC susceptibility we used the ACMS option provided with the PPMS.

The main components of the ACMS set consists of an ac drive coil set, detection gradiometer pickup coils and an ac compensation coil set. A schematic of the ACMS coilset is shown in Fig. 2.15. The ac driven coil-set applies an alternating excitation field on the sample, while the detection coil-set captures combined inductive response of the sample as well as the excitation field. The ac compensation coil-set helps to get rid of the effects of the drive excitation. All the coil-sets are situated within the ACMS insert, concentric with the superconducting DC magnet of the PPMS cryostat.

2.3.6 Capacitive dilatometry

A capacitance dilatometer can be used to study the thermal expansion/contraction of a given specimen as a function of temperature and magnetic field. These dilatometers possess a parallel plate capacitor with a one stationary plate, and one moveable plate. Any change in sample length results in displacement of the movable plate and this changes the gap between the plates. Since the capacitance is inversely proportional to the gap, any change in sample dimension results in change in the capacitance of the parallel plate capacitor.

In this thesis, capacitive dilatometry was carried out in zero field for the $R_4Ni_3O_{10}$ (R = La, Pr and Nd) samples. The dilatometer setup used could measure the thermal expansion of the sample from 300 K to 2 K, with a resolution of 0.02 Å at low temperatures [162].

2.3.7 Single crystal neutron diffraction

To study the crystal structure of $Ca_3NiNb_2O_9$ sample down to low temperatures (up to 1.5 K) and to estimate its magnetic structure below the ordering temperature, the single crystals of $Ca_3NiNb_2O_9$ were studied using the four-circle single-crystal neutron diffractometer D10 at the Institute Laue-Langevin, Grenoble, France.

Fig. 2.16 shows the schematic representation of the D10 instrumental setup. When the D10 is setup in a four-circle geometry, it works in the following fashion:

- A suitable wavelength is chosen by the monochromater when a polychromatic beam reaches it from the thermal neutron guide (H24). The monochromater is either a pyrolyticgraphite (PG) or a Cu (200) crystal. The PG monochromater can access wavelengths in the range of 1.8 to 6.0 Å, while the Cu monochromater can access wavelengths in the range of 1.1 to 3.0 Å.

- The slit system then limits the beam size of the monochromatic beam before it reaches the sample.

- The single crystal sample is kept at the centre of the eulerian cradle, preferably in a gas flow helium cryostat. The three axes, namely, ω, χ and ϕ of the Eulerian cradle are rotated until a given set of atomic planes diffract into the equatorial plane.

- The detector is rotated to the location of the diffracted beam, which is then scanned step by step. This allows the recording of intensities of a large number of Bragg reflections, from which the atomic structure of the sample can be determined.
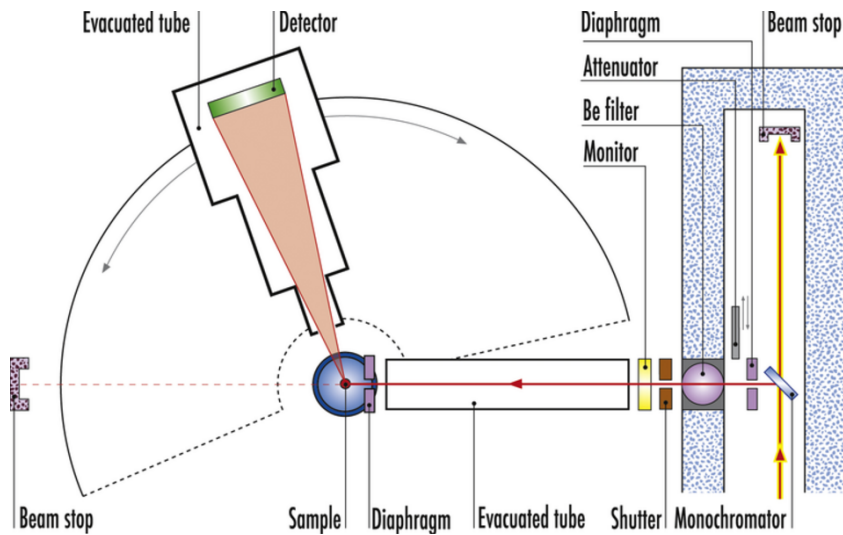
Figure 2.16: Schematic representation of the four circle single crystal neutron diffractometer - D10 at ILL, France. Taken from Ref. [163].

Parameters	Details
incident energy range	$2.5 < E_0 < 68$ meV
Flux	$\geq 5 \times 10^6$ cm^{-2}s^{-1} (for $\lambda = 2.36$ Å; PG monochromater and filter)
relative energy resolution $\frac{\delta E}{E}$	5×10^{-3}
Beam size	10×8 mm^2
Detector	94×94 mm^2 area detector or single 3He detector

Table 2.6: Specifications of four-circle single crystal diffractometer (D10) in ILL, Grenoble, France.

Chapter 3

Crystal growth

Crystal growth refers to the process by which a highly ordered arrangement of atoms or ions is formed, leading to the formation of a crystal. Crystal growth can occur naturally, through processes such as evaporation or precipitation, or it can be artificially induced in a laboratory setting through techniques such as vapor deposition or solution growth. The availability of quantum magnets in the form of sufficiently large and high-quality single crystals holds the key to clearly understanding their ground state properties and helps in the advancement of fundamental research.

There are many kinds of crystal growth techniques that have been developed for growing various materials like inorganic oxides, intermetallics and organic compounds, however, the crystal growth from melt is one of the most preferred methods as it enables us to grow large, high quality crystals in a short duration of time. These methods include flux growth [164, 165], Bridgman technique [166], Czochkralski method [167] and floating zone technique [168, 169]. In this chapter, we discuss the details of the crystal growth of transition metal oxide systems using the technique of four mirror optical floating zone furnace.

3.1 Brief history of floating zone technique

W.G. Pfann, a metallurgist, working at Bell Labs, wanted to obtain ultra pure samples of germanium and silicon for application in semiconductor technology. So, he ingeniously developed a technique where he filled a long tube with germanium and passed it repeatedly through a series of electrical heating coils. This caused the germanium to melt. He then allowed the
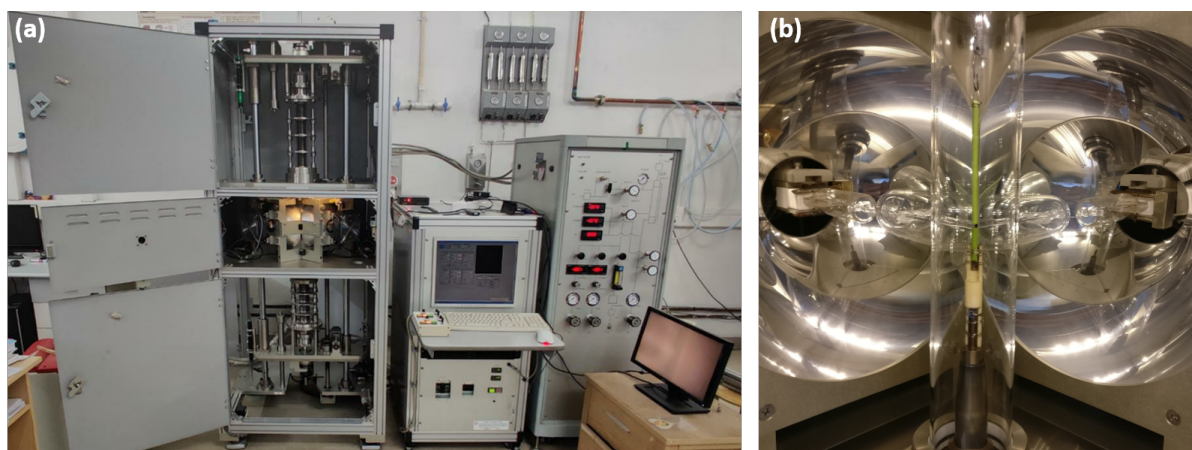
Figure 3.1: (a) Graphical representation of a four-mirror optical floating zone furnace (Crystal System Corporation, Japan); (b) shows the close-up view of the mirror-stage with the feed and seed rod aligned inside a quartz enclosure, before the beginning of a growth attempt.

melted portions to recrystallize by translating the tube from one end to another and this process was repeated several times. In doing so he obtained high purity specimens of germanium. Hence, in early 1950s, he developed the technique of "zone refining" [170] that resulted in ultra-pure samples of germanium that had an impurity concentration as low as one part in ten billion. However, this method did not work well for silicon as it had a higher melting point than germanium and reacted readily with the container in which it was melted. Hence, to overcome this problem, in 1952, Henry Theurer developed a variation on this technique. He clamped two ends of a silicon rod and then passed it vertically through a heating coil. In doing so, a small molten segment was produced between the two rods and it could float against the forces of gravity due to the surface tension of the liquid melt. It was named as the "float-zone refining" technique [171] and using this method he could produce high purity crystals of silicon. This process was also developed independently at other labs i.e., by P.H. Keck and M.J.E. Golay [172], at the U.S. Army Signal Corps, Fort Monmouth, New Jersey and by R.Emeis [173], who worked under the direction of Eberhard Spenke at Siemens in Pretzfeld, West Germany. In recent years, the optical floating zone furnace has gained significant attention due to the feasibility of growing large, high quality single crystals of a variety of materials (both conducting and non-conducting) with the user having precise manual control over the growth parameters.
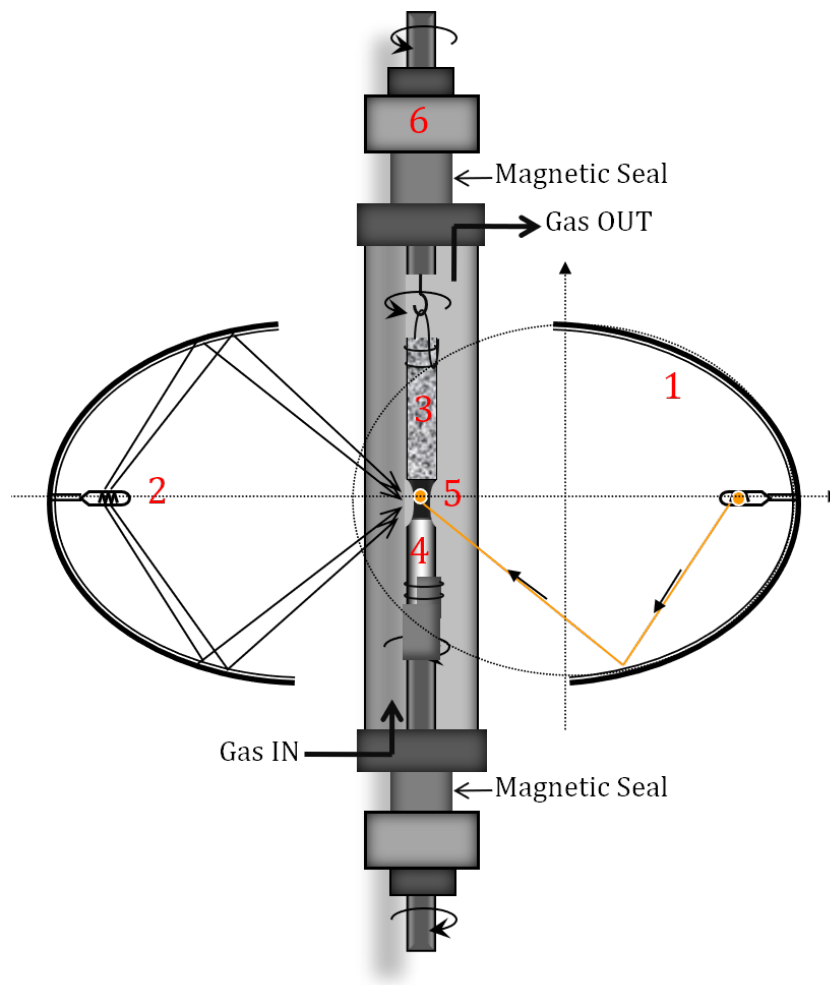
Figure 3.2: (a) Schematic showing the vertical section of a four-mirror optical float zone furnace. Here (1) is ellipsoidal mirror, (2) is halogen lamp, (3) is feed rod, (4) is seed rod, (5) is float zone and (6) is nitrogen chamber.

3.2 Description of an image furnace

In this thesis, the crystal growth was carried out using a four-mirror-optical-floating-zone furnace (Model: FZ-T-10000-H-HR-I-VPM-PC) from Crystal System Corporation, Japan. A schematic representation of the mirror stage of the furnace is shown in Fig. 3.2. It consists of four ellipsoidal mirrors that have halogen lamps fitted at one of their foci. The lamp power can be varied according to the melting point of the material under consideration. The second foci of these mirrors is at a common point, where all the energy flux of the lamps is concentrated and is used to melt the material whose crystal is to be grown. Before the growth process, the polycrystalline powder of the sample is pressed in the form of a long cylindrical rod (feed rod)

and is suspended from the upper shaft of the furnace with the help of a hook made up of nickel wire. A smaller rod of the same material is used as a seed rod and is tied to the alumina holder with the help of a nickel wire. Since nickel metal has a high melting point of 1455°C, it is used to tie the feed and seed rod. The entire growth process happens inside a quartz enclosure, which is transparent to near-infrared and visible radiations. The upper and lower shafts are sealed into the quartz chamber with the help of magnetic fluid seal and this prevents the contamination of the chamber atmosphere with atmospheric air. The sealing does not obstruct the free rotation or the vertical movement of the shafts. However, during the crystal growth experiments that require application of gas pressure, one needs to maintain a differential pressure of 0.1 MPa or more to ensure that the magnetic seals don't break. For this purpose, an excess of N_2 pressure is applied from the outside on the magnetic seal. The entire growth process can be viewed in real time on a screen with the help of a camera and hence the growth parameters can be modified as per the requirement of the experiment.
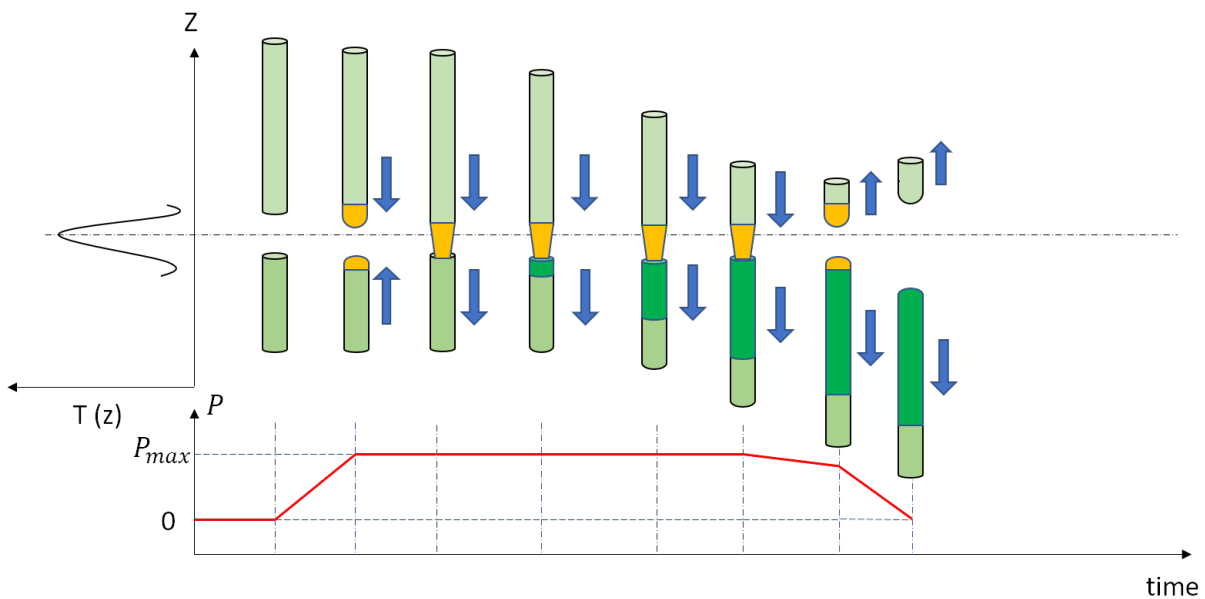
Figure 3.3: (a) Schematic showing the various stages during a crystal growth experiment using the four-mirror optical float zone furnace.

3.3 Principle of working of Optical float zone furnace

The general working principle of a floating-zone crystal growth process is shown in Fig. 3.3. The process begins by gradually increasing the power to the lamps such that the tip of the feed

rod starts melting and forms a bulb at the centre of the float zone. Then the feed rod is slowly joined with the seed rod and while both the rods are counter rotated so that the weight of the melt in the float zone can be balanced against the forces of gravity. Moreover, the counter rotation of the rods helps in uniform mixing of the liquid in the float zone that results in better zone stability. The process continues while both the seed and feed rod slowly traverse down with the help of the downward motion of the shafts. When a polycrystalline seed is used, large number of crystallites are formed on the surface of the seed rod. As the growth progresses in an uninterrupted manner, one of the preferably oriented domains grows larger in size than the others and takes over the other domains and thus the single crystal growth process begins. On the other hand, if one uses a single crystal as a seed rod to begin with, the epitaxial growth of the single crystal is initiated right from the start of the process. The size and quality of the grown crystal depends on various growth parameters that need to be carefully optimized, which are discussed below:
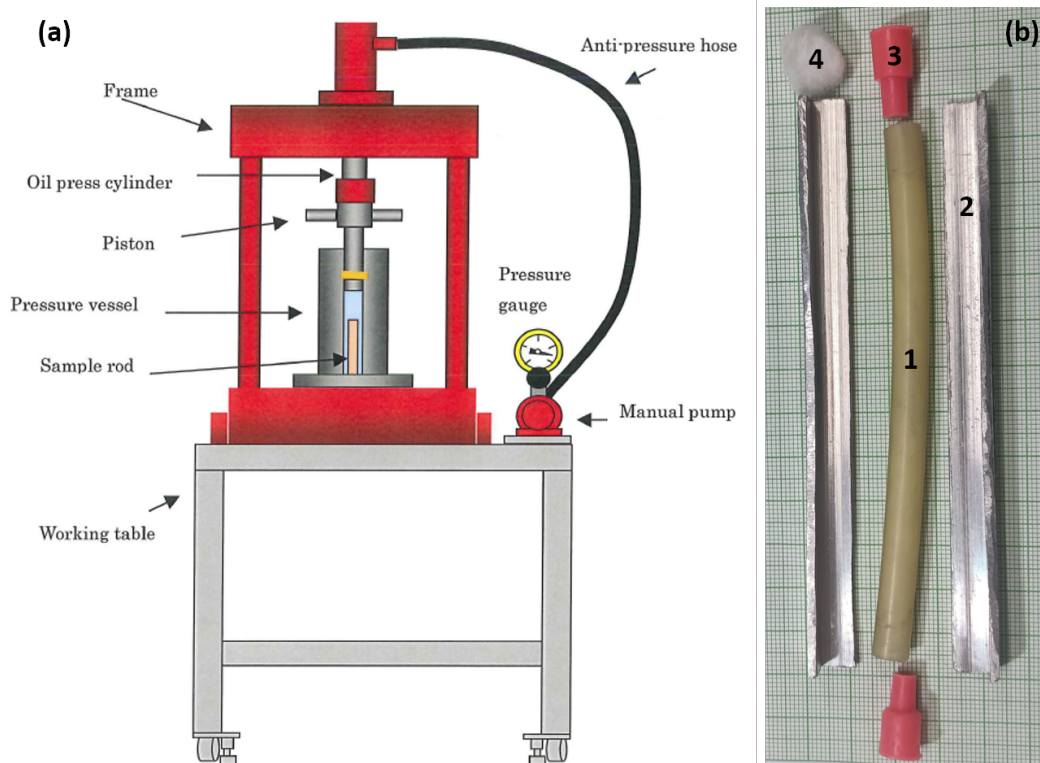
Figure 3.4: (a) A schematic representation of the hydrostatic press system from RIKEN SEIKI CO. LTD; (b) The components used for making the feed rod; (1) is the silicone tube, (2) is the L - shaped alumina plate, (3) is the rubber septa and (4) is the cotton plug.

(a) **Preparation of feed and seed rod**: For the smooth operation of the crystal growth

process, both the feed and seed rod need to be of uniform diameter and density. Any abrupt changes in any of these parameters can lead to uncontrollable changes to the float zone (e.g. bubble formation in the melt, penetration of the melt into the feed rod, etc) and the curvature of the solid-liquid interface, which in turn, can disrupt the growth process. For the preparation of feed and seed rod, finely ground polycrystalline powder of the compound is filled in a silicon tube, whose one end is sealed by a cotton plug followed by a silicon septa. While filling the powder in the silicon tube, which is held straight by a L-shaped alumina plate assembly, the entire setup is tapped continuously with brute force to ensure that there are no air gaps in the filled column. Once the tube is filled to the brim, its open end is sealed with a cotton plug followed by a rubber septa (see Fig. 3.4(b)). Then the filled tube is pressed in a hydraulic press under a maximum pressure of 700 bar for a few minutes. Thereafter, the pressure is released very slowly and the tube is taken out from the press and dried in an oven at around 80°C for few minutes. Then the polycrystalline rod is slowly pushed out of the silicon tube with the help of a glass rod. Care must be taken while transfering this pressed polycrystalline rod onto an alumina crucible (boat) since it can break under its own weight. Depending on the phase stability of the polycrystalline sample, the rods are sintered at temperatures as high as 1400 to 1500°C in a box furnace to make them dense. Since the rods are fairly long, they tend to bend when they are sintered at high temperatures in an alumina crucible. Hence to overcome this issue, the rods are sintered by keeping them on the inner edge of the rectangular alumina crucible with an alumina plate pressing on it with its weight to keep it straight.

(b) **Growth parameters**: While using the floating zone technique, one has to optimize several growth parameters that are essential for obtaining a large single crystal of high quality. These parameters include pulling rate of the feed and seed rod, their rotation speed, lamp power, growth atmosphere, gas flow rate, gas pressure and width of the float zone. One has to observe carefully the effect of each of these parameters on the growth process and hence tune them accordingly. For a better understanding of how these parameters can affect the resultant crystal properties, one can refer to the review article by Koohpayeh *et al.* [168]. As every method has its associated pros and cons, the floating zone method of growing crystals has also its own set of advantages and disadvantages that are listed below:

Advantages of using the floating zone technique:

1. Its a crucible free method and hence the grown crystal boule is not contaminated with impurities that can come from a crucible.

2. This method of zone melting was initially developed by W. G. Pfann [170] as a process to "refine" the melt and hence helps to eliminate the impurities that might be present in the feed rod during the initial stages of preparation.

3. The entire growth process can be viewed on the screen and hence one can control the growth parameters in real time.

4. The heating profile can be varied by using lamps of requisite power.

5. Single crystals of incongruently melting compounds can also be grown using the travelling solvent floating zone technique.

6. The crystal growth can be performed under various atmospheres like oxygen, argon, helium, etc .

7. Magnetic fluid seals provided with the quartz enclosure enables establishment of high vacuum during the growth. Moreover, gas pressures as high as 10 bar can be applied to suppress the evaporation of volatile components from the float zone and feed rod.

Disadvantages associated with a floating zone furnace:

1. For compounds having a very high melting point and highly volatile constituents, the crystal growth cannot be sustained for long using this method. Also, the maximum pressure that can be applied in the growth chamber is limited to 10 bars. Hence, compounds that grow under pressures higher than 10 bar cannot be grown using this furnace.

2. The temperature of the floating zone cannot be measured directly and hence, one cannot estimate the exact melting temperature of the compound being grown.

3. This method is not suitable for materials that have high reflectivity as these materials do not absorb the radiation effectively and it becomes difficult to melt these materials.

3.4 Melting behaviour of solids

Prior to growing a single crystal of a compound, one must be aware of its melting behaviour. One straightforward way to know this behaviour is by taking the help of a phase diagram for the given system. A phase diagram is a pictorial representation of the different phases of a substance that can exist under different conditions of temperature, pressure and composition. The two main types of melting behaviour that we shall be dealing with during the crystal growth process from melt are - congruently melting and incongruently melting. The congruently and incongruently melting behaviour is clearly depicted in the binary phase diagram shown in Fig. 3.5 and Fig. 3.6 respectively.
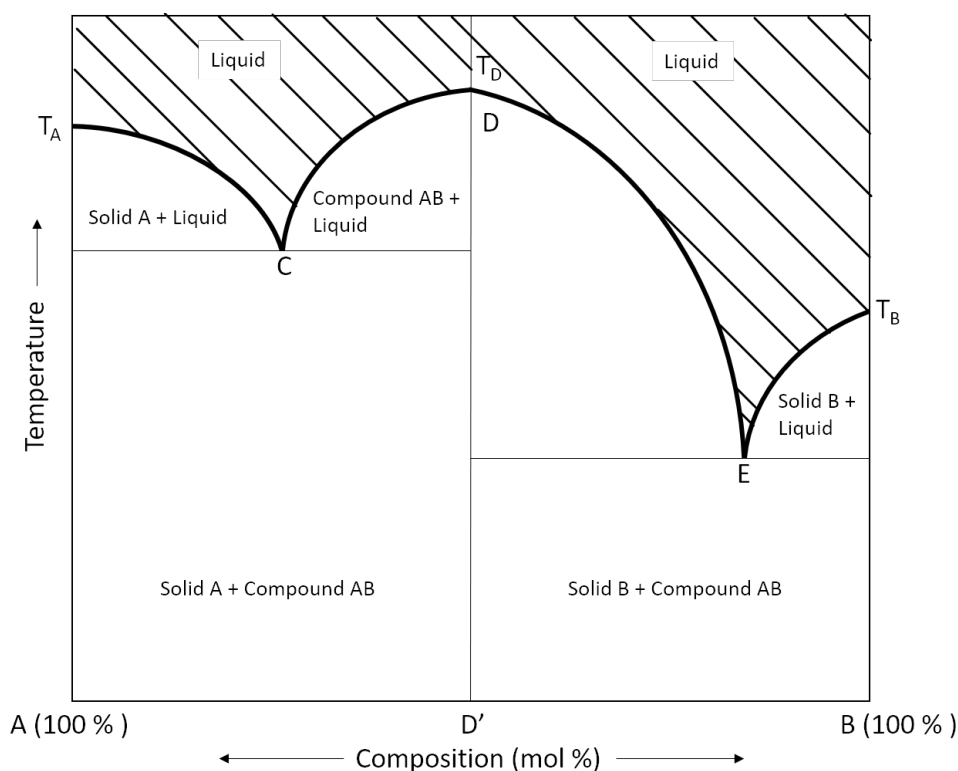
Figure 3.5: (a) Schematic representation of a binary phase diagram of components A and B.

Congruent melting: Compounds are said to be congruently melting if the composition of the liquid that forms during its melting is the same as the composition of the solid from which it is formed. The temperature at which this transformation takes place, is called the congruent melting point (T_D). To understand this phenomena better, we take the help of a binary phase diagram as shown in Fig. 3.5. This phase diagram is for two components - A and

B such that the leftmost point has a composition as A(100%) + B(0%) and the rightmost point has a composition as B(100%) + A(0%). The vertical axis denotes the temperature and T_A and T_B denote the melting point of A and B respectively. Here T_D marks the temperature at which the solid (D') and its melt (of the same composition) coexist in equilibrium. Hence, the compound (D') is said to exhibit a congruently melting behaviour i.e., above T_D its in the liquid phase with the composition same as D' and below T_D it immediately transforms into a solid with a composition same as D'. In this thesis, we grew three congruently melting compounds, namely, $Ca_3NiNb_2O_9$, $Ca_3MgNb_2O_9$ and $SmFe_{0.75}Mn_{0.25}O_3$. The details pertaining to the crystal growth of $Ca_3NiNb_2O_9$ and $Ca_3MgNb_2O_9$ will be discussed in Chapter 6 of the thesis.

Incongruent melting: Consider a compound such that it starts decomposing before its melting point is reached. It gives rise to a new solid phase and a liquid/melt that has a composition which is different from the original solid from which it was formed. Such a compound is said to exhibit an incongruently melting behaviour and the temperature at which this decomposition happens is called the "peritectic or meritectic point". Fig. 3.6 shows a general binary phase diagram containing compositions that melt incongruently. Suppose here A and B are two components that react to form the compound AB_2. The point T_D here represents the incongruent melting point of the compound AB_2 and below this point AB_2 decomposes into B and a liquid. If AB_2 had not decomposed at this temperature, its congruent melting point would have been at $T_{D'}$. Hence, $T_{D'}$ represents the hypothetical congruent melting point of the compound AB_2.

The crystal growth of incongruently melting compounds is relatively difficult as compared to that of congruently melting compounds. Most of the conventional crystal growth techniques like the Bridgman and Czochralski technique cannot be employed to grow large crystals of incongruently melting compounds. In such cases, a special technique, called the travelling solvent floating zone (TSFZ) method [174, 175] is employed with the pre-existing optical float zone furnace. In the TSFZ method, the composition of the float zone differs from that of the compound whose crystal needs to be grown. The composition of the float zone is chosen in such a way that it acts as a solvent in which the feed rod gradually dissolves as the melt zone moves up along the length of the feed rod. For the success of this process, the rate of dissolution of the feed rod needs to be exactly same as the rate of crystallization of the solute
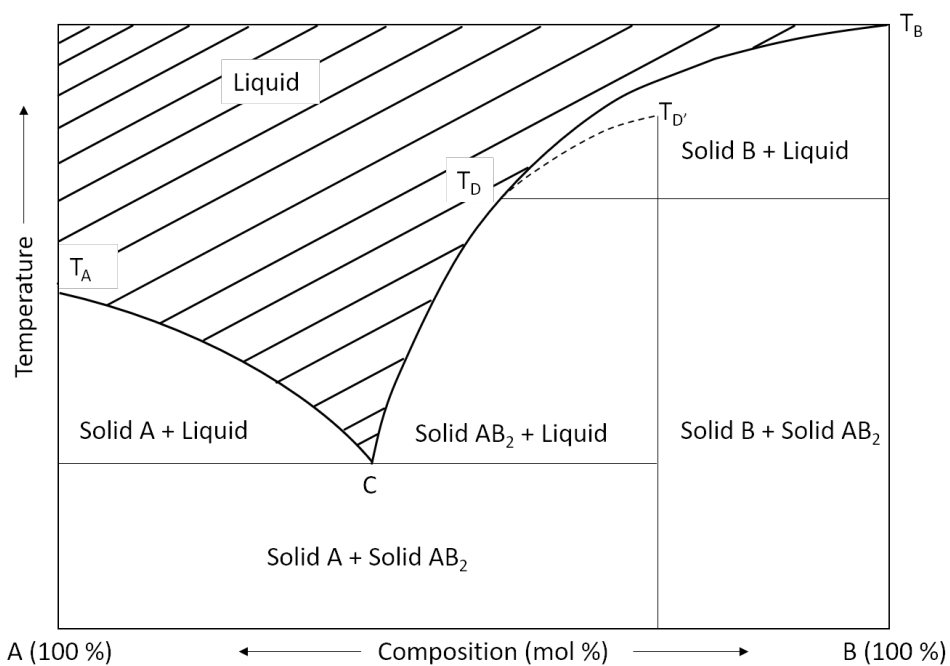
Figure 3.6: (a) Schematic representation of a binary phase diagram of components A and B that form compounds with incongruent melting points.

on the surface of the seed rod. Since, this thesis does not deal with compounds that had an incongruently melting behaviour, the details pertaining to crystal growth such compounds have not been discussed in detail.

Chapter 4

Study of n = 3 member of the Ruddlesden Popper nickelate family – $R_4Ni_3O_{10}$ (R = La, Pr and Nd)

The contents of this chapter has been published in Physical Review B under the title "Structural and physical properties of trilayer nickelates $R_4Ni_3O_{10}$ (R = La, Pr and Nd)" [176].

- The thermal expansion measurements were done in collaboration with Prof. Ruediger Klingeler from the Kirchhoff Institute for Physics, Heidelberg, Germany.

- The preliminary sample preparation and characterization work was done in collaboration with Sanchayeta Ranajit Mudi [177].

4.1 Introduction

The transition metal oxides based on nickel, or the nickelates for short, have witnessed a resurgence of interest in the last few years due to their strongly coupled charge, spin and lattice degrees of freedom, which can be manipulated to engineer novel electronic and magnetic phases [178–180]. Another reason for this resurgence can be attributed to the discovery of superconductivity in $Nd_{0.8}Sr_{0.2}NiO_2$ by Li *et al.*in the year 2019, which, in fact, led to the fulfillment of a long-sought-after quest for superconductivity in the nickelates [84]. Nearly two years before this momentous discovery, an ARPES study on single crystals of $La_4Ni_3O_{10}$,

which is the $n = 3$ member of the Ruddlesden Popper (RP) $La_{n+1}Ni_nO_{3n+1}$ $(n = 1, 2, 3 \ldots \infty)$ series, revealed a large hole Fermi surface that closely resembles the Fermi surface of optimally hole-doped cuprates [68] (see also Ref. 69). This discovery is important since the infinite layer $NdNiO_2$ (called the T' phase) is related to the perovskite $NdNiO_3$ ($n = \infty$ member of RP series) from which the T' phase is obtained through a process of chemical reduction. In general, there is a whole range of infinite layer T' phases given by the general formula $R_{n+1}Ni_nO_{2n+2}$ $(n = 1, 2, 3 \ldots \infty)$, where R is usually an alkaline earth or rare-earth ion, that are analogously related to their corresponding RP $R_{n+1}Ni_nO_{3n+1}$ phases. The nickelates of the RP series, therefore, constitute the primary phases with perovskite-type structure elements from which other nickelates, including the infinite layer T' variants, can be derived. A survey of past literature on the nickelates of the RP series reveals that the $n = \infty$ member, namely, $RNiO_3$ (where R is a tripositive rare-earth ion) are amongst the most intensively investigated members of the RP series [181]. In contrast, the $n = 1, 2, 3$ and ∞, members are relatively much less investigated – an exception to this being $La_2NiO_{4-\delta}$ ($n = 1$), which shows an interesting phase diagram as a function of its oxygen off-stoichiometry δ (see for example: Ref. 71). In fact, the intermediate members between $n = 1$ and $n = \infty$ exhibit a mixed-valent phase, ranging from 2+ for $n = 1$ to 3+ for $n = \infty$. Such a mixed-valency is well-known to give rise to strongly coupled electronic and magnetic phases (see for example Ref. 182). Hence, there is a significant interest to study them in the recent years.

4.2 Motivation to study the n = 3 members of the Ruddlesden Popper nickelate family

The $n = 3$ member of the RP series represented by the formula of $R_4Ni_3O_{10}$ ($R =$ La, Pr and Nd) are a rare class of metallic oxides that constitute the parent samples from which the intriguing $R_4Ni_3O_8$ [69] phases are obtained. These $R_4Ni_3O_{10}$ compounds with an average Ni valence of 2.67, have been considered close electronic and strucural analogs of high Tc super-conducting cuprates [68]. Previous studies have shown that $R_4Ni_3O_{10}$ compounds undergo a metal-to-metal transition (MMT) in the temperature range 135 K to 160 K depending on the identity of the R ion. Over the last few years several papers have been published on these trilayer nickelates [68, 73, 183–187]. However, these papers have mainly focused on under-

standing the nature of MMT, where Ni $3d$ electrons play a crucial role, in these compounds. The magnetic ground state of the rare-earth sublattice or of the $4f$ electrons, and the interplay of $3d$ and $4f$ electrons have not been studied in detail so far. Moreover, the crystal structure at room-temperature and the question of whether there is a structural phase transition associated with MMT or not are both unsettled issues over the years. Hence these open questions motivated us to synthesize these samples in highly pure form and study their physical properties in detail.

4.3 Synthesis protocol

Conventional solid state synthesis of the higher members (n $\geq$ 3) of the Ruddlesden Popper family leads to the formation of mixed phases and intergrowth [188, 189], which greatly influences their physical properties. A typical example of intergrowth in the n = 2 member of the RP nickelate series is clearly shown in Fig. 4.1(a). Since the lower members of the RP series are less conducting than the higher members (see Fig. 4.1(b)), such intergrowths result in an increment of the resistivity of the as-synthesized higher members. Hence, we adopted a wet chemical method also known as the citrate route [188], to synthesize pure phase of the $R_4Ni_3O_{10}$ (R = La, Pr and Nd) compounds.

This sol-gel route yields precursors of nanoparticle size and hence it facilitates the rate of the reaction. Stoichiometric amounts of R_2O_3 (R = La, and Nd) or Pr_6O_{11} (Sigma Aldrich, 99.99%, preheated at 1000°C prior to use in each case), and NiO (Sigma Aldrich, 99.999%) were added to 15M nitric acid solvent with continuous stirring using a magnetic stirrer. The solution was heated till the precursors dissolved and formed a clear, transparent, light green solution. Then an equimolar amount of anhydrous citric acid powder (ACS reagent, $\geq$ 99.5%) was added and this solution was slowly heated up to 280°C, whereby reddish brown vapours of nitrous oxide evolved and the solution attained a green gel-like texture. The gel was further dried by heating it up to 300°C till it turned off-white with a yellowish tinge. At around 350°C, the citrates were decomposed by auto-ignition process and this yielded very fine grey powder of the oxide precursors. The resultant powders were cold pressed into pellets and heated in flowing oxygen for 24 h with intermediate grinding and pelletizing. The entire synthesis protocol is shown pictorially in Fig. 4.2. The sinterings were carried out at 1100°C for
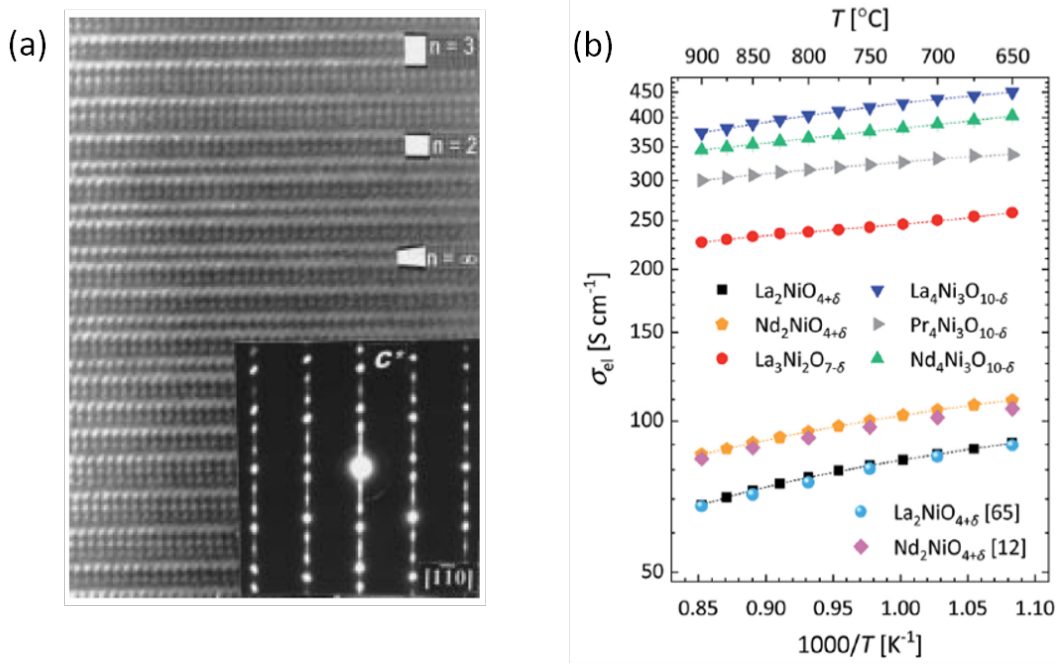
Figure 4.1: (a) High resolution electron microscopy image of $La_3Ni_2O_{7-\delta}$ prepared using citrate route, visualized along [110] zone axis, taken from [188]. (b) Electrical conductivity as a function of 1000/T in air atmosphere for the Ruddlesden Popper nickelates, taken from [190].

$La_4Ni_3O_{10}$, 1050°C for $Pr_4Ni_3O_{10}$ and 1000°C for $Nd_4Ni_3O_{10}$. Such temperature profile was choosen because with smaller rare earth ionic radius, the structural distortion increases (given by the Goldschmidt's tolerance factor (see equation 4.1)), hence a lower sintering temperature and a longer sintering time is advised [75]. The pure phase of the samples was obtained after four sinterings.

$$t = \frac{r_A + r_B}{\sqrt{2}(r_B + r_O)} \tag{4.1}$$

Here r_A is the radius of the A-cation, r_B is the radius of the B-cation and r_O is the radius of the anion (usually oxygen). The ideal value of t is 1 and with increasing distortion from the ideal cubic structure, the value of t keeps on decreasing.

4.4 Structural characterization

The crystal structure of $R_4Ni_3O_{10}$ stabilizing in monoclinic symmetry of $P2_1/a$, $Z = 4$ is shown in Fig. 4.3. It comprises triple perovskite block (PB) layers $(RNiO_3)_3$, which consist of corner-linked NiO_6 octahedra. These triple PB layers are separated by RO layers with the
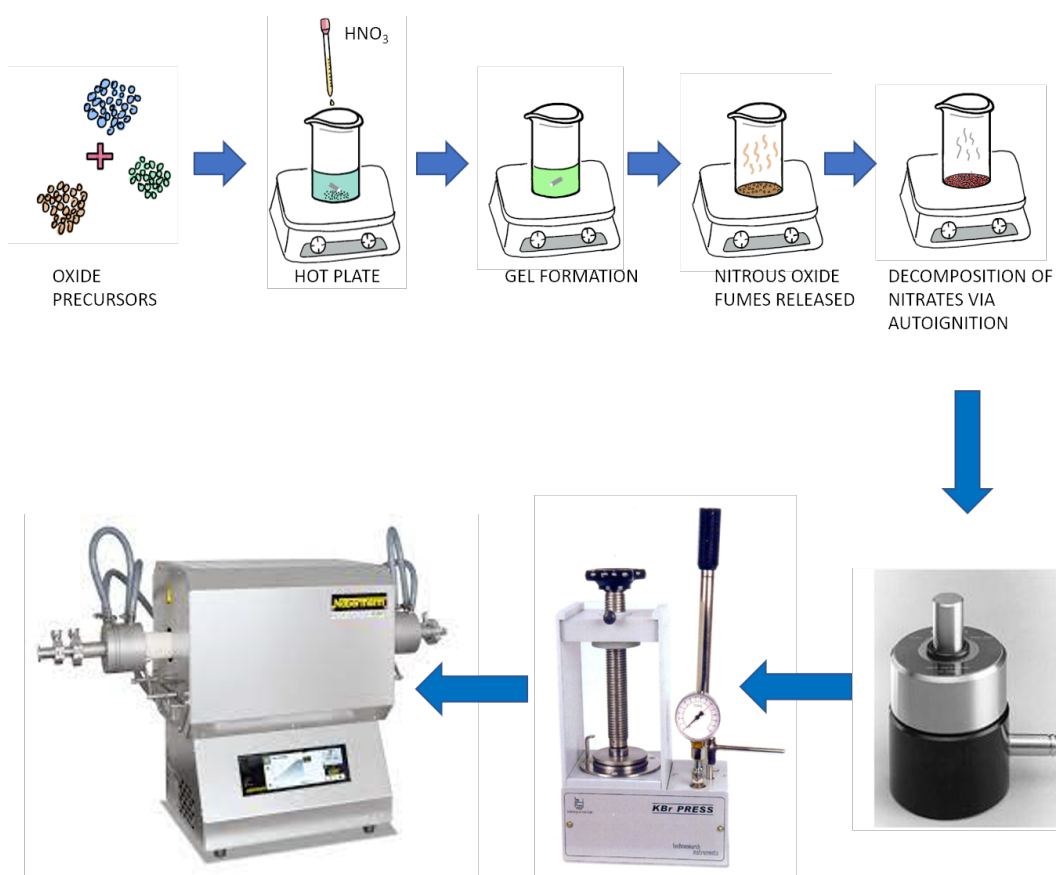
Figure 4.2: Graphical representation of the steps involved during the sol-gel synthesis process, followed by pelletization and solid-state reaction in oxygen flow in a Nabertherm tube furnace.

rocksalt (RS) structure. There are four inequivalent $R-$atoms, two of these are located within the PB layers ($R3$, $R4$). They have a deformed $12-$fold coordination analogous to the perovskites RNiO$_3$ as shown in Fig. 4.3. The remaining two $R-$atoms are located within the RS layers ($R1$, $R2$) with a $9-$fold coordination. Likewise, there are four distinct crystallographic sites for the Ni atoms. These Ni atoms have been labeled as Ni1, Ni2: located in the inner layer (ILs), and Ni3, Ni4: located in the outer layer (OL) that faces the RO layer on one side and PB layer on the other. In Sec 4.5.4, we shall see that due to the different crystallographic environment faced by the rare earth ions, new low temperature anomalies are captured in the magnetization and specific heat data, which were not explained in detail in previous reports.

4.4.1 Lab-based PXRD

The phase purity after each sintering of the R$_4$Ni$_3$O$_{10}$ (R = La, Pr and Nd) samples was monitored using a lab-based Bruker D8 Advance powder X-ray diffractometer. It was previ-
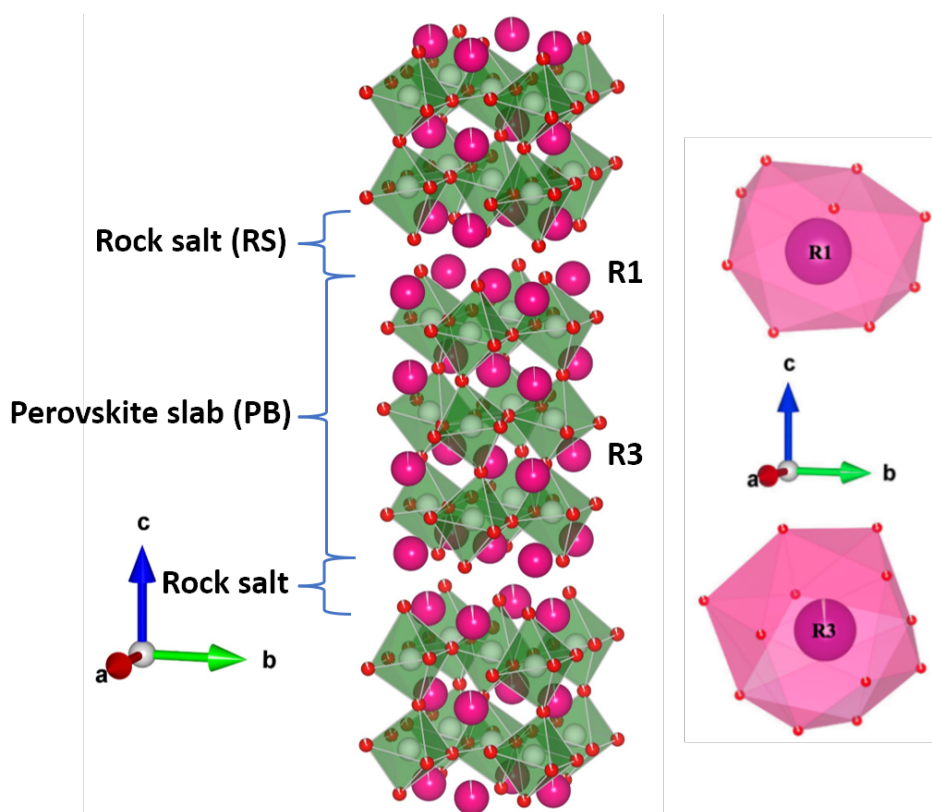
Figure 4.3: Schematic diagram of the crystal structure of trilayer $R_4Ni_3O_{10}$ (R = La, Pr and Nd) nickelates stabilizing in the monoclinic symmetry of $P2_1/a$. Here PB represents the perovskite block layers and RS represents the rocksalt layers. R1 and R3 denote ninefold and 12-fold coordinated rare-earth ions located in RS and PB layers, respectively.

ously reported in literature [75] that $La_4Ni_3O_{10}$ forms in air atmosphere at $1100°C$ whereas $Pr_4Ni_3O_{10}$ and $Nd_4Ni_3O_{10}$ compounds are formed in flowing oxygen atmosphere at a sintering temperature of $1050°C$ and $1000°C$ respectively. However, in case of $La_4Ni_3O_{10}$ we observed that sintering in air resulted in the formation of the $La_3Ni_2O_7$ phase alongwith the primary $La_4Ni_3O_{10}$ phase after the 4th sintering cycle as shown in Fig. 4.4. This observation is consistent with the fact that with increase in the nickel oxidation state from $Ni^{2.5}$ in $La_3Ni_2O_7$ to $Ni^{2.67}$ in $La_4Ni_3O_{10}$, oxidative environment is needed to stabilize the $La_4Ni_3O_{10}$ phase. Hence, further sinterings were carried out in oxygen atmosphere for the $La_4Ni_3O_{10}$ sample to restrict the formation of the lower member of the RP series. Similar observation was also reported by Zhang *et al.* [186] during the high pressure floating zone crystal growth of $La_4Ni_3O_{10}$, where they show that $La_3Ni_2O_7$ phase forms at a lower partial pressure of oxygen while $La_4Ni_3O_{10}$ is stabilized at a higher oxygen partial pressure.

For the $Pr_4Ni_3O_{10}$ and $Nd_4Ni_3O_{10}$ samples, the single phase was obtained after 4 sinter-
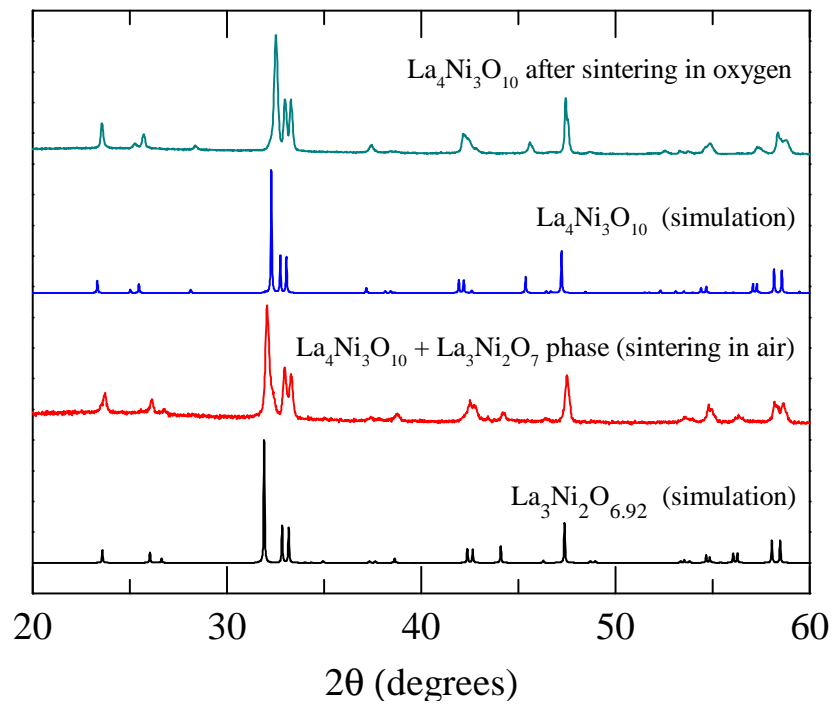
Figure 4.4: Formation of lower member ($La_3Ni_2O_7$) of the RP phase during the synthesis of $La_4Ni_3O_{10}$ in air atmosphere, confirmed using lab based XRD.
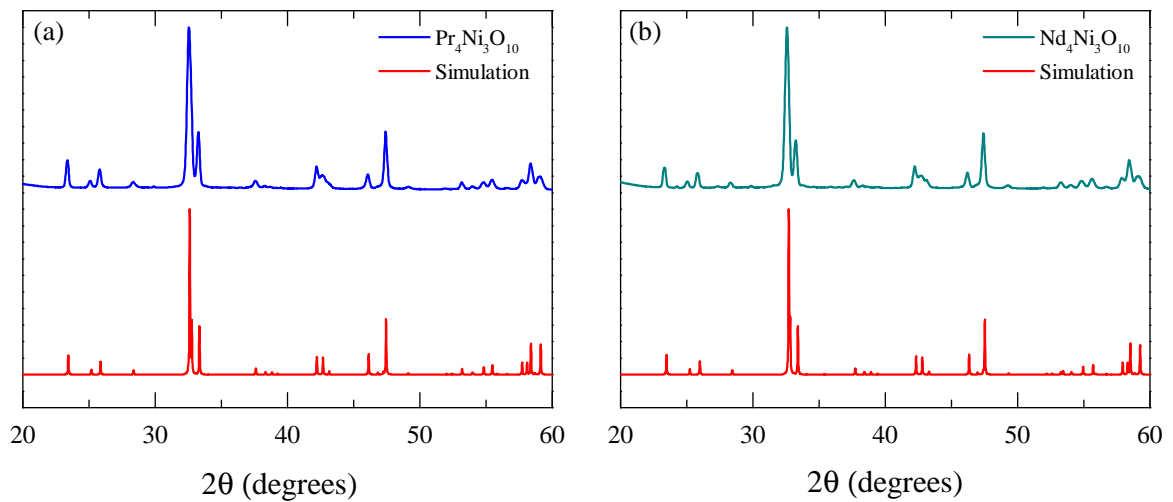
Figure 4.5: (a) and (b) show the comparison of the PXRD data of $Pr_4Ni_3O_{10}$ and $Nd_4Ni_3O_{10}$ respectively with the simulated pattern using $P2_1/a$ (Z = 4) space group.

ings in oxygen atmosphere as shown in Fig. 4.5 (a) and (b) respectively.

4.4.2 FESEM and EDAX

The FESEM images of all the samples was obtained at an electron beam energy of 20 kV.

Fig. 4.6 shows a comparison of the morphology all three samples on the same scale of 2μm.

The particle size and shape looks similar for all three samples and hence the effect of grain boundary on the resistivity behaviour of these samples should be similar.
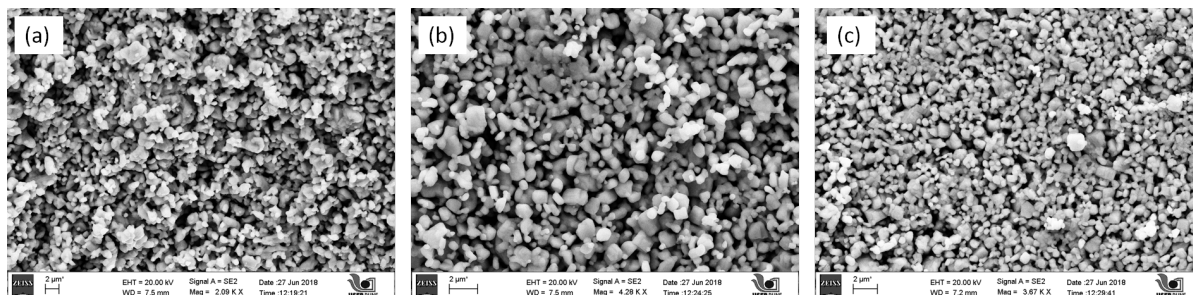
Figure 4.6: (a), (b) and (c) show the FESEM images of $La_4Ni_3O_{10}$, $Pr_4Ni_3O_{10}$ and $Nd_4Ni_3O_{10}$ samples respectively, showing the sample morphology.

EDS spectra was obtained by taking area scans over more than 10 regions for each sample. For each sample, the rare-earth ion's atomic percentage was compared with that of nickel. Oxygen was not taken into consideration as it is a lighter element and EDAX measurements are not very accurate when such elements are taken into consideration. The R:Ni ratio was 1.45, 1.38 and 1.42 for R = La, Pr and Nd respectively. The ideal value of R:Ni for all the three samples is 1.33. The difference between the theoretical and the experimental values could arise from the higher error bars associated with the EDS measurement.

4.4.3 TGA analysis

Methods such as thermogravimetric analysis (TGA) and redox titrations are usually employed to determine the oxygen content in oxide materials. These methods can be used in conjunction with neutron diffraction experiments to precisely determine the oxygen content and the oxidation state of the transition metal cation present in the RP compound. Since the structural and electronic properties of RP phases often show strong dependence on the oxygen stoichiometry, we carried out complete decomposition of our samples under 90% Ar - 10% H_2 atmosphere in a high resolution TGA setup (Netzsch STA 449 F1) as shown in Fig. 4.7. The following set of reactions occur one after the other when the decomposition of $R_4Ni_3O_{10}$ phase is carried out in 90% Ar - 10% H_2 atmosphere:

- $R_4Ni_3O_{10} + H_2 \longrightarrow R_4Ni_3O_9 + H_2O$
- $R_4Ni_3O_9 + H_2 \longrightarrow R_4Ni_3O_8 + H_2O$

(The transformation of $La_4Ni_3O_{10}$ to $La_4Ni_3O_8$ does not take place unless ultra high pure H_2
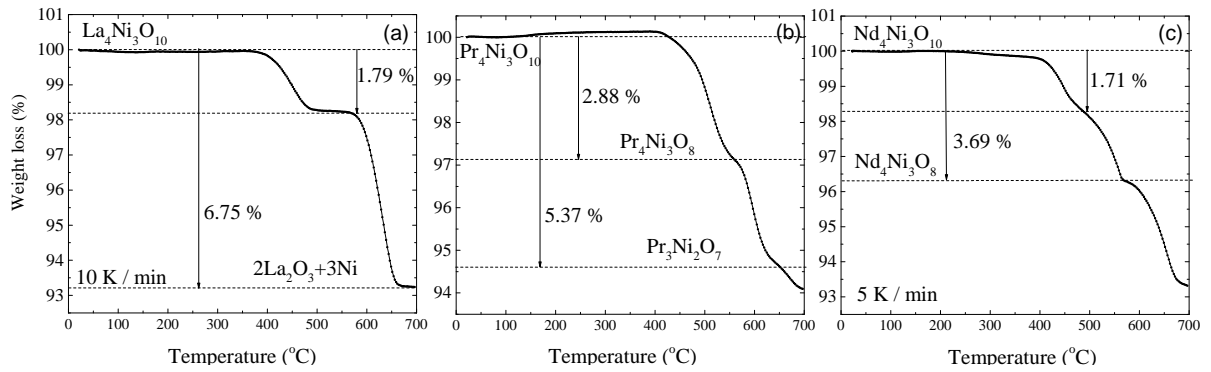
Figure 4.7: (a), (b) and (c) show the TGA plots for $La_4Ni_3O_{10}$, $Pr_4Ni_3O_{10}$ and $Nd_4Ni_3O_{10}$ samples, carried out in 90% Ar - 10% H_2 atmosphere.

is used)

- $$R_4Ni_3O_8 + 2\,H_2 \longrightarrow 2\,R_2O_3 + 3\,Ni + 2\,H_2O$$
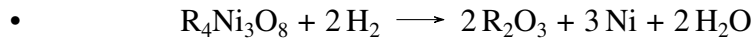
After the $R_4Ni_3O_{10}$ (R = La, Pr and Nd) samples were completely decomposed in the TGA setup, the weight loss was recorded and using it the oxygen stoichiometry was back calculated. From the analysis of the weight loss during the TGA run, the oxygen off-stoichiometry (δ) in $R_4Ni_3O_{10-\delta}$ was found to be -0.25, -0.11 and -0.2 respectively for R = La, Pr and Nd.

4.4.4 Synchrotron XRD

In order to solve the long standing ambiguity related to the room temperature crystal structure of $La_4Ni_3O_{10}$ and to check whether there is any structural anomaly associated with the metal-to-metal transition (MMT) in these compounds, we carried out high resolution synchrotron powder X-ray diffraction experiments at the MSPD-BLO4 beamline of the ALBA synchrotron center in Barcelona, Spain. The samples were prepared in the form of finely ground powders that were placed in a borosilicate capillary tube of 0.5 mm inner diameter. For low temperature XRD (down to 90 K), the sample was cooled using an Oxford Cryostream 700 series nitrogen blower, and the diffractograms were collected in the range $0^o \leq 2\theta \leq 30^o$ with a step size of 0.003^o. The incident beam energy was set at 38 keV ($\lambda = 0.3263$ Å) and a high resolution MAD26 detector with an angular resolution of about $4 \cdot 10^{-4}$ was used to resolve any subtle structural modifications [191]. We integrated the data at each temperature for 30 min, which gives a very high statistics in addition to the high-quality data.

4.4.4.1 Space group screening for room temperature crystal structure of La$_4$Ni$_3$O$_{10}$

There is a great deal of ambiguity in literature regarding the space group that correctly defines the crystal structure of La$_4$Ni$_3$O$_{10}$. The earliest work by Seppänen *et al.*reported an orthorhombic space group $Fmmm$ [192]. However, Tkalich *et al.* [193], and Voronin *et al.* [194] used the space group $Cmca$. Ling *et al.* [195], on the other hand, found the orthorhombic space group $Bmab$ (unconventional setting for $Cmca$) to be more suitable for refining their neutron powder diffraction data. Zhang *et al.* carried out structural refinement on the powders obtained by crushing high-pressure floating-zone grown single crystalline specimens [186]. They propose that La$_4$Ni$_3$O$_{10}$ crystallizes in a mixture of $Bmab$ and $P2_1/a$ (Z = 2); the phase fraction between the two phases being a function of the cooling condition employed [196]. For example, the phase $Bmab$ transforms almost completely to $P2_1/a$ (Z = 2) when annealed under flowing oxygen. Finally, in a recent synchrotron based study by Kumar *et al.*, the space group symmetry $P2_1/a(Z = 4)$ has been endorsed [197].

Table 4.1: Refinement results for La$_4$Ni$_3$O$_{10}$ using various space groups. The lattice parameters are correct to the third decimal place with an estimated error bar of the order of ± 0.0002

Space group	Phase fraction	Space group No.	Phase Type	a (Å)	b (Å)	c (Å)	Unit cell volume (Å^3)	χ^2	R_{WP}	R_{EXP}	R_{P}
$P2_1/a$	-	14	monoclinic	5.4242	5.4744	28.0096	831.736	9.28	18.1	5.90	14.7
$Bmab$	-	64	orthorhombic	5.4247	5.4749	28.0092	831.864	10.2	18.8	5.89	15.8
$Pcab$	-	61	orthorhombic	5.4244	5.4746	28.0109	831.823	10.7	19.2	5.86	16.1
$Fmmm$	-	69	orthorhombic	5.4243	5.4747	28.0106	831.814	11	19.7	5.93	16.8
$Cmca$	-	64	orthorhombic	5.4244	28.0111	5.4746	831.829	12.0	20.7	5.96	17.1
$P2_1/a + Bmab$	86.3 : 13.7	-	-	-	-	-	-	7.18	15.9	5.95	13.0
$P2_1/a + Bmab+$ La$_3$Ni$_2$O$_7$	85.6 : 7.8 : 6.6	-	-	-	-	-	-	6.15	14.7	5.90	11.7

In order to find the most appropriate space group from among those that were previously reported, we started refining the diffraction pattern using one space group at a time. To avoid biasing this procedure, every space group was tried till the refinement could not be improved further. Table 4.1 summarizes the results of the Rietveld refinement using the various space groups that were previously reported for La$_4$Ni$_3$O$_{10}$.

Fig 4.8 shows the comparison of calculated and experimental diffraction profiles at select 2θ values for the space groups $P2_1/a$, $Bmab$, $Pcab$, $Fmmm$, $Cmca$, and $P2_1/a + Bmab$. From a visual inspection of the calculated profile and the difference plot (blue line), and the values of the R-factors, we infer that the monoclinic symmetry with space group $P2_1/a$, $Z = 4$
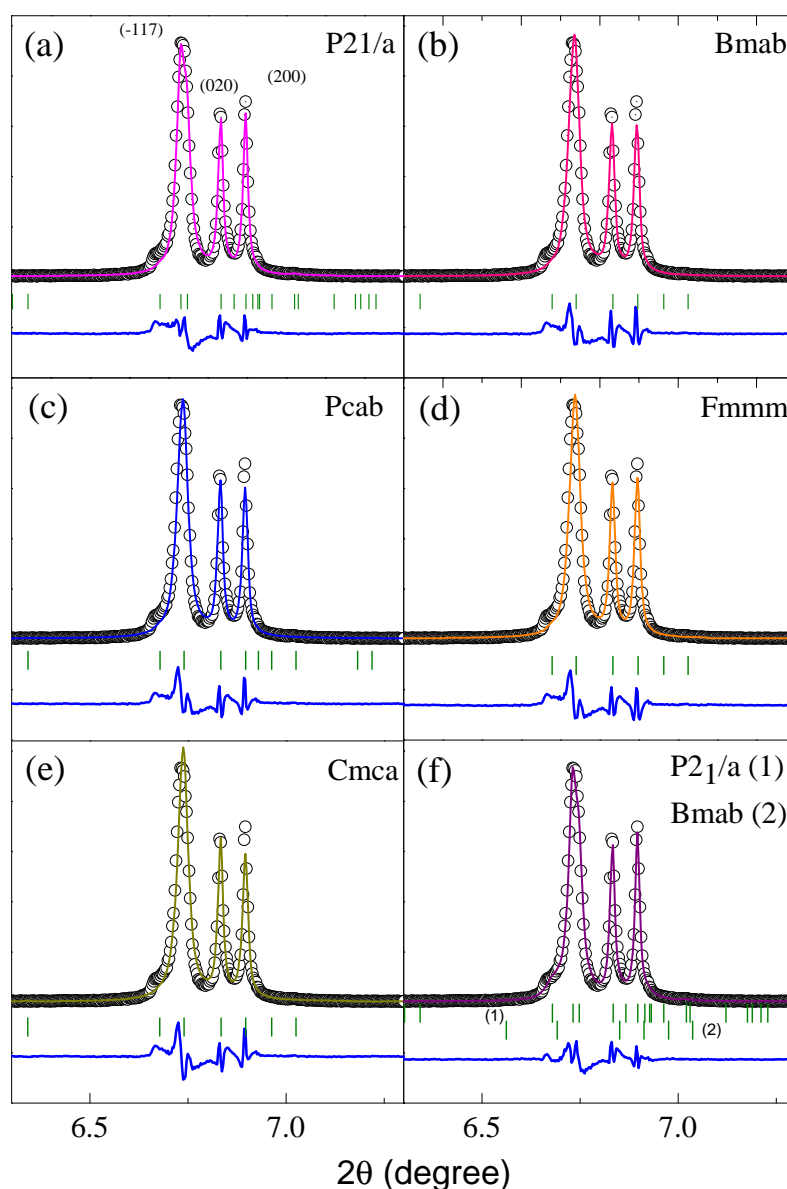
Figure 4.8: Comparative plots showing results of Rietveld refinement on the synchrotron powder X-ray diffraction data of $La_4Ni_3O_{10}$ at $T = 300$ K for various space groups; ○ represents the observed data, line through the data points represent the calculated profile; the difference plot (observed intensity minus calculated intensity for various 2θ) is shown at the bottom of each panel using blue color, and the Bragg peak positions are shown using the green vertical bars. The y-scale (intensity) in same in each panel.

fits the observed profile better compared to space groups $Bmab$, $Pcab$, $Fmmm$, and $Cmca$. While the space group $P2_1/a$ fits the intensities of (020) and (200) peaks satisfactorily, the small shoulder peak near $6.65°$ (on the lower angle side of the most intense $\bar{1}17$) peak) remained poorly fitted. In order to account for this discrepancy, we carried out a 2–phase re-

finement, whose results are shown in Fig. 4.8 (f). In this 2–phase refinement, we used the monoclinic space group of $P21/a$ and the orthorhombic space group $Bmab$ (SG no. 64). For this case, the calculated profile was closer to the observed data and the shoulder peak was also better accounted for. This improvement is also reflected in the difference plots and the values of R-factors given in Table. 4.1. Also, the phase fraction for this refinement was $P2_1/a : Bmab \equiv 86.3 : 13.7$. Finally, we included the n = 2 member of the RP series i.e., $La_3Ni_2O_7$ (with an orthorhombic space group $Cmcm$ (SG no. 63) to see if we can improve the fitting further. This lead only to a marginal improvement over the 2–phase refinement as depicted in Fig 4.9.
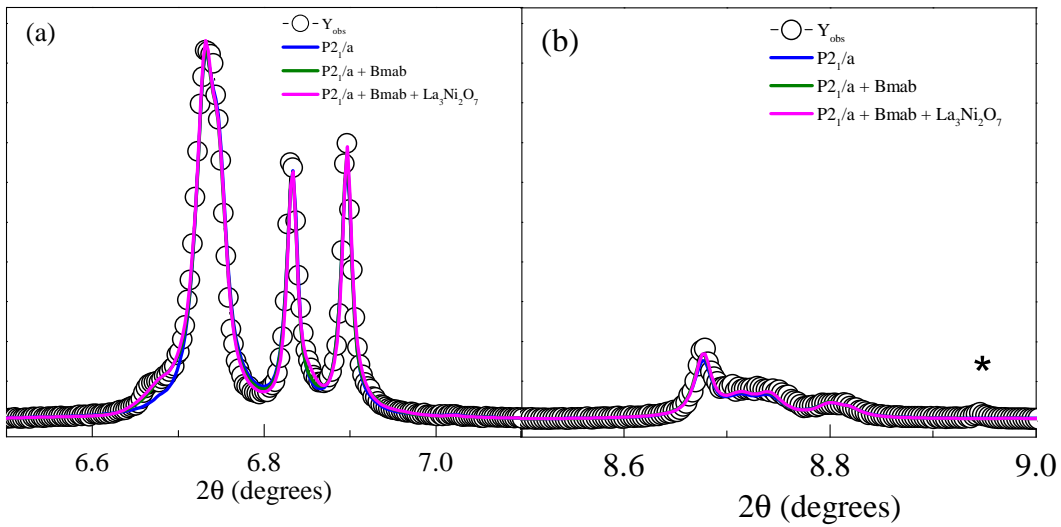
Figure 4.9: Comparison of three different refinement procedures: $P21/a$ (blue), $P21/a + Bmab$ (green), and $P21/a + Bmab$ and $La_3Ni_2O_7$ (magenta) in the case of $La_4Ni_3O_{10}$. The green and magenta curves almost overlap over the whole range shown, indicating that addition of the phase $La_3Ni_2O_7$ results only in a very marginal improvement over the two phase refinement. The y-scale is same for both the plots. Shown with $*$ is an impurity peak which could not be indexed.

In this case, we find the ratio of three phases to be $P2_1/a : Bmab : La_3Ni_2O_7 \equiv 85.6 : 7.8 : 6.6$. Clearly, in both 2– and 3–phase refinements, the phase fraction of the primary phase $P2_1/a$ remains more or less unchanged. Since the $R-$factors quantifying the quality of fit are slightly lower for the 3–phase refinement, we have chosen this model to be the best fit. Finally, even in the 3−phase refinement some mismatch between the observed and calculated intensities around $2\theta = 10°$ remains; this has been reported in the previous studies also and may arise from stacking faults [198]. It should also be remarked, that a small extra peak,

$\sim 1\%$ of the intensity of the main peak, near $2\theta = 8.95°$, is also observed which indicates the presence of a small unidentified parasitic phase. In each case, the strain model (-2) with Laue class $112/m$ was used to account for slight anisotropic strain broadening in the peaks with (hkl) values of (400), (040), (004), (220), (202), (022), (112), (310) and (130).

4.4.4.2 Low temperature synchrotron XRD of La$_4$Ni$_3$O$_{10}$

Fig. 4.10 (a) shows the room temperature crystal structure of La$_4$Ni$_3$O$_{10}$ refined using the three phases – $P2_1/a$, $Bmab$ and La$_3$Ni$_2$O$_7$ and panels (b – d) show the temperature variation of the lattice parameters of the $P2_1/a$ phase. The lattice parameters decrease monotonically upon cooling exhibiting clearly discernible anomalies at T_{MMT}.

The $b-$axis, in fact, undergoes an expansion upon further cooling below T_{MMT}. The diffraction patterns recorded below T_{MMT} reveal neither the appearance of any new diffraction peak nor any peak splitting, which suggests that the structural reorganization across the MMT, if any, is rather subtle without any noticeable change of the lattice symmetry (see, Fig. 4.11). The negative thermal expansion along the $b-$axis is in agreement with that reported by Kumar et al. (Ref. 197). The temperature variation of angle β, shown in panel 4.10 (e), shows an increasing behavior upon cooling with a perceptible dip at T_{MMT}. For comparison, the normalized lattice parameters are shown in Fig. 4.10 (g).

4.4.4.3 Low temperature synchrotron XRD of Pr$_4$Ni$_3$O$_{10}$

Fig. 4.12(a) shows the results of Rietveld refinement for Pr$_4$Ni$_3$O$_{10}$. In this case, the refinement was done using the monoclinic space group $P2_1/a$ (SG no. 14, $Z = 4$) alone, which resulted in a satisfactory fit except near the highest intensity peak where the calculated profile does not exactly match the observed data. Inclusion of strain improved the fitting to some extent but did not resolve the issue completely. Similar inconsistency over the same 2θ range has also been previously observed [196]. Whether the stacking faults or the intergrowth of lower RP members is the reason could not however be reliably ascertained. Also, analogous to La$_4$Ni$_3$O$_{10}$, some intensity mismatch is observed near $2\theta = 10°$ (peak $\bar{2}21$), which may be due to the stacking faults [198].

As shown in Fig. 4.12(b-d), in the temperature range around 156 K, where MMT is expected to occur, a clear anomaly in the lattice parameters is observed. The $b-$axis parameter shows
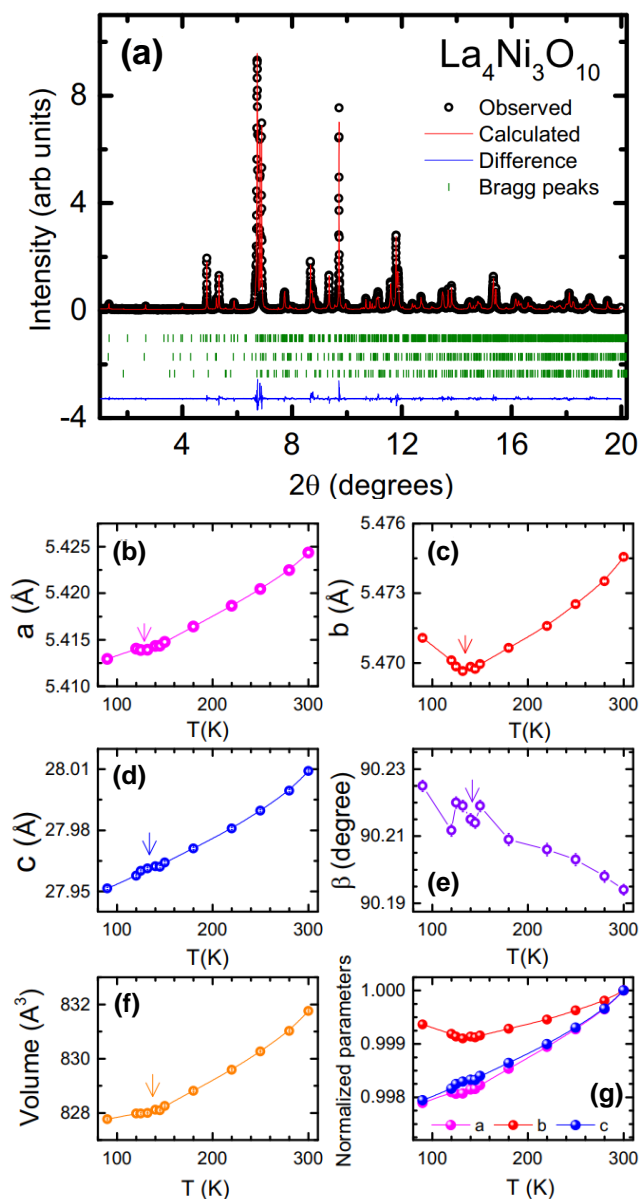
Figure 4.10: (a) Shows the Rietveld refinement results of the room temperature synchrotron powder X-ray diffraction data for $La_4Ni_3O_{10}$. In panel (a) the first, second, and third row of Bragg peaks correspond to $P2_1/a$, $Bmab$ and $La_3Ni_2O_7$ phases, respectively. Panels (b), (c) and (d) show the temperature variation of lattice parameters a, b and c, respectively; panels (e) and (f) show the temperature dependence of angle β and unit cell volume, respectively; panels (g) shows the normalized unit cell parameters. In some cases the size of the error bars is smaller than that of the data points.

an increase upon cooling below the MMT, analogous to $La_4Ni_3O_{10}$. In the temperature dependence of angle β, an appreciable non-monotonic variation has also been observed between the MMT and room-temperature.
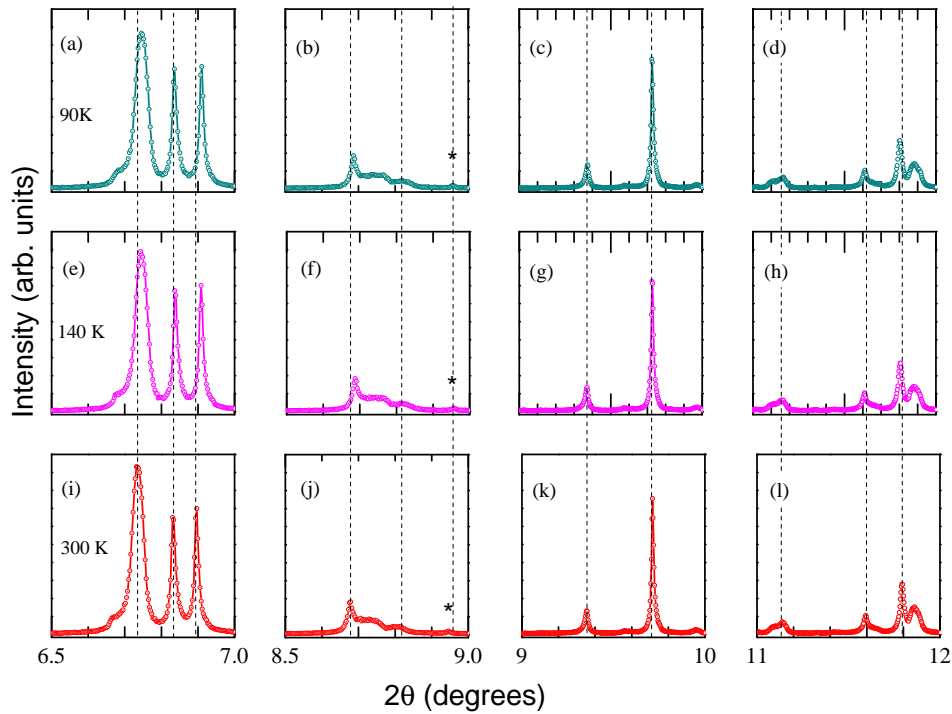
Figure 4.11: Synchrotron powder X-ray diffraction data for $La_4Ni_3O_{10}$ at three representative temperatures: 90 K (top row), 140 K (middle row) and 300 K (bottom row) over select 2θ ranges. The dashed vertical lines are shown as a guide to the eye. The y-scale in each panel is kept the same. Asterisk indicates an unidentified peak.

4.4.4.4 Low temperature synchrotron XRD of $Nd_4Ni_3O_{10}$

Fig. 4.13(a) shows the results of Rietveld refinement for $Nd_4Ni_3O_{10}$ at room-temperature. The structural refinement in this case too is done using the monoclinic space group $P2_1/a$ (SG no. 14; $Z = 4$) alone. Though all the observed peaks could be satisfactorily accounted for, the highest intensity peak was found to be unusually broad and the strain model 2 is used to account for it.

As shown in Fig. 4.13(b-e) the lattice parameters of $Nd_4Ni_3O_{10}$ decrease monotonically upon cooling with a weak anomaly around 160 K, which coincides with T_{MMT} previously reported for this compound. This anomaly is most prominent in the variation of the $b-$parameter. However, unlike the case of $La_4Ni_3O_{10}$ and $Pr_4Ni_3O_{10}$ the $b-$parameter in this case continues to decrease upon cooling below the MMT. The temperature variation of angle β is shown in panel 4.13(e). Upon cooling below room temperature, β first increases down to about $T = 200$ K and decreases upon further cooling showing a broad peak near $T = 200$ K which
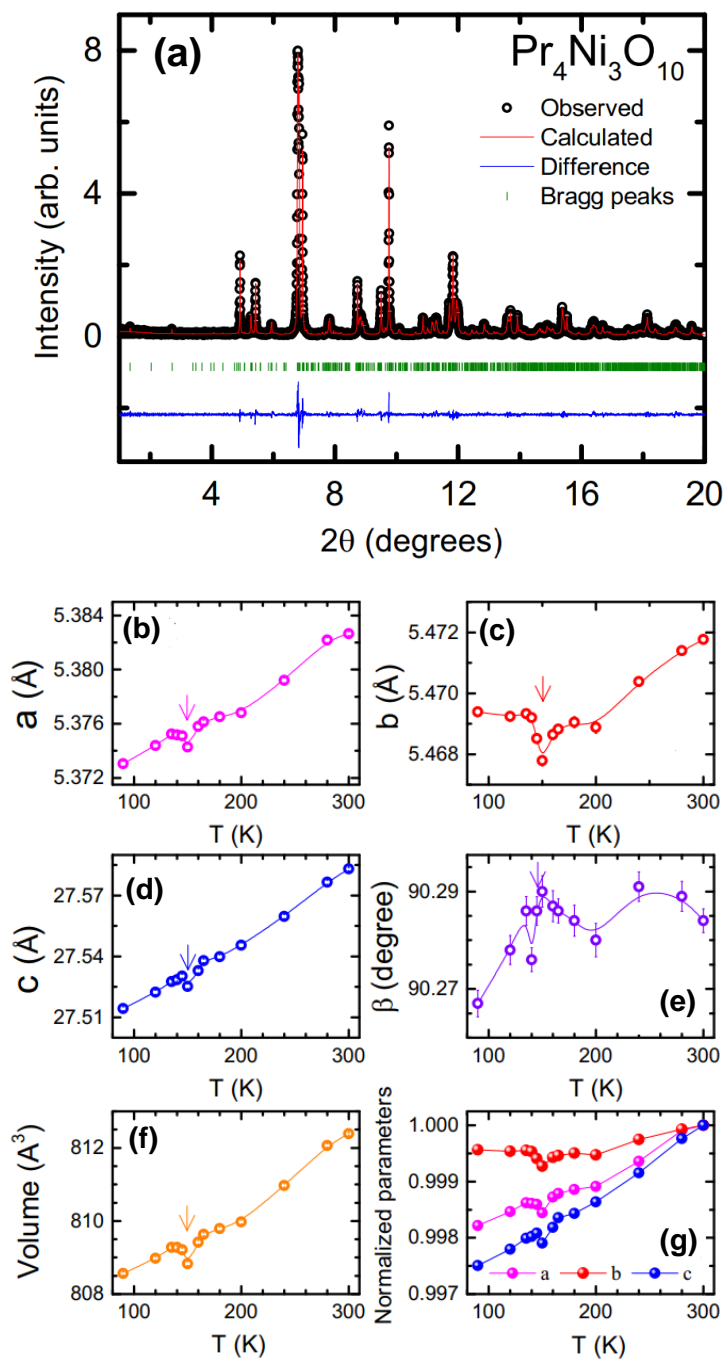
Figure 4.12: (a) Shows the Rietveld refinement results of the room temperature synchrotron powder X-ray diffraction data for $Pr_4Ni_3O_{10}$. Panels (b), (c) and (d) show the temperature variation of lattice parameters a, b and c, respectively; panels (e) and (f) show the temperature dependence of angle β and unit cell volume, respectively; panels (g) shows the normalized unit cell parameters.

may indicate the presence of a rather continuous but subtle and non-monotonic structure evolu-
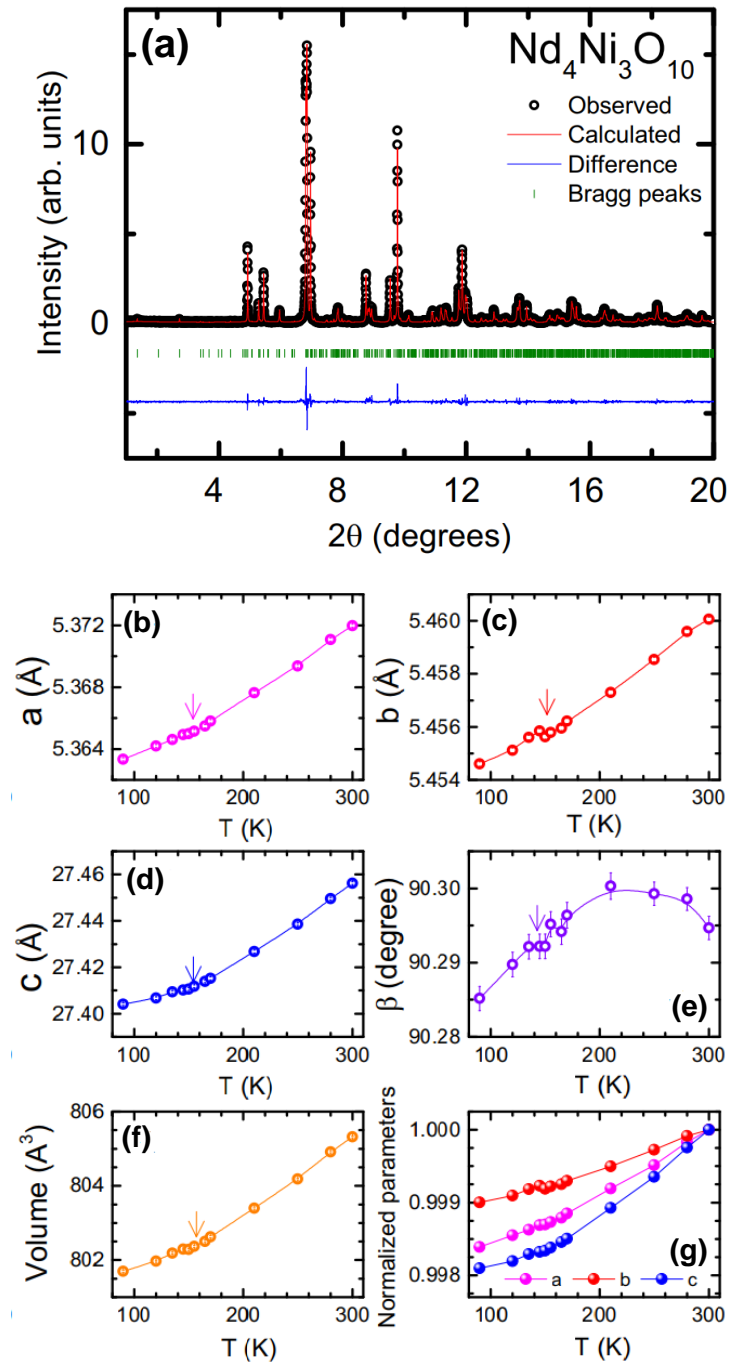
Figure 4.13: (a) Shows the Rietveld refinement results of the room temperature synchrotron powder X-ray diffraction data for $Nd_4Ni_3O_{10}$. Panels (b), (c) and (d) show the temperature variation of lattice parameters a, b and c, respectively; panels (e) and (f) show the temperature dependence of angle β and unit cell volume, respectively; panels (g) shows the normalized unit cell parameters.

tion occurring even above the MMT, analogous to the case of $Pr_4Ni_3O_{10}$. However, to confirm

Specimen	Space group	SG No.	Phase Type	Phase %	a($\mathring{A}$)	b($\mathring{A}$)	c($\mathring{A}$)	β	χ^2	R_{WP}	R_{EXP}	R_{P}
$La_4Ni_3O_{10}$	$P2_1/a$	14	M†	85.6	5.4243(5)	5.4748(5)	28.0053(4)	90.192^o(3)	6.15	14.7	5.90	11.7
	$Bmab$	64	O†	7.8	5.4040	5.4621	28.5542	90°				
	$Cmcm$	63	O†	6.6	20.1250	5.4638	5.4638	90°				
$Pr_4Ni_3O_{10}$	$P2_1/a$	14	M†	100	5.3826(4)	5.4717(4)	27.583(4)	90.284^o(3)	3.86	19.0	9.67	16
$Nd_4Ni_3O_{10}$	$P2_1/a$	14	M†	100	5.3719(4)	5.46(5)	27.4560(4)	90.299^o(3)	4.57	15.8	7.41	12.7

M† : monoclinic and O† : orthorhombic

Table 4.2: Refinement parameters obtained using the high-resolution synchrotron data for room the temperature crystal structure of R_4Ni$_3$O$_{10}$ ($R = La, Pr$ and Nd). The error bar in the lattice parameters is estimated to be of the order of ± 0.0002 in the fourth decimal place

if this is real or an experimental artifact, data at the intermediate temperatures for all the samples will be useful.

Table 4.2 summarizes the refinement details for the room temperature crystal structures of R_4Ni$_3$O$_{10}$, R = La, Pr and Nd. The room temperature lattice parameters for all three samples are listed in Table 4.2, which agree well with the values reported in previous literature [197, 199, 200].

4.5 Low temperature physical characterization

After carrying out detailed structural characterization of the R$_4$Ni$_3$O$_{10}$ (R = La, Pr and Nd) samples using synchrotron XRD, we carried out bulk physical characterization of the samples using various thermodynamic measurements. These complementary measurement techniques helped us probe further into the origin of the MMT, as shall be discussed next.

4.5.1 Electrical transport

Fig. 4.14 shows the temperature dependence of resistivity (ρ) for all three samples. Upon cooling below room temperature, $\rho(T)$ for all three samples decreases monotonically down to a temperature of approximately 136 K (La), 156 K (Pr) and 160 K (Nd). Upon further cooling, ρ increases in a step like fashion, which can be identified with the MMT. The temperature at which the step occurs (T_{MMT}), agrees well with the temperature where the lattice parameters show an anomaly. The resistivity discontinuity ($\Delta\rho$) at T_{MMT} appears to be first-order like, however, no measurable thermal hysteresis at T_{MMT} could be observed between the heating and cooling data. However, thin films of Nd$_4$Ni$_3$O$_{10}$ grown by Julia Mundy's group [87, 201]

do show a weak hysteresis around the MMT, indicating that it could be a first order transition.
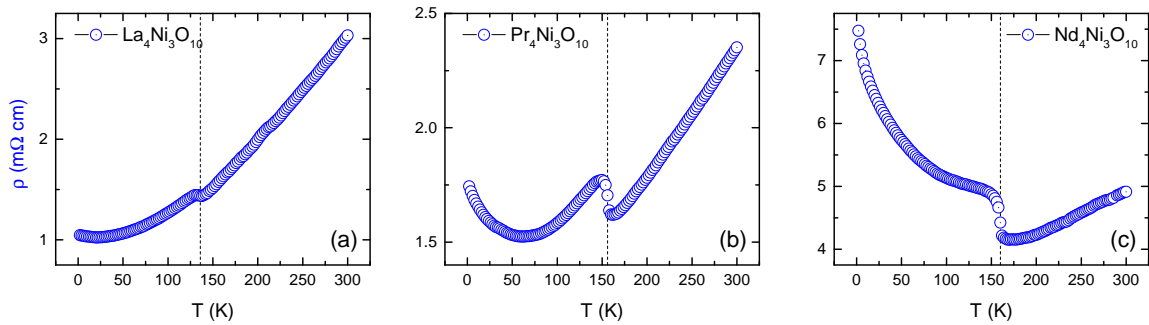
Figure 4.14: Panels (a), (b) and (c) show the temperature variation of resistivity (ρ) for $La_4Ni_3O_{10}$, $Pr_4Ni_3O_{10}$ and $Nd_4Ni_3O_{10}$ respectively.

Below the MMT, the resistivity for $La_4Ni_3O_{10}$ and $Pr_4Ni_3O_{10}$ continue to decrease down to some temperature T_0, which is followed by an upturn or a region of negative $d\rho/dT$ that persists down to 2 K. T_0 is $\simeq 20$ K and $\simeq 80$ K for $La_4Ni_3O_{10}$ and $Pr_4Ni_3O_{10}$, respectively. These observations concerning behavior of $\rho(T)$ in the La and Pr compounds are in good agreement with previous reports [185, 197, 199, 202].
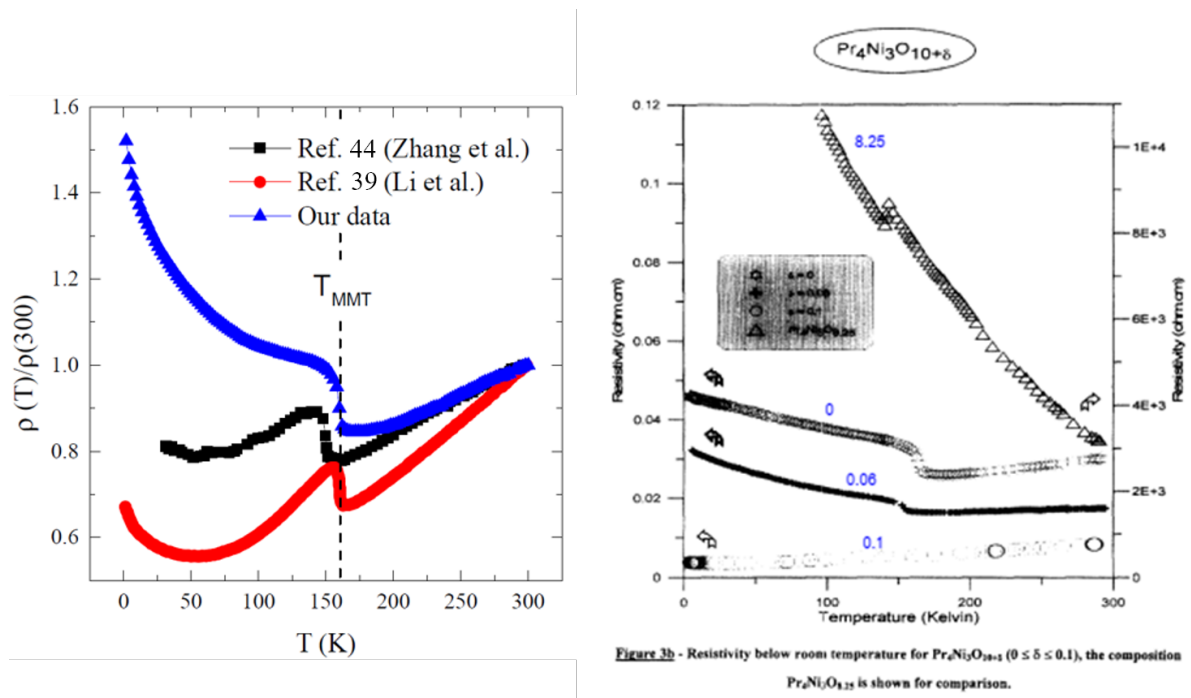
Figure 4.15: (a) Shows the normalized resistivity as a function of temperature for $Nd_4Ni_3O_{10}$ samples; (b) shows the resistivity as a function of temperature for $Pr_4Ni_3O_{10-\delta}$ samples ($\delta = 0$, 0.06 and 0.1) and for $Pr_4Ni_3O_{8.25}$ as reported in Ref. [199]

In $Nd_4Ni_3O_{10}$, however, $d\rho/dT \simeq 0$ down to about 100 K, and < 0 upon further cooling

followed by a steep increase below about 50 K. The upturn in this case is also more pronounced than for La and Pr. The published resistivity data for $Nd_4Ni_3O_{10}$ however show a region of negative $d\rho/dT$ for $T < T_{MMT} < 50$ K [75, 185]. The observed difference can however arise due to slight differences in the oxygen off-stoichiometry between various samples. From the TGA data shown in Fig. 4.7 (c), it is clear that our $Nd_4Ni_3O_{10}$ sample is oxygen deficient with actual oxygen stoichiometry close to 9.8 rather than 10. On the other hand, the $Nd_4Ni_3O_{10}$ sample of Ref. [185] had been reported to have been prepared under a pressurized oxygen atmosphere of 5 bar at $1100°$C for 24 h. Similarly, in Ref. [75], the sample was prepared by annealing it under oxygen flow for a period of close to 120 h to 150 h as opposed to 24 h in our case. The oxygen deficient samples tend to more insulating as shown in a previous study by Bassat *et al.* [199] on several $Pr_4Ni_3O_{10}$ compounds of varying oxygen off-stoichiometry [199]. The dependence of resistivity of the samples as a function of oxygen stoichiometry is shown in Fig. 4.15 (b).

4.5.1.1 Discussion on resistivity upturn at low temperatures

In previous studies, the low-temperature resistivity upturn seen in $R_4Ni_3O_{10}$ samples has been variously interpreted. While it is attributed to the weak localization due to inelastic electron-electron interactions in Ref. 197, the Kondo effect was claimed to be the reason in Ref. 185. In order to resolve this issue, we replotted the low-temperature data for all three compounds on two different temperature scales: (i) $T^{0.5}$, and (ii) $\ln T$ scales. The results are shown in Fig. 4.16. Clearly, the data for all three samples are best described by a $-\sqrt{T}$ dependence which persists down to the lowest temperature of 2 K. Very slight departure from this scaling for $Pr_4Ni_3O_{10}$ and $Nd_4Ni_3O_{10}$ near 10 K can be attributed to the short-range ordering of the rare-earth moments. On the contrary, the $-\ln T$ behavior does not describe the upturn in ρ satisfactorily or does so only over a narrow temperature range, with significant departure at low temperatures. Attempts to fit the low-temperature upturn to the Arrhenius or Variable Range Hopping (VRH) models (with or without interactions) also did not give satisfactory results (not shown). The analysis above clearly favors a $-\sqrt{T}$ dependence over other functional dependences commonly used to describe the low-temperature upturn in resistivity. The validity of $-\sqrt{T}$ behavior suggests that at low-temperatures weak localization due to inelastic electron-electron scattering is possibly what causes the resistivity upturn in all three compounds, which is typical of disordered metals and alloys [203]. Here, the structural disorder might be in
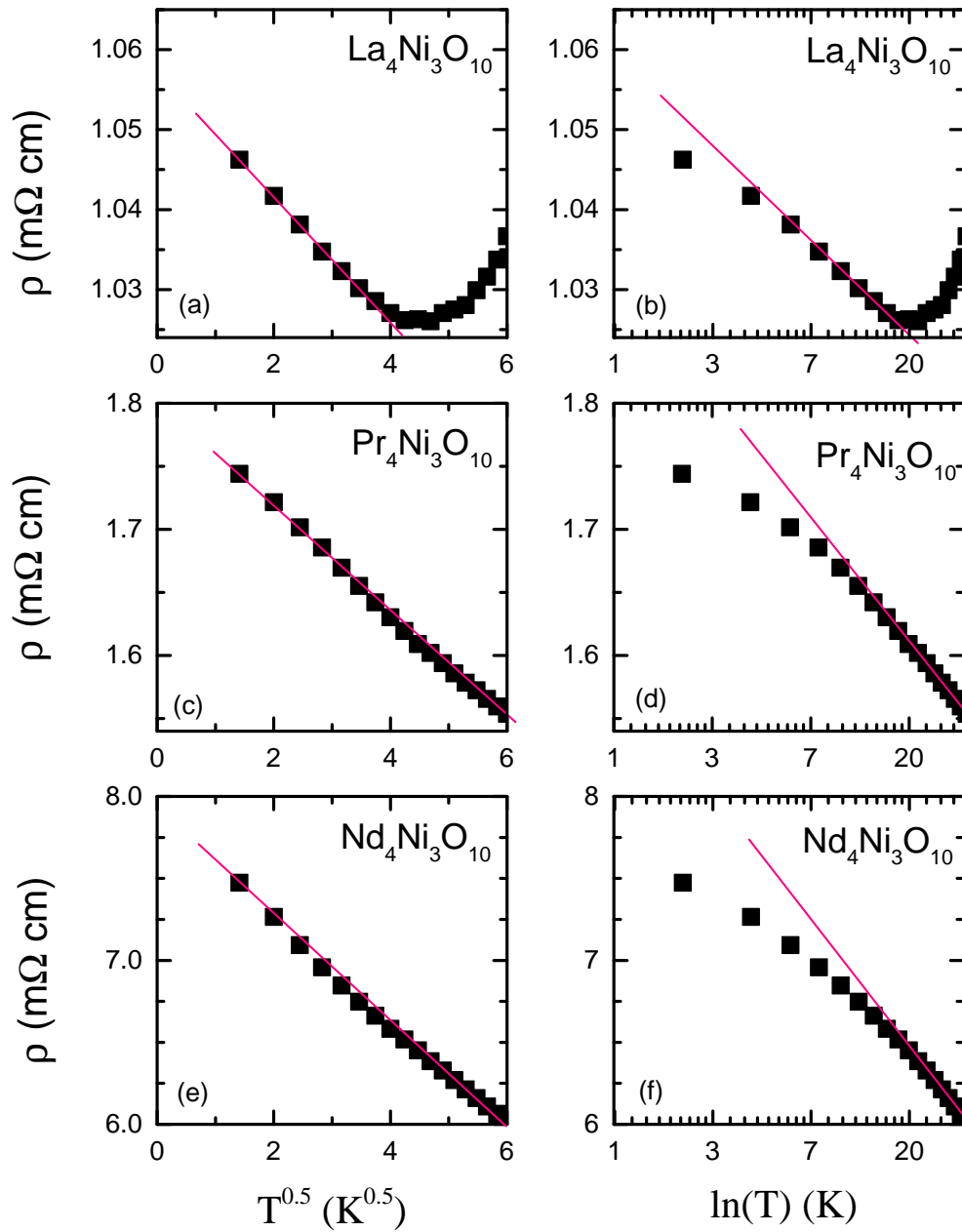
Figure 4.16: Temperature (T) variation of resistivity (ρ) of La$_4$Ni$_3$O$_{10}$ (a and b), Pr$_4$Ni$_3$O$_{10}$ (c and d) and Nd$_4$Ni$_3$O$_{10}$ (e and f) is shown on a $T^{0.5}$ scale (left panels), and a lnT scale (right panels).

the form of stacking faults and intergrowth whose presence is reflected in the powder X-ray diffraction. This conclusion is also in agreement with Ref. 197. On the other hand, the evidence for the Kondo effect in our data is rather weak.

4.5.2 Thermal transport

Thermal transport measurements were carried out on all three samples from room temperature down to 2 K in a four probe measurement geometry. The thermopower measurement was used to determine the sign of the charge carriers as well as to quantitatively comment on the evolution of the electronic structure below the MMT. On the other hand, thermal conductivity was used as a probe to understand the combined response of the phonons and electrons to the heat conduction in these materials.

4.5.2.1 Thermopower

The thermopower (S) of these samples is shown in panel (a), (b) and (c) of Fig. 4.17. All the samples have small values of thermopower, which is expected for a metallic phase. The overall behavior and the range of variation of S for the three samples is comparable to that previously reported [199, 204]. The temperature variation of S parallels that of ρ in the sense that at T_{MMT}, $S(T)$ exhibits a sharp jump, which can be understood based on the Mott's formula for thermopower, which is given by:

$$S = \frac{\pi^2}{3} \frac{k_B^2 T}{e} \left(\frac{\partial \ln \sigma(E)}{\partial E} \right)_{E=E_F} \tag{4.2}$$

where k_B is the Boltzmann constant, $\sigma(E)$ is the electrical conductivity, e the electronic charge, and E_F is the Fermi energy. Since, σ can be expressed as: $\sigma = n(E)q\mu(E)$, where $n(E) = D(E)f(E)$: $D(E)$ is the density of states, and $f(E)$ the Fermi-Dirac distribution function, and μ is the carrier mobility, one can rewrite eq. 4.2 with a term in S proportional to the quantity dn/dE at E_F, i.e., change in carrier concentration with respect to energy at E_F, which is expected to vary drastically due to opening of a gap at E_F below the MMT as shown in the previous ARPES studies [68].

For $T > T_{\mathrm{MMT}}$, the sign of $|S|$ is negative, implying that the electrons are the majority charge carriers in this temperature range. We notice that, for $T > T_{\mathrm{MMT}}$, $|S|$ increase almost linearly with increasing temperature as is typically seen for metals. Naively, one can use
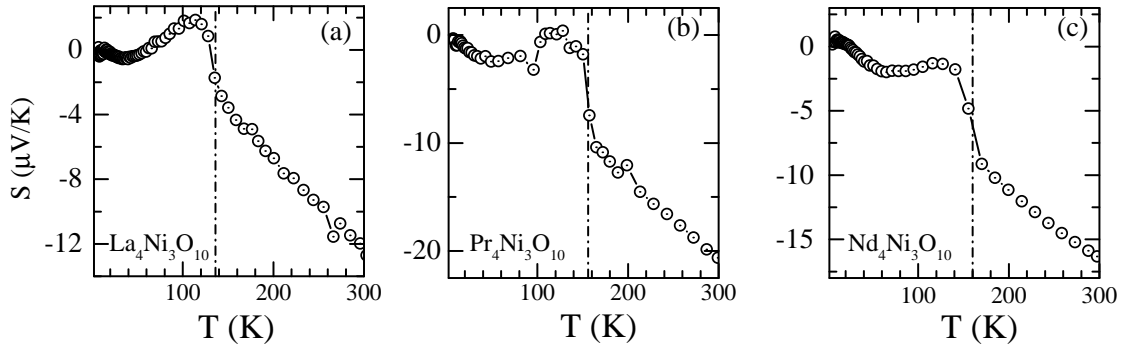
Figure 4.17: (a), (b) and (c) show the thermopower of $La_4Ni_3O_{10}$, $Pr_4Ni_3O_{10}$ and $Nd_4Ni_3O_{10}$ samples as a function of temperature respectively.

the single parabolic band model approximation to rewrite the Mott formula in eq. 4.2 in the following form:

$$S = \frac{8\pi^2 k_B^2 m^*}{3eh^2} \left(\frac{\pi}{3n}\right)^{\frac{2}{3}} T \tag{4.3}$$

where m^* is the band effective mass of the charge carriers. By fitting S above T_{MMT} using $S = a_o T$, where a_0 is the prefactor in eq. 4.3, one can estimate m^*. For this purpose, we use n obtained from the Hall coefficient $R_H \approx 10^{-3} \text{cm}^3/\text{C}$ at $T = 300$ K [205]. Following this procedure, we get $m^* \simeq 3.0 m_0$ for $La_4Ni_3O_{10}$, $3.9 m_0$ for $Pr_4Ni_3O_{10}$, and $2.8 m_0$ for $Nd_4Ni_3O_{10}$. Additionally, for $La_4Ni_3O_{10}$, we see a crossover from n to p - type behaviour at around 130 K. Again in the vicinity of T $\sim$ 61 K, it undergoes a p to n - type transition. These crossovers were not clearly captured in previous literature and suggest that the charge transport in $La_4Ni_3O_{10}$ involves both electrons and holes below the MMT.

4.5.2.2 Thermal conductivity

The temperature variation of thermal conductivity (κ) is shown in Fig. 4.18(a–c). For all three samples the T_{MMT} is manifested in κ as a small but clearly discernible kink. For $R = $ La and Pr, we measured the data both while heating and cooling and found some hysteresis around T_{MMT}. However, since no hysteresis was found in ρ, it is difficult to conclude if this is an intrinsic feature or a measurement issue. At low-temperatures, κ increases upon heating as $\sim T^3$, which suggests that in this temperature range the acoustic phonons contributes dominantly to κ. Upon further heating, a noticeable change in the functional form of κ takes place for

$T \gtrsim 50$ K: In La$_4$Ni$_3$O$_{10}$ κ shows a broad peak in the range from 50 K to 100 K with a peak value of 3 Wm^{-1}K^{-1} around 80 K; in Pr$_4$Ni$_3$O$_{10}$ κ shows an increasing behavior all the way up to 300 K, albeit with a much slower rate $T \gtrsim 50$ K; and, in Nd$_4$Ni$_3$O$_{10}$, κ gradually levels off with a saturated value of ≈ 1 Wm^{-1}K^{-1} for $T > 100$ K. Thus, the behavior of κ in all three cases is rather similar at low-temperatures, but differs somewhat depending on R in the range $T \gtrsim 50$ K.
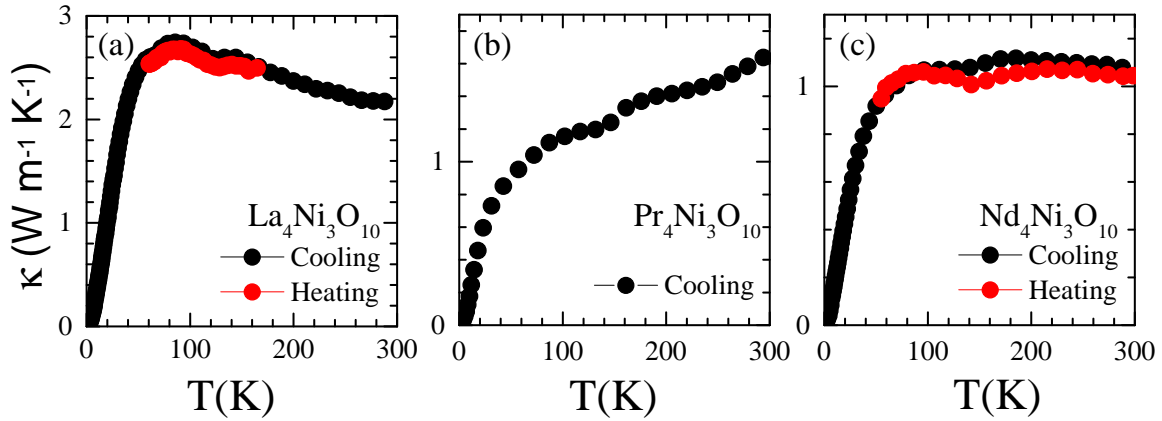
Figure 4.18: (a), (b) and (c) shows the temperature dependence of thermal conductivity measured for La$_4$Ni$_3$O$_{10}$, Pr$_4$Ni$_3$O$_{10}$ and Nd$_4$Ni$_3$O$_{10}$ using the four-probe method.

It is interesting to note that in spite of their reasonably high electrical conductivities (ranging from 100-1000 S cm^{-1}), the thermal conductivities of these nickelates, ranging from 1 m^{-1}K^{-1} to 3 Wm^{-1}K^{-1}, is rather low, which, in turn, implies that the lattice thermal conductivity in these nickelates is intrinsically very low. This may be related to their complex layered structure. The low thermal conductivity and metal-like electrical conductivity above the MMT together indicates that the trilayer nickelates are potential oxide thermoelectric materials.

4.5.3 Magnetization

The temperature as well as magnetic field dependence of the magnetization of all the samples was studied using the DC magnetization measurements. The details of the experiments are discussed as follows:

4.5.3.1 Magnetic susceptibility

La$_4$Ni$_3$O$_{10}$:

The magnetic susceptibility (χ) of La$_4$Ni$_3$O$_{10}$ is shown in Fig. 4.19 (a). Our data shows a

good agreement with previous reports [197, 205, 206]. In $La_4Ni_3O_{10}$, χ exhibits a discernible kink at $T = 136$ K, which corresponds well with the MMT. The overall behavior of χ in $La_4Ni_3O_{10}$ is found to be rather peculiar for the following two reasons: First, the decreasing behavior with cooling at high temperatures ($T > T_{MMT}$) is uncharacteristic of a local moment system in the paramagnetic regime. On the other hand, had it been Pauli paramagnetic due to a possible itinerant nature of Ni $3d$ electrons, the measured $\chi(T)$ would have remained been nearly temperature independent, which is not the case either. Kobayashi *et al.* [205] measured $\chi(T)$ of $La_4Ni_3O_{10}$ up to higher-temperatures and found it to show a broad hump near $T = 400$ K. One may argue that this hump is a characteristic feature of low-dimensional spin systems; however, in $R_4Ni_3O_{10}$ the superexchange pathways are not strictly limited to one or two dimensions. While it is true that these are layered structures and to that effect some degree of low-dimensionality may play a role, however, the hybridization between Ni $3d$ and O $2p$ orbitals increases significantly with increasing thickness of the PB layer. As a result, the $d_{3z^2-r^2}$ band, which is highly localized in La_2NiO_4, is expected to broaden-up considerably in $La_4Ni_3O_{10}$ leading to delocalized or itinerant behavior. The second peculiar feature in $\chi(T)$ of $La_4Ni_3O_{10}$ concerns the sharp rise at low-temperature which has been, so far, overlooked in the previous literature or is interpreted as arising due to paramagnetic impurities. We fitted this upturn in the range $2\,\mathrm{K} \leq \mathrm{T} \leq 10\,\mathrm{K}$ using the modified Curie-Weiss law: $\chi = \chi_o + C/(T - \theta_P)$, yielding $\chi_0 = 10^{-3}$ emu mol^{-1}Oe^{-1}, the Curie-constant $C = 1.7 \times 10^{-2}$ emu mol^{-1}Oe^{-1}K^{-1}, and the paramagnetic Curie-temperature $\theta_P \approx 2.7$ K. From the value of C, we obtained an effective magnetic moment of about 0.3 $\mu_B/f.u.$, which is too large to be attributed to the presence of paramagnetic impurities. The value of χ_0 is positive and also rather high (about one to two orders of magnitude higher than the Pauli paramagnetic susceptibility due to the free electrons). The value of θ_p is positive, which indicates ferromagnetic interactions between the Ni spins. However, in our susceptibility of specific heat data no signs of long- or short-range magnetic ordering nor a tendency towards it has been observed even though short range AFM/FM correlations of the type Ni^{2+}–O–Ni^{2+} and Ni^{2+}–O–Ni^{3+} are expected to be present.

As shown in the ARPES experiments, below the MMT, the $d_{3z^2-r^2}$ band (or more precisely the γ band with $d_{3z^2-r^2}$ character [68]) develops a significant energy gap of ≈ 20 meV, which, upon cooling, would gradually lead to localization of $d_{3z^2-r^2}$ electrons, which is possibly the
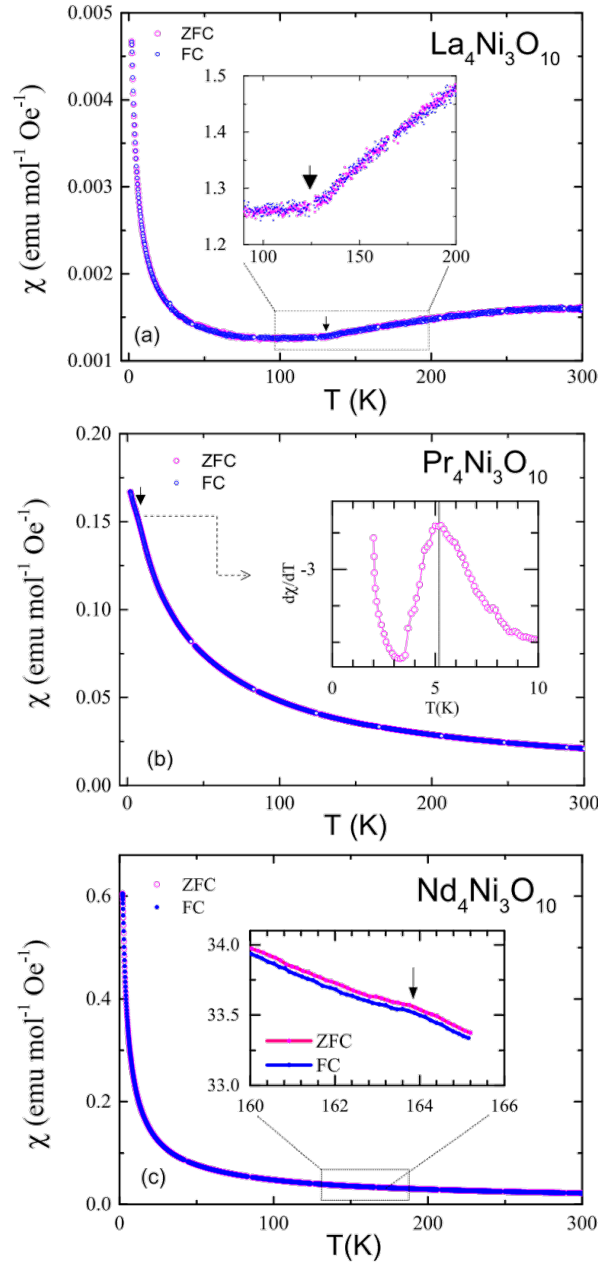
Figure 4.19: Zero-field-cooled (ZFC) and field-cooled (FC) susceptibility (χ) of (a) $La_4Ni_3O_{10}$, (b) $Pr_4Ni_3O_{10}$, and (c) $Nd_4Ni_3O_{10}$ measured under an applied field of 5 kOe. The inset in: (a) shows a kink in susceptibility at T_{MMT}, (b) the low-temperature anomaly is emphasized in the first derivative plot, (c) the kink in susceptibility at T_{MMT}.

reason for the observed increase in χ upon cooling below the MMT. In short, it seems that the overall magnetic behavior in $La_4Ni_3O_{10}$ is an interplay of itinerant and local moment behavior which gets more intriguing below MMT. Though not very significant, to some degree the low-dimensionality due to the layered structure may also play a role.

Pr$_4$Ni$_3$O$_{10}$:

The magnetic susceptibility of the Pr$_4$Ni$_3$O$_{10}$ is dominated by the Curie-Weiss (CW) behavior associated with the Pr^{3+} moments. Additionally, a weak anomaly is also observed around $T \simeq 5$ K. This anomaly is more easily discernible in the derivative plot where $d\chi/dT$ is shown to exhibit a peak. The specific heat of Pr$_4$Ni$_3$O$_{10}$ also shows a peak at the same temperature, which suggests a probable magnetic ordering of the Pr^{3+} moments. The high-temperature χ could be fitted using the modified CW law yielding: $\chi_0 \approx 2.8 \times 10^{-3}$ emu mol^{-1}Oe^{-1}, C $\approx$ 6.3 emu mol^{-1}Oe^{-1}K^{-1}, and $\theta_p \approx -36$ K in good agreement with literature [199]. The value of χ_0 is positive and comparable in magnitude to that for La$_4$Ni$_3$O$_{10}$. The negative sign of θ_p indicates antiferromagnetic nature of exchange between the Pr^{3+} moments. The experimental effective magnetic moment per formula unit can be estimated using the formula: $\mu_{\text{eff}} = \sqrt{8C}$ which gives $\approx 7.2 \ \mu_B$. Theoretically, $\mu_{\text{eff}}/f.u.$ is given by $[4.\mu_{\text{eff}}^2(Pr) + 3.\mu_{\text{eff}}^2(Ni)]^{\frac{1}{2}}$. Substituting the theoretical value of $\mu_{\text{eff}} = 3.58 \ \mu_B$ per Pr^{3+} ion results in a relatively negligible moment on the Ni-ions.

Nd$_4$Ni$_3$O$_{10}$:

The temperature dependent magnetic susceptibility of Nd$_4$Ni$_3$O$_{10}$ is shown in Fig. 4.19 (c). Though effective magnetic moments of Nd^{3+} and Pr^{3+} are nearly the same in free space, the low-temperature χ in Nd$_4$Ni$_3$O$_{10}$ is almost four times as large as that of Pr$_4$Ni$_3$O$_{10}$. This suggests the presence of strong crystal field effect that renders one-half of the Pr-moment effectively non-magnetic at low-temperature due to their singlet ground state. Near $T = 2.5$ K, the susceptibility exhibits a very weak anomaly (not shown). This corroborates the specific heat of Nd$_4$Ni$_3$O$_{10}$ which increases upon cooling below $T = 10$ K due to short-range interactions between the Nd-moments. Since magnetic ordering in Nd$_2$O$_3$ sets in only below $T = 0.5$ K [207], this feature cannot be due to some small quantity of unreacted Nd$_2$O$_3$ that may have possibly gone undetected in the powder X-ray diffraction. The possibility of lower member Nd$_3$Ni$_2$O$_7$ ordering at this temperature however cannot be ruled out, though it should be stressed that in our X-ray diffraction we did not find any evidence of the presence of this phase. The CW fit in this case resulted in: $\chi_0 \sim 3.8 \times 10^{-3}$ emu mol^{-1}Oe^{-1}, $C \sim 6.3$ emu mol^{-1}Oe^{-1}K^{-1}, and $\theta_p = -46.5$ K. These values are in close agreement with those recently reported by Li *et al.* [185]. From C, the experimental μ_{eff} is estimated to be $\approx 7.1 \mu_B/f.u.$

which is practically all due to the Nd^{3+}, suggesting that the local moment associated with Ni is comparatively negligible. The value of θ_p is high given the absence of any magnetic ordering, suggesting that a strong magnetic frustration is at play in these nickelates.

4.5.3.2 Isothermal magnetization

The isothermal magnetization for all the three samples is shown in Fig. 4.20. For the case of $La_4Ni_3O_{10}$, the $M(H)$ is linear above the MMT with $M(H)|_{250K} > M(H)|_{150K} > M(H)|_{100K}$ over the whole range, which is in agreement with $\chi(T)$ which shows an increasing behavior with temperature over this T-range. The $M(H)$ data below 5 K is non-linear and it keeps on increasing with applied field with no signs of saturation suggesting the presence of mixed ferro and antiferromagnetic interactions.
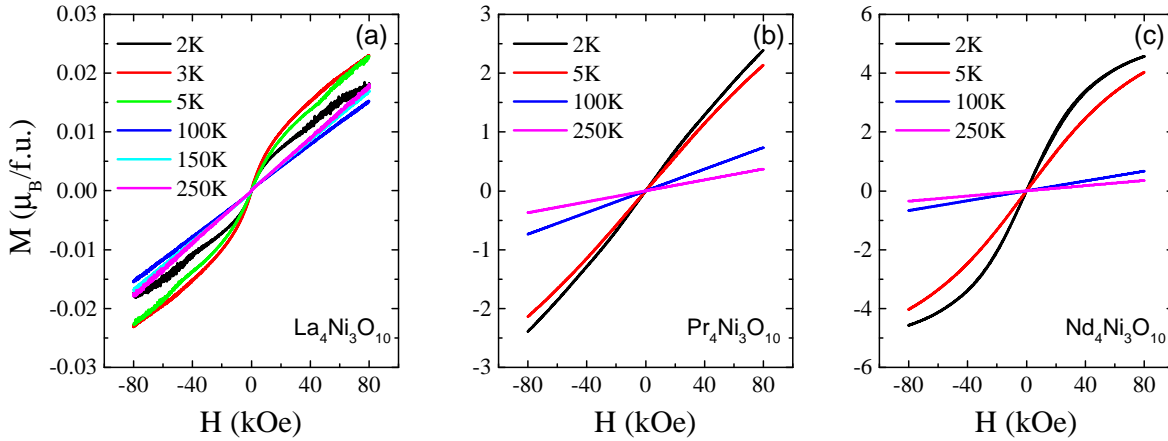
Figure 4.20: (a), (b) and (c) shows the isothermal magnetization of $La_4Ni_3O_{10}$, $Pr_4Ni_3O_{10}$ and $Nd_4Ni_3O_{10}$ as a function of applied field at various temperatures.

For the case of $Pr_4Ni_3O_{10}$ the $M(H)$ is linear above the MMT while at low temperatures it becomes non-linear. At low temperatures, the magnetization increases almost linearly with increasing field reaching a value of $\approx 2\mu_B/f.u.$ or $\approx 0.5\ \mu_B/Pr^{3+}$, which is significantly smaller than the theoretical saturation moment of $3.13\ \mu_B/Pr^{3+}$, which is partly due to the fact that $1/2$ of the Pr-moments have a singlet ground state, the remaining $1/2$ are antiferromagnetically ordered near $T = 5$ K.

The $M(H)$ data for $Nd_4Ni_3O_{10}$ is shown in Fig. 4.20 (c). The $M(H)$ at $T = 2$ K shows a Brillouin function dependence; however, the saturation moment ($\approx 5\ \mu_B/f.u.$ or $1.25\ \mu_B/Nd$) is appreciably smaller than the theoretical value ($g_J J = 3.3\mu_B/Nd$), which is, once again, a

possible manifestation of the crystal field splitting. At $T = 100$ K, and 250 K, $M(H)$ increases in a linear manner with $M(H)|_{100K} > M(H)|_{250K}$, which is in line with the paramagnetic nature of the Nd^{3+} moments in this temperature range.

4.5.4 Specific heat

The specific heat (c_p) data of $R_4Ni_3O_{10}$ compounds was measured from room temperature to 2 K at both 0 T and 5 T. The specific heat data exhibits a sharp anomaly at their respective MMTs which is particularly pronounced for $Pr_4Ni_3O_{10}$ and $Nd_4Ni_3O_{10}$. The low temperature specific heat associated with the $4f$ electrons shows additional anomalies, associated with the rare-earth sublattice that were not previously reported in literature.

4.5.4.1 Specific heat of La$_4$Ni$_3$O$_{10}$

In La$_4$Ni$_3$O$_{10}$ the specific heat anomaly occurs at 136 K as shown in Fig. 4.21. It should be emphasized that in a La$_4$Ni$_3$O$_{10}$ crystallizing in the $Bmab$ space group the specific heat anomaly occurs at a temperature of ≈ 150 K, and it is at 136 K for the $P2_1/a$ phase [196]. This is consistent with our assessment of $P2_1/a$ as the majority phase in our samples. The applied magnetic field of 50 kOe (not shown) was found to have practically no effect on this anomaly. At low-temperatures, c_p can be fitted using the equation: $c_p = \gamma T + \beta T^3$, where γ and β represents the electronic and lattice contributions, respectively (see the lower inset in Fig. 4.21). The best-fit yields: $\gamma \simeq 15$ mJ-mol^{-1}K^{-2}, $\beta \simeq 0.43$ mJ mol K^{-4}. The Debye temperature (Θ_D) is calculated from β using the relation: $\beta = 12\pi^4 Nk_B/5\Theta_D^3$, which gives a value of $\Theta_D \approx 450$ K. The values of Θ_D and γ obtained here are comparable to those previously reported [206]. From the value of γ one can readily estimate the density of states at the Fermi energy, D(E$_F$), using the expression: D(E$_f$)$= 3\gamma/\pi^2 k_B^2$, which gives a value of $\approx 3.0 \times 10^{22}$ states eV^{-1} cm^{-3}. Now, using the carrier density n, one can estimate the corresponding density of states D$°$(E$_F$) at E_F using the free-electron model. Taking $n \approx 6.3 \times 10^{21}$ cm^{-3} [205], one gets D$°$(E$_F$) $\approx 7.6 \times 10^{21}$ states eV^{-1} cm^{-3}. From the ratio D(E$_F$)/D$°$(E$_F$)$= m^*/m_\circ$, we estimate the effective mass (m^*) for La$_4$Ni$_3$O$_{10}$ to be $m^* \approx 3.9m_\circ$, where $m_\circ$ is the bare electron mass, which is comparable to the value of m^* from the thermopower ($\approx 3.0m_\circ$). The small difference between the two can be due to the possible Fermi surface reconstruction below the MMT. Also, we have not accounted for the valley

degeneracy, if any, which makes the the effective mass derived from the density of states higher than the band effective mass by a factor $N^{2/3}$ where N is the valley degeneracy. In any case, the important point is that from the value of m^* one can conclude that the electronic correlations in $La_4Ni_3O_{10}$ are only modestly enhanced.

4.5.4.2   Specific heat of $Pr_4Ni_3O_{10}$

Fig. 4.21 shows the specific heat of $Pr_4Ni_3O_{10}$ where a sharp transition is observed at 156 K, which agrees nicely with the anomaly associated with the MMT in the transport data. In this case, too, the position and shape of the anomaly remains unaffected by the application of an external magnetic field. Apart from the expected peak at MMT, an additional broad anomaly is seen at low temperatures centered around $T_1 = 5$ K, which coincides with the anomaly in χ at the same temperature. Interestingly, the applied field up to 50 kOe has no significant effect on the shape or position of this anomaly ruling out its Schottky-like origin. To examine the contribution of $4f$ electrons associated with Pr to the specific heat (designated as c_{4f}^{Pr} in the following) at low temperatures, we subtracted the specific heat data of $La_4Ni_3O_{10}$ from that of $Pr_4Ni_3O_{10}$. Since both are isostructural, with very similar molecular weights, it is, therefore, reasonable to approximate the lattice specific heat of $Pr_4Ni_3O_{10}$ with that of $La_4Ni_3O_{10}$. Furthermore, we assume that the small contribution due to Ni 3d electrons to the specific heat does not vary much upon going from La to Pr, at least well below the MMT. This is a reasonable first-order approximation to make given that T_{MMT} for the these nickelates is not very sensitive to the choice of R, in wide contrast with the members of the $n = \infty$ RP series where the variation of concomitant magnetic and metal-to-insulator transition is huge [181].

c_{4f}^{Pr} obtained using this procedure is shown in Fig. 4.21b (lower panel) over the temperature range 2 K $\leq T \leq 100$ K. Interestingly, beside the peak at $T_1 = 5$ K, c_{4f}^{Pr} also exhibits an additional broad peak around $T_2 = 36$ K. This new feature is likely a Schottky anomaly arising due to the crystal field splitting of the lowest $J = 4$ multiplet of the Pr^{3+} ions. To understand this further, we estimate the magnetic entropy (s_{4f}) buried under the peak at T_1 using the formula: $s_{4f} = \int_0^T (c_{4f}^{Pr}/T')dT'$. For our rough estimate, we extrapolate c_{4f}^{Pr} below $T = 2$ K linearly to $T = 0$ K. The calculated s_{4f} is shown as an inset in the lower panel of Fig. 4.21. It shows a relatively steep rise up to 10 K, but continues to increase, albeit at a slower rate, upon heating beyond 15 K. The region between 10 K and 15 K is where
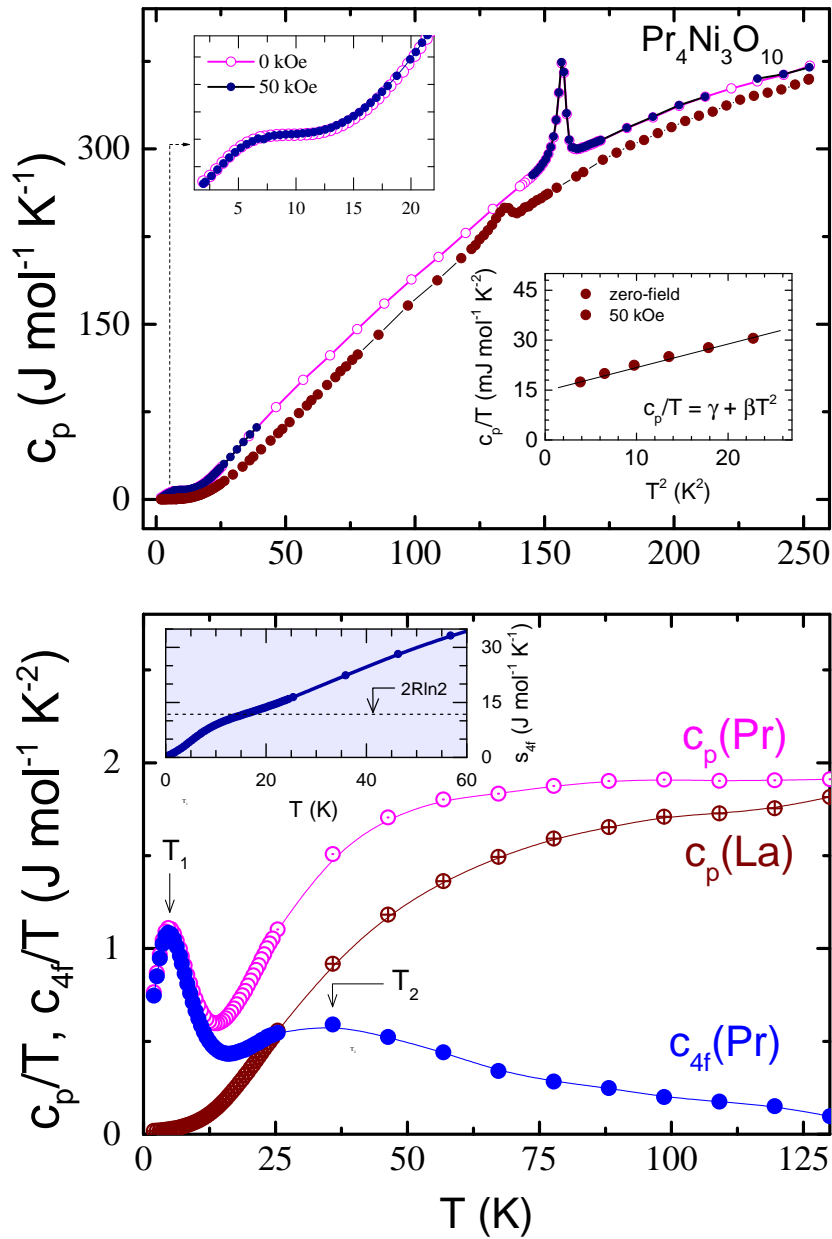
Figure 4.21: (a) Temperature (T) variation of the specific heat (c_p) of $La_4Ni_3O_{10}$ and $Pr_4Ni_3O_{10}$. The upper inset in (a) highlights the presence of a broad anomaly in c_p of $Pr_4Ni_3O_{10}$ at low temperature measured under zero-field and a field of 50 kOe. The immunity to magnetic field of this peak rules out its Schottky-like origin. The lower inset shows c_p/T vs. T^2 of $La_4Ni_3O_{10}$ at low-temperatures. The dashed line is a linear-fit to the data. (b) $\frac{c_p}{T}$ against T. $c_{4f}(Pr)$ represents the specific heat associated with the $4f$ electrons of Pr^{3+} which is obtained by subtracting the specific heat of $La_4Ni_3O_{10}$ from that of $Pr_4Ni_3O_{10}$ (see text for details). Temperature variation of entropy associated with the $4f$ electrons of Pr^{3+} is shown as an inset.

the crossover from higher ($T < 10$ K) to slower ($T > 15$ K) rates happens. The magnetic entropy released in the temperature range $T \leq 15$ K ($\approx 3T_1$) is ≈ 11.5 J mol^{-1}K^{-1}, i.e.,

≈ 2.9 J Pr-mol^{-1}K^{-1}, which is approximately $\frac{1}{2}$ of $R\ln 2$. What this suggests is that the peak at T_1 is likely due to the magnetic ordering of $\frac{1}{2}$ of the Pr^{3+} ions per Pr$_4$Ni$_3$O$_{10}$ formula unit, which is plausible since there are 2-types of Pr coordinations in this structure: $9 - $ fold (RS layers) and $12 - $ fold (PB layers). Incidentally, Pr^{3+} in the perovskite PrNiO$_3$ has a non-magnetic singlet ground state [208]. Since the coordination of Pr^{3+} ions in the PB layers of Pr$_4$Ni$_3$O$_{10}$ is analogous to that in PrNiO$_3$, it is reasonable to assume that they, too, have a singlet ground state with no magnetic ordering. Therefore, we can tentatively associate the broad peak in the specific heat at T_1 to the magnetic ordering of the $9-$fold coordinated Pr^{3+} ions. The increase in s_{4f} beyond 15 K can be attributed to the higher lying crystal field levels as discussed further. A similar scenario has been previously reported for the compounds Pr$_3$RuO$_7$ which has two types of Pr coordinations, namely, eightfold and sevenfold, with Pr ions in the sevenfold coordination having a crystal field split singlet ground state, and those in the eightfold coordination a doublet [209].

However, the question arises as to why the peak associated with the magnetic ordering of Pr^{3+} ions in the RS layer is not as sharp as is typically seen at a long-range ordered magnetic transitions. To answer this question, one should see that for the $9-$fold coordinated Pr^{3+} ions there are, in fact, two distinct crystallographically sites (Pr1 and Pr2). Due to minor differences in bond angles and bond lengths around Pr1 and Pr2, the exchange integrals J_{11} (within the Pr1 sublattice), J_{22} (within the Pr2 sublattice), and intersite J_{12} may differ slightly, which could be one of the reasons for the c_p anomaly at T_1, associated with ordering of Pr1 and Pr2, to be broad. The other reason could be related to the fact that the Pr^{3+} moments in one RS layer is only weakly coupled to the Pr^{3+} moments in the RS layer above it (see Fig. 4.3), leading to a quasi-two-dimensional behavior.

Let us now turn our attention to the peak at T_2 which seems to arise due to the crystal field splitting of the lowest J-multiplet of Pr^{3+} ions. In a previous inelastic neutron scattering study on the perovskite compound PrNiO$_3$ [208], it was found that the $9-$fold degenerate J-multiplet of the Pr^{3+} ion splits into 9 singlets due to the crystal field effect. The energy difference between the ground state singlet (E_0^1) and the first excited state (E_1^1) is 6.4 meV or approximately 70 K. In the first order approximation, the crystal field splitting of Pr ions in the PB layers of Pr$_4$Ni$_3$O$_{10}$ can be assumed to be similar to that in the compound PrNiO$_3$. Within

this assumption, the Schottky anomaly due to the ground and first excited singlet is expected to be centered slightly below $T = (E_1^1 - E_0^1)/2k_B \approx 35$ K, which is remarkably close to the position of the peak at T_2. Since the second excited singlet for Pr in the PB layers is located around $E_2^1 = 15$ meV (≈ 165 K), it is too high up to have any significant effect on the Schottky anomaly arising due to the E_0^1/E_1^1 pair.

It can therefore be concluded that the Pr ions in the PB layer have a singlet ground state due to a crystal field effect, with a broad Schottky anomaly associated with ground and first excited singlet pair. On the other hand, Pr ions in the RS layers have a crystal field split doublet as their ground state, and undergo magnetic ordering around T_1. The observed increase in s_{4f} above $2\,T_1$ is partly due to E_0/E_1 excitations associated with Pr-ions in the PB layer, and partly due to the higher lying crystal field split levels of Pr ions in the RS layers. In the absence of a detailed crystal field splitting scheme for the Pr ions in the RS layers, a quantitative analysis of the low-temperature specific heat is left as a future exercise.

4.5.4.3   Specific heat of Nd$_4$Ni$_3$O$_{10}$

Fig. 4.22(a) shows the specific heat of Nd$_4$Ni$_3$O$_{10}$, which is characterized by a sharp anomaly at $T = 160$ K. The position of this anomaly is in a fairly good agreement with the MMT inferred from the transport data, and is found to be independent of an applied magnetic field at least up to 50 kOe. The low temperature c_p is characterized by an upturn below $T = 10$ K. Under an applied magnetic field, this upturn evolves leading to a broad peak, centered around 4 K under $H = 50$ kOe, which progressively shifts to higher temperatures with increasing magnetic field. This behavior is reminiscent of a Schottky-like anomaly, which often arises in the rare-earth based compounds due to the crystal field splitting.

To investigate this further, we estimate the specific heat associated with $4f$ electrons of Nd, labeled c_{4f}^{Nd}. The specific heat of La$_4$Ni$_3$O$_{10}$ is used as a lattice template, and also to subtract the small magnetic specific heat associated with the Ni sublattice. c_{4f}^{Nd} obtained in this manner is displayed in the lower panel of Fig. 4.22 (inset). At $T = 2$ K, it has a value of about ~ 6.9 J mol^{-1}K^{-1}, which decreases sharply upon heating but remains substantial (~ 3.5 J mol^{-1}K^{-1}) even at $T = 12$ K, and increases again upon further heating, exhibiting a broad Schottky like anomaly near $T = 50$ K that can be attributed to the higher-lying crystal field split levels
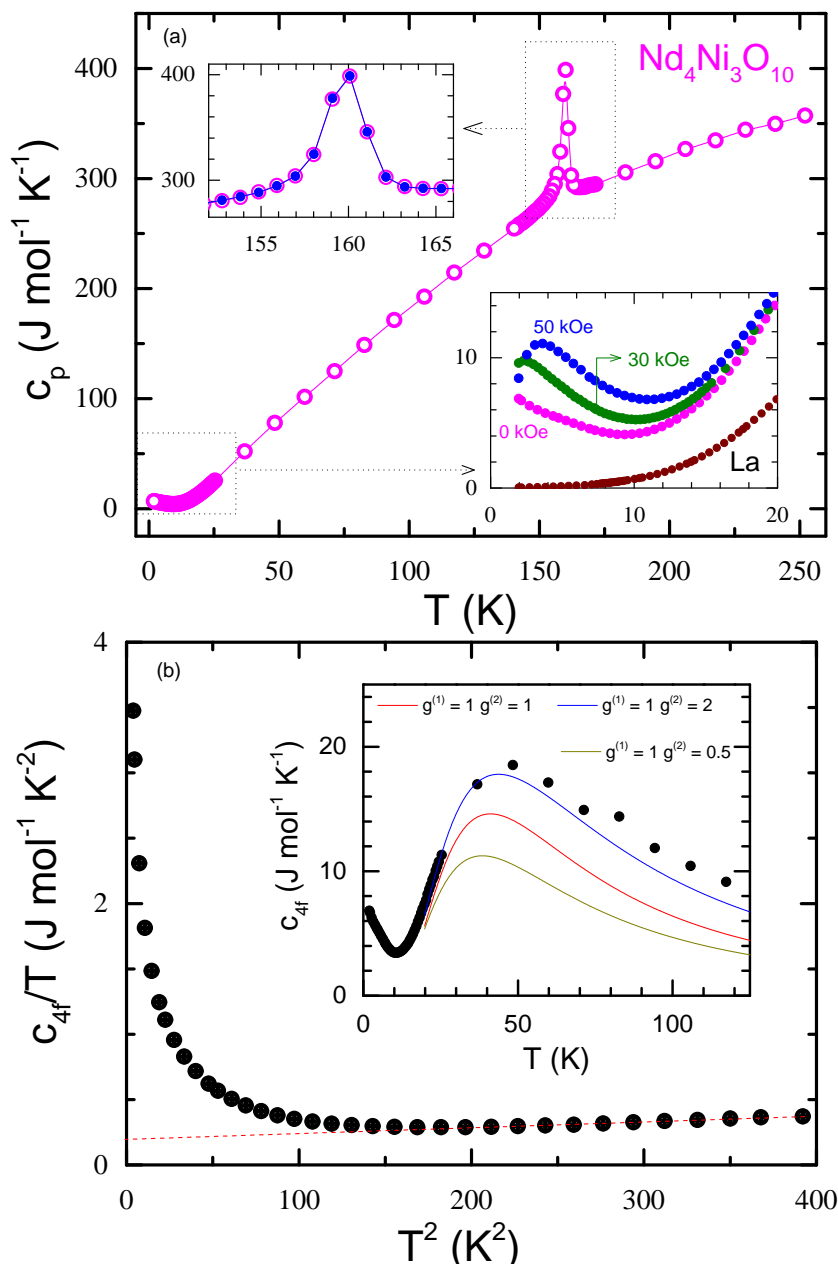
Figure 4.22: (a) Specific heat (c_p) of $Nd_4Ni_3O_{10}$. Lower inset shows c_p in the low-temperature range for an applied field of 0 kOe, 30 kOe and 50 kOe; c_p of $La_4Ni_3O_{10}$ is also shown for comparison. Upper inset shows an expanded view of the anomaly at MMT under zero-field and a field of 50 kOe. (b) Low-temperature specific heat associated with the $4f$ electrons of $Nd_4Ni_3O_{10}$ is plotted as c_{4f}/T versus T^2; inset shows c_{4f} versus T up to $T = 120$ K to show the presence of a pronounced Schottky anomaly near $T = 40$ K. The modified Schottky fittings for three cases: $g^{(1)} = 1$, $g^{(2)} = 1$ (red), $g^{(1)} = 1$, $g^{(2)} = 2$ (blue), and $g^{(1)} = 1$, $g^{(2)} = 0.5$ (khaki) (see text for details)

of Nd^{3+} ions. In $NdNiO_3$, for example, the lowest $^4I_{9/2}$ multiplet of Nd^{3+} ion splits into *five* Kramers doublets with the first excited doublet situated around 100 K above the ground doublet [210]. Since Nd^{3+} ions in the PB layers of $Nd_4Ni_3O_{10}$ are analogously coordinated,

one can assume a similar crystal field splitting scheme for them. On the other hand, for the 9–fold coordinated Nd^{3+} ions the splitting scheme may be different. However, since Nd^{3+} is a Kramers ion with 3 electrons in the f–orbitals, in the absence of a magnetic field each crystal field split level should at least be two fold degenerate: i.e., for the 9–fold coordinated Nd^{3+} ions the ground and first excited state crystal field split levels can have degeneracies as follows: $g_0 = 2$, $g_1 = 2$, $g_0 = 2$, $g_1 = 4$, or $g_0 = 4$, $g_1 = 2$. Thus, the ratio $\frac{g_1}{g_0}$, which appears in the expression for the Schottky anomaly, can take values 1, 2 or 0.5, respectively. Note that for Nd^{3+} ions in the PB layer this ratio will be 1. With this as an input, one can try fitting the broad peak in c_{4f} near 40 K using the expression: $c_{Sch} = c_{Sch}^{(1)} + c_{Sch}^{(2)}$, where:

$$c_{Sch}^{(i)} = 2R \left(\frac{\Delta_i}{T} \right)^2 \frac{g^{(i)} exp(\frac{-\Delta_i}{T})}{[1 + g^{(i)} exp(\frac{-\Delta_i}{T})]^2} \tag{4.4}$$

In this expression, R is the universal gas constant, Δ is the splitting between the ground and first excited state, and g is the ratio $\frac{g_1}{g_0}$. Here, the index i is used for the the two types of coordinations, *viz*, $i = 1$ corresponding to the 12–fold coordination, and $i = 2$ corresponding to the 9–fold. The prefactor 2 account for the number of Nd^{3+} ions per formula unit in each type of layers. The fitting result for $g^{(1)} = 1$, $g^{(2)} = 1$ (fit1), $g^{(1)} = 1$, $g^{(2)} = 2$ (fit2), and $g^{(1)} = 1$, $g^{(2)} = 0.5$ (fit3) are shown in the inset of Fig. 4.22(b). The corresponding values of Δ_1 and Δ_2 for these fits are: 98 K and 98 K for (fit1), 150 K and 95 K for (fit2), and 93 K and 93 K for (fit3), respectively. Clearly, the best fit corresponds to (fit2), which implies that the ground state of Nd^{3+} ions in the 9–fold coordination is also a Kramers doublet, with a quartet for the first excited state.

Let us now turn our attention to the increase in c_{4f}^{Nd} upon cooling below $T = 10$ K. In $NdNiO_3$ a similar upturn leading to a broad peak around $T = 1.7$ K had been previously reported [210]. It was argued to arise from the exchange splitting of the ground state doublet. However, unlike $NdNiO_3$, in $Nd_4Ni_3O_{10}$ the Ni moments are not ordered and hence the Ni–Nd exchange field in this case is almost non-existent. On the other hand, it might be that this upturn is precursory to an impending magnetic ordering of the Nd moments at further low-temperatures. After all, the Nd-Nd exchange, as inferred from the high temperature Curie-Weiss fit, is about -45 K, which is rather high. This could then be a case closely analogous to the case of Nd_2O_3 recently reported, which also exhibits a high $\theta_p \simeq -24$ K, but with long-

range order setting in only below $T = 0.55$ K. Surprisingly, c_p of Nd_2O_3 shows not only a sharp peak at 0.55 K corresponding to the long-range ordering of Nd moments but also a broad feature centered around 1.5 K. The authors report that the entropy associated with this broad peak must be taken into account in order to recover the $R \ln 2$ entropy expected from a ground state doublet suggesting a complex two-step ordering of the Nd moments. The c_p of $Nd_4Ni_3O_{10}$ also shows a broad peak at $T \approx 1.8$ K [185] which suggests that a phenomenology analogous to Nd_2O_3 might also be at play here. Further studies down to much lower temperatures would be interesting to explore this analogy further and to understand the true ground state of the Nd sublattice.

Finally, c_{4f}^{Nd}/T versus T^2 is plotted in the lower panel of Fig. 4.22. The data from 12 K to 20 K can be fitted to a straight line whose intercept on the $y-$axis is ~ 150 mJ mol^{-1}K^{-2}. Indeed, in Ref. 185, a high γ value of 146 mJ mol^{-1}K^{-2} is reported by fitting c_p/T versus T^2 to $\gamma + \beta T^2$ in this temperature range. However, caution must be exercised while interpreting the intercept value in this case since c_p in this temperature range, as shown in the inset of Fig. 4.22b, is overwhelmed by the Schottky contribution arising from the crystal field split lowest $J-$multiplet of Nd^{3+} ions. It is for this reason we believe that the high γ value in Ref. 185, which led the authors of this study to conclude a "novel" heavy-electron behavior in $Nd_4Ni_3O_{10}$, is a gross overestimation. As is well documented in the heavy fermion-literature, if the electronic specific heat γ in such cases is derived by extrapolating the high-temperature specific heat data to $T = 0$ K using $\gamma T + \beta T^3$ unusually large values are obtained, which can be falsely interpreted as arising due to the heavy fermion behavior.

4.5.5 Capacitive dilatometry

The temperature dependence of length changes studied by capacitive dilatometry, shown in Figs. 4.23, follows the volume dependence as measured using the X-ray diffraction data. However, while there is quantitative agreement for $Pr_4Ni_3O_{10}$, discrepancies are noticed for $La_4Ni_3O_{10}$ and $Nd_4Ni_3O_{10}$. Specifically, the dilatometric length changes are about 25% and 45% larger than suggested by X-ray diffraction, respectively. The data are isotropic, i.e., we find the behavior to be the same when measuring along different directions of the polycrystalline cuboids, which excludes a simple non-random orientation effect to cause this discrepancy. Instead, the data suggest a non-uniform internal stress distribution within the polycrys-

talline samples which can lead, in porous materials, to larger thermal expansion than in the bulk [211].
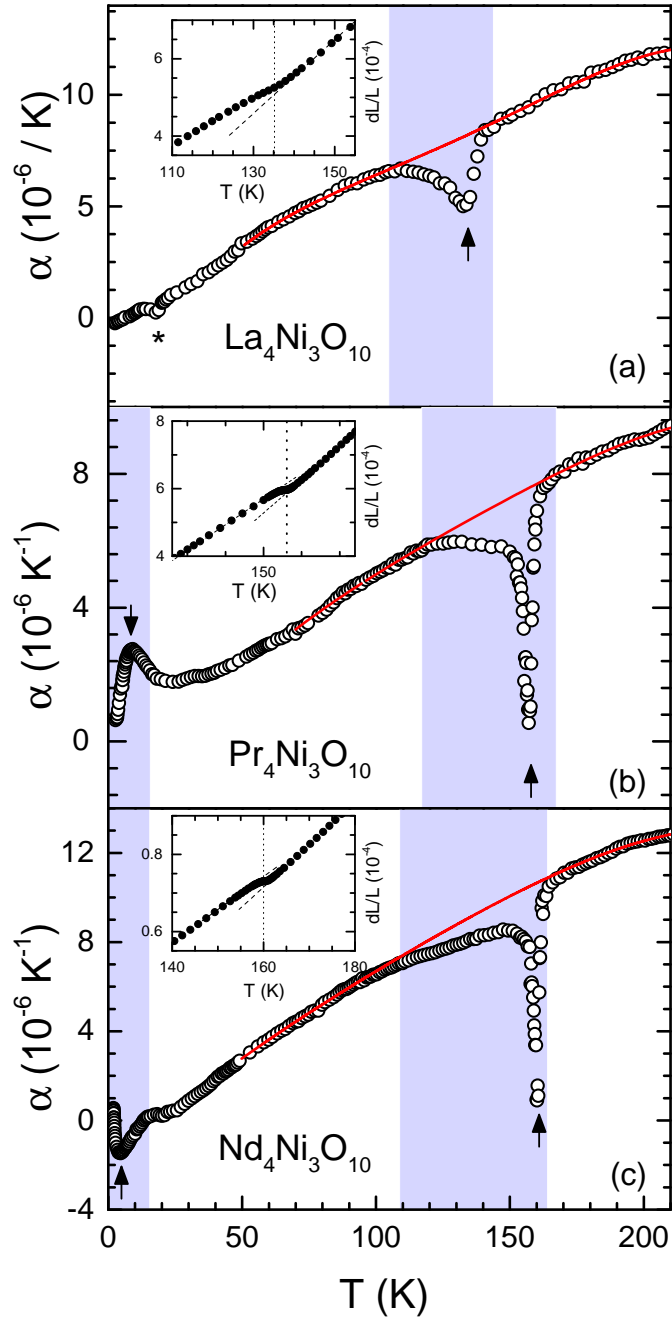
Figure 4.23: Temperature dependence of the thermal expansion coefficient α of $La_4Ni_3O_{10}$, $Pr_4Ni_3O_{10}$, and $Nd_4Ni_3O_{10}$. The red line shows a polynomial estimate of the background (see text for details). The arrows marks the position of T_{MMT}. The asterisk in the upper panel indicates an experimental artifact. The additional low-temperature peak in $Pr_4Ni_3O_{10}$ and $Nd_4Ni_3O_{10}$ is likely due to the crystal field excitations. The inset shows length change (dL/L) around T_{MMT}; the dotted line is a guide to the eye.

Table 4.3: Total anomalous length and entropy changes $\Delta_t L/L = \int \Delta\alpha dT$ and $\Delta_t S = \int \Delta c_{\mathrm{p}}^{\mathrm{MMT}}/T dT$, discontinuous length changes $\Delta_d L/L$, Grüneisen parameter Γ and hydrostatic pressure dependence of T_{MMT} of $R_4\mathrm{Ni}_3\mathrm{O}_{10}$ (see the text).

	$\Delta_t L/L$ ($\cdot 10^{-5}$)	$\Delta_d L/L$ ($\cdot 10^{-5}$)	$\Delta_t S$ (J/mol-K)	Γ ($\cdot 10^{-7}$ mol/J)	dT_{MMT}/dp (K/GPa)
$\mathrm{La}_4\mathrm{Ni}_3\mathrm{O}_{10}$	−4(1)	-	1.0(3)	−4.9(9)	−8(2)
$\mathrm{Pr}_4\mathrm{Ni}_3\mathrm{O}_{10}$	−5(1)	−3.1(6)	3.1(6)	−2.3(6)	−4(1)
$\mathrm{Nd}_4\mathrm{Ni}_3\mathrm{O}_{10}$	−5.1(4)	−2.6(2)	3.5(9)	−1.4(4)	−3(1)

The length changes in $R_4\mathrm{Ni}_3\mathrm{O}_{10}$ evidence significant coupling of electronic and structural degrees of freedom. Specifically, there are pronounced anomalies at T_{MMT} in all studied materials. In $\mathrm{La}_4\mathrm{Ni}_3\mathrm{O}_{10}$, the data in Fig. 4.23 displays a broad feature which signals shrinking of the sample volume upon exiting the MMT phase while heating the sample. Qualitatively, this implies negative hydrostatic pressure dependence $dT_{\mathrm{MMT}}/dp < 0$. The minimum of the thermal expansion anomaly appears at $T_{\mathrm{MMT}} = 134$ K, suggesting either a weak first-order character of the transition or a somehow truncated λ-like behavior similar to what is indicated by the specific heat anomaly (see Fig. 4.21).

In order to estimate the background contribution to the thermal expansion coefficient, a polynomial was fitted to the data well below and above the thermal expansion anomaly as shown in Fig. 4.23 [212]. The background α^{bgr} mainly reflects the phonon contribution. Due to the large size of the anomaly, using different temperature ranges for the determination of the background and/or choosing different fit functions does not change the result significantly. Subtracting α^{bgr} from the data yields the anomaly contribution to the thermal expansion coefficient $\Delta\alpha$ as shown in Fig. 4.24a. Recalling the discrepancy of dilatometric and XRD length changes mentioned above for $\mathrm{La}_4\mathrm{Ni}_3\mathrm{O}_{10}$ and $\mathrm{Nd}_4\mathrm{Ni}_3\mathrm{O}_{10}$, for the following quantitative analysis of both we have scaled the dilatometric data to the XRD results. Quantitatively, our analysis then yields total anomalous length changes $\Delta_t L/L = \int \Delta\alpha dT = -4.2(9) \cdot 10^{-5}$.

When replacing La by Pr and Nd in $R_4\mathrm{Ni}_3\mathrm{O}_{10}$, the anomalies in the thermal expansion at T_{MMT} become significantly sharper and evidence rather discontinuous behavior (see Figs. 4.23). In addition, there are pronounced features at low temperatures (marked by arrows) that are associated with the rare-earth sublattice. In particular, the data clearly confirm negative volume expansion in $\mathrm{Nd}_4\mathrm{Ni}_3\mathrm{O}_{10}$ below ~ 20 K. At higher temperatures, the sharp anomalies at 156 K

(R = Pr) and 160 K (R = Nd) at T_{MMT} are accompanied by a regime of rather continuous length changes which extends from T_{MMT} down to about 110 K, i.e., it is significantly larger than the anomaly regime in $La_4Ni_3O_{10}$. Applying the procedure described above for determining the background yields the thermal expansion anomalies as displayed in Fig. 4.24b and 4.24c for the two compounds.
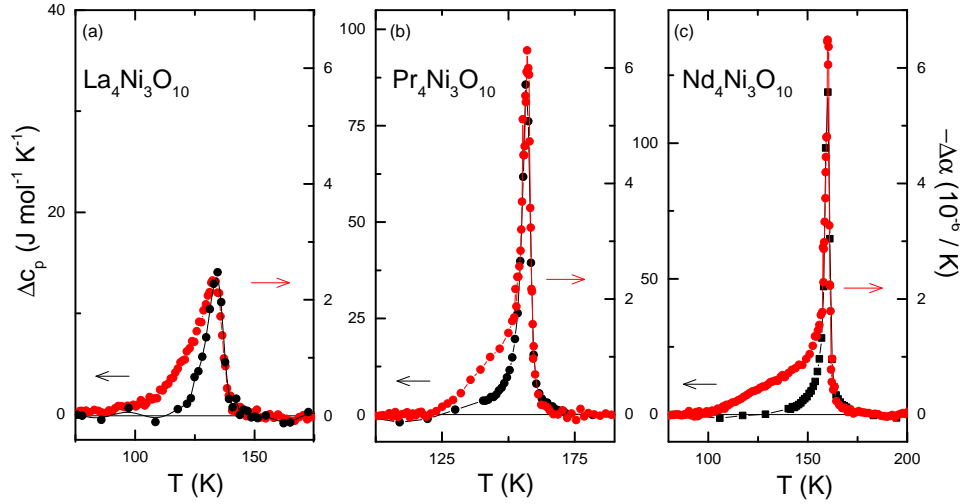
Figure 4.24: Anomalies in the specific heat and the negative thermal expansion coefficient of $R_4Ni_3O_{10}$ with R = La, Pr, and Nd. The anomaly size in (a) and (c) has been rescaled according to the X-ray diffraction results (see the text). Note the same scale of the thermal expansion ordinate in all graphs.

The anomalies $\Delta\alpha$ in the thermal expansion coefficients at T_{MMT} are presented in Fig. 4.24 together with the respective anomalies of the specific heat. The latter have been derived by estimating the background specific heat analogously to the procedure used for the thermal expansion data and by using the same fitting regimes in both cases [212]. For each composition, scaling of Δc_{p} and $\Delta\alpha$ has been chosen to obtain the best overlap of the specific heat and thermal expansion data around T_{MMT} and above. The fact that the thermal expansion and specific heat anomalies are proportional at T_{MMT} implies a T-independent Grüneisen parameter describing the ratio of pressure and temperature dependence of entropy changes in this temperature range. This observation implies the presence of a single dominant energy scale ϵ [213]. In contrast, the fact that Grüneisen scaling starts to fail at around 10 K below T_{MMT} indicates the presence of more than one relevant degree of freedom. In the temperature regime around T_{MMT} and above, the corresponding scaling parameter is the Grüneisen parameter [214]:

$$\Gamma = \frac{3\Delta\alpha}{\Delta c_{\mathrm{p}}} = \frac{1}{V} \left.\frac{\partial \ln \epsilon}{dp}\right|_T \tag{4.5}$$

Our analysis yields the Γ values summarized in Table 4.3. Using the Ehrenfest relation, the obtained values of Γ yield the hydrostatic pressure dependencies of the ordering temperature at vanishing pressure, i.e., $dT_{\mathrm{MMT}}/dp = T_{\mathrm{MMT}}V_{\mathrm{m}}\Gamma$. The results deduced using the molar volume V_{m} are shown in Table 4.3.

The obtained initial slopes of hydrostatic pressure dependencies of T_{MMT} are comparable to values reported from measurements of the electrical resistivity under pressure. Specifically, Wu *et al.* report -6.9 K/GPa for $La_4Ni_3O_{10}$ which nicely agrees to the results of the Grüneisen analysis presented above. The comparison with $Nd_4Ni_3O_{10}$ studied in Ref. 185 is, however, ambiguous. On the one hand, Li *et al.* [185] report discontinuous shrinking of the unit cell volume at T_{MMT} by 0.08 % while cooling, which, both, qualitatively and quantitatively, contrasts our data (cf. inset of Fig. 4.23c). In particular, this value implies a *positive* hydrostatic pressure dependence of about $+35$ K/GPa [1]. However, at the same time an initial *negative* hydrostatic pressure dependence of about -8 K/GPa is reported in Ref. 185 which thermodynamically contradicts the reported volume changes at T_{MMT} but is reasonably consistent with the results of our Grüneisen analysis.

The broad region of anomalous length changes between T_{MMT} and ~ 100 K signals clear temperature variation of the Grüneisen ratio, in this temperature regime, the reason of which is not fully clear. In general, the fact that capacitance dilatometry is obtained under small but finite pressure, which in the case at hand is estimated to about $0.6(1)$ MPa, may affect measurements in particular on polycrystalline samples. The fact that the dilatometer detects volume increase however renders a scenario as observed in recent studies of electronic nematicity of LaFeAsO rather unlikely, where the shear modulus C_{66} is the elastic soft mode of the associated nematic transition so that dilatometry under finite pressure results in associated volume decrease [215, 216]. We also exclude that variation of Γ is associated with incompletely resolved strain from the discontinuous transition at T_{MMT} because the measurements have been performed upon heating and the temperature regime of the observed anomaly is very large. Instead, we conclude the presence of a competing ordering phenomenon as suggested by the

---

[1]We have applied the Clausius-Clapeyron equation and used $\Delta S = 2.8$ J/(mol K) as reported in Ref. [185].

failure of Grüneisen scaling [213]. Intriguingly, a temperature regime of unexpected behavior has also been detected in the out-of-plane resistivity $\rho_\perp$ in $Pr_4Ni_3O_{10}$ single crystal where, in contrast to the in-plane resistivity, an increase of $\rho_\perp$ upon cooling, i.e., insulating behavior, is observed in a large temperature regime [73]. It is tempting to trace back this intermediate temperature regime of $d\rho_\perp/dT < 0$, i.e., a metal-to-insulator-like behavior of $\rho_\perp$ at T_{MMT}, to the competing degree of freedom which manifests in the thermal expansion coefficient and change of Grüneisen parameter shown in Fig. 4.24 (b).

4.6 Summary

We investigated the trilayer nickelates $R_4Ni_3O_{10}$ (R = La, Pr and Nd) that are $n = 3$ members of the RP series. We focused our investigations on understanding the following important aspects concerning the physical properties of these compounds: (i) what is the correct space group characterizing the room-temperature crystal structure of these compounds, (ii) is there a structural phase transition at T_{MMT}, (iii) how do various thermodynamic quantities, including resistivity, magnetic susceptibility, specific heat, thermopower, thermal conductivity and thermal expansion coefficient vary across MMT, and (iv) to understand the magnetic behavior of the rare-earth sublattices in $Pr_4Ni_3O_{10}$ and $Nd_4Ni_3O_{10}$.

In order to address these questions, we synthesized high-quality samples using the sol-gel method. These samples were then subject to a high-resolution synchrotron powder X-ray diffraction at the ALBA synchrotron source, both at 300 K and lower temperatures down to 90 K. A thorough analysis confirms that these compounds crystallize in the monoclinic $P2_1/a, Z = 4$ phase. Absence of new peaks emerging or splitting of the existing peaks ruled out any lowering of the lattice symmetry accompanying this transition. The thermal expansion coefficient also captured the anomaly at T_{MMT} rather vividly. From the analysis of $\Delta\alpha$, we conclude that the MMT anomaly becomes more first order-like as we go to smaller lanthanide ionic radii (and thereby larger distortions from the perovskite structure).This was further corroborated by temperature variation of various physical properties.

Resistivity data of all samples exhibit sharp jump or discontinuity at their respective T_{MMT} and an upturn, i.e., with $d\rho/dT < 0$, at low-temperatures. We show that this upturn is likely a consequence of weak-localization arising due to inelastic electron-electron interactions. This

result is in agreement with Ref. [197] where resistivity of $La_4Ni_3O_{10}$ has been analyzed in considerable details. In particular, we excluded a Kondo-like mechanism in the Ni-sublattice leading to $d\rho/dT < 0$ as has been proposed recently [185]. This result is further strengthened by thermopower and specific heat experiments. From thermopower and specific heat, we found the band effective mass of the charge carriers to range from around $3m_o$ to $4m_o$, which indicates that the electronic correlations are at best moderately enhanced.

The magnetic ground state of the $R-$ions in $Pr_4Ni_3O_{10}$ and $Nd_4Ni_3O_{10}$ is shown to be rather interesting. First, the Curie-Weiss temperature (θ_p) for both these compounds is of the order of -40 K; however the long-range ordering remains suppressed down to temperatures as low as 5 K for $Pr_4Ni_3O_{10}$ and less than 2 K for $Nd_4Ni_3O_{10}$ suggesting the presence of strong magnetic frustration, which may be related to their layered structure that renders the R^{3+} moments located in the RS layers quasi-two-dimensional. From the analysis of c_p and χ, we infer that in $Pr_4Ni_3O_{10}$, the Pr^{3+} ions located in the PB layers exhibit a crystal field split non-magnetic singlet ground state, while those located in the RS layers show a ground state doublet with an antiferromagnetic ordering below about 5 K.

In $Nd_4Ni_3O_{10}$, on the other hand, all four Nd-ions in the formula unit exhibit a Kramers doublet ground state with first excited state as doublet for one-half of the Nd ions and quartet for the remaining half, giving rise to a pronounced Schottky-type anomaly centered around $T = 35$ K. The low-temperature specific heat of both $Pr_4Ni_3O_{10}$ and $Nd_4Ni_3O_{10}$ is found to be overwhelmed by the Schottky-like contributions arising from the crystal field excitations associated with the lowest J–multiplet of the rare-earth ions, which tends to *falsely* inflate the value of γ.

In summary, the rare-earth sublattice in $R_4Ni_3O_{10}$ compounds with $R =$ Pr and Nd, exhibit very intriguing behavior which should be subject to further examination using specific heat down to much lower temperatures, inelastic and elastic neutron scattering. With the possibility of single-crystal growth, the interesting low-temperature behavior of these compounds as shown here should attract significant further interest.

Chapter 5

Crossover from a charge/spin stripe insulator to a correlated metal in the n $= 3$ member of the T' nickelate family

- The preliminary sample preparation and characterization work was done in collaboration with Sanchayeta Ranajit Mudi [177].

- The low temperature transport and magnetization measurements were done in collaboration with Dr. Rajeev Rawat from UGC DAE Consortium for Scientific Research in Indore, Madhya Pradesh, India.

5.1 Introduction

With the discovery of high temperature superconductivity in cuprates by Bednorz and Müller [50] in 1986, enormous efforts are underway to find superconductivity in other transition metal based oxide systems. In this regard, the most obvious place to look for is nickelates, isostructural and isoelectronic to high T_C cuprates. Almost three decades back Anisimov *et al.* [82] had theoretically predicted that if Ni^{1+} (S $= 1/2$) is forced into a square planar coordination with O-ions, it can lead to an AFM insulating ground state, which can be hole doped to realize the superconducting ground state in analogy with the high T_C cuprates. The recent discovery of superconductivity in the thin films of hole doped $NdNiO_2$ [84], $LaNiO_2$ [86, 217] and $PrNiO_2$ [85, 218] reinvigorated the study of nickelates. Here $RNiO_2$ is the n $= \infty$ member of a

much broader infinite layer nickelate family with a general formula of $R_{n+1}Ni_nO_{2n+2}$ (R can be an alkaline earth or a rare-earth ion and n can take values starting from 1, 2, 3,....,∞). These infinite layered nickelates can be mapped onto the cuprate phase diagram based on the Ni d electron count [69, 90]. Infact, the validity of this mapping got further reinforced when super-conductivity was observed in the thin films of "quintuple - layer" compound $Nd_6Ni_5O_{12}$ (n = 5) [87], which naturally lies in the optimally doped region of the cuprate phase diagram [219].

5.2 Motivation to study the n = 3 members of the infinite layer nickelate family

In this work, we focus our attention on the n = 3 member of the T' nickelate family i.e., $R_4Ni_3O_8$ (where R = La, Pr and Nd). They crystallize in the tetragonal space group of $I4/mmm$ (space group No. 139) with three infinite layer NiO_2 planes separated by an intervening fluorite layer (RO_2) as shown in Fig. 5.1 (right panel). These mixed valent nickelates contain Ni^{1+}/Ni^{2+} in the ratio of 2:1 and resemble the $3d^9/3d^8$ electronic configuration of Cu^{2+}/Cu^{3+} present in high T_C cuprates. The average Ni valence in $R_4Ni_3O_8$ is +1.33 i.e., a d filling value of 8.67, which essentially lies in the overdoped, Fermi liquid regime of the cuprate phase diagram [89]. Even though the n = 3 members do not undergo a superconducting transition, their similarities with cuprates, including large orbital polarization of the unoccupied e_g states [69], strong Ni $3d$ and O $2p$ hybridization [220], and a square planar arrangement of Ni ions are reasons enough to investigate their physical properties at low temperatures. Although $La_4Ni_3O_8$,$Pr_4Ni_3O_8$ and $Nd_4Ni_3O_8$ belong to the same crystallographic space group, they exhibit contrasting ground state properties. For example, $La_4Ni_3O_8$ is a charge/spin (CS) stripe ordered insulator which features a sharp metal-to-semiconductor transition (hence-forth, we shall loosely refer to it as a metal-to-insulator or MIT) concomitant with the onset of charge/spin-stripe ordering below 105 K [221–225]. On the other hand, $Pr_4Ni_3O_8$ is reported to be a correlated metal [89, 226] in the measured temperature range of 2 K to 300 K with no indications of charge-stripe or spin ordering on Ni or Pr sublattices, and $Nd_4Ni_3O_8$ has been reported to show both metallic [87, 227] and semiconducting [74] temperature dependence depending on the sample preparation condition. Understanding these stark differences in the ground state properties as a function of R-site ionic radius and a careful analysis of the mag-

netic properties of the R-sublattice in Pr and Nd analogues, which remains largely unexplored, are important. However, these compounds require Ni to be in an unfavourable oxidation state of +1, which makes the sample synthesis highly challenging. Hence, the detailed study of their physical characteristics has been limited. In this study, we investigate the ground state of $Pr_4Ni_3O_8$ and $Nd_4Ni_3O_8$. At the same time, to understand the role of R-site ionic radius on the concomitant antiferromagnetic and MIT observed in $La_4Ni_3O_8$, we studied solid solutions of the form $(R, La)_4Ni_3O_8$ (R = Pr, Nd).
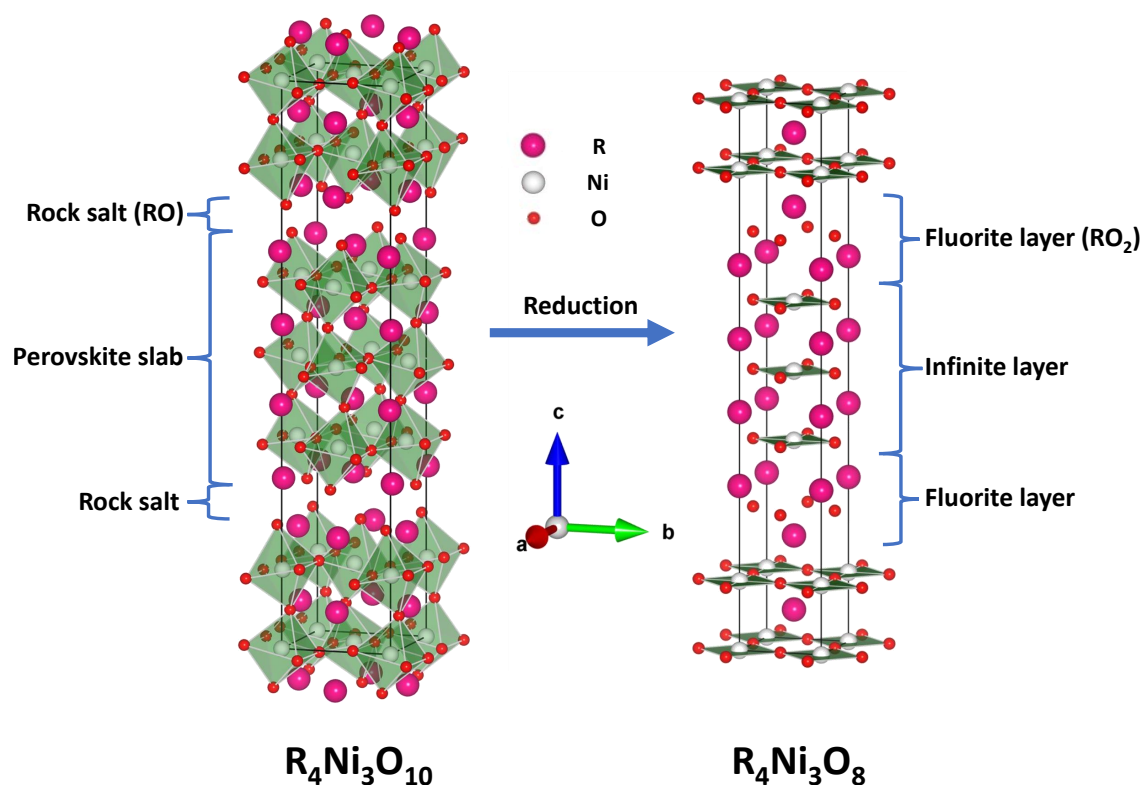
Figure 5.1: The crystal structure of the n = 3 member of the parent Ruddlesden-Popper nickelate phase (left) and their reduced T' variants (right). Here the magenta, white and red colored balls represent the rare earth, nickel and oxygen atom respectively.

5.3 Crystal structure of $R_4Ni_3O_8$ compounds

The room temperature crystal structure of $R_4Ni_3O_8$ (R = La, Pr and Nd) is shown in Fig. 5.1 (right panel). All the three members crystallize in the same tetragonal space group of $I4/mmm$ (space group No. 139) with three infinite layer NiO_2 planes being separated by an intervening fluorite layer (RO_2) as shown in Fig. 5.1 (right panel). These T' infinite layer nickelates are derived from their parent Ruddlesden Popper phases via the method of reduction.
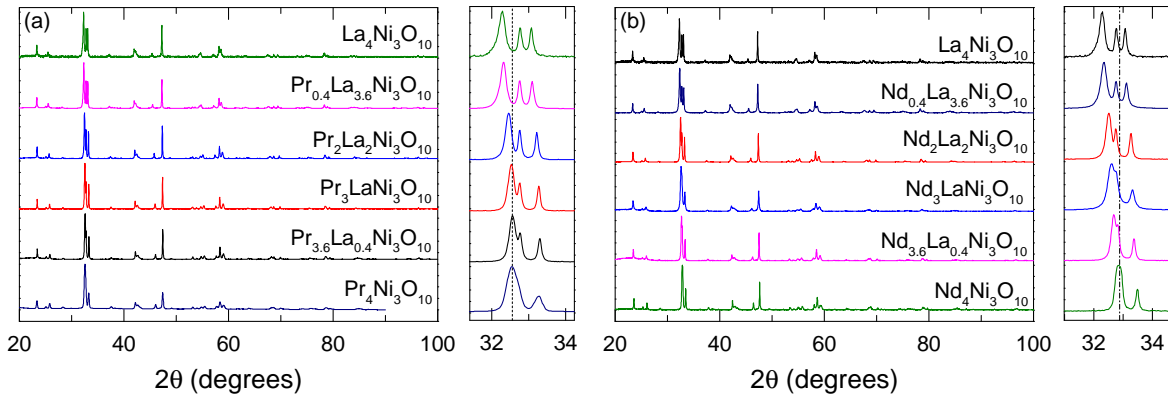
Figure 5.2: (a) and (b) show the lab-based PXRD of the $(La_{1-x}Pr_x)_4Ni_3O_{10}$ and $(La_{1-x}Nd_x)_4Ni_3O_{10}$ series respectively with $0 \leq x \leq 1$. The zoomed in regions of the xrd peaks in the 2θ range of $32°$ to $34°$ show the monotonic variation of xrd peaks towards higher 2θ angle with increasing Pr/Nd content at La-site.

During the reduction process, the apical oxygen atoms are removed from the NiO_6 octahedra present in the perovskite slab. Furthermore, a rearrangement of O - atoms takes place in the rock salt layer that gives rise to the fluorite - type arrangement of $R/O_2/R$ that acts as a buffer layer between the NiO_2 trilayers. Hence, the reduction process changes the octahedral arrangement around Ni atoms found in the parent RP phase to that of a square planar arrangement in the T' phase. The T' structure has 2 distinct rare - earth sites denoted by R1 and R2, sitting at the Wyckoff site of 4e. Here R1 sits in the infinite layer block while R2 faces the fluorite layer on one side and the infinite layer block on the other. Likewise there are 2 distinct crystallographic sites for the Ni atoms denoted by Ni1 and Ni2, sitting at Wyckoff site of 2a and 4e. Here Ni1 sits within the trilayers and Ni2 is sandwitched between the fluorite block and the trilayer block.

5.4 Synthesis and structural characterization

High purity polycrystalline samples of the n = 3 member of the parent Ruddlesden Popper (RP) phases i.e., $(La_{1-x}R_x)_4Ni_3O_{10}$ (R = Pr, Nd; x = 0, 0.1, 0.5, 0.75, 0.9 and 1.0) were prepared using the citrate method as described in [176]. The phase purity of these parent RP phases was confirmed using a Bruker D8 Advance powder X-ray diffractometer as shown in Fig. 5.2. High purity $R_4Ni_3O_8$ samples were prepared by reducing the parent RP phases under suitable conditions. To obtain these optimal conditions, the parent RP phases were first

decomposed completely in a TGA setup under Ar - H_2 (10%) atmosphere as shown in Fig. 5.3. The results of these TGA experiments were used as a guide to decide the temperature profile and isotherm duration for obtaining the $R_4Ni_3O_8$ phase.
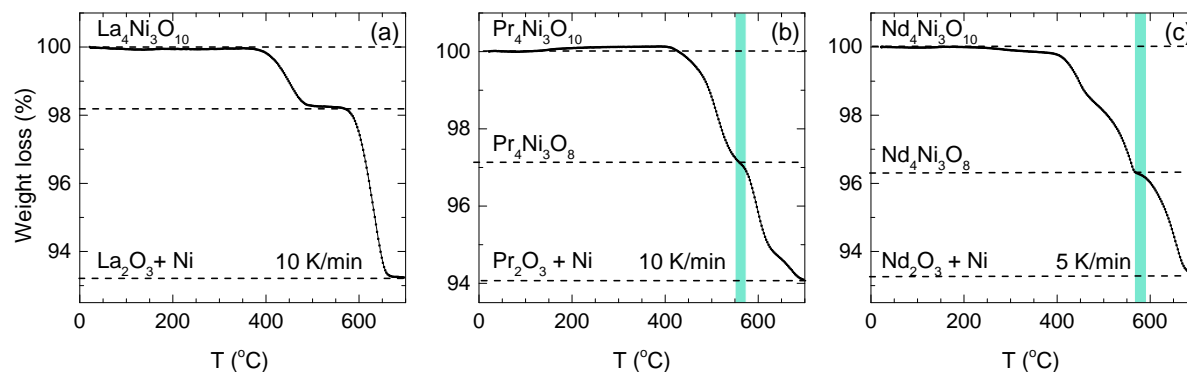
Figure 5.3: (a), (b) and (c) show the TGA of $La_4Ni_3O_{10}$, $Pr_4Ni_3O_{10}$ and $Nd_4Ni_3O_{10}$ respectively, carried out in Ar - H_2 (10%) atmosphere to determine the synthesis protocol for $R_4Ni_3O_8$ samples. The aqua-blue rectangle marks the plateau region where $R_4Ni_3O_8$ (R = Pr and Nd) phase is stabilized.

Before beginning the reduction reaction, the tube furnace was thoroughly purged with Ar - H_2 (10%) gas for one hour to remove any traces of air or oxygen. Thereafter the temperature of the furnace was ramped up to the desired isotherm temperature. From the optimization runs carried out in the tube furnace, it was concluded that $(Pr/Nd)_4Ni_3O_8$ samples and the $(La_{1-x}R_x)_4Ni_3O_8$ samples having (R = Pr/Nd) content $\geq$ 50 %, can be obtained by keeping the isotherm temperature at 360°C and the isotherm duration in the range of 19 to 22 h. Moreover, this reaction time could be further reduced by increasing the isotherm temperature to 500°C (isotherm time: 1 h 18 min) and 470°C (isotherm time: 5 h) for $Pr_4Ni_3O_{10}$ and $Nd_4Ni_3O_{10}$ respectively. However, for the reductions at these higher temperatures, the gas flow had to be changed from Ar - H_2 (10%) to an inert gas like Ar, immediately at the end of isotherm via a T-connector valve system (see Fig. 5.4). If this protocol was not followed and the sample was allowed to cool down in a stream of Ar - H_2 (10%) flow, it led to sample decomposition.

Now from the TGA data in Fig. 5.3(a) it was clear that $La_4Ni_3O_8$ could not be obtained under Ar - H_2 (10%) atmosphere. This is also in accordance with the TGA data obtained by Laccore *et al.* [77] where they claim that the step corresponding to $La_4Ni_3O_8$ only appears in the presence of ultra high pure (U.H.P) H_2 and is absent in the case of diluted H_2 atmosphere. Hence, we modified our existing tube furnace setup (see Fig. 5.4) and made use of U.H.P. H_2 to obtain the $La_4Ni_3O_8$ phase. Since hydrogen gas is highly flammable in presence of trace
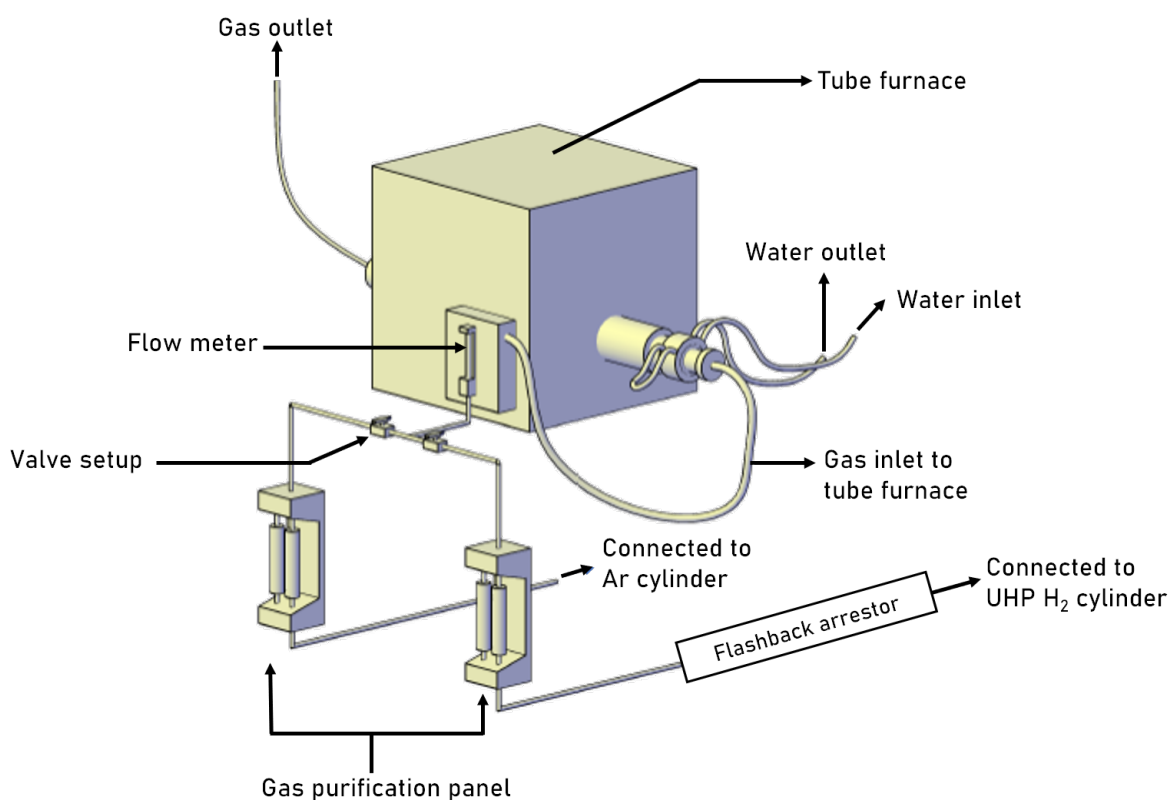
Figure 5.4: Shows the schematic of a Nabertherm tube furnace that was modified to carry out the synthesis of $R_4Ni_3O_8$ samples either by using ultra high pure hydrogen gas flow or Ar (90 %) - H_2 (10%) gas flow.

amount of ordinary air and an ignition source, utmost care was taken during these reduction reactions.

The tubes carrying H_2 gas to the furnace were made of stainless steel, owing to the corrosive nature of H_2 gas towards rubber tubing. A flashback arrestor (Model DGN, MESSER) was also connected between the flow meter to the furnace and the H_2 cylinder to prevent backflow of the gas from the furnace to the cylinder in case of an accidental fire.

For these reactions, the tube furnace was first purged with an inert gas like Ar for 2 hr and then purged by U.H.P. H_2 for 2 hr. This ensured that there were no traces of air or oxygen present in the tube furnace. Here we carried out multiple trials to obtain the $La_4Ni_3O_8$ phase by varying the sample mass, isotherm duration, gas flow rate and isotherm temperature that the parent $La_4Ni_3O_{10}$ sample was subjected to. After many trials, we concluded that an isotherm temperature of 470°C for a duration of 28 min with sample mass of parent RP phase ranging from 40 - 50 mg are ideal for obtaining the $La_4Ni_3O_8$ phase. Slight increment in the isotherm
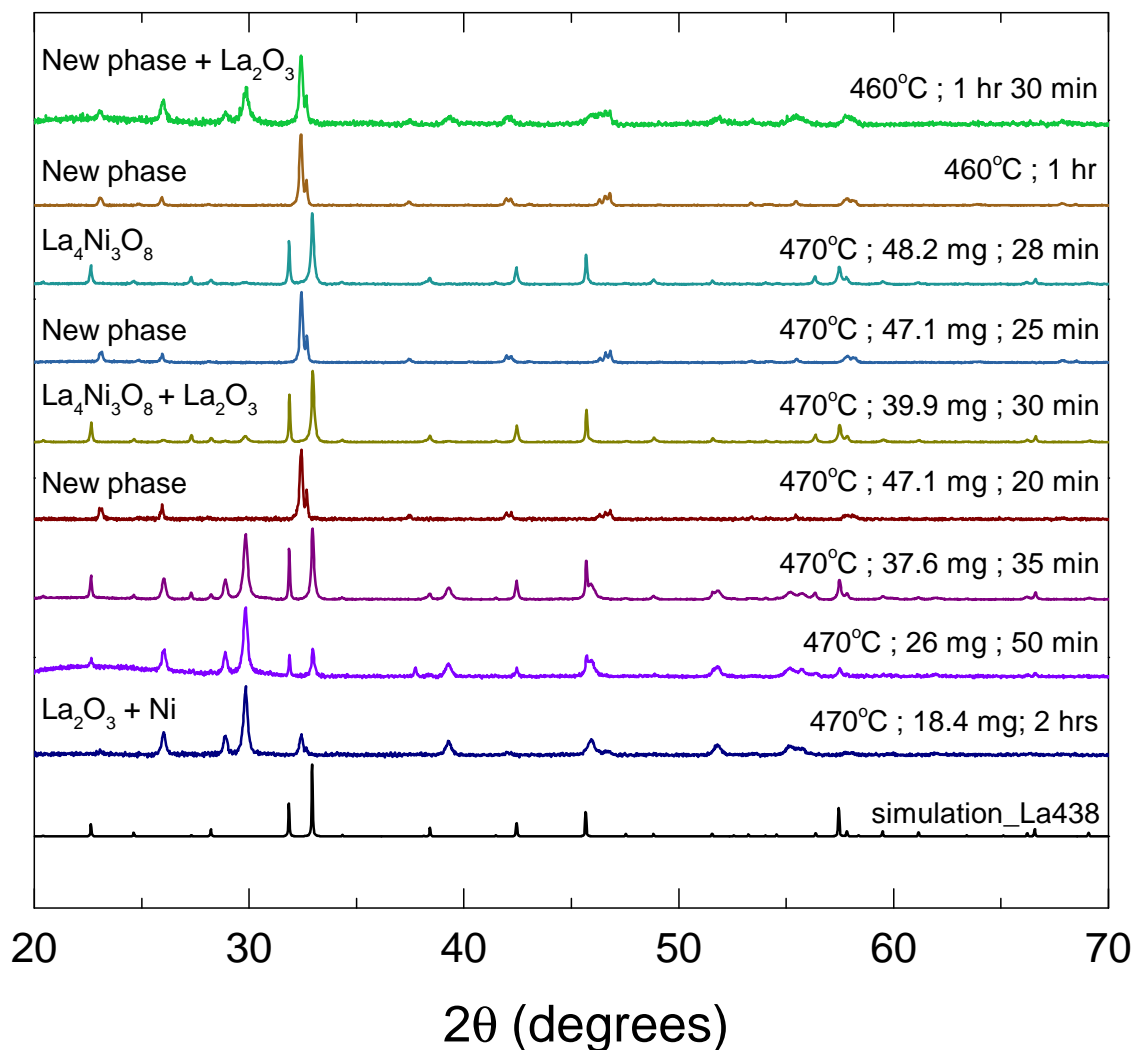
Figure 5.5: The various reduction trials carried out on the parent $La_4Ni_3O_{10}$ sample in U.H.P. H_2 to obtain the $La_4Ni_3O_8$ phase. The isotherm time and temperature and sample weight are mentioned alongwith the xrd pattern obtained after the reduction process. The black curve denotes the simulated pattern for $La_4Ni_3O_8$ in the tetragonal space group of $I4/mmm$.

duration resulted in decomposition of the sample to La_2O_3 and Ni metal. Interestingly, we could also capture an intermediate phase when the isotherm duration was in the range of 20 - 25 min for similar sample mass and same isotherm temperature (see Fig. 5.5). This relatively unexplored phase could either correspond to the $La_4Ni_3O_9$ phase reported by Laccore *et al.* [77] or it could be related to the $T^\dagger$ phase of $La_4Ni_3O_8$ reported by Cheng *et al.* [223]. Further detailed structural characterization experiments are needed to ascertain the exact crystal symmetry of this new phase. We also synthesized $La_4Ni_3O_8$ and 10% (Pr/Nd) doped $La_4Ni_3O_8$ sample using the method of topotactic reduction i.e., by using CaH_2 as a source of
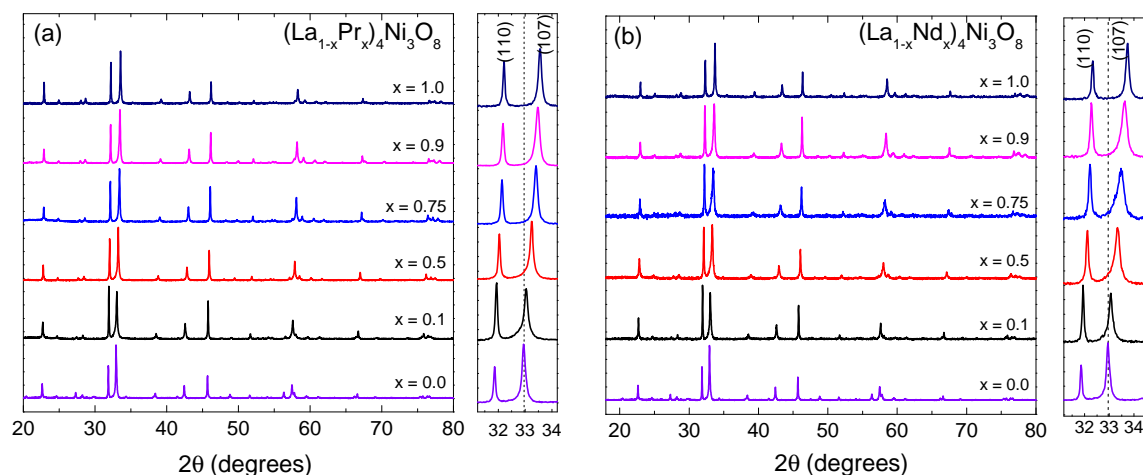
Figure 5.6: (a) and (b) show the lab based PXRD data for the $La_{1-x}Pr_xNi_3O_8$ and $La_{1-x}Nd_xNi_3O_8$ (x = 0, 0.1, 0.5, 0.75, 0.9 and 1.0) samples respectively. The zoomed in regions of the xrd peaks in the 2θ range of $31°$ to $34°$ show the monotonic variation of xrd peaks towards higher 2θ angle with increasing Pr/Nd content at La-site.

H_2. Here a sintered rectangular bar of the parent RP phase was covered in a calculated amount of CaH_2 powder in a quartz ampoule in an argon-filled glove box. The quartz ampoule was then evacuated to a pressure of 10^{-5} Torr and carefully sealed. It was then subjected to an isotherm temperature of $360°C$ for a period of 36 h. At the end of the reaction, the ampoules were broken in an argon-filled glove box and the reduced samples were carefully extracted. The room temperature lab based PXRD shown in Fig. 5.6 confirms the phase purity of the reduced samples. For both the series there is a monotonic displacement of the peak positions towards higher 2θ angle with increasing Pr/Nd doping at the La-site, thus confirming the successful doping at La-site. For the $(La_{1-x}Pr_x)_4Ni_3O_8$ series, the peaks are relatively sharper as compared to the peaks of the $(La_{1-x}Nd_x)_4Ni_3O_8$ series. This could hint at a possible non-homogeneous doping in the $(La_{1-x}Nd_x)_4Ni_3O_8$ series as compared to the $(La_{1-x}Pr_x)_4Ni_3O_8$ series.

5.4.1 FESEM and EDAX

The FESEM images of the parent samples i.e., $La_4Ni_3O_8$, $Pr_4Ni_3O_8$ and $Nd_4Ni_3O_8$ is shown in Fig. 5.7 (a), (b) and (c) respectively. The images demonstrate the layered morphology, which is typical of the T' trilayer phase.

EDAX analysis confirmed that the samples were of ideal stoichiometry. Fig. 5.8 shows
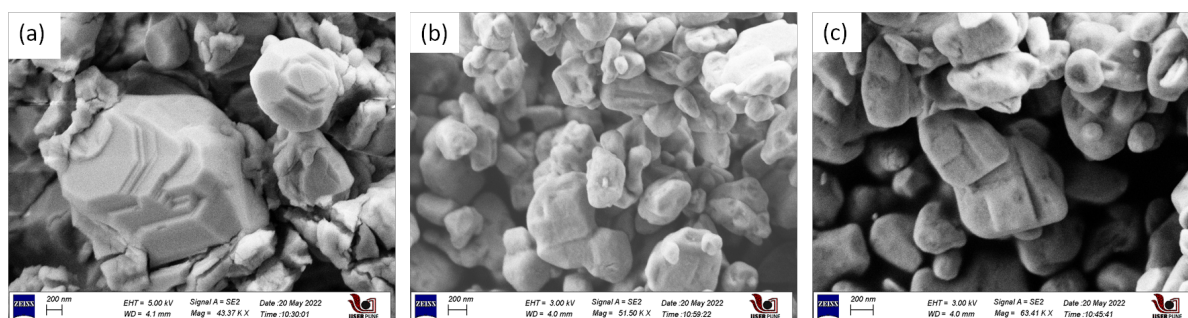
Figure 5.7: (a), (b) and (c) show the FESEM images for $La_4Ni_3O_8$, $Pr_4Ni_3O_8$ and $Nd_4Ni_3O_8$ respectively on a scale of 200 nm, showing the particle size and morphology.

Table 5.1: The doping concentration in $(La_{1-x}R_x)_4Ni_3O_8$, R = (Pr and Nd) series, calculated from EDAX measurements.

x in $(La_{1-x}R_x)_4Ni_3O_8$, R = (Pr and Nd)	La:R (calculated)	La:Pr (experimental)	La:Nd (experimental)
0.1	9.0	11.53	9.54
0.5	1.0	1.17	1.08
0.75	0.33	0.37	0.36
0.9	0.11	0.13	0.12

the FESEM images for the $La_{1-x}Pr_xNi_3O_8$ and $La_{1-x}Nd_xNi_3O_8$ series for the doping concentrations of x = 0.1, 0.5, 0.75 and 0.9. The La:Pr and La:Nd ratio was measured for the $La_{1-x}Pr_xNi_3O_8$ and $La_{1-x}Nd_xNi_3O_8$ series respectively using EDAX. The data was averaged over 10-15 regions of a freshly cleaved pellet. The EDAX results are summarized in Table 5.1.

5.4.2 TGA analysis

After successful synthesis of the samples of Pr and Nd series, it was essential to determine the oxygen content of all the samples as it directly affects the oxidation state of Ni ion. Hence, a complete decomposition of all the samples was carried out by conducting isotherm runs at 600°C using Ar - H_2(10%) atmosphere at a heating rate of 10 K/min in a high resolution TGA setup (Netzsch STA 449 F1). The TGA data for the parent samples is shown in Fig. 5.9.

The oxygen content for the parent samples is shown in Table 5.2. From the results, we infer that the oxygen content of the samples is close to the ideal stoichiometry.
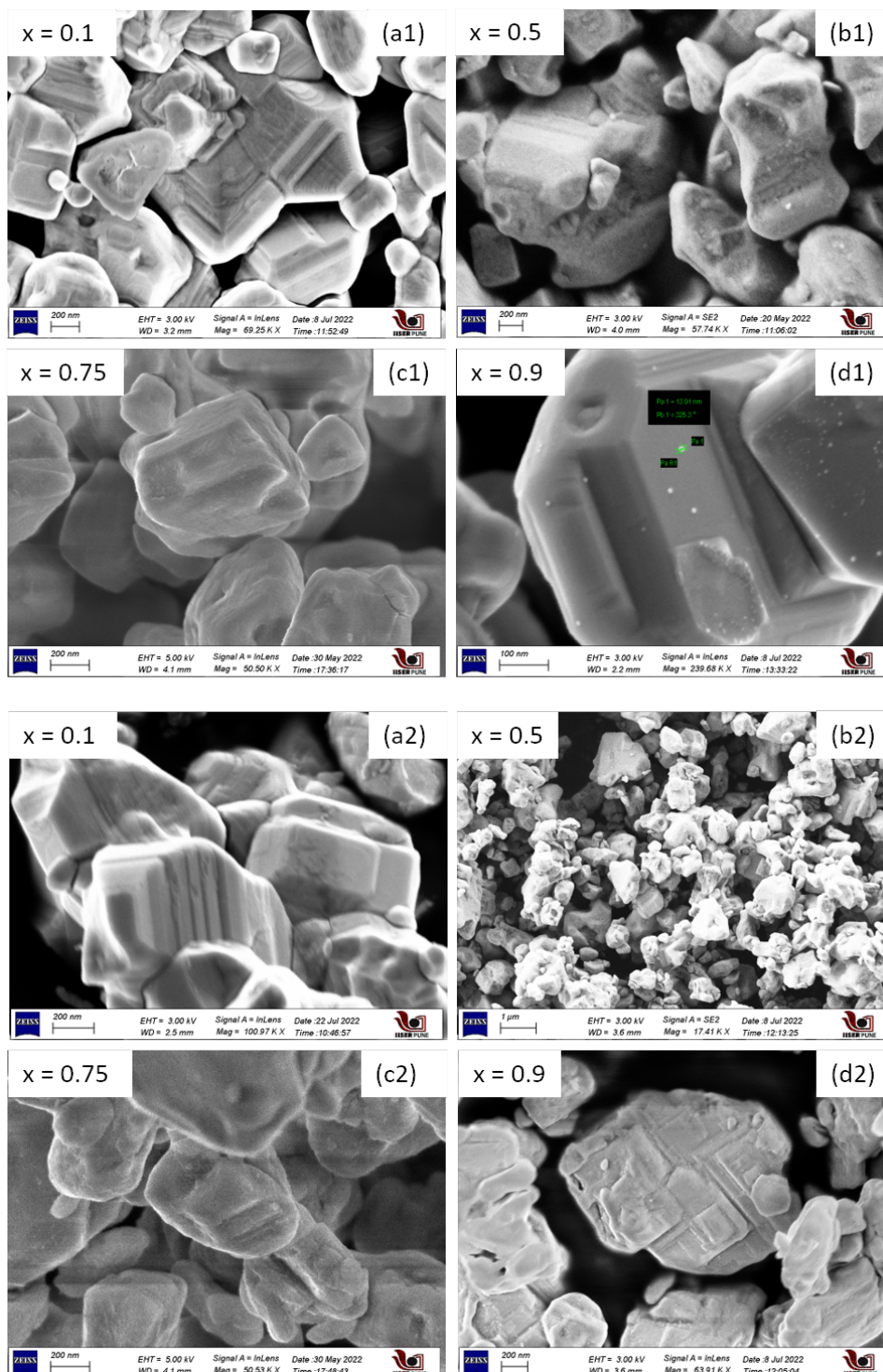
Figure 5.8: (a1-d1) and (a2-d2) shows the FESEM images of the $La_{1-x}Pr_xNi_3O_8$ and $La_{1-x}Nd_xNi_3O_8$ series respectively.
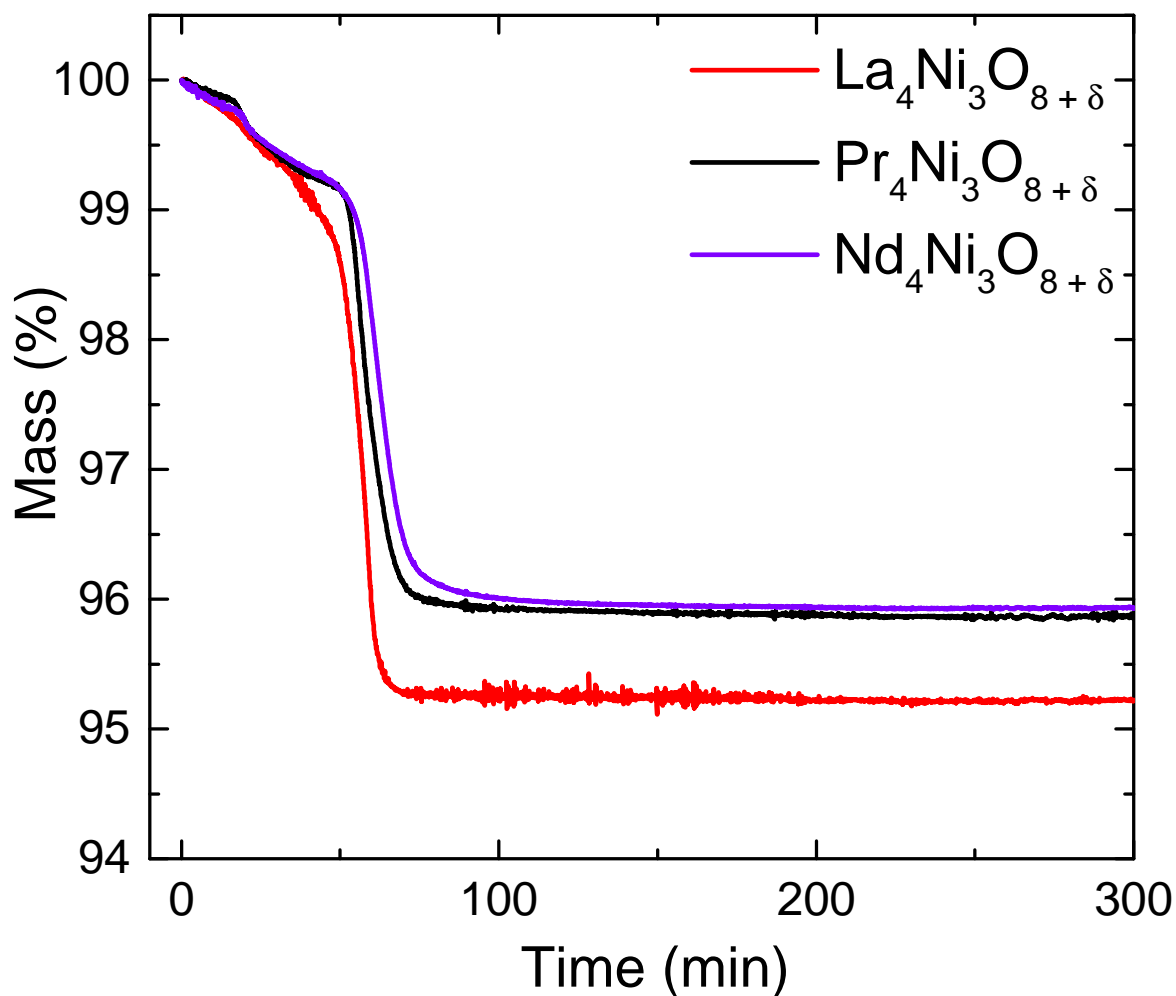
Figure 5.9: Shows the TGA isotherms carried out at 600°C in Ar-H_2 (10%) atmosphere for the parent $R_4Ni_3O_8$ samples.

Table 5.2: Oxygen content of the $R_4Ni_3O_{8\pm\delta}$ samples estimated using TGA setup.

Sample	Method of synthesis	δ
$La_4Ni_3O_{8\pm\delta}$	using CaH_2	+ 0.29
$Pr_4Ni_3O_{8\pm\delta}$	Ar-H_2 (10%)	- 0.004
$Nd_4Ni_3O_{8\pm\delta}$	Ar-H_2 (10%)	- 0.13

5.4.3 High resolution transmission microscopy (HRTEM)

High-resolution transmission electron microscopy (HRTEM) was carried out using a JEOL JEM 2200FS 200keV TEM instrument. The powder samples were finely ground in high purity

ethanol using an agate mortar and pestle to reduce formation of agglomerates. Thereafter, less than few mg of the ground powder was dispersed in ethanol solution and was subjected to sonication for a period of 30 min. A few droplets of the resultant suspension were drop-casted onto a TEM Cu-grid using a micropipette. The Cu grid was then dried for 12 h in an evacuated desiccator, preheated at 60°C in an oven for 15 min, and eventually loaded into the TEM sample chamber. Both HRTEM and SAED (Selected Area Electron Diffraction) patterns were collected for all the samples and the analysis of the images was carried out using DigitalMicrograph (GMS -3) software package.
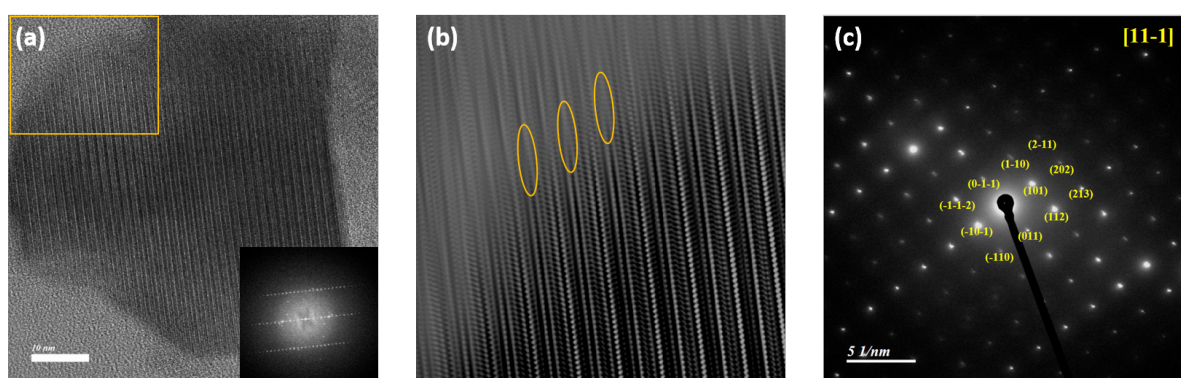
Figure 5.10: (a) HRTEM micrograph of $Pr_4Ni_3O_8$; inset at right bottom shows the FFT image of the micrograph. (b) IFFT of the region inside the yellow box shown in (a), showing the presence of stacking faults in the sample; (c) shows the SAED pattern taken on a highly crystalline region of the specimen, along the [1 1 -1] zone axis with the hkl indices marked in yellow.

Fig. 5.10 (a) shows the HRTEM micrograph of $Pr_4Ni_3O_8$ sample. The majority of the sample shows nicely lined up crystal planes with few defects in the form of stacking faults as shown in yellow ellipses in Fig. 5.10 (b). No sign of intergrowth due to lower and higher n members, which typically plagues the sample quality, could be seen in our samples. The SAED pattern consists of sharp spots indicative of a high crystallinity of the sample. The SAED pattern shown in Fig. 5.10 (c) nicely satisfies the reflection conditions expected for the $I4/mmm$ space group as was shown in previous HRTEM studies on $Nd_4Ni_3O_8$ [228].

5.4.4 Low temperature synchrotron XRD

Fig. 5.11 shows the temperature variation of lattice parameters of the parent $R_4Ni_3O_8$ (R = La, Pr and Nd) samples down to 10 K, measured at the ALBA synchrotron centre in Spain. As is evident from Fig. 5.11 (a1, a2 and a3), there is a clear anomaly at T $\sim$ 105 K for the
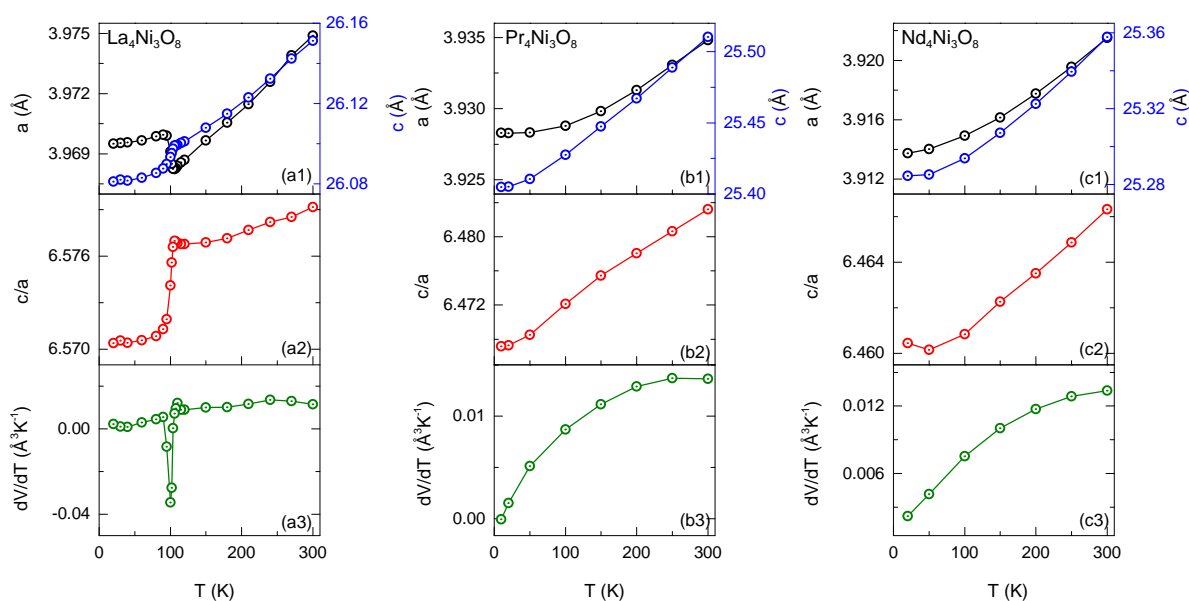
Figure 5.11: (a1 - a3), (b1 - b3) and (c1 - c3) show the temperature variation of lattice parameters, c/a ratio and dV/dT for the $La_4Ni_3O_8$, $Pr_4Ni_3O_8$ and $Nd_4Ni_3O_8$ sample respectively.

$La_4Ni_3O_8$ sample. This coincides with the temperature where the MIT is previously reported. The MIT is accompanied by a negative thermal expansion (NTE) of the a - axis and contraction of the c - axis and an overall expansion of the unit cell volume upon cooling (NTE) as shown in Fig. 5.11 (a3), which is in agreement with previous reports [69, 223]. The a - axis expands by approximately 0.04 % while the c - axis contracts by 0.052 % across the transition. At the same temperature, the c/a ratio undergoes a sharp jump. However, no such anomaly was seen in the entire measured temperature range for the $Pr_4Ni_3O_8$ or $Nd_4Ni_3O_8$ samples. For both the samples, the lattice parameters decrease monotonically with decrease in temperature in concurrence with the fact that they do not feature any MIT in their electrical resistivities.

Similar low temperature PXRD characterization was carried out for $La_2Pr_2Ni_3O_8$ and $La_2Nd_2Ni_3O_8$ samples as shown in Fig. 5.12. Upon 50% Pr doping at La site, the anomaly corresponding to the MIT transition is suppressed down to 55 K. Here again, the a - axis undergoes NTE and c - axis undergoes a slight contraction below the transition temperature. For the 50% Nd doped sample, it is very difficult to ascertain the position of MIT. The weak response of the lattice parameters in the range of 60 to 70 K could be due to puddles where the La concentration might be higher than 50 % and hence it demonstrates signatures of MIT.

The unit cell volume is shown respectively in panels (a3) and (b3). As expected based on
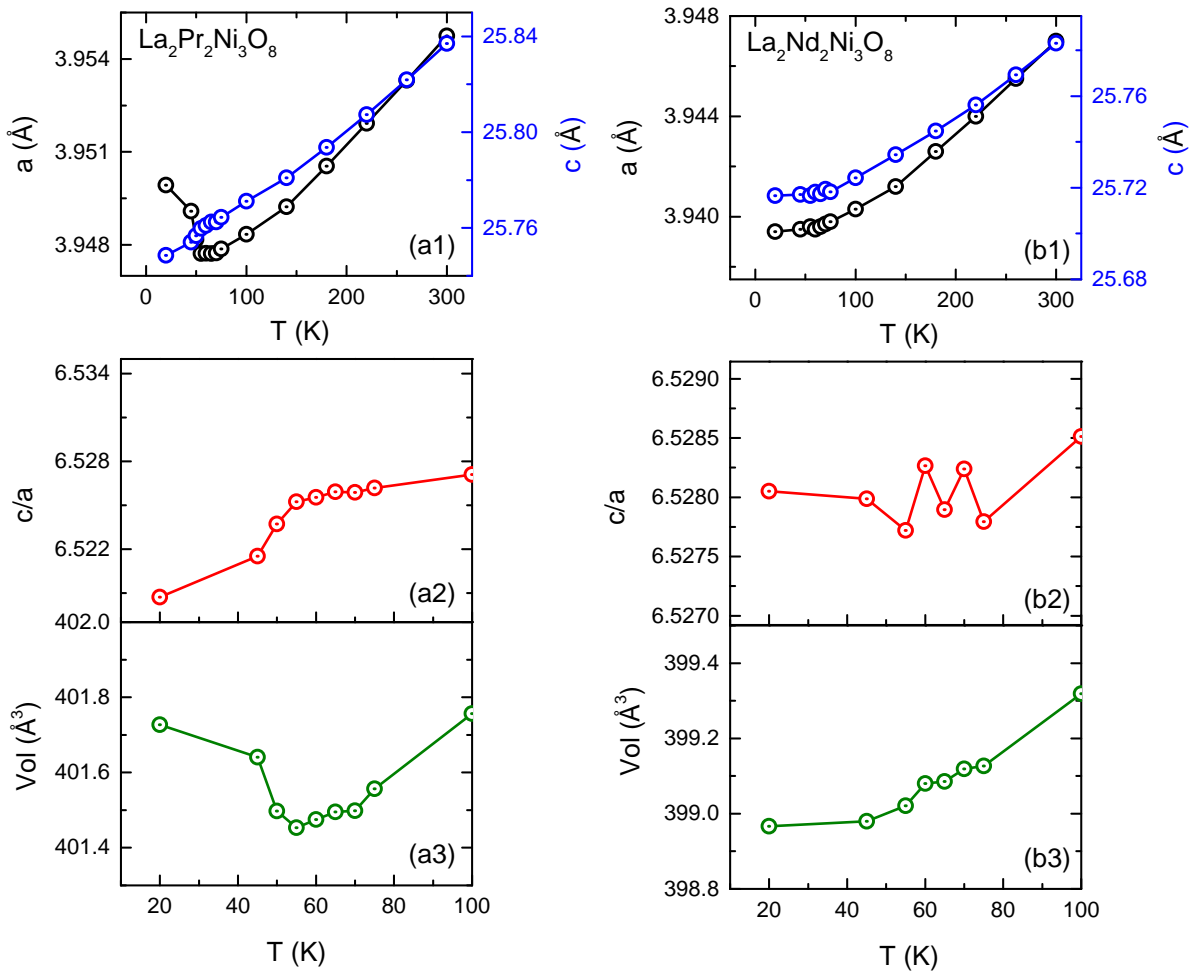
Figure 5.12: (a1 - a3) and (b1 - b3) show the temperature variation of lattice parameters, c/a ratio and unit cell volume for the $La_2Pr_2Ni_3O_8$ and $La_2Nd_2Ni_3O_8$ sample respectively.

the variation of a and c parameters across the transition, in Pr case the cell volume increases below the anomaly and in the Nd case the change is rather weak but overall there is a decrease in the cell volume. It is to be noted that it was theoretically predicted by Pardo and Pickett [229] that the charge stripe ordering seen in $La_4Ni_3O_8$ is due to a transition from a metallic low spin (LS) state to an insulating and antiferromagnetic high spin (HS) state. Since for a given ligand coordination the LS ionic radius is typically smaller than the ionic radius in the HS state, one expects the unit cell volume to increase below the transition in concurrence with the experimental data for $La_4Ni_3O_8$ and its Pr and Nd doped variants. Qualitatively similar behavior is observed in a recent pressure study where the LS persists to lower temperatures under high external pressure [223].

5.5 Low temperature physical characterization

Apart from low temperature synchrotron xrd, we also carried out electrical transport, specific heat and magnetization measurements to see the variation of MIT as a function of Pr/Nd doping at La-site. In addition to that, we also discovered some new low temperature anomalies as discussed next:

5.5.1 Magnetization

Fig. 5.13(a & b) show the normalized magnetization (M/H) as a function of temperature for the $(La_{1-x}Pr_x)_4Ni_3O_8$ and $(La_{1-x}Nd_x)_4Ni_3O_8$ samples, respectively. For $La_4Ni_3O_8$ (x = 0), the concomitant charge/spin-stripe ordering is seen as a kink in the M/H plot near 105 K (this is more clear in the inset which shows a zoomed-in view of this feature).

The temperature at which this anomaly appears in M/H is in good agreement with the previous reports [221–223]. In the $La_4Ni_3O_8$ sample, the Curie-Weiss analysis of the data taken at 9 T in the temperature range of 4 K to 20 K gives the following values of fitting parameters: $\chi_0 = 3.3 \times 10^{-3}$ emu mol^{-1} Oe^{-1}, C = 0.05 emu K mol^{-1} Oe^{-1} and $\theta_p = -41$K. From the Curie constant, we estimated the effective moment per f.u. which turned out to be 0.61 μ_B per f.u., which indicates that a fraction of the magnetic moment on Ni sublattice remains unordered. Also, the value of this effective moment is too large to be attributed to the presence of paramagnetic impurities in the sample. Upon doping with Pr or Nd the transition is suppressed. However, an important difference between the two series of samples is that the magnetization of the Nd series at low temperatures is significantly high compared to the corresponding Pr series. For example, for $Pr_4Ni_3O_8$, M/H at T = 5 K is about $\approx 6 \times 10^{-2}$ emu mol^{-1} Oe^{-1} whereas for Nd M/H at the same temperature is $\approx 26 \times 10^{-2}$emu mol^{-1} Oe^{-1}; therefore, the magnetization of $Pr_4Ni_3O_8$ is about 4 to 5 times reduced compared to that of $Nd_4Ni_3O_8$. This difference is also reflected in the isothermal magnetization plots shown in Fig. 5.13(c & d). Since the calculated effective magnetic moment of a free Pr^{3+} ion is not very different from that of Nd^{3+} (3.58 μ_B and 3.62 μ_B, respectively), the reduced values of M/H for Pr at low temperatures is likely due to crystal field splitting of the lowest J-multiplet. Previously, we observed a similar contrast between $Pr_4Ni_3O_{10}$ and $Nd_4Ni_3O_{10}$, which was explained on the basis of the singlet ground state for one of the two crystallographically inequivalent Pr ions in
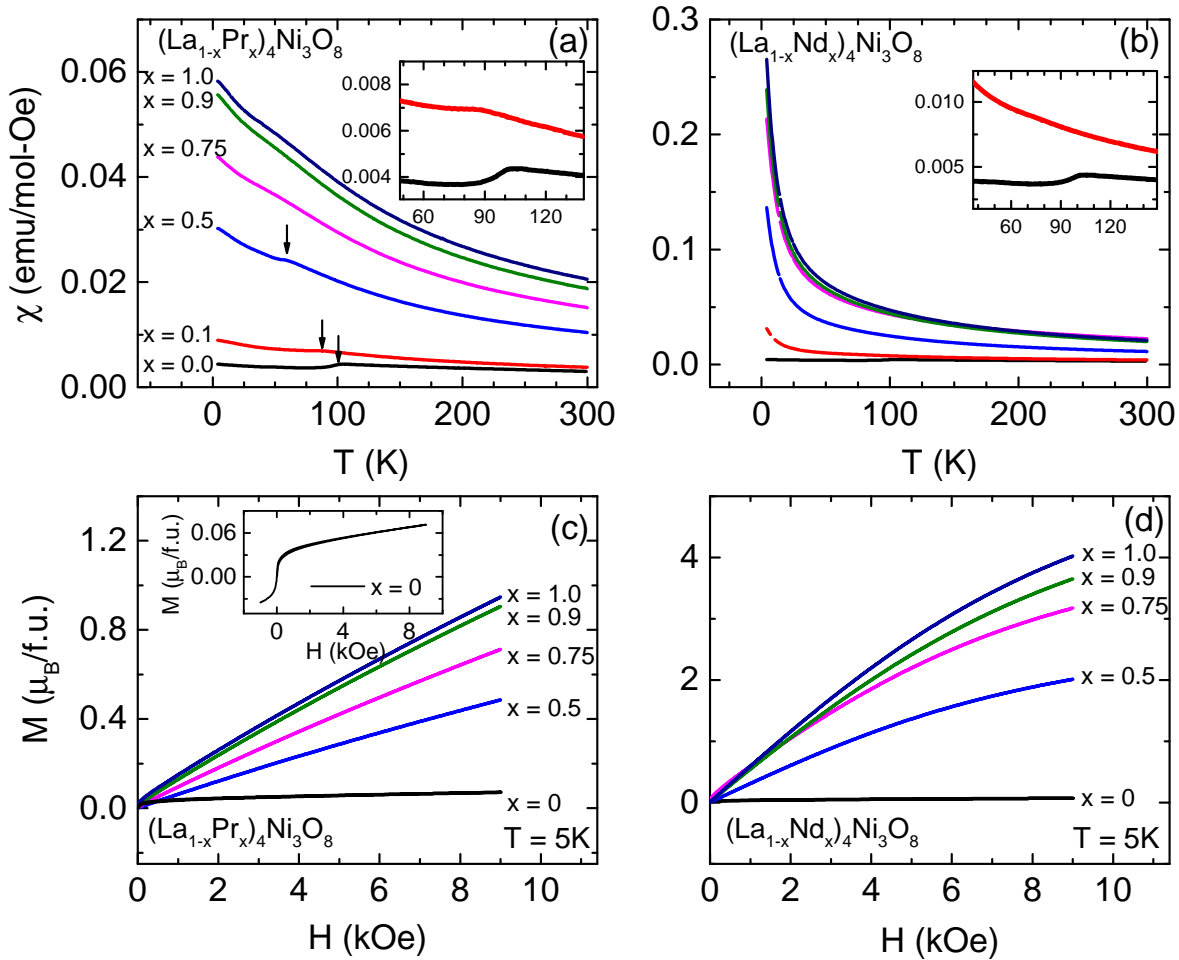
Figure 5.13: (a) and (b) show the susceptibility as a function of temperature for the $La_{1-x}Pr_xNi_3O_8$ and $La_{1-x}Nd_xNi_3O_8$ (x = 0, 0.1, 0.5, 0.75, 0.9 and 1.0) samples respectively at an applied field of 9 T. The insets in panel (a) and (b) show the zoomed in region, capturing the CS stripe anomaly. Panel (c) and (d) show the isothermal magnetization at T = 5 K for the Pr and Nd series respectively. The inset in panel (c) shows the M vs.H behaviour for the $La_4Ni_3O_8$ sample upto an applied field of 16 T.

$Pr_4Ni_3O_{10}$ [176]. A similar scenario seems to be present in the T' analogue $Pr_4Ni_3O_8$.

Coming back to the temperature variation of M/H shown in Fig. 5.13(a & b).

In $(La_{1-x}Pr_x)_4Ni_3O_8$ series, the anomaly due to CS-stripe ordering is clearly discernible up to x = 0.5. The transition temperature from the M/H plots (indicated by the position of arrows) is in fairly good accord with the temperature-dependent PXRD data discussed in the previous section, and with the transition temperature reported for the $(La_{1-x}Pr_x)_4Ni_3O_8$ series in Ref. [230]. Beyond x = 0.5, we continue to see the presence of a weak hump around 35 K. In Fig. 5.14, the derivative plots of susceptibility clearly captures the presence of this feature. It should be noted that this feature appears even in the $Pr_4Ni_3O_8$ sample (in fact, it is less domi-
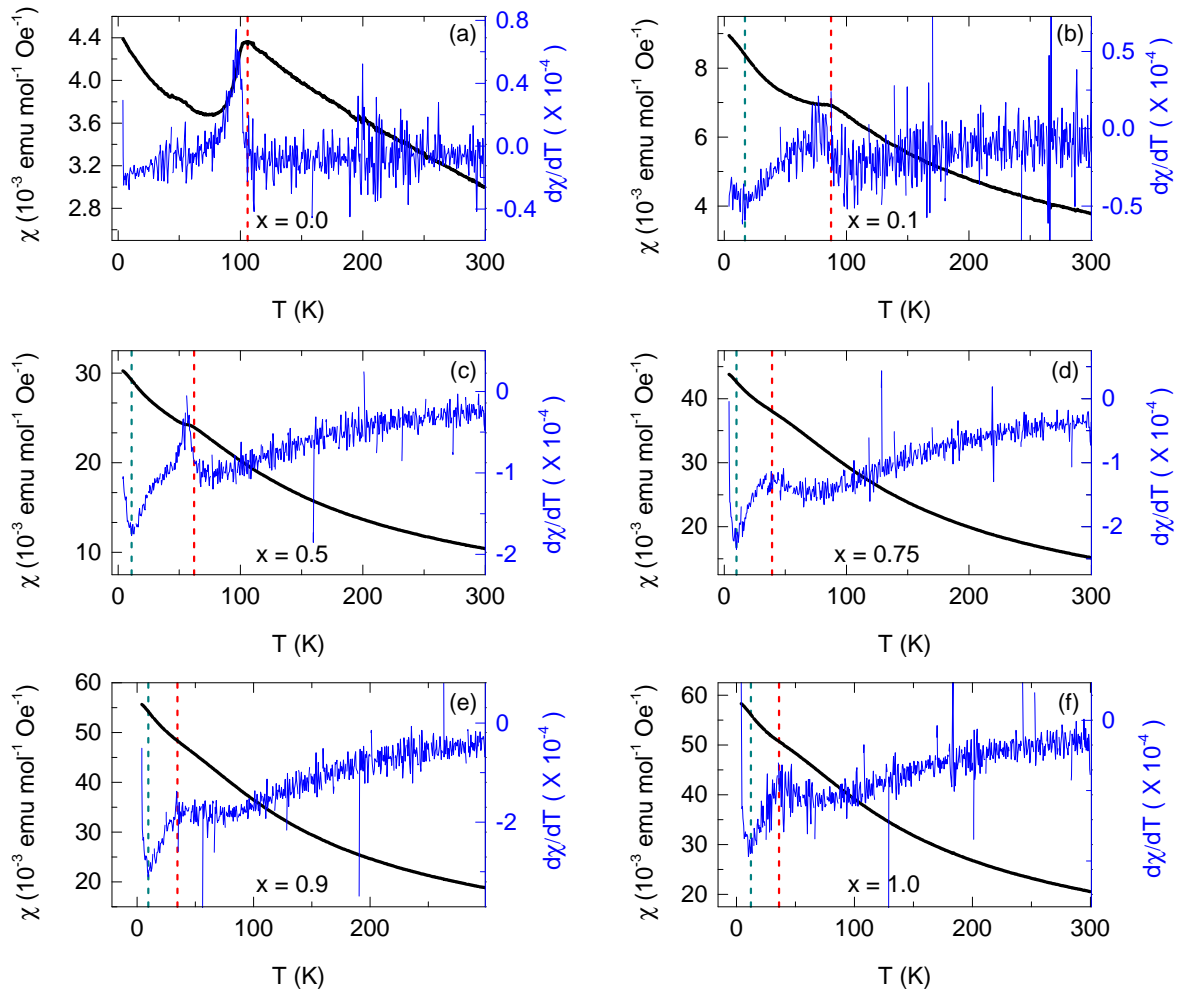
Figure 5.14: (a - f) show the magnetic susceptibility and its first order derivative for the $La_{1-x}Pr_xNi_3O_8$ samples. The red and cyan dotted lines mark the presence of the broad hump and a low temperature upturn respectively.

nant in x = 0.9 and 0.75), which suggests that this feature is not related to the charge/spin-stripe ordering. Since the size of this feature scales with Pr concentration, it is fair to conclude that it originates from the Pr-sublattice and likely a manifestation of the crystal field splitting of the lowest J multiplet of Pr^{3+} (J = 4) ion. In the previous works (see Refs. [230], [231]), a more pronounced hump is reported for the $Pr_4Ni_3O_8$ sample near 100 K followed by a minimum near 30 K. However, as shown in the Supporting Information of Ref. [230], the M/H for our samples agrees fairly well with the M/H data for H $\parallel$ *ab* plane. This 100 K hump is pronounced only for H $\parallel$ *c* axis.

Now let us look at the magnetization behaviour of the $Nd_4Ni_3O_8$ sample. Being a Kramers'

ion with three f electrons, the crystal field split ground state in Nd^{3+} case (J = 4) cannot be a non-magnetic singlet (i.e., the ground state of both Nd1 and Nd2 would be either a doublet or a quartet). Hence, at low temperatures, both Nd sites contribute to magnetization. As a result of this, the overwhelming paramagnetic background due to Nd moments in $Nd_4Ni_3O_8$ masks the CS-stripe ordering associated with the Ni sublattice even in a sample with 10% Nd (x = 0.1). For higher doping values, the Curie-like behaviour dominates over the whole temperature range.

For both the $Pr_4Ni_3O_8$ and $Nd_4Ni_3O_8$ samples, χ^{-1} vs. T plots look fairly linear above about 150 K. However, there is an undeniable presence of a small curvature that cannot be negated. We therefore fitted the high temperature data using the modified Curie-Weiss (CW) law: $\chi = \chi_0 + C/(T - \theta_p)$, where C is the Curie-constant from which the value of the effective magnetic moment (μ_{eff}) can be obtained using $\mu_{eff} = \sqrt{8C}$, and θ_p is the Weiss temperature, and χ_0 is the temperature independent contribution arising from the core-diamagnetism, Van Vleck type and Pauli paramagnetism. Treating χ_0, C and θ_p as the fitting parameters, the best fit over the temperature range 150 K to 300 K using the modified Curie-Weiss equation led to the following values of the fitting parameters: For $Pr_4Ni_3O_8$, $\chi_0 = 2.0 \times 10^{-3}$ emu mol^{-1} Oe^{-1}, C = 7.3 emu mol^{-1} Oe^{-1} K, and $\theta_p = -96$ K. The corresponding values for $Nd_4Ni_3O_8$ are: $\chi_0 = 1.6 \times 10^{-3}$ emu mol^{-1} Oe^{-1}, C = 6.8 emu mol^{-1} Oe^{-1} K and $\theta_p = -49$ K. If we assume the contribution of Ni sublattice to this to be negligible then we should get $\mu_{eff}/Pr^{3+} = 3.83\mu_B$ in $Pr_4Ni_3O_8$, which exceeds the Hund's rule derived free-ion value (3.58 μ_B) substantially despite a significant positive χ_0 contribution. This clearly indicates that the magnetization of the Ni sublattice cannot be neglected and the Ni sublattice also contributes to the net magnetization. Now, we know that the ratio Ni^{1+}/Ni^{2+} in T' structure is 2 : 1, and Ni^{1+} is spin 1/2 while Ni^{2+} can take two possible spin states: spin 0 (LS) or spin 1 (HS). Accordingly, the value that quantity $3(\mu_{Ni})^2$ can take can be 14 μ_B^2 (HS) or 6 μ_B^2 (LS) (assuming g to be 2 in each case). The calculated value of $3(\mu_{Ni})^2$ using the relation: $\sqrt{4(\mu_{Pr})^2 + 3(\mu_{Ni})^2} = 8C$ where $\mu_{Pr} = 3.58$ μ_B and C = 7.3 emu mol^{-1} Oe^{-1} K turns out to be ≈ 8.4 μ_B^2, which is closer to the LS case. Let us now look at the case of $Nd_4Ni_3O_8$. In this case, using $\sqrt{4(\mu_{Nd})^2 + 3\mu_{Ni}^2} = 8C$ where C = 6.8 μ_B^2 and $\mu_{Nd} = 3.62$ μ_B, gives $3\mu_{Ni}^2 \approx 2$. This value is smaller than for $Pr_4Ni_3O_8$ which is consistent with the experimental

observation that our $Nd_4Ni_3O_8$ is electrically more conducting than $Pr_4Ni_3O_8$ (*vide infra*). This rather crude analysis of M/H above 160 K appears to indicate that Ni d-electrons become more itinerant as the ionic-radius of R^{3+} decreases. The high value of θ_p and χ_0 in both cases are likely a consequence of large crystal field splitting. It should be recalled that for an accurate estimate θ_p, χ_0, and μ_{eff}, the fittings should ideally be performed over a temperature range satisfying $k_B T >> \Delta_{CF}$, where Δ_{CF} is the overall crystal field splitting of the lowest J-multiplet. We also tried to fit the low-temperature data for $Pr_4Ni_3O_8$ and $Nd_4Ni_3O_8$ to extract the magnetic moment in the crystal field slit ground state level. In $Nd_4Ni_3O_8$, a satisfactory fit could be obtained between 10 K and 25 K, yielding fitting parameters as follows: $\chi_0 = 0.031$ emu mol^{-1} Oe^{-1}, C = 1.96 emu mol^{-1} Oe^{-1} K and $\theta_p = -4.7$ K. We see that the Curie constant has reduced considerably from its high-temperature value suggesting that the magnetic moment per Pr ion in the crystal field split ground state should be considerably smaller than the free ion value. In the case of $Pr_4Ni_3O_8$, satisfactory fits could not be obtained despite changing the temperature range. Below 10 K, the Pr moments appear to be highly correlated, indicating a more complex ground state.

The isothermal magnetization at T = 5 K in both the series scales with the mole fraction of the rare-earth element present (Fig. 5.13(c) and Fig. 5.13(d)). As pointed out earlier, the magnetization in the Pr series is substantially reduced compared to its Nd counterpart. Further, the magnetization under 9 T at 5 K in both cases is significantly smaller than the saturation magnetization of 12.8 μ_B/f.u. and 13.08 μ_B/f.u. for *free* Pr^{3+} and Nd^{3+}, respectively. That is, even if we ignore the contribution of Ni, the observed magnetization (≈ 1 μ_B/f.u. for $Pr_4Ni_3O_8$ and ≈ 4 μ_B/f.u. for $Nd_4Ni_3O_8$) are considerably smaller than what one would expect from a simple Brillouin function calculation for J = 4 and J = 9/2 respectively. This can be attributed to the crystal field splitting. At 5 K, the magnetization is due to the low-lying crystal field split ground state energy levels. The temperature variation of M(H) is non-linear in both cases. In $Nd_4Ni_3O_8$ it has the characteristic Brillouin function dependence and in magnitude and manner of variation compares nicely to its RP analogue $Nd_4Ni_3O_{10}$ (see Supplementary Material in Ref. [176]). In $Pr_4Ni_3O_8$, on the other hand, the curvature is less pronounced and the M(H) looks more quasi-linear which is a similar trend as seen previously for its RP analogue $Pr_4Ni_3O_{10}$ (see Supplementary Material in Ref. [176]). However, while in

$Pr_4Ni_3O_{10}$, M(H) at 5 K under 8 T exceeds 2 μ_B/f.u., in $Pr_4Ni_3O_8$ it is half this value, which once again hints towards its complex ground state.

In the inset of Fig. 5.13(c), the M(H) for $La_4Ni_3O_8$ is shown, which is masked in the main panel due to magnetic Pr or Nd. At 5 K it shows a steep initial increase analogous to that in a ferromagnet but here M(H) does not saturate but rather continues to increase linearly above 6 T. This is qualitatively similar to the M(H) behaviour previously reported [69]. However, the saturation moment of the ferromagnetic component (obtained by extrapolating the linear part backwards to H = 0) is 0.2 emu g^{-1} in our sample but close to 0.75 emu g^{-1} in Ref. [69]. At the same time, dM/dH from the linear part is 2×10^{-3} emu mol^{-1} Oe^{-1} in both studies. These two components actually represent contributions from two different phases: the saturation is the Ni-metal phase, which would have easily formed during the reduction process. The linear increase at high fields represented the intrinsic contribution from the T' phase, which agrees well with the value of dM/dH from the two studies. Similarly, the M(H) of $Pr_4Ni_3O_8$ samples previously reported exhibit a large ferromagnetic component [221, 231], which is marginal for our $Pr_4Ni_3O_8$ sample. It should be pointed out that in Ref. [221] (Supporting Information), the authors delved into the intrinsic vs. extrinsic origin of the ferromagnetic component and concluded that their data are difficult to reconcile with the intrinsic argument put forward in Ref. [231]. The argument they came up with is that the ferromagnetic component is isotropic, unlike dM/dH which exhibits a significant anisotropy between the in-plane and out-of-plane data. Also, the FM component with a nearly constant saturation magnetization was observed in $La_4Ni_3O_8$ up to the highest measurement temperature of 120 K [69], which supports the presence of a ferromagnetic impurity which is likely present in the form of Ni metal. Our reduction experiments support this as well where we found that even a little (3-4 min) over the optimized duration (order of 28 min) under flowing H_2 gas led to complete decomposition of $La_4Ni_3O_8$ into La_2O_3 and Ni metal.

5.5.2 Specific heat

The molar specific heat (C_p) for the parent $R_4Ni_3O_8$ samples is shown in Fig. 5.16 (a - c). As shown in Fig. 5.16(a), the concomitant charge/spin (CS) stripe ordering in $La_4Ni_3O_8$ is clearly captured as a peak in C_p near T = 105 K. The temperature where the anomaly appears is in excellent agreement with previous reports [221–224]. However, the change in the entropy ΔS
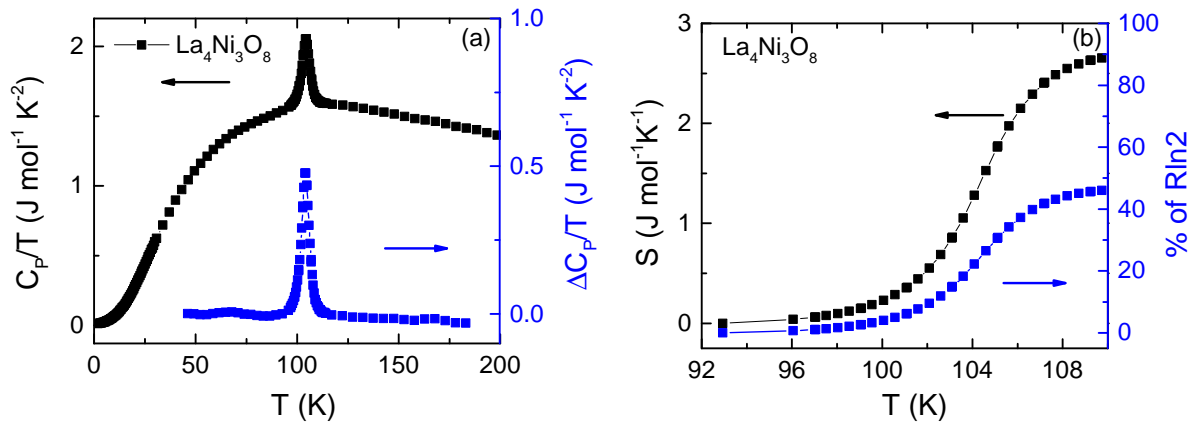
Figure 5.15: (a) Shows the C_P/T vs T plot (black) for $La_4Ni_3O_8$ sample alongwith the magnetic contribution to specific heat (blue), obtained by subtracting a polynomial background. In panel (b), the magnetic entropy associated with the peak at 105 K is shown in terms of Rln2.

associated with the transition is only ≈ 0.28Rln2 per f.u. (see, Fig. 5.15 (b)), which is nearly one-half of the value reported in Refs. [221, 222]. This is somewhat puzzling and at this point in time we do not have an explanation for it. Upon closer comparison of our data with that in Refs. [221, 222], we found that the height of the peak in [222] is comparable to our data but with the width is two times larger, which explains the doubling of the entropy; on the other hand, the peak in Refs. [221] is both higher and broader than for our sample, leading to twice the entropy we get. Ideally, if both the Ni^{1+} (spin 1/2) undergo long-range ordering, the net entropy change should be 2Rln2/f.u.. So, even Rln2/f.u. in Refs. [221, 222] is only 50% of the expected value. The reduced value may point to the fact that not all Ni moments participate in the magnetic ordering. Indeed, the low-temperature susceptibility shows that a sizable paramagnetic moment of ≈ 0.6 μ_B/f.u. that remains unordered down to 2 K. However, even discounting this fact would not account for the lost entropy completely. Another possible reason behind the discrepancy between our data and that reported in Refs. [221,222] could be due to oxygen off stoichiometry. Any increase in the oxygen content would result in conversion of Ni^{1+} to Ni^{2+}. The decreased quantity of Ni^{1+} due to a positive value of δ can possibly reduce the size of the specific heat anomaly. Of course, this raises other more significant questions concerning the position of the peak. It is natural to ask, why has it not changed? Or why does the magnetic behavior or the resistivity behavior (*vide infra*) remains practically unaffected when it is well-known that the oxygen off stoichiometry strongly affects the transport of transition metal oxides. An applied magnetic field of 8 T has a negligible effect on the specific

heat peak in agreement with [221].

The specific heat of $Pr_4Ni_3O_8$ and $Nd_4Ni_3O_8$ are shown in Fig. 5.16(b) and (c), respectively. For both these samples, the T variation of C_p is smooth over the whole temperature range indicating the absence of CS stripe ordering in these samples in line with the temperature-dependent PXRD and magnetization behaviors.

From the low temperature behaviour of specific heat, we try to qualitatively understand the response of the rare-earth sublattice in $Pr_4Ni_3O_8$ and $Nd_4Ni_3O_8$ samples. The specific heat of $Pr_4Ni_3O_8$ shows an anomalous behavior below T = 5 K. This is more clearly reflected in the C_p/T vs. T^2 plots shown in the inset in Fig. 5.16(b) where a sudden drop in C_p/T can be seen below 5 K. This low temperature feature does not show any field dependence up to the highest applied field of 9 T, which rules out its Schottky-type origin. On the other hand, the low temperature specific heat of $Nd_4Ni_3O_8$ exhibits a more conventional behavior, showing an upturn upon cooling below T = 5 K. Under the application of magnetic field, the onset of this upturn shifts to higher temperatures, featuring a broad peak near 5 K under an applied magnetic field of 9 T, reminiscent of the Schottky-like anomaly associated with lowest crystal field split level of Nd^{3+} ions. In the RP analogue $Nd_4Ni_3O_{10}$, a similar behavior due to the Zeeman splitting of the Kramers' doublet ground state was previously reported by us [176]. Another remarkable feature in the specific heat of $Nd_4Ni_3O_8$ is the sudden decrease in the C_p/T around 12 K, as shown in Fig. 5.16(e). These subtle anomalies are possibly related to the crystal field splitting. As such, no signatures of either long-range ordering or freezing of the rare-earth moments could be seen down to the lowest measurement temperature of 4 K in our experiments. From the manner of behavior, one can, however predict that Nd ions would undergo magnetic ordering at still lower temperatures. The behavior of Pr moments is more complex. As pointed out in the previous section, one of the two Pr-sites appears to host a non-magnetic singlet ground state. In future, the determination of crystal field levels using inelastic neutron scattering would be helpful in fully understanding the nature of magnetic ground state of the rare-earth sublattice in these compounds.

Coming now to the specific heat of $(La_{1-x}R_x)_4Ni_3O_8$ (R = Pr, Nd) samples. Here the CS stripe ordering is clearly captured only upto x = 0.1. For higher Pr/Nd doping, the anomaly is weak and a dominant phonon background makes it difficult for it to show up (see Fig. 5.17).
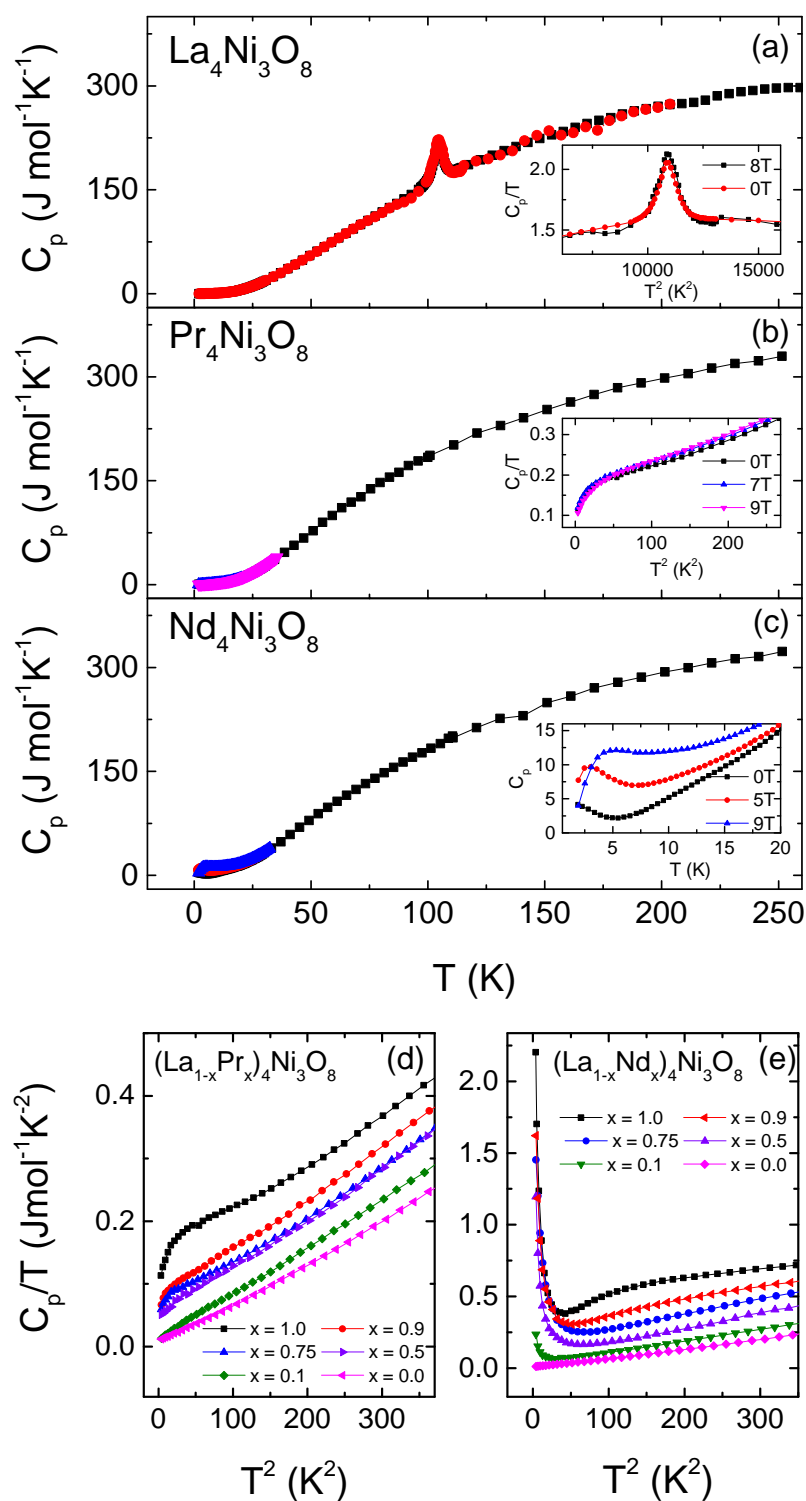
Figure 5.16: (a), (b) and (c) show the C_P vs T plot at for the $La_4Ni_3O_8$, $Pr_4Ni_3O_8$ and $Nd_4Ni_3O_8$ samples respectively. Inset in panels (a) and (b) shows the C_P/T vs T^2 plot and its corresponding field dependence, while the inset in panel (c) shows the field dependence of C_P for an applied field of 0, 5 and 9T. Panel (d) and (e) show the zero field C_P/T vs T^2 plot for the Pr and Nd series, respectively.
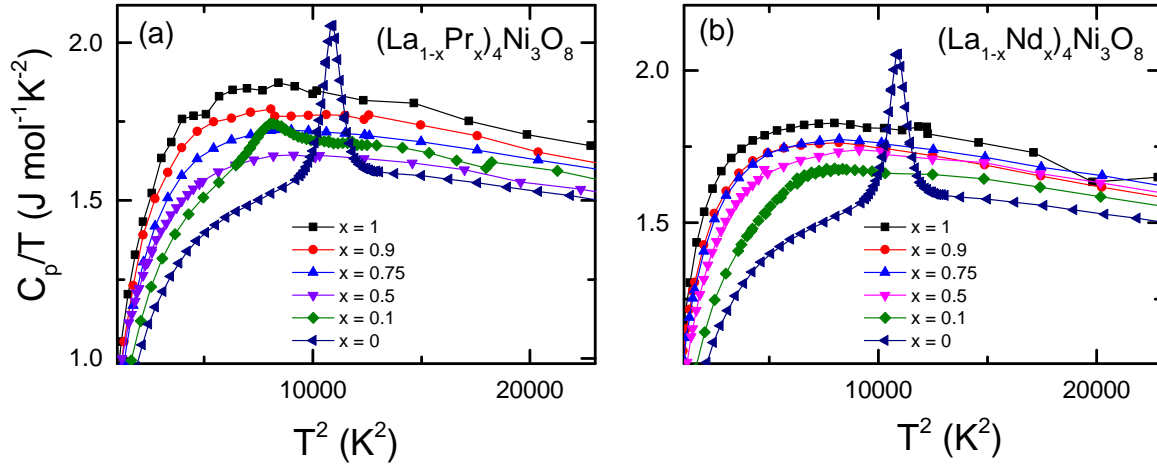
Figure 5.17: (a) and (b) show the C_P/T vs T^2 plot for the $(La_{1-x}Pr_x)_4Ni_3O_8$ and $(La_{1-x}Nd_x)_4Ni_3O_8$ series respectively in the high temperature range.

We tried fitting the low temperature C_p for both the $(La_{1-x}Pr_x)_4Ni_3O_8$ and $(La_{1-x}Nd_x)_4Ni_3O_8$ series using the equation: $C_p = \gamma T + \beta T^3$, where the coefficients γ and β represents the electronic and lattice contributions, respectively. Given the presence of low temperature anomalies associated with the rare-earth sublattice, one has to be careful in choosing the temperature range for fitting the above equation to estimate γ and β. We therefore avoided the region below 5 K in $Pr_4Ni_3O_8$ and 12 K in $Nd_4Ni_3O_8$. Above these temperatures, the C_p/T vs. T^2 plots look fairly linear over the temperature range shown (see Fig. 5.16 (d & e)). The estimated γ value increases from $10\,\mathrm{mJ\,mol^{-1}\,K^{-2}}$ for $La_4Ni_3O_8$ to $113\,\mathrm{mJ\,mol^{-1}\,K^{-2}}$ for $Pr_4Ni_3O_8$ or $485\,\mathrm{mJ\,mol^{-1}\,K^{-2}}$ for $Nd_4Ni_3O_8$. These values, especially for $Pr_4Ni_3O_8$ and $Nd_4Ni_3O_8$ are rather high, and one may be inclined to draw a conclusion that there is a possible heavy fermion behavior in the Pr and Nd rich samples. However, one has to first carefully discard the crystal field effects before arriving at such a conclusion. In the absence of a suitable non-magnetic lattice template for $Pr_4Ni_3O_8$ and $Nd_4Ni_3O_8$ this admittedly is a difficult task. One can think about using $La_4Ni_3O_8$ for this purpose, but as we know $La_4Ni_3O_8$ exhibits a CS stripe ordering near 105 K and the exact low-temperature magnetic behavior of the Ni sublattice below 105 K is not at all fully understood. In fact, the C_p/T vs. T^2 in $La_4Ni_3O_8$ itself shows some non-linearity near 10 K. This non-linearity might arise due to low-lying optical branches, but one may equally well argue that this might as well have a magnetic origin due to Ni d electrons. Fitting the data below 7 K in $La_4Ni_3O_8$ resulted in $\gamma = 9.7\,\mathrm{mJ\,mol^{-1}\,K^{-2}}$. Interestingly, γ

for $La_4Ni_3O_8$ is comparable to that for $La_4Ni_3O_{10}$ [176] that exhibits a metallic ground state. Since the ground state of $La_4Ni_3O_8$ is insulating, a fairly high γ value is somewhat puzzling. It is likely that the underordered Ni moments contribute to the linear term in the specific heat. These are some the issues that need further attention. As for the Debye temperature (Θ_D) calculated from β, a value of $\sim$380 K is obtained for $La_4Ni_3O_8$ which is significantly smaller than 450 K for $La_4Ni_3O_{10}$. These are widely different structures, and there is no reason why Θ_D for these two samples should have been the same.

5.5.3 Electrical transport

The temperature dependent electrical resistivity for the $(La_{1-x}Pr_x)_4Ni_3O_8$ and the $(La_{1-x}Nd_x)_4Ni_3O_8$ series is shown in Fig. 5.18(a) and Fig. 5.18(b), respectively. Here the resistivities have been normalized with respect to their respective room temperature values. The MIT associated with CS stripe ordering is clearly captured in $La_4Ni_3O_8$ near T = 105 K, which is in close agreement with previous reports [69, 221–223]. Below this temperature, the resistivity shows a sharp increase upon cooling. For the $(La_{1-x}Pr_x)_4Ni_3O_8$ series, as expected the MIT is suppressed with increasing Pr doping. The transition temperature in the Pr doped samples agrees fairly well with other techniques. Above 50% Pr-doping, the sharp increase in resistivity, characteristic of a MIT is not seen indicating that the critical doping required for the complete suppression of MIT should be close to 50% in agreement with Ref [221]. Although there possibly is no MIT present, the $\rho(T)$ for x = 0.75 still shows a shallow minimum centered around 50 K. This can be due to minor compositional inhomogeneities, i.e., the presence of La-rich regions where the MIT is not fully suppressed. At further lower temperatures, the resistivity shows an upturn. In x = 0.9 and 1, the shallow minimum disappears but the low-temperature upturn remains. Since this low-temperature upturn is also present in $Pr_4Ni_3O_8$, its presence in x = 0.9 and 0.75 does not seem to have any correlation with the MIT seen up to 50% of Pr doping. It is to be noted that this work is in agreement with several previous reports [69, 87, 226, 227, 232] where metallic temperature dependence is seen for both $Pr_4Ni_3O_8$ and $Nd_4Ni_3O_8$ samples. The metallic behavior is also in agreement with the theoretical calculations [88, 233, 234] where the presence of a large hole pocket contribution from the Ni-$d_{x^2-y^2}$ band at the Fermi level contributes to the charge transport. The insulating behavior seen in previous studies [74, 202] could be due to the oxygen off-stoichiometry aris-

ing during the process of RP to T' reduction. For our $Pr_4Ni_3O_8$ and $Nd_4Ni_3O_8$ samples the oxygen stoichiometry is very close to the nominal value as inferred from the high-resolution TGA measurements (see Fig.5.9). For the samples with Pr doping in the range $0 \leq x \leq 0.5$, a significant hysteresis can be seen between the heating and the cooling data. The degree of hysteresis becomes more pronounced as the Pr content at the La site increases. The residual resistivity ratio (RRR) for the samples in the Pr doping range $0.75 \leq x \leq 1$ varies from 1 to 2. Such low values of RRR for these samples could be due to the presence of microcracks and stacking faults (see Fig. 5.10(b)) that might have appeared during the reduction process. Similar behavior is also seen for the La-Nd series albeit with a difference that in this case a clear MIT is seen only up to x = 0.75. In x = 0.5, the hysteresis has diminished significantly as can be seen in the zoomed-in image shown in the inset. The upturn in the low-temperature resistivity of samples with x > 0.5 can arise due to a variety of reasons, including weak localization [235], electron-electron interaction or Kondo-like spin-dependent scattering mechanism [236]. To further narrow down the reason for the resistivity upturn, we tried to fit the low-temperature data to logarithmic temperature dependence (see, Fig. 5.19 (a1-d1)) as well as to a $T^{0.5}$ dependence (see, Fig. 5.19 (a2-d2)). Both scenarios result in fits that do not look completely satisfactory in one way or the other, hence making it difficult to assign either of the two scenarios in explaining the resistivity upturn.

Magnetoresistance: The magnetoresistance (MR) of a material is defined as the change in resistance of a material under the influence of applied magnetic field and is defined as $(\rho(B) - \rho(0))/\rho(0)$, where B is the externally applied magnetic field; $\rho(B)$ and $\rho(0)$ are the resistivities of the sample in presence and absence of magnetic field respectively. The MR data for the $Pr_4Ni_3O_8$ and $Nd_4Ni_3O_8$ sample is shown in Fig. 5.18 (c) and (d) respectively. At 10 K and 20 K, the MR for $Pr_4Ni_3O_8$ is completely positive and increases linearly with applied field up to 3 kOe and 3.5 kOe, respectively, resulting in a V-shaped plot which changes quickly to a quadratic field dependence as the field increases further and shows no sign of saturation. This B^2 dependence arises due to increase in the rate of scattering of charge carriers moving under the influence of the Lorentz force. The V-shaped MR is a signature of the weak antilocalization (WAL) [237–240], generally seen in layered materials. At lower temperatures (2 K and 5 K), however, the MR becomes negative and decreases linearly up to 2-3 T and thereafter increases
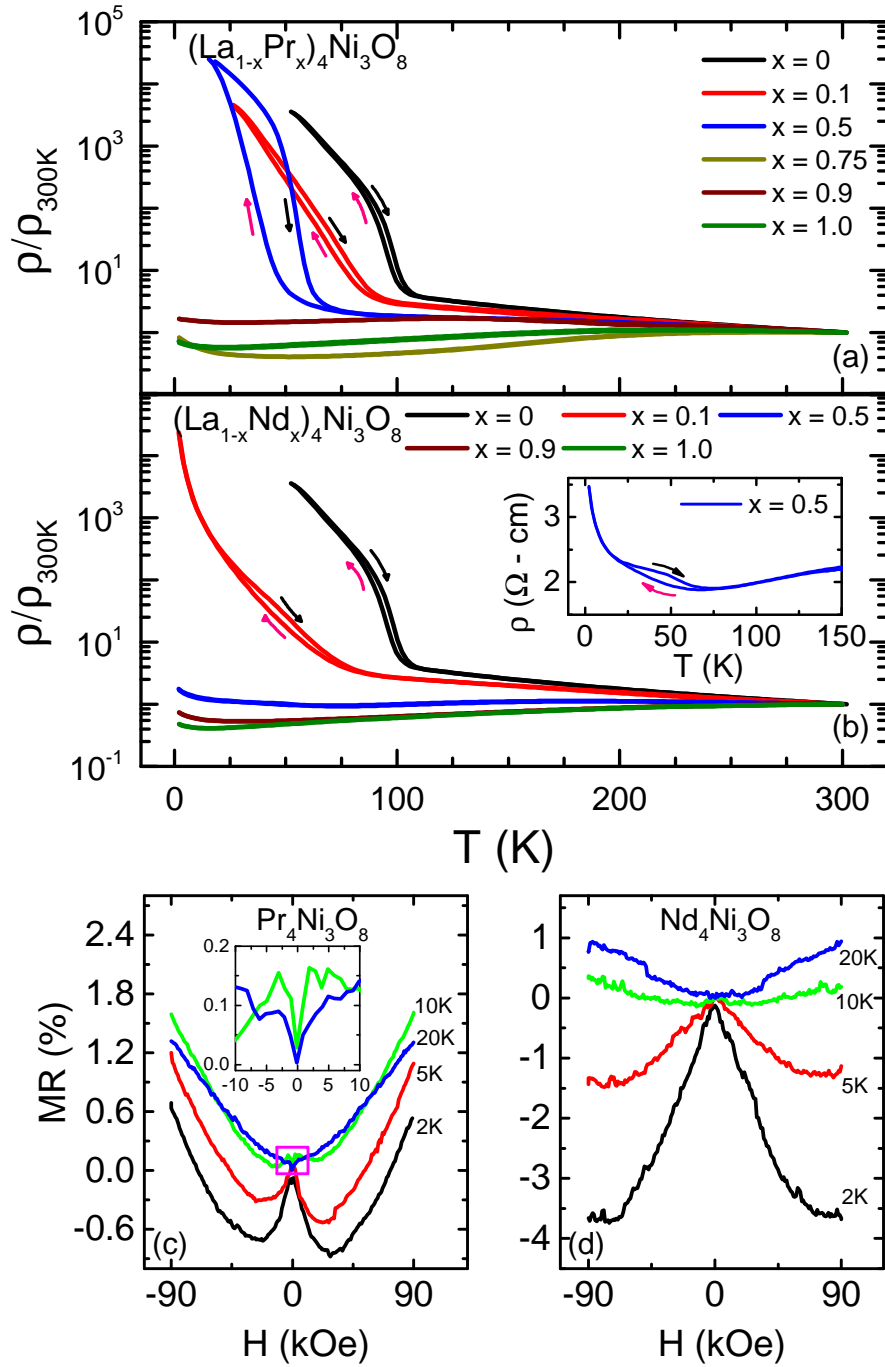
Figure 5.18: (a) and (b) show the value of $\rho(T)/\rho_{300K}$ plotted as a function of temperature for $La_{1-x}Pr_xNi_3O_8$ and $La_{1-x}Nd_xNi_3O_8$ ($0 \leq x \leq 1.0$) samples respectively. The pink and black arrows represent the data taken while cooling and heating the sample, respectively. The inset in panel (b) shows the hysteresis below the MIT captured for the $x = 0.5$ sample in the Nd series. Panel (c) and (d) show the magnetoresistance observed for the $Pr_4Ni_3O_8$ and $Nd_4Ni_3O_8$ samples, respectively, at temperatures of 2, 5, 10 and 20 K in the field range of -9 to 9 T. In panel (c), the region in the magneta box has been zoomed in and shown in the inset.

quadratically, becoming positive above ± 8 T. The negative MR @ 2 K and 5 K is likely due to short range ordering of the Pr moments which was observed both in magnetization and in specific heat measurements. The quadratic dependence at higher fields is due to Lorentz scattering as explained above.
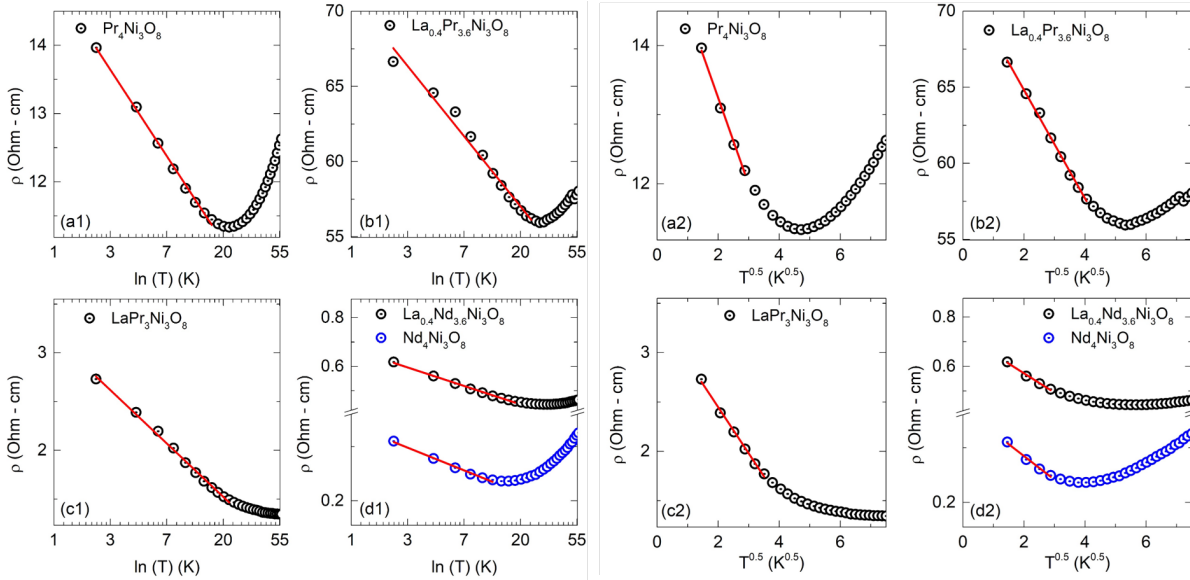
Figure 5.19: Temperature variation of resistivity (ρ) of $La_{1-x}Pr_xNi_3O_8$ (x = 1.0, 0.9 and 0.75) and $La_{1-x}Nd_xNi_3O_8$ (x = 1.0 and 0.9) samples shown on ln (T) scale (left panels) and $T^{0.5}$ scale (right panels). The solid red lines denote a linear fit to the data.

For the $Nd_4Ni_3O_8$ sample a negative MR of nearly 4 % has been observed at 2 K for a maximum applied field of ± 9 T. The magnitude of negative MR decreases as the temperature is increased from 2 K to 5 K. Thereafter, the MR shows a crossover from negative to small positive MR at 10 K and 20 K. We believe that the negative MR in $Nd_4Ni_3O_8$ sample at low temperatures is related to spin-disorder scattering [241]. Recall the presence of Schottky anomaly in the low-temperature specific heat of $Nd_4Ni_3O_8$. This Schottky anomaly is due to the Zeeman splitting of the lowest crystal field split level and at a given temperature as the magnetic field increases, more and more Nd-ions will occupy the lower Zeeman energy level, which is akin to saying that more and more Nd moments will line-up along the field direction, this would reduce the spin-disorder induced scattering, leading to a negative MR as seen here. An alternative possibility is that the negative MR in $Nd_4Ni_3O_8$ arises due to weak localization (WL) effect which may also be the case for 2 K and 5 K MR in $Pr_4Ni_3O_8$. Similar WL effects have also been observed for hole doped $NdNiO_2$ thin films that showcase

a resistivity upturn at low temperatures [242]. Since these are 2D systems, the presence of an arbitrarily small disorder such as stacking faults (see, Fig. 5.10 (b)) can give rise to confinement of electrons [243] and hence WL and WAL effects.

5.6   Rate of suppression of T_{MIT}

We tried to construct a diagram that showcases the variation of MIT temperature as a function of doping for both the Pr and Nd series, as shown in Fig. 5.20. The MIT temperatures were extracted from low-temperature lab-based XRD measurements.
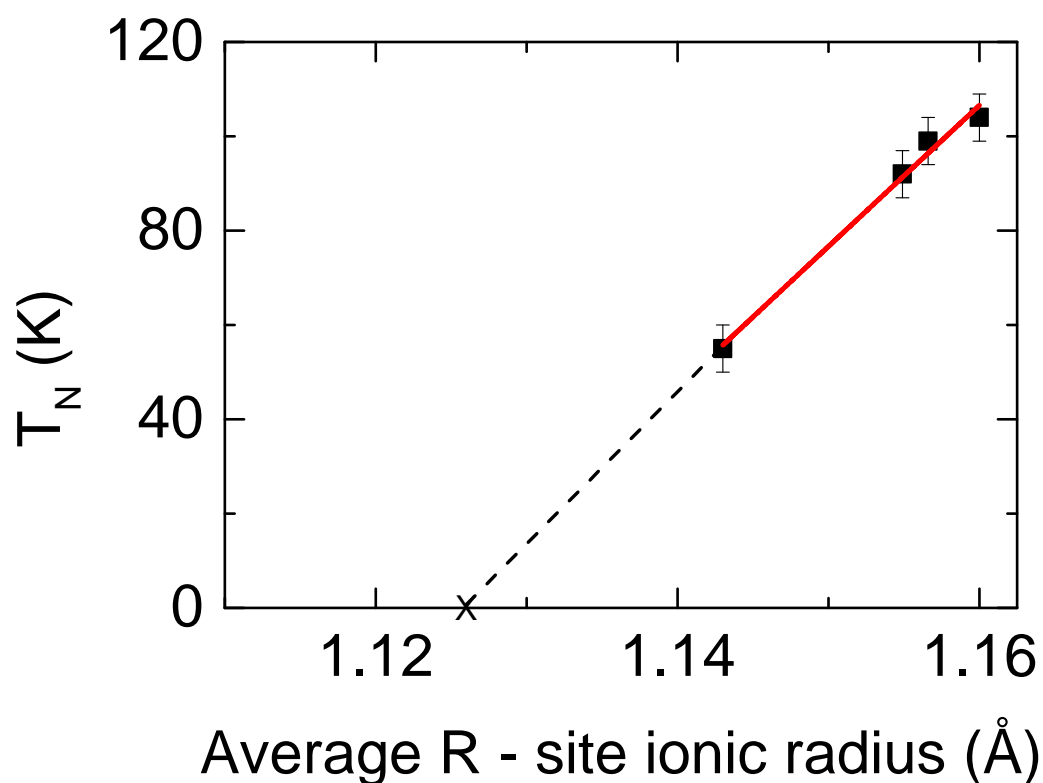
Figure 5.20: Shows the temperature variation of MIT as a function of average R-site ionic radius. The transition temperatures have been extracted from low-temperature lab-based XRD data. The dotted lines show the linearly extrapolated data down to T = 0 K for both series. The mark "X" denotes the ionic radius of Pr^{3+} ion in 8-fold coordination.

As is clear from Fig. 5.20, with increasing Pr/Nd content at the La site, the MIT is suppressed to lower temperatures. Beyond 50% doping concentration, no signatures of MIT are seen for the Pr series, while for the Nd series, we believe the MIT is suppressed at concentrations less than 50%. Looking at the spread of T_N estimated from various measurements, an error bar of $\pm$ 5 K has been used to plot T_N vs. Average R - site ionic radius in Fig. 5.20.

When we extrapolated the suppression of T_N as a function of average R - site ionic radius using linear regression, we see that the MIT gets completely suppressed at around $R_{avg} = 1.126$ Å, which is exactly equal to the ionic radius of Pr^{3+} ion in 8-fold coordination. Hence, $Pr_4Ni_3O_8$ lies exactly at the boundary where the crossover from a charge/spin stripe insulating phase to a correlated metallic phase takes place. Hence, this finding is very interesting and further studies are necessary to elucidate the possibility of a quantum critical point as a function of chemical doping in the Pr series.

5.7 Summary

We carried out detailed investigation into the nature of the semiconductor-to-insulator transition occurring at 105 K for the $La_4Ni_3O_8$ sample. We tried to understand the underlying mechanism behind this transition by carrying out doping at the La site with smaller Pr and Nd ion, since this transition is not seen for the $Pr_4Ni_3O_8$ or $Nd_4Ni_3O_8$ sample even though all three of them belong to the same crystallographic space group.

Clear signatures of CS stripe ordering were captured in the form of a semiconductor-to-insulator transition in the transport data. The degree of hysteresis between the heating and cooling data was enhanced with the increasing site mixing at La site with Pr/Nd. Beyond 50% doping, both the series demonstrated metallic behaviour with the presence of low-temperature resistivity upturn that could be related to weak localization effects. The presence of a weak localization effect was further confirmed by carrying out magnetoresistance measurements on $Pr_4Ni_3O_8$ and $Nd_4Ni_3O_8$ samples.

Heat capacity measurements clearly captured the CS stripe ordering as a sharp lambda like transition for $La_4Ni_3O_8$ sample at $T \sim 105$ K. New anomalies associated with the rare-earth sublattice were seen for the $(La_{1-x}Pr_x)_4Ni_3O_8$ and $(La_{1-x}Nd_x)_4Ni_3O_8$ series in the low-temperature regime. From the magnetic susceptibility, the CS stripe ordering was seen as a sudden drop in magnetization and was captured more distinctly for the $(La_{1-x}Pr_x)_4Ni_3O_8$ series as compared to the $(La_{1-x}Nd_x)_4Ni_3O_8$ series. By comparing the magnitude of low-temperature susceptibility for both series, we can qualitatively comment that in the Pr series, some of the Pr ions might be in a singlet ground state as compared to the Nd series. This enables us to capture the behaviour of the Ni sublattice in the Pr series at low temperatures,

which is otherwise masked by the large paramagnetic contribution coming from the Pr^{3+} ions.

We tried to construct a diagram that showcases the variation of MIT temperature as a function of doping for both the Pr and Nd series, as shown in Fig. 5.20. The MIT temperatures were extracted from low-temperature PXRD measurements. As is clear from Fig. 5.20, with increasing Pr/Nd content at the La site, the MIT is suppressed to lower temperatures. Beyond 50% doping concentration, no signatures of MIT are seen for the Pr series, while it is suppressed below 50% doping for the Nd series. For both series, the CS stripe order was accompanied by a sudden drop in the c/a ratio. It is interesting to note that $Pr_4Ni_3O_8$ sample lies exactly at the boundary between the CS stripe insulating phase and the correlated metallic phase.

Chapter 6

Ordered and disordered variants of the triangular lattice AFM - $Ca_3NiNb_2O_9$

The contents of this chapter has been published in Physical Review Materials under the title "Ordered and disordered variants of the triangular lattice antiferromagnet $Ca_3NiNb_2O_9$: Crystal growth and magnetic properties [244].

- The single crystal neutron diffraction experiments were conducted at the D10 beamline in ILL, France in collaboration with Dr. Markos Skoulatous and Mr. Ran Tang from Technical Univerisity of Munich, Garching, Germany.

- The high field magnetization measurements were carried out at the International Mega-Gauss Science Laboratory of ISSP, Japan in collaboration with Dr. Masashi Tokunaga.

6.1   Introduction

Triangular lattice antiferromagnets (TLAFs) exhibit an intricate interplay of geometrical frustration and low-dimensionality with novel magnetic phases and ground states [119, 121–125, 125–129]. The spin 1/2 TLAFs exhibit two competing ground states: one where the spins are long-range ordered in the three sublattice 120° spin structure (Fig. 6.1(a)) [245, 246], and another where the quantum fluctuations are expected to melt the long-range ordering, resulting in Resonating Valence Bonds (RVB) featuring a quantum spin liquid (QSL) ground state [116, 121]. Experimentally, both these scenarios (QSL versus 120°) have been observed.
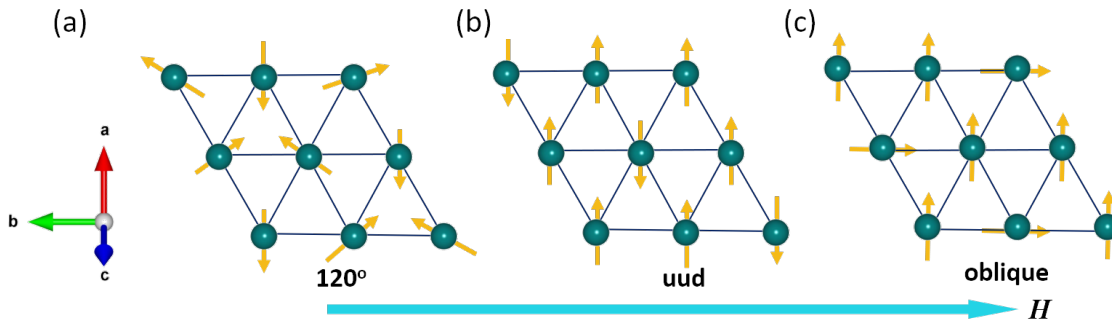
Figure 6.1: (a) shows the 120° ordered ground state, which undergoes transitions into uud and oblique states under an increasing applied magnetic (H) as shown in (b) and (c) respectively.

To give a few examples, consider $Ba_8CoNb_6O_{24}$, which shows no long-range magnetic ordering down to temperatures as low as 0.06 K [247]; similarly, in $Ba_3CuSb_2O_9$ [132] and $Sr_3CuSb_2O_9$ [105] no magnetic ordering has been seen down to very low-temperatures. Based on the temperature dependence of low-temperature specific heat and magnetic susceptibility, these TLAFs have been characterized as gapless QSLs. On the other hand, the 120° ground state has been observed in several spin 1/2 TLAFs, including the well-studied Cs_2CuCl_4 (T_N = 0.6 K) [248] and $Ba_3CoSb_2O_9$ (T_N = 3.8 K) [249–251]. However, even in these cases, the quantum fluctuations remain prominent and are manifested in the form of reduced ordered moment and appearance of one-third magnetization plateau in the isothermal magnetization measured below T_N [98, 120, 123, 128, 130, 131]. In the one-third plateau state, the spin structure changes from 120° to an up-up-down (uud) state, which further evolves into an oblique phase at higher fields (see, Fig. 6.1 (c)). It has also been argued by some that the presence of further neighbor exchanges or the interlayer exchange enhance frustration, resulting in the QSL ground state [252–254]. At the same time, it is well known that in the pure 2D Heisenberg limit, no long-range ordering is expected as demonstrated by Mermin and Wagner [255]. Hence, it would only be fair to conclude that the spin 1/2 TLAFs present an intriguing case where QSL and 120° order compete.

In contrast to this, in the semiclassical limit with spin > 1, the ground state is expected to be 120° long-range ordered only. However, even in these cases the uud magnetization plateau at one-third of the saturation magnetization has been observed, which is argued to be thermally assisted, i.e., the thermal fluctuations of the spin facilitate the occurrence of the one-third plateau in isothermal magnetization [97, 250, 256]. However, in the classical regime,

the easy-axis anisotropy is suggested to be crucial for the appearance of the magnetization plateau [256, 257].

The intermediate case of spin 1 on a triangular lattice, where the quantum fluctuations may still be strong, has not been explored in detail. The spin 1 TLAFs can be realized in nickelates with Ni^{2+} in the high spin state. Some examples of spin 1 TLAFs include, 6HA-$Ba_3NiSb_2O_9$ (hexagonal space group $P6_3/mmc$). In this compound, the ground state is shown to be 120° long-range ordered [119]. Other examples of spin 1 TLAFs with 120° ground state include $Ba_3NiNb_2O_9$ [98], $Ba_2La_2NiTe_2O_{12}$ [258], and $Na_2BaNi(PO_4)_2$ [259]. Interestingly, not all spin 1 TLAFs exhibit 120° ground state which distinguishes them from the spin > 1 case. For example, the quantum fluctuations induced quantum spin liquid ground state has been reported in the 6HB-$Ba_3NiSb_2O_9$ (hexagonal space group $P6_3mc$) [260, 261]. The possibility of realizing QSL in 6HB-$Ba_3NiSb_2O_9$ was also investigated theoretically. While Serbyn *et al.* [262] and Xu *et al.* [263] independently reached at the conclusion that the observed constant magnetic susceptibility and linear in T low temperature specific heat in 6HB-$Ba_3NiSb_2O_9$ are indeed signatures of QSL, Chen *et al.* [264] refuted it. They claimed that the observed behavior can be understood in terms of a conventional picture of a proximity to a frustrated critical point. These observations clearly suggest that spin 1 TLAFs are as exciting as their spin 1/2 analogues. In both cases, the 120° spin structure lies in the close proximity of a QSL ground state. Further studies on spin 1 TLAFs would be useful in deciphering details that control these ground states and hence pave way for their better theoretical understanding.

6.2 Motivation to study $Ca_3NiNb_2O_9$

Here, we focus on the spin 1 TLAFs of $A_3^{2+}(M'^{2+}M_2^{5+})O_9$ family, structurally analogous to $Ba_3NiSb_2O_9$. These are called triple-perovskites in which the magnetic ions (M') form the triangular lattice [119, 124, 125, 130, 265]. Their structure is derived from the perovskite ABO_3 structure with a 1:2 ordering of M' and M ions at the B-site [104, 266, 267]. Henceforth, we shall refer to this as B-site ordering. In general, whether the B-site ordering is present or not depends on the charge and ionic radii differences between the M' and M cations. Generally, when the charge difference is > 2, the cations undergo B-site ordering, but for values less than 2, a disordered structure is favored unless the ionic radii difference between M' and M is
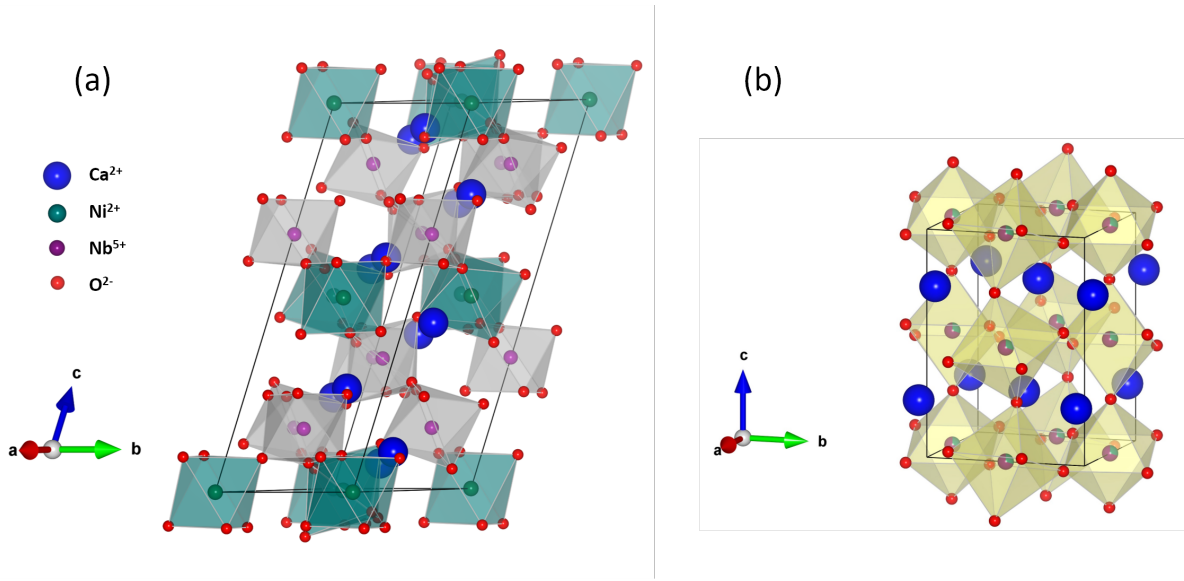
Figure 6.2: (a) shows the crystal structure of B-site ordered $A_3^{2+}(M'^{2+}M_2^{5+})O_9$. For A = Ca, M' = Ni, and M = Nb the structure is monoclinic with space group $P12_1/c_1$; (b) shows the crystal structure of $A(M'_{1/3}M_{2/3})O_3$. For A = Ca, M' = Ni, and M = Nb the structure is orthorhombic with space group *Pbnm*. The solid black lines denote the unit cell for each space group

significantly large [121, 268, 269].

The ordered structure of $A_3^{2+}(M'^{2+}M_2^{5+})O_9$, shown in Fig.6.2(a), consists of triangular layers of M' cations in the *ab*-plane. These triangular layers are well separated from each other by corner-sharing M_2O_{11} double octahedra and A^{2+} ions. The M_2O_{11} double octahedra serve as a non-magnetic buffer layer, rendering the spin-system quasi-two-dimensional. The disordered structure, on the other hand, typically has a higher symmetry and is characterized by a statistical distribution of M and M' cations over the B-site in the perovskite ABO_3 structure as shown in Fig.6.2(b).

The compound studied in this work is $Ca_3NiNb_2O_9$. The low temperature structural and magnetic properties of polycrystalline $Ca_3NiNb_2O_9$ were previously reported by Ma *et al.* [270] where a comparative study of the $A_3NiNb_2O_9$ (A = Ba, Sr and Ca) compounds was performed. In $A =$ Ba, the triangular lattice formed by Ni^{2+} ions has an ideal equilateral geometry. However, in $A =$ Ca and Sr, the triangles are isosceles. In $Ba_3NiNb_2O_9$ only a single antiferromagnetic transition was observed near $T_N = 5$ K. However, in $Ca_3NiNb_2O_9$ and $Sr_3NiNb_2O_9$ analogues show two closely spaced transitions at $T_{N_1} = 4.6$ K (Ca), 5.5 K (Sr), and $T_{N_2} = 4.2$ K (Ca), 5.1 K (Sr). We shall refer to this as a two-step ordering in our work. Recently, a

similar two-step ordering has also been reported for $Sr_3NiTa_2O_9$ where the triangular motif is analogously isosceles [271]. However, $Ba_3NiSb_2O_9$, which also has an equilateral triangular motif, showcases a two-step transition at 13.5 and 13 K [119]. It has been suggested that successive phase transitions in the Heisenberg type TLAFs reults from an interplay of single-ion anisotropy and the anisotropy of the exchange interactions. The two-step ordering therefore appears to be a common feature among the spin 1 nickelates. Understanding this generic behavior mandates a detailed study preferably on single crystals, which forms the basis of the present work.

6.3 Single crystal growth of $Ca_3BNb_2O_9$, B = Ni, Mg

Single crystals of $Ca_3NiNb_2O_9$ and $Ca_3MgNb_2O_9$ were grown using the four-mirror optical floating-zone furnace (Crystal System Corporation, Japan). This method was adopted as it was previously reported by Fratello *et al.* [272] that $Ca_3NiNb_2O_9$ melts congruently at temperatures close to 1650°C. However, no details were given regarding the length of the grown crystal nor its structural characterization. As far as $Ca_3MgNb_2O_9$ is concerned, its crystal growth has not been reported before, to the best of our knowledge.

6.3.1 Synthesis of feed and seed rods

Polycrystalline samples of $Ca_3NiNb_2O_9$ and $Ca_3MgNb_2O_9$ were prepared using the solid-state synthesis method. For this, stoichiometric mixtures of $CaCO_3$ (Sigma Aldrich 99.995 %), NiO (Sigma Aldrich 99.99 %) [or MgO (Alfa Aesar 99.99 %)] and Nb_2O_5 (Sigma Aldrich 99.9 %) were thoroughly ground using an agate mortar and pestle and calcined at 1250°C in air. This heat treatment was repeated several times with intermediate grindings until the desired phase formed completely. $CaCO_3$ and MgO were preheated at 700°C for 10 h and were weighed immediately after removing from the furnace at 300°C to avoid absorption of moisture. The phase purity of the polycrystalline powders was confirmed using the x-ray powder diffraction technique using a Bruker D8 Advance powder diffractometer with Cu Kα radiation. For preparing feed rods, approximately 6-8 g of phase-pure powder was packed in a silicone tube and compressed under a hydraulic pressure of 700 bar to obtain cylindrical rod measuring about 6-8 mm in diameter and 100 mm in length. Several such rods were placed in an alumina boat and sintered in the temperature range from 1250°C to 1450°C. These rods

were used in the crystal growth experiments in a four-mirror optical float-zone furnace. Shorter rods of length (2-3 cm) were cut from the sintered rods to be used as seeds or support to initiate the growth. The phase purity of the sintered rods was analyzed using the lab-based xrd.

6.3.2 Crystal growth of $Ca_3NiNb_2O_9$

Several attempts were made to grow large single crystals of $Ca_3NiNb_2O_9$ using the four mirror optical floating zone furnace. In our initial attempts we made use of 300 W halogen lamps in flowing air. But since the percentage of lamp power required was close to 90%, subsequent growth attempts were done using a set of 500 W halogen lamps, which could stabilize the float zone at a lower percentage of total lamp power.
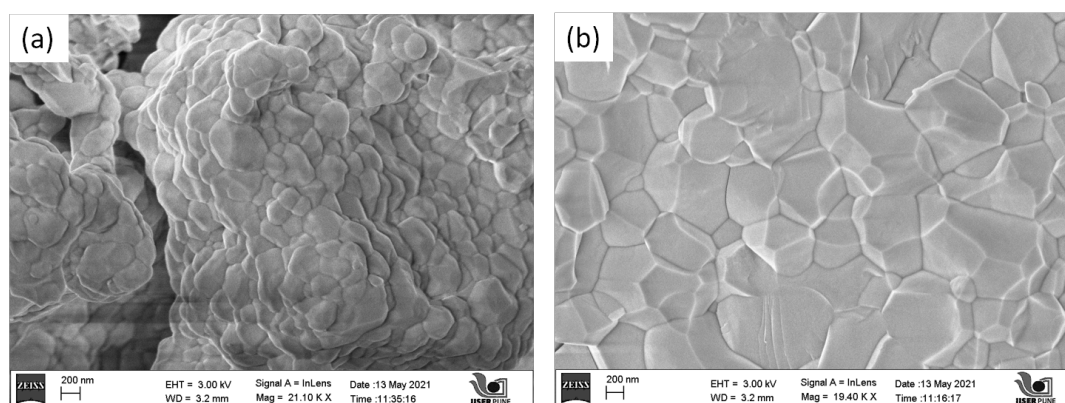
Figure 6.3: (a) and (b) show the FESEM image of a portion of feed rod of $Ca_3NiNb_2O_9$ sintered at 1250° C and at 1400° C respectively.

During our first growth experiment, we used a feed-rod sintered at 1250^oC. The growth was carried out under flowing synthetic air. The flow-rate was set at $2\,\mathrm{l\,min^{-1}}$ throughout the experiment. Other growth parameters are listed in Table 6.1 (see growth 1 in Table 6.1). A stable molten-zone could be achieved though there was a tendency for the melt to creep-up into the feed-rod due to its high-porosity, which required continuous monitoring of the zone-length and furnace power. The grown crystal boule consisted of a very large number of cracks. Due to these cracks, the boule was fragile and tended to break easily into mm-size crystals that were either pale-green (translucent) in color or black (opaque). These grains were distributed in nearly equal proportion all along the length of the boule (See, Fig. 6.5(a)).

To overcome the difficulties faced in the first growth attempt, we tried several procedures by combining the steps from (a) to (e) listed as follows:

(a) Density of feed rod: For the next growth attempts, both the feed and seed rod were sintered at a higher temperature of 1400 - 1450° C in order to improve their density, reduce their porosity and prevent the melt from creeping up the feed rod. Fig. 6.3(a) and (b) show a comparison of the SEM images of a portion of feed rod sintered at 1250°C and 1450°C respectively. Clearly, there is a change in morphology of the sample and the packing of grains is improved as the sintering temperature is increased. Moreover. small crystallites start forming when the sintering temperature reaches closer to the melting point of $Ca_3NiNb_2O_9$.
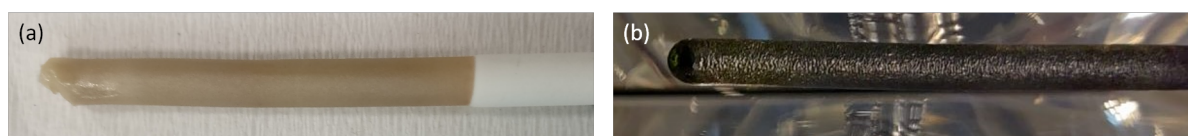
Figure 6.4: (a) and (b) show the representative images of feed rod of $Ca_3MgNb_2O_9$ and $Ca_3NiNb_2O_9$ that have undergone in - situ sintering in an image furnace prior to the start of growth.

(b) In-situ sintering or pre-melting of feed rod: The feed rod was sintered in-situ at a lower lamp power of about 5% below the melting point of $Ca_3NiNb_2O_9$. For this purpose, a feed rod, sintered at 1200° C in a box-furnace prior to in-situ sintering, was suspended on the upper shaft of the image furnace. The lower shaft was fitted with the support $Ca_3NiNb_2O_9$ rod as is usually done during the crystal growth using an image furnace. The feed and seed were then fused at their melting temperature. Subsequently, the furnace power was reduced by 5%, and the support-rod and feed-rod were synchronously translated down through the hot zone at a speed of 10 mm h^{-1}. Once the entire feed rod has passed through the central, hot zone, the translation is reversed to come back to the starting point, where the two rods were initially fused. After waiting here for some time, the furnace power was gradually increased to initiate melting and form the floating zone for the growth experiment to proceed. After the pre-melting procedure, the color of the feed rod changed from dark green to black, as can be seen from Fig. 6.4 (b). We also observed the formation of tiny crystallites along the entire length of the pre-melted feed rod that were translucent green in appearance. This procedure also helped to densify the feed-rod further and prevented the creeping of the liquid up the feed rod, which usually happens when the feed rod is porous. The theoretical density of $Ca_3NiNb_2O_9$ is 4.75 g cm^{-3} while that of the feed rod of $Ca_3NiNb_2O_9$ sintered at 1400°C is around 4.12 g cm^{-3}. After pre-melting the feed rod in the image furnace, its density improved to a value of 4.31

g cm^{-3}, which is nearly 91% of the theoretical density of Ca$_3$NiNb$_2$O$_9$. Similar premelting procedure was also adopted for the growth of the TLAF Ba$_3$CoSb$_2$O$_9$ by Boothroyd *et al.* [273] since this material also suffered from extensive cracks while cooling.

(c) Pulling rate: In order to further reduce the crack formation, we adopted lower pulling rates, which would also to some extent help reduce the thermal stress along the length of growing boule. At higher pulling rates (4-5 mm h^{-1}) a stable floating zone could be sustained, and the length of grown boule up to 60 mm could be obtained (see growth no.2 in Table 6.1). However, the bi-colour formation was more pronounced in these growths. At the lowest speed used, which is 1 mm h^{-1}, the growth proceeded without much need of tweaking the growth parameters and the grown crystal had a uniformly light green color (a representative image of the grown crystal boule is shown in Fig.6.5(b)), and the length of crystal was about 60 mm (see growth no.5 in Table 6.1). However, the cracks in the crystal boule were still present, and the crack density was nearly the same as under the higher pulling rates. Also, at the slower rate the NiO deposition was seen on the quartz enclosure, which was confirmed by carrying out xrd on the deposited material.
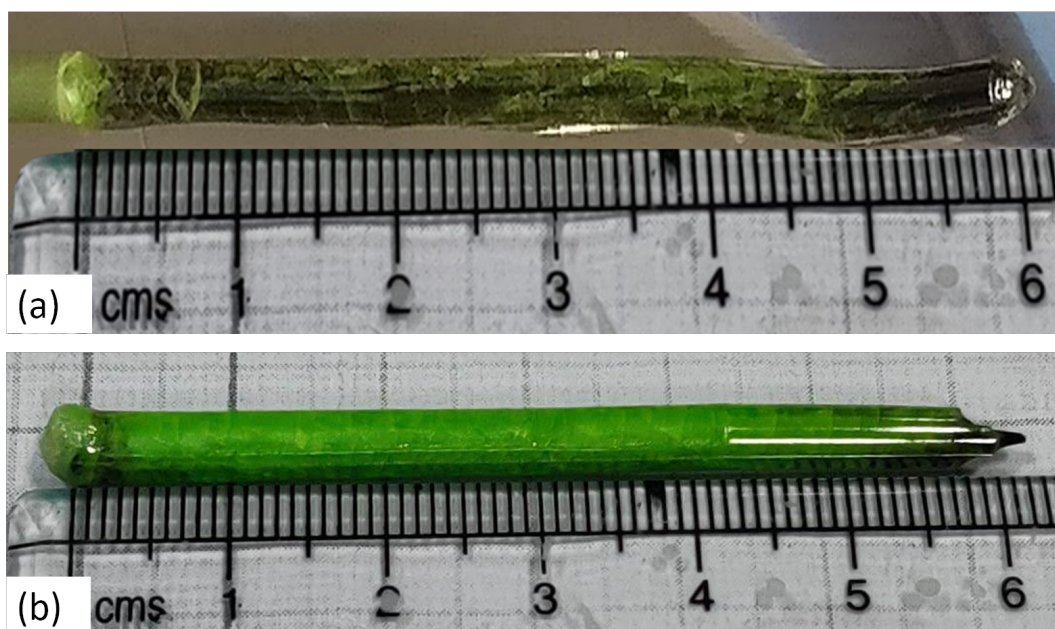
Figure 6.5: (a) and (b) show the representative images of the crystals of Ca$_3$NiNb$_2$O$_9$ grown in air at 4 mm h^{-1} and 1 mm h^{-1} respectively.

(d) Growth atmosphere: We also tried to check if the crystal growth environment has an effect on the growth stability conditions. Hence the growth was tried in air, oxygen and argon

atmosphere to see if this resulted in elimination of one of the colored grains. We found that under a pure oxygen atmosphere the floating-zone was unstable (see growth no.4 in Table 6.1). For these experiments, the feed rod was sintered at 1400^oC. The grown crystal started showing cracks that reached upto the solid-liquid interface (in the first growth attempts under air, the portion of the grown crystal in the field of view of the camera did not show any cracks, i.e., the cracks appeared at some point a cm or so below the interface; on the other hand, in case of oxygen atmosphere the cracks were seen right below the interface. In fact, as the growth proceeded, the cracks propagated further up causing the molten zone to collapse. Moreover, numerous bubbles were formed in the molten zone, which further reduced the stability of the growth process. In case of argon atmosphere, the growth was fairly stable; however, the grown material appeared grainy without any facets, which is different from the growth under air atmosphere where diametrically opposite facets readily form after about 1 cm of growth. This led us to conclude that air atmosphere works best for the growth of $Ca_3NiNb_2O_9$.
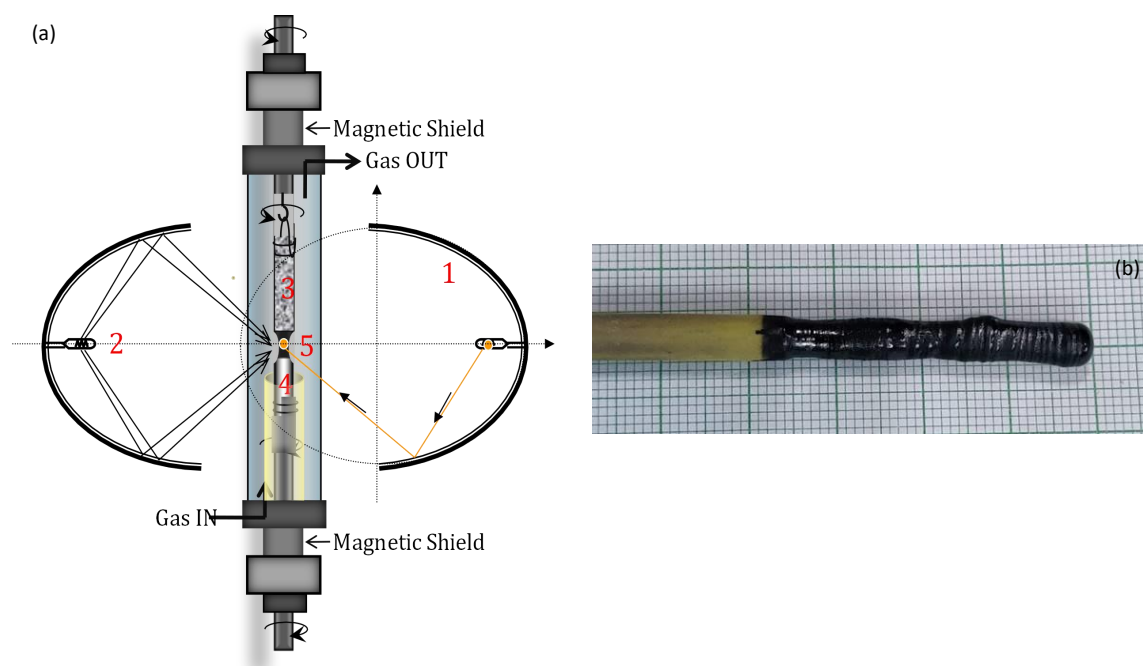
Figure 6.6: (a) Shows the schematic of a modified image furnace setup using an alumina tube as an after - heater. Here 1: elliptical mirror; 2:Halogen lamp; 3:Feed rod; 4:Seed rod and 5:Float zone, which is also the common focus of all the elliptical lamps. (b) Shows the representative image of the crystal of $Ca_3NiNb_2O_9$ grown in air at 3 mm h^{-1} using an after - heater.

(e) After - heater: In an attempt to overcome the formation of cracks in the grown crystal boule, we used a modified setup wherein an alumina tube is used as an after heater or a heat-

Table 6.1: The parameters used during the crystal growth experiments of $Ca_3NiNb_2O_9$. The experiments 1 to 4, 5 to 6 and 7 are done using 300 W, 500 W and 1000 W lamps respectively in a 4-mirror float zone furnace.

Growth No.	Lamp power %	T_S °C	Growth atmosphere	v_f mm h^{-1}	v_g mm h^{-1}	ω_f rpm	ω_g rpm	G_L mm
1	88.3%	1250º C	Air	5.0	5.0	23.7	7.0	20
2	87.4 %	1400º C	Air	4.0	4.0	16.1	13.3	60
3	90.0%	1450º C	Air	3.2	3.0	12.5	12.2	27
4	88.0%	1400º C	Oxygen	2.5	2.5	12.5	12.7	-
5	69.2%	1400º C	Air	1.0	1.0	15.2	15.2	60
6*	78.4%	1400º C	Air	3.0	3.0	14.1	14.1	33
7*	79.2%	1400º C	Air	3.0	2.95	14.1	14.1	27
8	60.0%	1400º C	Air	3.0	3.0	14.4	14.4	22

* These growths were carried out using an after-heater as described in the text; T_S: feed rod sintering temperature, v_f: speed at which the upper shaft is lowered, v_g: growth rate, ω_f: rotation speed of the feed rod, ω_g: rotation speed of the seed rod, G_L : growth length

reservoir [274]. The alumina tube used had an inner diameter of 32 mm and it was placed inside the quartz enclosure with its upper end reaching about a few mm below the melt-crystal interface as shown in Fig. 6.6(a). The lower end was supported on a water-cooled flange. The power required to stabilize the crystal growth using a set of four 500 W lamps was 78.4% and 69.2% with and without the after-heater, respectively. The extra power consumed in the presence of the heat reservoir went into heating-up the alumina tube. Kimura *et al.* [274] had shown that in the presence of an after-heater of this kind, the temperature gradient along the length of grown crystal can decrease dramatically. They reported a drop from about 450°C cm^{-1} to almost 100°C cm^{-1} or less depending on the exact location of the alumina tube in a two-mirror image furnace using a set of 1.5 KW lamps at 1500°C. In the case of a four-mirror set-up, the gradient would be even smaller using a set of 500 W lamps [275]. In this experiment, we used a crystal growth rate of 3 mm h^{-1} leading to a 40 mm long crystal boule (see growth no.6 in Table 6.1). The grown crystal boule was black and opaque with fewer cracks, see Fig. 6.6(b).

Figure 6.7: (a) and (b) show the representative images of the crystals of $Ca_3MgNb_2O_9$ grown at 5 mm h^{-1} and 2 mm h^{-1} respectively in flowing air atmosphere.

6.3.3 Crystal growth of $Ca_3MgNb_2O_9$

During our first growth attempt of $Ca_3MgNb_2O_9$, we used a feed rod sintered at 1400° C, lamp power of 300 W and an air flow rate of 200 cc min^{-1}. It was observed that even 90% of lamp power was insufficient to melt the feed rod. Moreover, since the color of the feed rod was white, most of the incident light was reflected and could not be used to raise the temperature of the feed rod close to its melting point. Hence, during the subsequent growth attempts, the lamp power was changed to 1000 W to facililate the melting procedure.

During the first growth attempt using 1000 W lamps, we observed that the feed rod began melting at 75% lamp power but the incident power had to be continuously increased to prevent the float zone from drying up. Hence, a stable float zone could not be established and the growth was stopped. In order to overcome this issue, we carried out in-situ sintering of the feed rod before the growth process was started. During this pre-melting process, the feed rod was fused with the seed rod at 73% of lamp power, which ensured that the feed rod remained straight while it was being passed through the zone. The in - situ sintering was carried out at 65% of lamp power and the feed rod was translated down through the zone at a faster rate of 7 mm h^{-1} without any rotational motion. After the entire feed rod had undergone sintering, its motion was reversed at a faster rate of 10 mm h^{-1} till it reached the point at which the feed and seed rod were fused.

At this point, the lamp power was ramped up to 70.7% and the growth process was started.
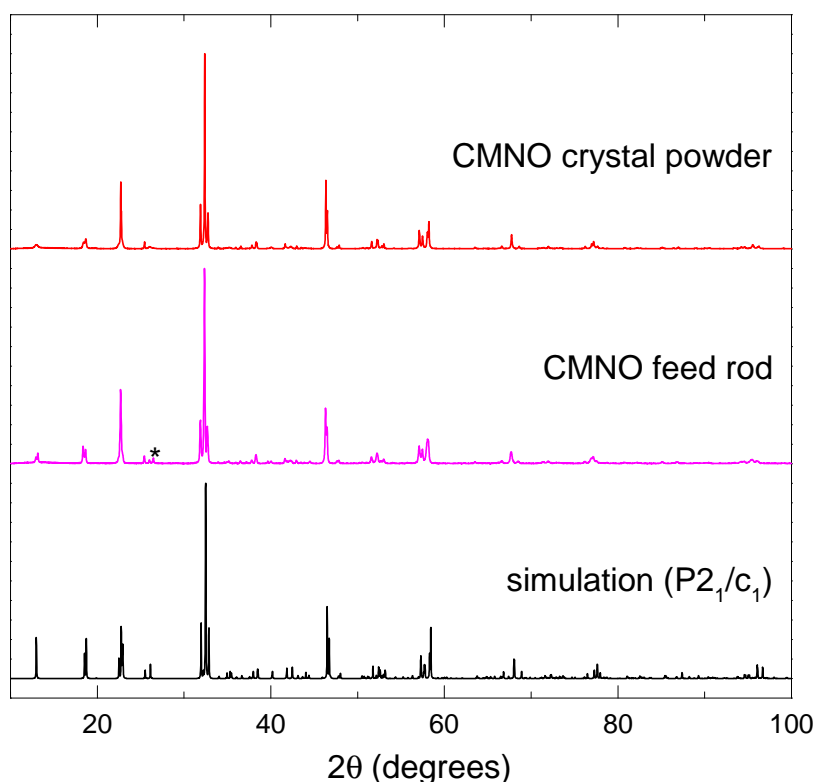
Figure 6.8: Shows the comparison of the lab based xrd of the as - grown crystal of $Ca_3MgNb_2O_9$ with the simulation of monoclinic space group, $P12_1/c_1$. Here * marks an unknown peak present in the feed rod sintered at $1300°C$.

Due to this pre-melting procedure not only did the density of the feed rod increase substantially (the diameter of feed rod reduced by 20%), the color of the feed rod changed to dark, golden (see Fig. 6.4 (a)) which enabled it to absorb the incident light better, which in turn stablized the float zone better. However, the grown crystal boule had multiple cracks (see Fig. 6.7(a)) similar to that seen during the growth of $Ca_3NiNb_2O_9$. Hence, in an attempt to improve the crystal quality and reduce the formation of cracks, we tried a growth at a slower pulling rate of 2 mm h^{-1} (see Fig. 6.7(b)). However, such slow pulling rates caused the liquid from the float zone to flow down the grown crystal boule before it could be crystallized. This made the diameter of the grown crystal boule very uneven (see growth no.2 in Table 6.2) and the growth process had to be optimized every now and then. However, the cracks still persisted in this grown crystal boule as is commonly seen during the crystal growth of niobates [276–278].

Table 6.2: The parameters used during the crystal growth experiments of $Ca_3MgNb_2O_9$. Both the growths were carried out using 1000 W lamps in a 4-mirror float zone furnace.

Growth No.	Lamp power %	T_S °C	Growth atmosphere	v_f mm h^{-1}	v_g mm h^{-1}	ω_f rpm	ω_g rpm	G_L mm
1	70.7%	1400° C	Air	5.0	5.02	8.0	8.0	56.0
2	71.8 %	1400° C	Air	2.0	2.0	16.4	16.9	51.0

T_S: feed rod sintering temperature, v_f: speed at which the upper shaft is lowered, v_g: growth rate, ω_f: rotation speed of the feed rod, ω_g: rotation speed of the seed rod, G_L : growth length

6.4 Structural and compositional characterization

6.4.1 Powder x-ray diffraction

As mentioned in the crystal growth section, we obtained bicolor grains during the crystal growth of $Ca_3NiNb_2O_9$ at higher growth rates. These were mechanically separated for further structural characterizations. Since the post growth annealing was also done under various atmospheres, for the ease of reading, we have used the following notation:

AGO - as-grown, dark-green and opaque specimen

AGT - as-grown, pale-green and translucent specimen

AGH - specimen grown using the after-heater

AGQ - specimen quenched in the image furnace

ANT - air-annealed specimen of AGO The xrd pattern of the crystal specimen after each annealing treatment is shown in Fig. 6.9(a) alongwith the simulated pattern of the monoclinic space group $P12_1/c_1$, for the purpose of comparison. The results of argon annealing are not discussed in detail as the sample undergoes decomposition after argon annealing treatment. On the other hand, the results of oxygen and air annealing are similar and is treated on equal footing. The sample ANT is obtained by air annealing an AGO crystal piece at 1200°C for 12 h. After annealing, the specimen changed its appearance from dark-green and opaque (Fig. 6.10(d)) to translucent light-green (Fig. 6.10(e)). No change of weight was observed after the annealing procedure in air, which suggests that the stark change in appearance is not due to oxygen off-stoichiometry. This was further confirmed by Thermogravimetric Analysis (TGA) where no weight change was seen at least up to 1400°C upon heating in oxygen atmosphere
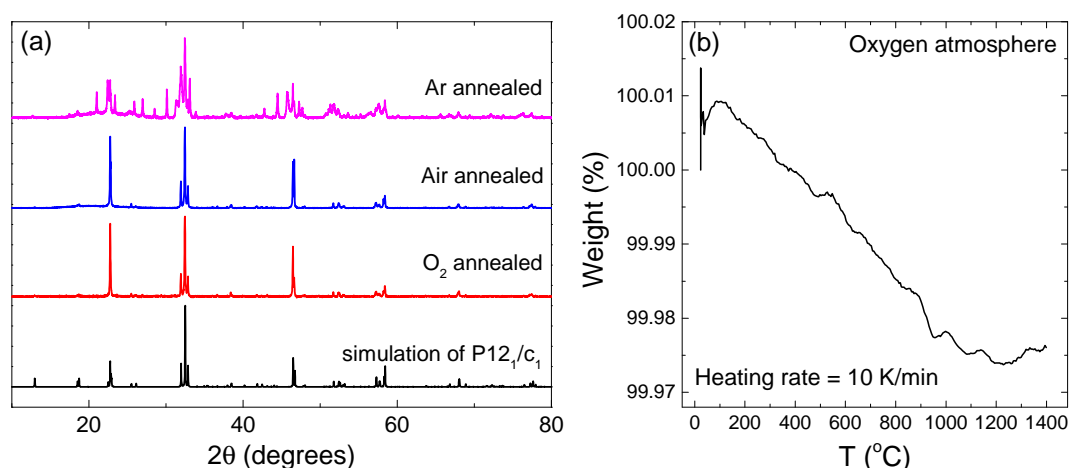
Figure 6.9: (a) Shows the comparison plot of the PXRD of annealed samples with the simulation of monoclinic space group $P2_1/c_1$. (b) Shows the TGA carried out on an as-grown crystal specimen from growth No.7 in Table 6.1 in oxygen atmosphere at a heating rate of 10 K min^{-1}.

(see Fig. 6.9(b)). In order to understand the structural differences between AGO, AGT and ANT we carefully examined their xrd patterns. The overall xrds for three samples look rather similar. This can be seen from Fig. 6.10(a) where the room temperature xrds are shown for AGO, AGT and ANT in the 2θ range of $10°$ to $70°$. However, upon careful inspection one finds several subtle differences. To exemplify this we show the xrds over select 2θ ranges in Fig. 6.10(b) and (c). Here the data has been scaled-up as per the multiplication factor indicated in the figure panels (b) and (c).

As shown in panel (b), the peaks at $12.9°$, $18.5°$ and $18.7°$, expected for the monoclinic symmetry ($P12_1/c_1$) that was previously reported for $Ca_3NiNb_2O_9$ [270], are *absent* in the AGO sample. Instead, a single peak around $19.8°$ is observed. Similarly over the 2θ range shown in panel (c), AGO has only one peak at $25.4°$ but the simulated pattern for $P12_1/c_1$ has two peaks at $25.5°$ and $26.1°$ in the same range. These observations suggest that the AGO sample stabilizes in a space group of higher symmetry. After an intensive literature survey on double and triple perovskites [107, 266, 279, 280], we came to the conclusion that orthorhombic space group $Pbnm$ (SG No. 62) matches most favorably with the observed diffraction pattern of AGO. In the $Pbnm$ symmetry there is only one peak near $19.8°$ over the 2θ range shown in panel (b). This peak coincides with the single peak in the observed xrd of AGO. Similarly, in panel (c) the simulated xrd for the $Pbnm$ symmetry has only one peak that matches well with the observed peak in AGO. In the $Pbnm$ structural model, M and
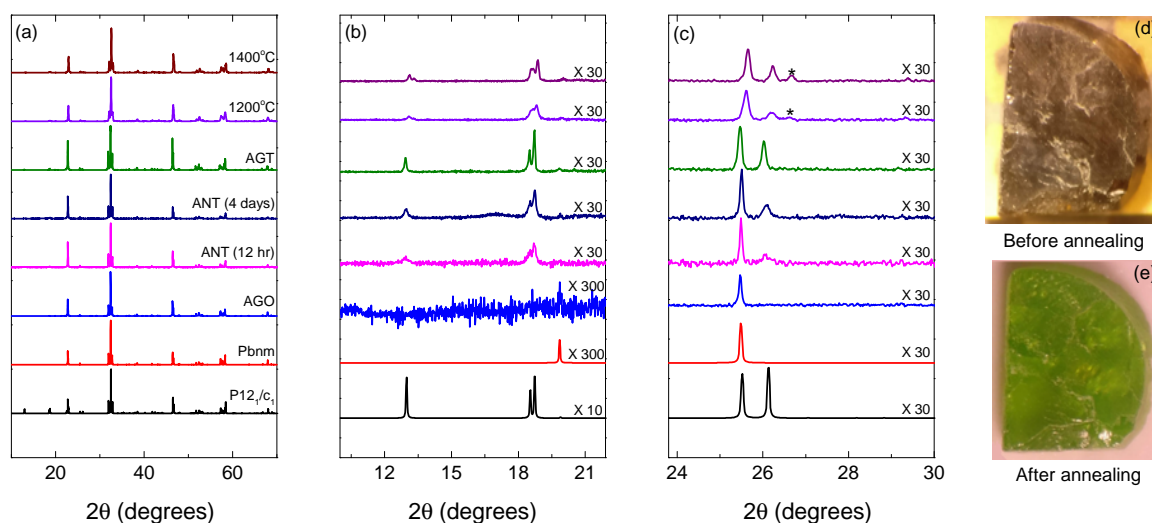
Figure 6.10: (a) shows the comparison of room temperature lab based xrd data of AGO, ANT (from growth No.2 in Table 6.1), AGT (from growth No.5 in Table 6.1), polycrystalline sample of $Ca_3NiNb_2O_9$ sintered at 1200°C and 1400°C with the simulated pattern of $P12_1/c_1$ and $Pbnm$ in the 2θ range of 10° to 70°. Panel (b) and (c) show selected 2θ ranges for comparison. Here the data is normalized with respect to the highest intensity peak. "*" denotes an unidentified peak. Panels (d) and (e) show representative images of a crystal specimen before (black) and after (green) air annealing for a period of 12 h.

M' cations are distributed statistically over the B-site [4b (0.5, 0, 0)] of the perovskite $CaBO_3$ structure. This observation is in line with some previous reports [see Ref. 107, 268, 279] on other double and triple perovskites where the random distribution of cations on the B-site results in a disordered structure of *higher* symmetry. In fact, the Rietveld refinement of the synchrotron data of an AGO specimen showed a better convergence with the space group $Pbnm$ than with $P12_1/c_1$. The refinement done using the orthorhombic $Pbnm$ space group is shown in Fig. 6.11(a). During the refinement procedure, the Ni^{2+} and Nb^{5+} occupancies were constrained to add up to 100 % at the $4b$ site. The strain model (3) with the Laue class *mmm* was used to account for slight anisotropic strain broadening present for certain hkl peaks. The site mixing at the 4b site for Ni^{2+} and Nb^{5+} ions comes out to be 3:7 (Table 6.3) as required. Hence, we conclude that the AGO sample stabilizes in the disordered structure of the form $Ca(Ni_{0.3}Nb_{0.7})O_3$. The lattice parameters obtained for the AGO sample are: a = 5.4599(5) Å, b = 5.6162(6) Å and c = 7.8026(6) Å with $\alpha = \beta = \gamma = 90°$.

From the xrds of ANT and AGT samples in Fig. 6.10(b) and (c), we notice that the peaks expected in the B-site ordered monoclinic symmetry are indeed present for these specimens.
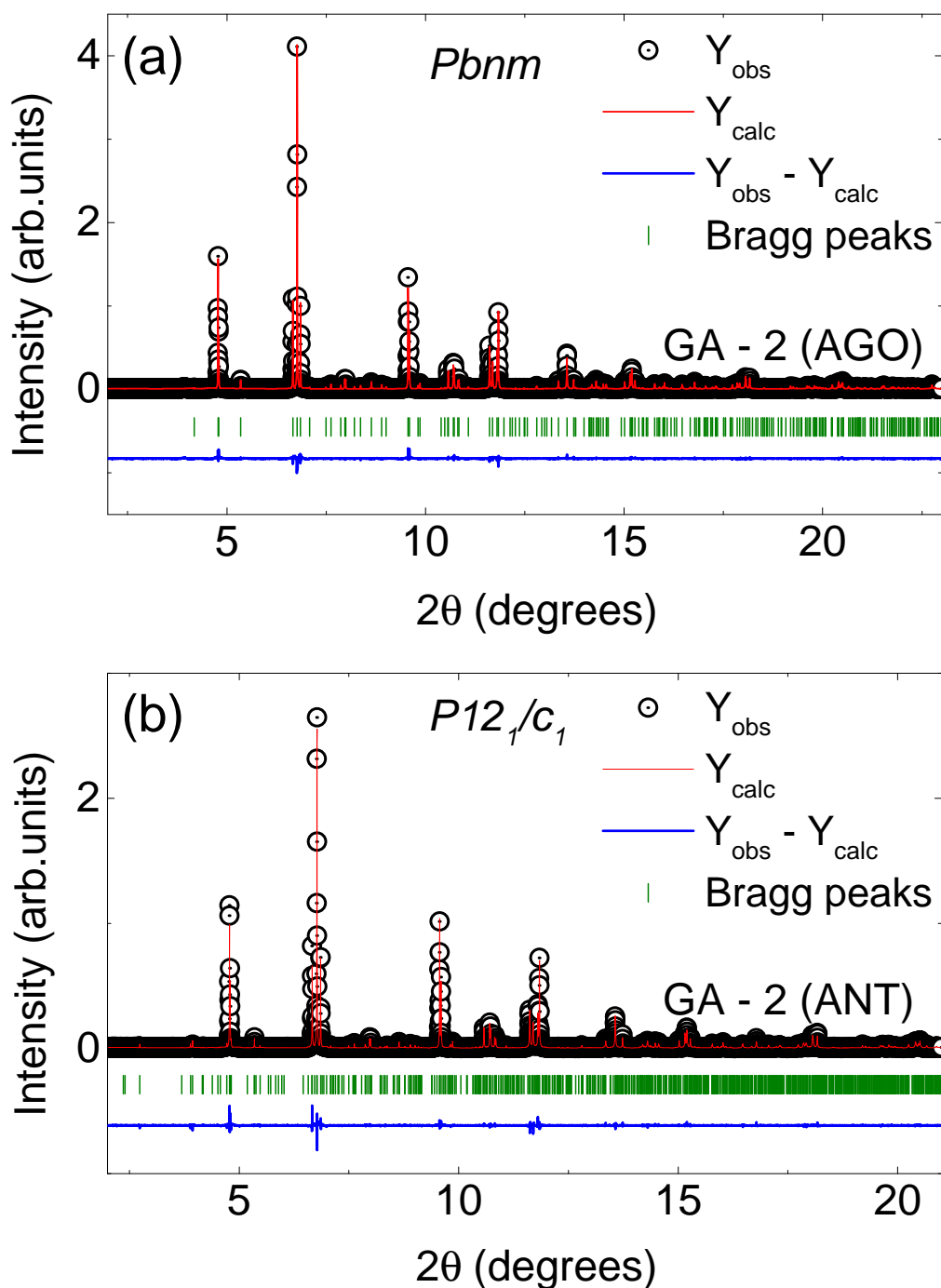
Figure 6.11: Room temperature synchrotron xrd data for the AGO and ANT sample (growth No.2, Table 6.1) refined using (a) orthorhombic ($Pbnm$) and (b) monoclinic ($P12_1/c_1$) space group.

The intensity of these peaks gets more and more pronounced upon increasing the annealing period from 12 h to 4 days. The AGT sample grown at 1 mm h^{-1}, appears to exhibit a close to perfect B-site ordering. The Rietveld refinement of the synchrotron data for an ANT spec-
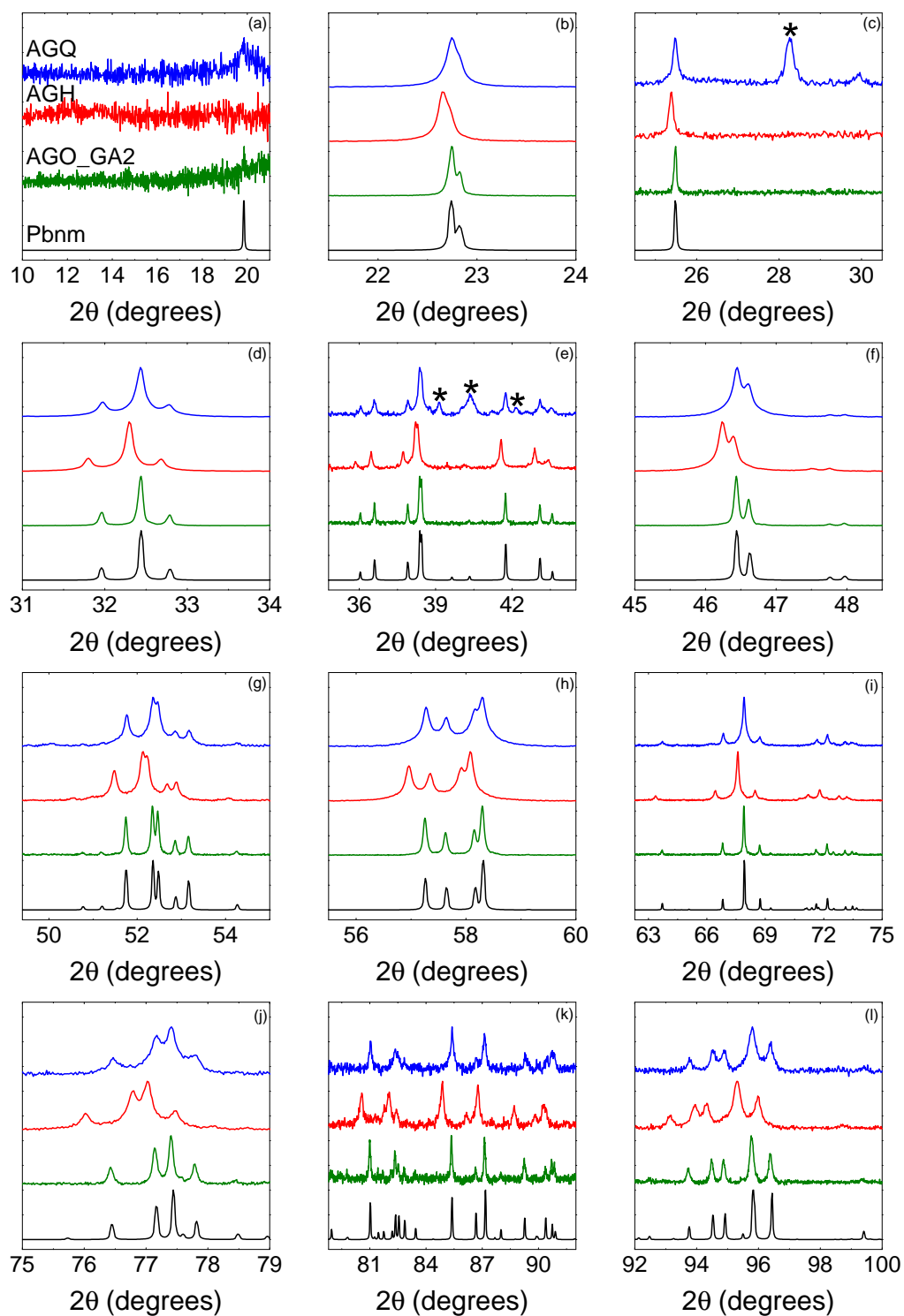
Figure 6.12: Panel (a-f) shows the comparison of the room temperature xrd data of AGO sample (green), growth done using after - heater (red) and a specimen quenched in image furnace (blue) with the simulated pattern for the orthorhombic space group Pbnm. Here "*" marks the presence of extra/unidentified peaks.

Table 6.3: Atomic positions, thermal isotropic factors and occupancies for $Ca_3NiNb_2O_9$ (AGO) at 300 K as determined from Rietveld refinement of synchrotron powder XRD data using the orthorhombic space group $Pbnm$.

Atom	Site	x	y	z	B_{iso}	Occupancy
Ca	4c	0.01201	-0.04842	0.25	0.89733	1.0
Ni	4b	0.5	0	0	0.15025	0.3
Nb	4b	0.5	0	0	0.15025	0.7
O(1)	8d	0.69865	0.30086	-0.05315	0.92	1.0
O(2)	4c	0.89920	0.53694	0.25	0.92	1.0

$$\chi^2 = 5.99; R_P = 20.2; R_{WP} = 22.5 \text{ and } R_{EXP} = 9.52$$

Table 6.4: Atomic positions, thermal isotropic factors and occupancies for $Ca_3NiNb_2O_9$ (ANT) at 300 K as determined from Rietveld refinement of synchrotron powder XRD data using the monoclinic space group $P12_1/c1$.

Atom	Site	x	y	z	B_{iso}	Occupancy
Ni(1)	2a	0	0	0	0.59339	1.0
Ni(2)	2d	0.5	0.5	0	0.16730	1.0
Nb(1)	4e	0.50307	0.5	0.33600	0.51169	1.0
Nb(2)	4e	0.00141	0	0.33569	0.36839	1.0
Ca(1)	4e	0.25225	0.49953	0.06578	0.46661	1.0
Ca(2)	4e	0.74156	-0.01297	0.09073	0.70881	1.0
Ca(3)	4e	0.24139	0.01721	0.22755	0.70649	1.0
O(1)	4e	0.9571	0.7051	0.2506	0.53	1.0
O(2)	4e	0.5408	0.7939	0.2783	0.53	1.0
O(3)	4e	0.25	0.593	0.2564	0.53	1.0
O(4)	4e	0.9521	0.6934	0.9125	0.53	1.0
O(5)	4e	0.0387	0.1956	0.9065	0.53	1.0
O(6)	4e	0.445	0.28	0.8802	0.53	1.0
O(7)	4e	0.5512	0.7997	0.9453	0.53	1.0
O(8)	4e	0.7425	0.093	0.9072	0.53	1.0
O(9)	4e	0.2425	0.593	0.9272	0.53	1.0

$$\chi^2 = 5.03; R_P = 19.8; R_{WP} = 23.3 \text{ and } R_{EXP} = 10.45$$

imen using the monoclinic space group, $P12_1/c1$ is shown in Fig. 6.11(b). Here the Ni^{2+} and Nb^{5+} ions occupy two different Wyckoff sites as required for the 1:2 ordered structure. The lattice parameters obtained for the ANT sample are: a = 9.6135(5) Å, b = 5.4579(7) Å and c = 16.8413(6) Å with $\beta = 125.775(5)°$. The strain model (-2) with Laue class $112/m$ was

used to account for slight anisotropic strain broadening for certain hkl peaks. Other details pertaining to the refinement are shown in Table 6.4.

The structural model used here does have some inadequacies. For example, it cannot correctly account for the apparent reversal of intensities of the (004) and (-213) peaks with respect to the calculated (or simulated) intensities. Incorporation of strain improves on this to some extent, which suggests that these crystals might be strained because of the high-temperature order-disorder transition. In an attempt to improve the model further, refinements were attempted by treating the Ni and Nb occupancies as variables to allow for antisite disorder (ASD). However, this did not result in a satisfactory fitting. After allowing for Ni-Nb ASD, we obtained the sample stoichiometry as $Ca_3(Ni_{0.644}Nb_{0.355})(Nb_{1.73}Ni_{0.26})O_9$. This would mean that nearly 35% of the Ni sites in the triangular layers are diluted by the non-magnetic Nb ions. However, with such high degree of ASD, one would expect the magnetic behavior to be very different from what is reported for the ordered samples. For example, in the presence of a large ASD, a significantly reduced ordering temperature is expected due to non-magnetic site-dilution [281]. However, this is contrary to the observed behavior (*vide infra*), which led us to abandon this structural model.

The crystal boule grown using an after-heater (AGH) was completely black and had fewer cracks when compared to other growth attempts without an after-heater. The xrd of a crushed AGH specimen conforms better to the $Pbnm$ space group of orthorhombic symmetry (see Fig. 6.12). Since during growth the molten zone temperature is at least 1650°C (melting temperature of $Ca_3NiNb_2O_9$, the temperature of the crystal boule below the melt-crystal interface remains rather high in the presence of the after-heater. If we assume a temperature gradient of 100°C cm^{-1}, the temperature will still be higher than 1250°C at the lower end of the 40 mm long boule. Thus, almost the entire crystal length remains above the structural transition temperature, which explains the result of this growth experiment.

Concerning AGQ, we first briefly describe the quenching procedure before coming to the effect of quenching. The quenching was done in the image furnace by melting the lower end of the feed rod completely and then pulling it away from the molten zone rapidly at ≈ 100 mm min^{-1}. The frozen-in section was black in appearance. Its xrd pattern looks similar to that of AGH, indicating clearly that the quenched phase has an orthorhombic symmetry. However,
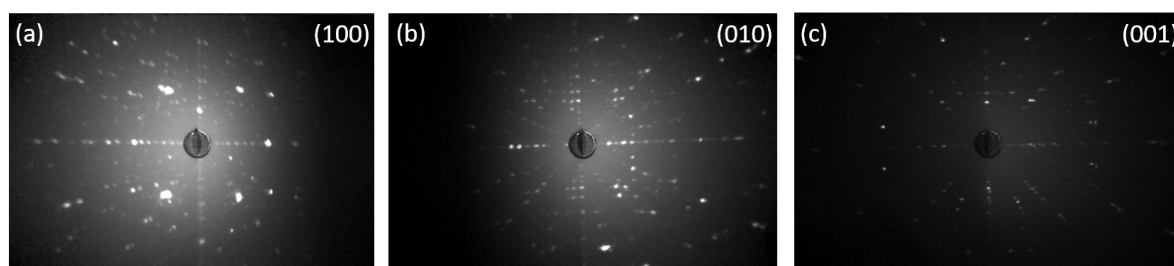
Figure 6.13: (a), (b) and (c) show the Laue images of the (100), (010) and (001) crystallographic plane respectively of an AGT specimen of $Ca_3NiNb_2O_9$ from growth No.5 in Table 6.1

in addition to the peaks due to the primary orthorhombic phase, small extra peaks were also seen, which indicate the presence of a secondary phase (see Fig. 6.12). This points towards a more complex melting behavior of $Ca_3NiNb_2O_9$ than the congruent melting behavior reported previously [272].

6.4.2 Laue diffraction

Owing to the presence of multiple cracks and possible twinning, the Laue images of an AGT crystal from growth No.5 in Table 6.1 show spot doubling as well as elongation of certain hkl reflections. Fig. 6.13 (a), (b) and (c) show the (100), (010) and (001) oriented planes respectively of the AGT specimen. The as-grown crystals of $Ca_3MgNb_2O_9$ also demonstrates similar Laue pattern (not shown) as that of $Ca_3NiNb_2O_9$.

6.4.3 Scanning electron microscopy and optical microscopy

Fig. 6.14 (a) and (b) show the representative optical image under polarized light of a polished section of the crystal boule of $Ca_3NiNb_2O_9$ and $Ca_3MgNb_2O_9$ respectively. As is evident from the image, the grown crystal disc of $Ca_3NiNb_2O_9$ exhibits more cracks as compared to that of $Ca_3MgNb_2O_9$. This could be related to the fact that $Ca_3NiNb_2O_9$ undergoes an order-disorder transition while cooling and $Ca_3MgNb_2O_9$ does not exhibit any such transition. There was no visual detection of any secondary phase as both the optical images showcased uniform contrast. From the FESEM images of the as-grown crystals taken in ASB mode, we concluded that there was no phase segregation for both the $Ca_3NiNb_2O_9$ and $Ca_3MgNb_2O_9$ crystals.

On the other hand, the FESEM micrograph of a polished section of AGH shows the presence of dendritic patterns near the surface of the boule (see Fig. 6.15). These dendritic patterns are rich in Ni concentration as is evident from the EDAX analysis. The clear regions have a
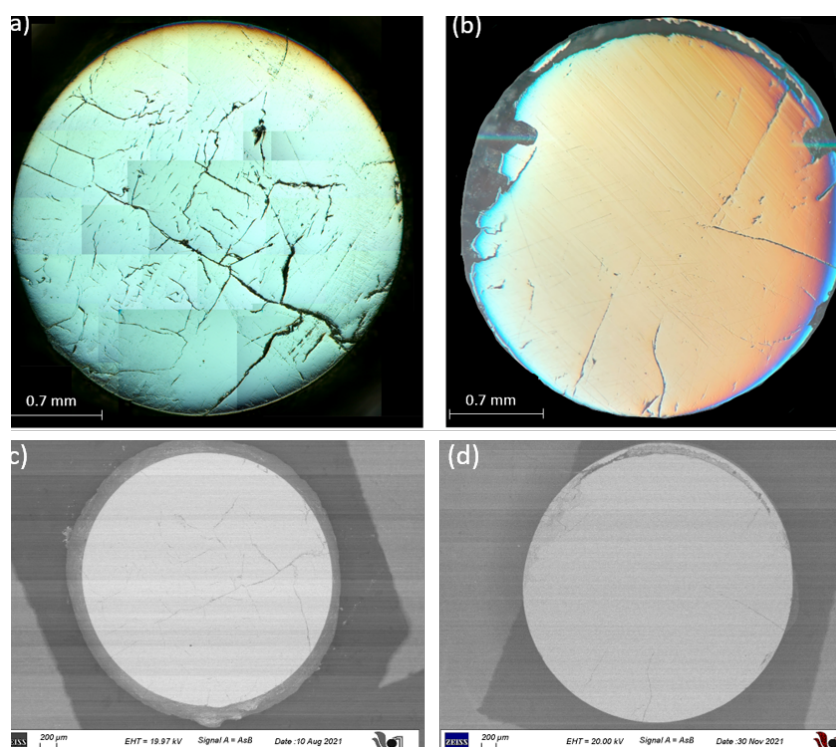
Figure 6.14: (a) and (b) show the representative optical image under polarized light of a polished section of the crystal boule of $Ca_3NiNb_2O_9$ (from growth No.7 in Table 6.1)and $Ca_3MgNb_2O_9$ (from growth No.1 in Table 6.2) respectively. (c) and (d) show the FESEM images of the polished discs of $Ca_3NiNb_2O_9$ and $Ca_3MgNb_2O_9$ respectively, taken in ASB mode, confirming sample homogeneity.

Ca (at. %)	Ni (at. %)	Nb (at. %)
51.2650	13.2035	35.5285

Ca (at. %)	Ni (at. %)	Nb (at. %)
18.3383	67.8266	13.8316
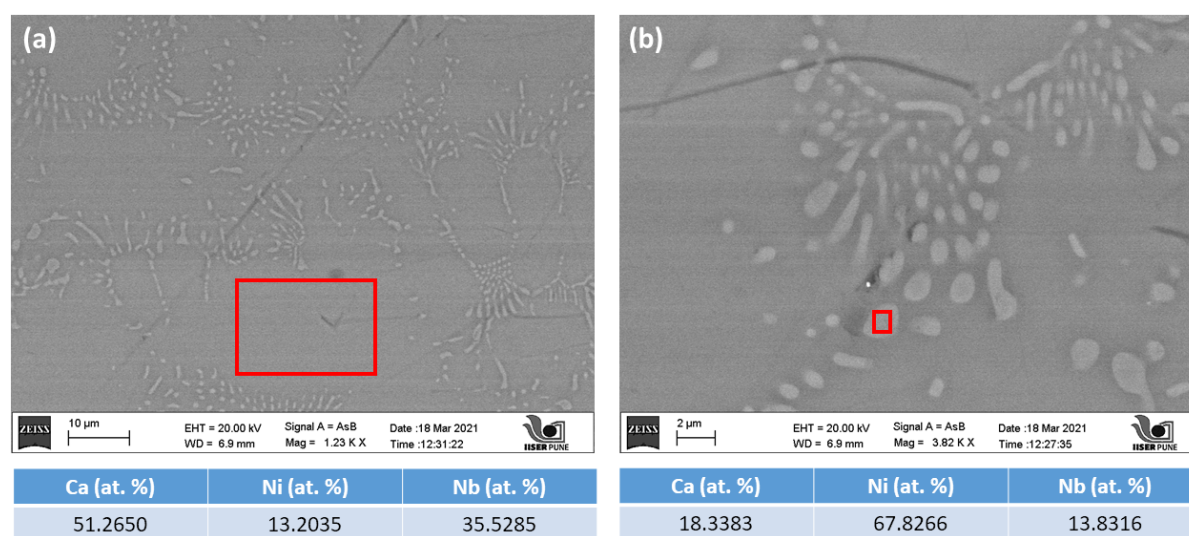
Figure 6.15: (a) shows the FESEM micrograph of a polished section of AGH (from growth No.6 in Table 6.1) in ASB mode that displays the presence of dendritic patterns near the surface of the boule. Here the elemental composition inside the red box is shown in the table below the figure. (b) shows the zoomed in view of the dendritic pattern with the red box indicating Ni rich regions.

composition that corresponds to a disordered sample of the form $Ca(Ni_{0.27}Nb_{0.73})O_3$.

6.4.4 High resolution transmission microscopy (HRTEM)

A high resolution transmission electron microscope (HRTEM) image of an AGT specimen (growth No.5 in Table 6.1) is shown in Fig. 6.16(a). The SAED pattern and the corresponding inverse fast Fourier transform (IFFT) pattern are shown, respectively, in panels (b) and (c). The Ni and Nb cations exhibit the desired 1:2 ordering along the length of the yellow box indicated in panel (c). The intensity profile along the length of the box is shown in Fig. 6.16(d). A periodic intensity modulation with 1:2 period confirms the presence of B-site ordering.
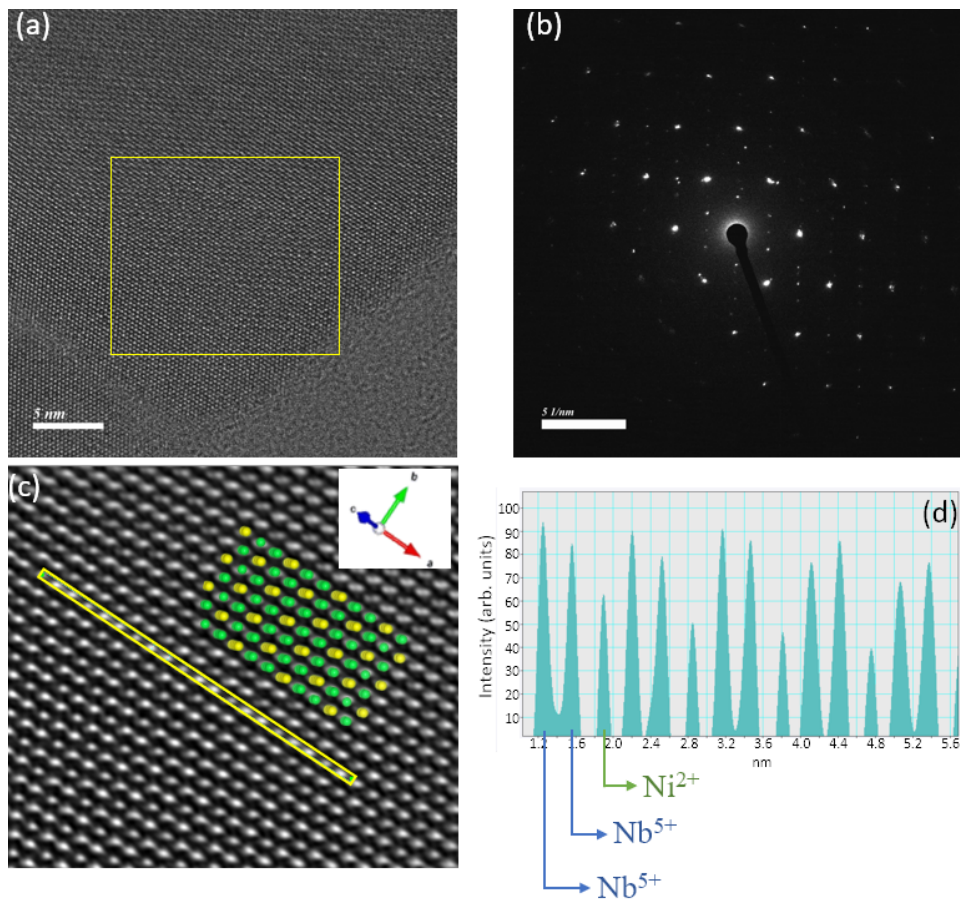
Figure 6.16: (a) to (c) show the TEM images of the AGT sample:(a) HRTEM image of a small region of a micrograin of the sample; the yellow box shows the region whose SAED pattern is shown in (b) that exhibits the diffraction spots associated with 1:2 ordering. (c) shows the IFFT pattern that clearly shows the 1:2 ordered arrangement with brighter contrast for Nb as compared to Ni; for ease of comparison, Ni atoms are shown in yellow and Nb atoms are shown in green and the orientation of the plane is marked on the top right corner of the panel (d) shows the intensity line profile of the atoms marked in the yellow box in (a).

6.5 Physical characterization

After carrying out detailed structural characterization of the various crystal specimens using XRD, SEM and HRTEM, we carried out bulk physical characterization of the samples using various thermodynamic measurements. These complementary measurement techniques served as a diagnostic tool to differentiate between the ground states of the various crystal specimens obtained during the growth process.

6.5.0.1 Specific heat

The low temperature specific heat of AGO and ANT samples is plotted as a function of temperature in Fig. 6.17(a) and Fig. 6.17(d) respectively.
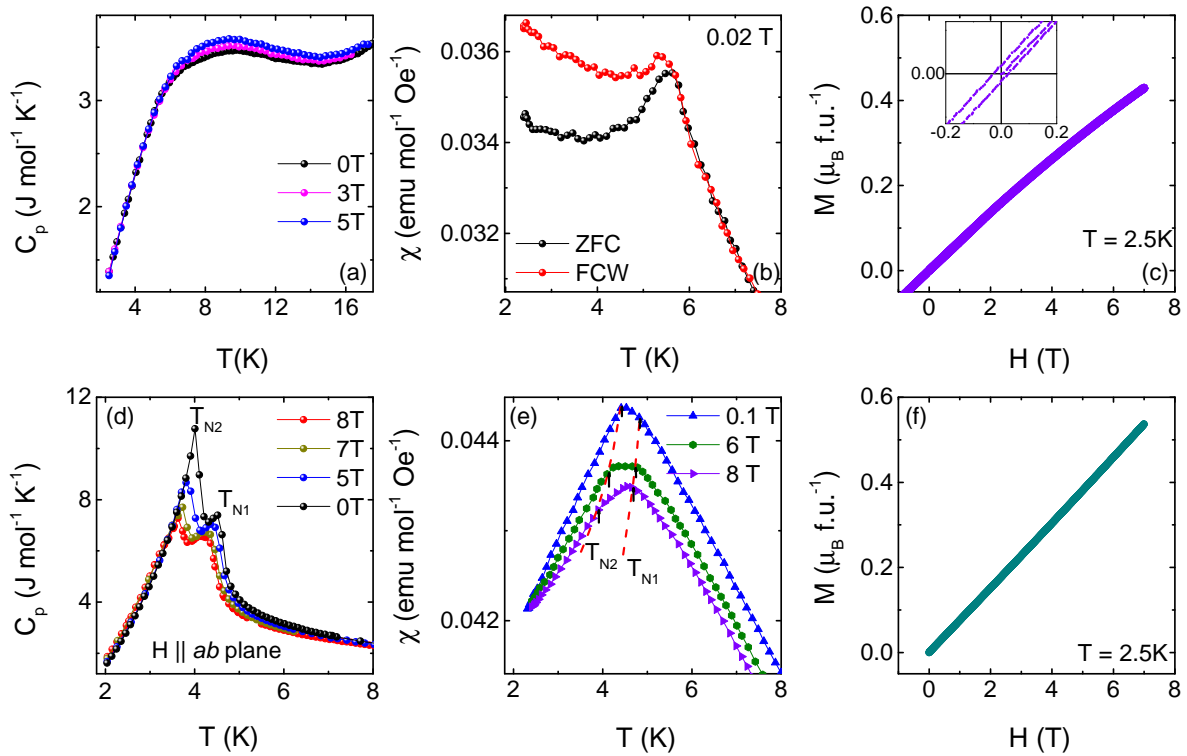
Figure 6.17: (a - c) and (d - f) show the specific heat, magnetic susceptibility and low field magnetization for the AGO and ANT samples respectively from growth 2 in Table 6.1. (a) shows the C_p vs T data at an applied field of 0, 3 and 5 T; (b) shows the magnetic susceptibility at an applied field of 0.02 T; (c) shows the magnetization as a function of field at a temperature of 2.5 K. (d) shows the C_p vs T data at an applied field of 0, 5, 7 and 8 T, applied parallel to the *ab* plane; (e) shows the susceptibility data at an applied field of 0.1, 6 and 8 T; (f) shows the M vs H behavior at a temperature of 2.5 K.

AGO - For the disordered as-grown/opaque (AGO) sample, the specific heat exhibits a broad peak centered around 9 K. Upon application of magnetic field, this peak remains rel-

atively unaffected. This feature is in stark contrast with the long-range ordering reported at 4.2 K for the polycrystalline sample by Ma *et al.* [270]. The absence of any sharp λ-type anomaly and the insensitivity of the broad peak in the heat capacity to the applied magnetic field, indicates the absence of long-range magnetic ordering. This is consistent with the fact that magnetic Ni^{2+} ions are randomly distributed over the B-site.

ANT - In the annealed specimen (ANT), C_p exhibits two successive transitions near $T_{N_2} = 4.2$ K and $T_{N_1} = 4.8$ K. These transitions are clearly resolved, which was not the case with the sintered sample where the presence of two transitions was inferred from the derivative plot [270]. Upon application of magnetic field, both transitions shift to lower temperatures, indicating an antiferromagnetic nature of the ground state. The suppression rates for the two transitions are: $dT_{N_1}/dH \approx 0.08$ K/T and $dT_{N_1}/dH \approx 0.06$ K/T for a magnetic field applied parallel to the triangular layer (see Fig. 6.18). A similar field dependence of T_{N_1} and T_{N_2} was also seen previously for some other TLAF systems [271, 282].
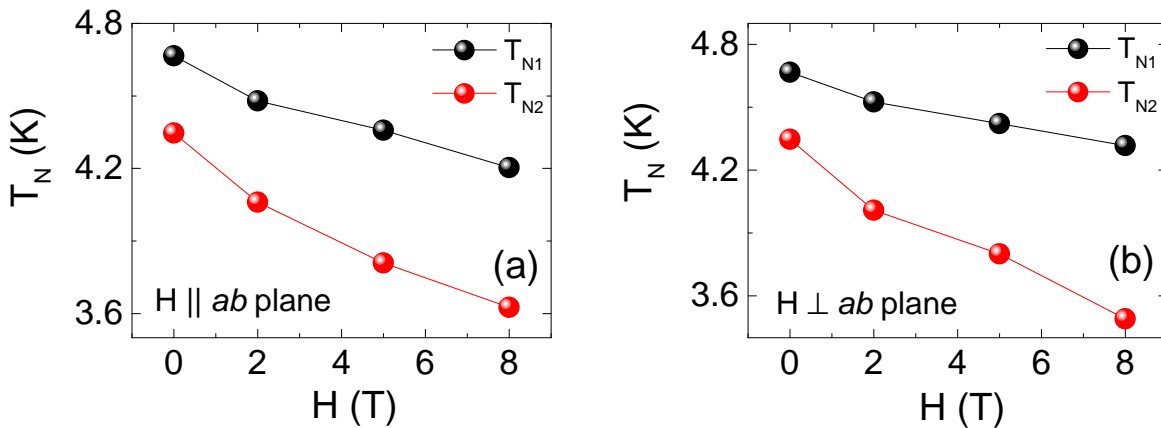
Figure 6.18: (a) and (b) show the field dependence of the transition temperatures T_{N_1} and T_{N_2} for ANT sample (growth No.2 in Table 6.1) with magnetic field applied parallel and perpendicular to the *ab* plane.

Comparison of C_p **of AGO, ANT & AGT** - A comparison of the low-temperature specific heat of AGO (from growth No.2 in Table 6.1), ANT (from growth No.2 in Table 6.1) and AGT (from growth No.5 in Table 6.1) is shown in Fig. 6.19. The AGT and ANT samples both exhibit two-step ordering expected in B-site ordered samples. The anomalies are slightly sharper in AGT as compared to ANT. A more quantitative assessment is done by estimating the magnetic contribution. Since the molecular weight of $Ca_3MgNb_2O_9$ is significantly different from that

of $Ca_3NiNb_2O_9$, we synthesized and measured the specific heat of $Ca_3ZnNb_2O_9$ (CZNO) to be used as a non-magnetic template. The magnetic contribution (in blue) is shown in Fig. 6.19.
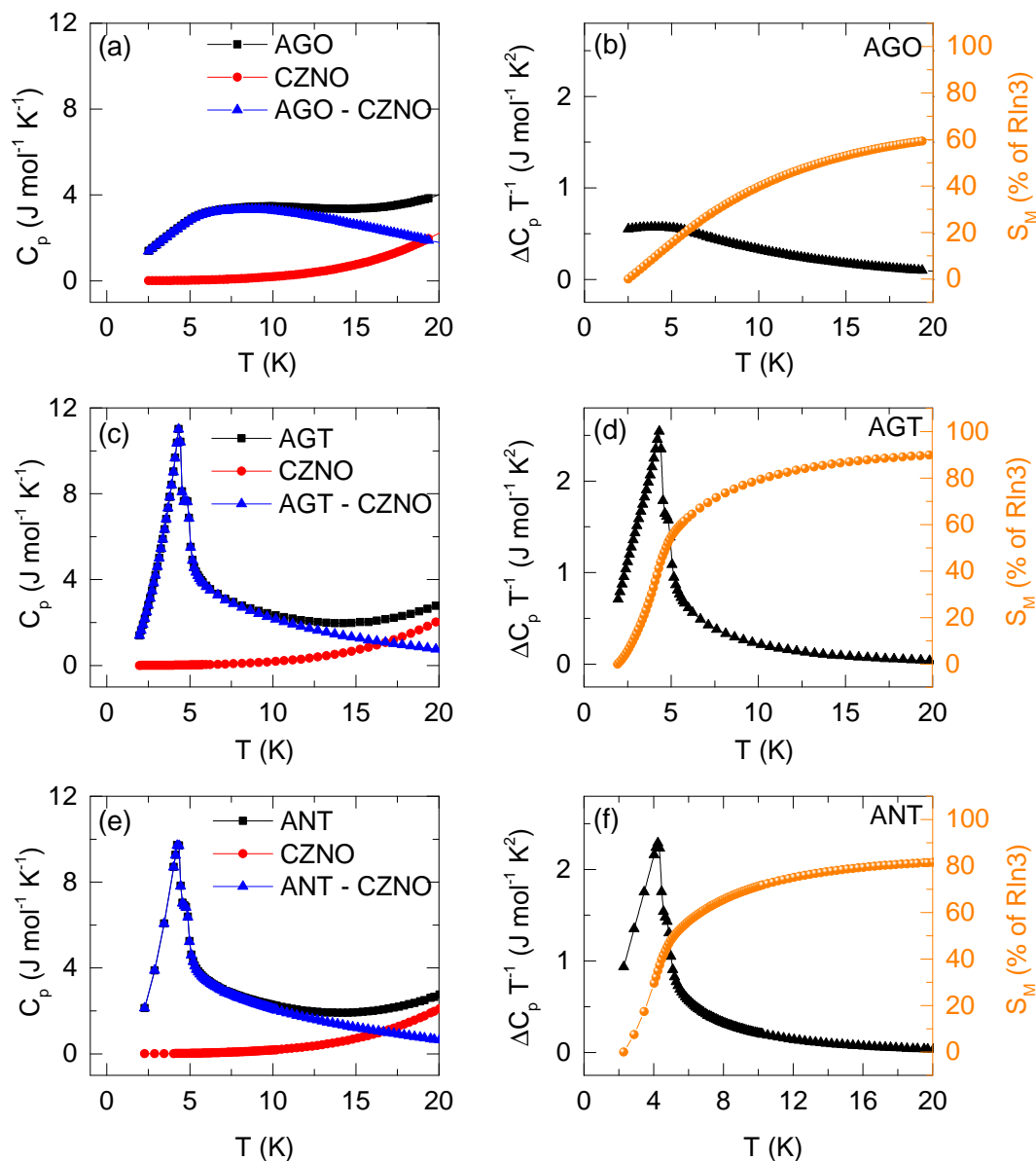
Figure 6.19: Calculation of magnetic entropy using CZNO as a non - magnetic lattice template for AGO (from growth 2 in Table 6.1), AGT (from growth 5 in Table 6.1) and ANT (from growth 2 in Table 6.1) crystal specimens. In panel (a) the y scale for CZNO was scaled by a factor of 0.9 while in panel (c) and (e), it was scaled by a factor of 0.85.

Significant deviations from the measured specific heat are seen only above 10 K suggesting that below this temperature the specific heat is primarily of magnetic origin. The magnetic entropy (S_m) is estimated by integrating C_p/T from 2 K to 20 K. Fig. 6.19(b), (d) and (f) show

S_m as a function of temperature for AGO, AGT and ANT samples, respectively. In AGO, the recovered entropy up to 20 K is only 60% of the expected value of Rln3 (9.13 J mol^{-1} K^{-1}). For this sample, $S_m(T)$ also shows an increasing behavior with no signs of saturation up to 20 K, indicating that in AGO the short-range magnetic correlations are present up to much higher temperatures. In contrast to this, in both AGT and ANT the recovered entropy over the same temperature range is close to 92% and 82%, respectively. Given that a small fraction of entropy buried below 2 K has not been accounted for, the entropy recovered is very close to 100%. The slightly less value for ANT as compared to AGT can be understood from the fact that the B-site ordering for this sample is not complete.

6.5.0.2 Magnetization

AGO - Fig. 6.17(b) show the susceptibility ($\chi(T)$) of an AGO specimen. $\chi(T)$ exhibits a sharp peak near 5.5 K. Below this peak, a ZFC-FC bifurcation is seen. The isothermal magnetization $M(H)$ at 2.5 K, on the other hand, shows nonlinearity and a minor hysteresis as shown in panel (c). The occurrence of a cusp in $\chi(T)$ along with a ZFC-FC bifurcation, a broad peak in specific heat at a temperature higher than the $\chi(T)$ cusp, and the presence of a small but finite coercive field are all tell-tale signs of a glassy ground state [283]. This is not surprising given that Ni and Nb are statistically distributed over the B-site in the CaBO$_3$-type structure of the AGO sample. However, due to a large concentration of the magnetic Ni-ions ($\approx$ 30% of the total B-site occupancy), presence of Ni agglomerates or clusters of varying sizes cannot be ruled out. The existence of polymorphism with many closely related structures in Ca(Ca$_{1/3}$Nb$_{2/3}$)O$_3$ is known from previous works [284]. Therefore, cluster of the type Ca(Ni$_{1/3}$Nb$_{2/3}$)O$_3$, Ca(Ca$_{1/3}$Nb$_{2/3}$)O$_3$, Ca$_{1-x}$Ni$_x$(Ni$_{1/3-x}$Ca$_x$Nb$_{2/3}$)O$_3$, or Ca$_{1-y}$Nb$_y$(Ni$_{1/3}$Ca$_y$Nb$_{2/3-y}$)O$_3$, etc, may co-exist and their relative proportion may vary depending on the synthesis condition. Their detailed study is outside the scope of the present work. However, in support of this hypothesis, we rather serendipitously observed that a second AGO sample from a different growth experiment (growth No.8 in Table 6.1) but with matching xrd pattern (*Pbnm*) and slightly broadened diffraction peaks shows a cusp in χ with ZFC-FC splitting below 2.5 K instead of 4.5 K (See Fig. 6.20 (b)). This suggests that in B-site disordered sample, the distribution of Ni is rather inhomogeneous.

ANT - The B-site ordered ANT sample shows a peak at 4.4 K, but with no ZFC/FC bi-
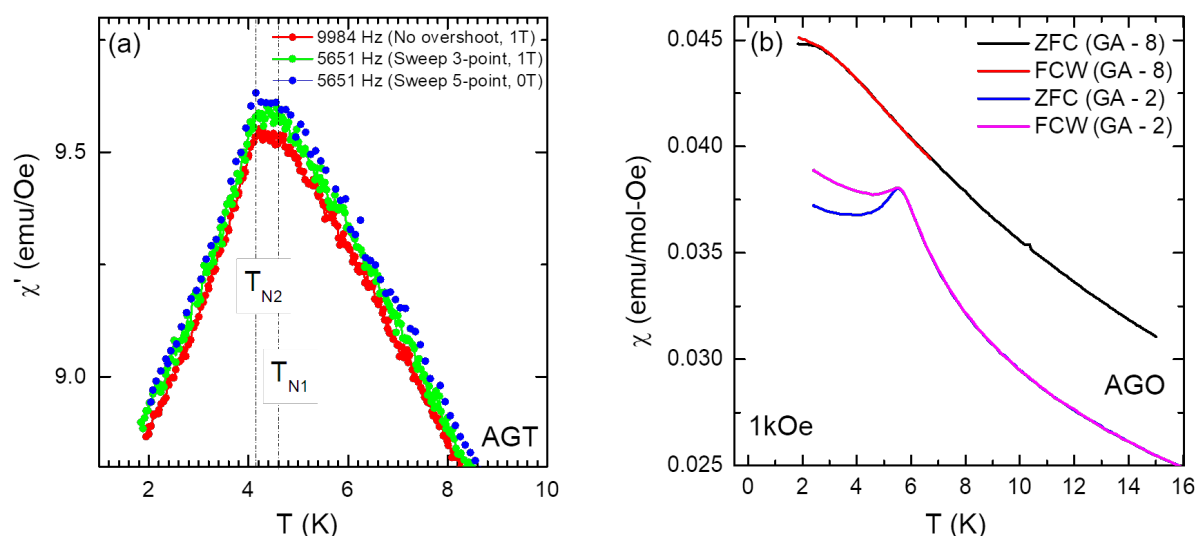
Figure 6.20: (a) AC susceptibility data for a B-site ordered AGT crystal (growth no. 5 in Table 6.1) carried out at frequencies of 5651 and 9984 Hz. At 5651 Hz, the measurements were done with and without a DC magnetic field of 1T; (b) DC magnetic susceptibility of two AGO samples from two different growth experiments are compared.

furcation down to the lowest temperature. The isothermal magnetization, $M(H)$, in this case exhibits a linear behavior, corroborating the long-range ordered antiferromagnetic ground state for the B-site ordered sample. The agreement with the published data [270] on a sintered sample is excellent with respect to the magnitude and shape of the susceptibility peak and its position on the temperature axis. The field dependence of χ is also studied and is shown in Fig. 6.17(e). It is in agreement with the field dependence of specific heat where both transitions are suppressed comparably in the presence of an increasing applied magnetic field. These features of the magnetic susceptibility of the B-site ordered $Ca_3NiNb_2O_9$ specimen corroborates the antiferromagnetic nature of the ground state. The magnetic susceptibility of AGT sample varies in the same manner as expected (see Fig. 6.21(c)). The AC susceptibility of on AGT sample measured at two different frequencies (5651 Hz and 9984 Hz) did not show any frequency dependence (see, Fig. 6.20 (a)).

Comparison of magnetic susceptibility of AGO, ANT, & AGT - For the purpose of comparing AGO, ANT and AGT samples, their susceptibilities were measured under an applied field of 1 kOe as shown in Fig. 6.21. The high-temperature susceptibility in all three cases was fitted using the modified Curie-Weiss law $\chi = \chi_0 + C/(T - \theta_p)$, where C is the Curie-constant from which the value of the effective magnetic moment (μ_{eff}) can be obtained using
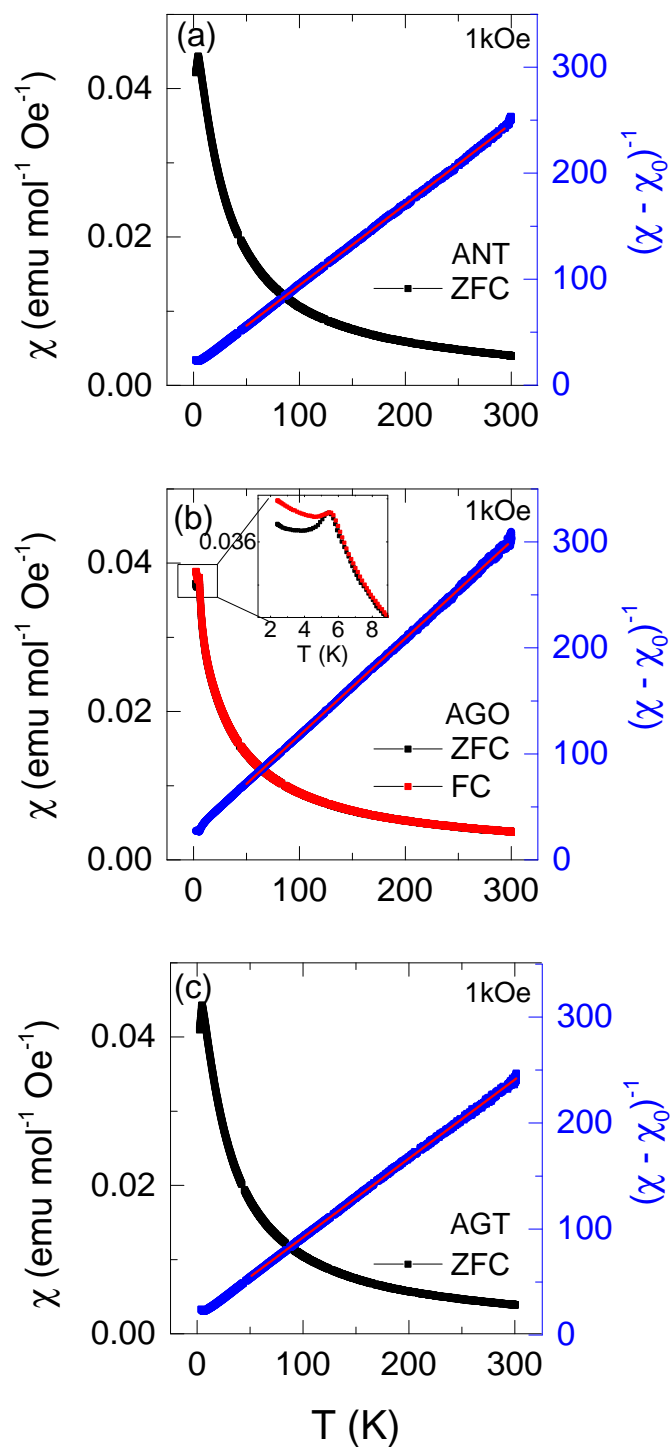
Figure 6.21: (a), (b) and (c) show the magnetic susceptibility data for ANT, AGO and AGT sample respectively, at an applied field of 1 kOe. The axes on the right panels show the inverse susceptibility free from the temperature independent susceptibility term (χ_0). The red line represents the fit to the Curie-Weiss law in the temperature range of 150 to 300 K.

$\mu_{\text{eff}} = \sqrt{8C}$, θ_p is the Weiss temperature, and χ_0 is the temperature independent contribution arising from core-diamagnetism and paramagnetic van-Vleck-like contribution from the magnetic ions. Here, we treat χ_0, C and θ_p as fitting parameters. For AGT, $1/\chi$ is almost linear down to almost 20 K. The fitting for AGT in the range from 50 K to 300 K yields a μ_{eff} value of 3.27 μ_B/Ni. This value is in close agreement with that previously reported for a sintered sample [270]. The ideal value for spin 1, taking the Landé g factor as 2 (spin only) is 2.83 μ_B. A slightly enhanced value of μ_{eff} obtained here could be an indication that the Landé g factor in $Ca_3NiNb_2O_9$ is slightly greater than 2. The sign of $\theta_p = $ -25 K is negative, which indicates antiferromagnetic correlations between Ni^{2+} spins. Given that the ordering temperature T_N is $\sim$ 5 K, the frustration index ($f = \theta_p/T_N$) of 5 is obtained, which suggests moderate to high degree of frustration. For ANT, we carried out a similar fitting procedure between 50 K and 300 K, which yielded an effective moment of $\mu_{\text{eff}} = 3.23$ μ_B/Ni and $\theta_p = $ -23 K. These values are close to that for the ANT sample.

The fitting for the AGO sample in the range 50 to 300 K yielded a μ_{eff} value of 2.95 μ_B/Ni and $\theta_p = $ -28 K. The main difference however is in the value of the temperature independent term χ_0, which is small and negative for AGT and ANT samples ($\sim -10^{-5}$ emu/mol), in agreement with the previous work on sintered samples [270], but large and positive ($\sim 10^{-4}$) for the AGO sample. The large positive value for AGO likely arises due to the presence of Ni clusters at all length scales. In the B - site disordered samples where Ni and Nb occupy the B-site randomly, there may exist regions where the Ni atoms are surrounded only by other Ni atoms forming Ni-clusters. Depending on how many Ni atoms surround a central Ni atom the cluster size may vary. The exchange coupling between these clusters is expected to be complex due to the random B-site occupancy which would result in random exchange pathways. The inter-cluster interaction is therefore expected to vary with the size and separation between these clusters in a complex manner, which in the first-order approximation can be represented by a temperature independent term in the susceptibility. Similar competing exchange interactions have also been observed in other double and triple perovskite systems [269, 285] where the B-site disorder governs whether the ground state should be ferromagnetic or antiferromagnetic.

High-field magnetization - The high-field magnetization for the ANT specimen is shown in Fig. 6.22. The measurements were carried out at T = 1.4 K and up to an applied field of 50
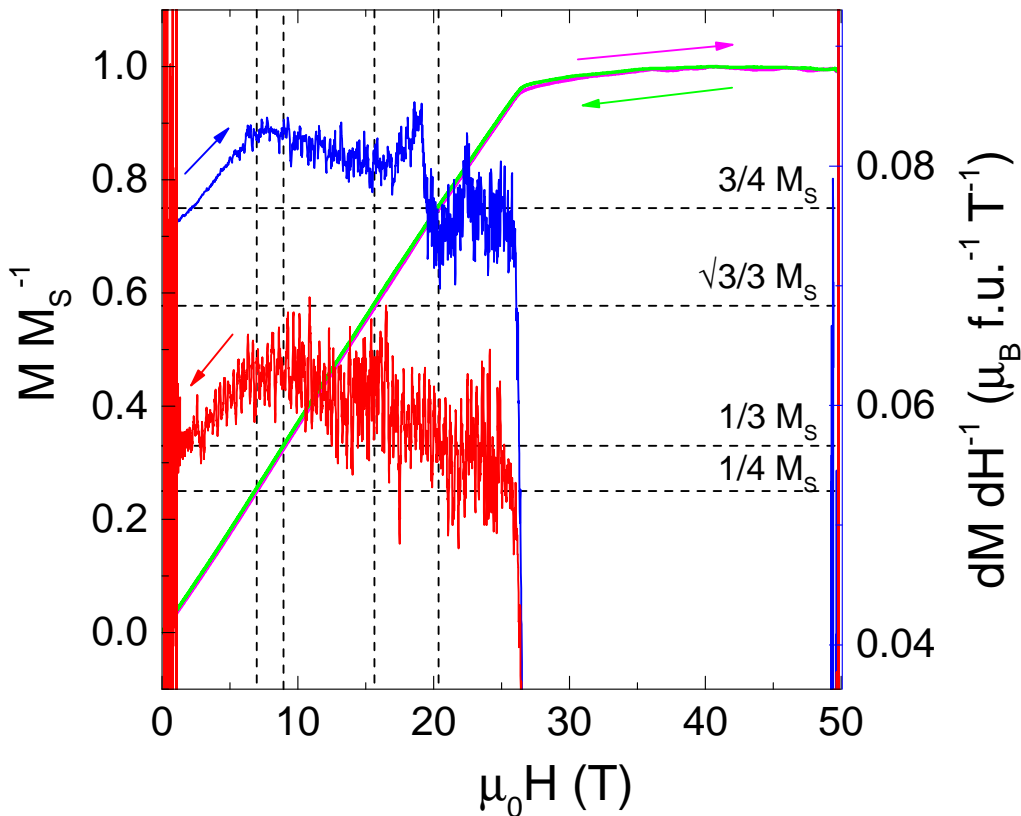
Figure 6.22: The isothermal DC-magnetization curves measured on an ANT sample at 1.5 K up to 50 T. The pink and the green curve represent the M vs. H data in the field ramp-up and ramp-down mode, respectively. The blue and the red curves show the first-order derivative (dM/dH) during the field ramp-up and ramp-down mode, respectively. Here the red curve has been shifted down by a value of $0.02\mu_B$/f.u.-T for clarity. The dotted lines mark are guide to the eye.

T. The measurements were performed in both magnetic field ramping-up and ramping-down modes. The saturation moment is close to $2.1\mu_B$/Ni^{2+}, corresponding to a g-factor value close to 2, suggesting that the Ni spins are Heisenberg-type. The saturation field is around ~ 26 T. The first order derivative plots show a clear anomaly in the form of a cusp around ~ 7 T. In the ramp-up mode the cusp appears to be closer to $M_s/4$ than to $M_s/3$, whereas in the ramp-down run it shifts more towards $M_s/3$. We cannot therefore claim with certainty that this anomaly corresponds to one-third magnetization plateau. At this juncture, it would be useful to mention that for the Kagome Heisenberg antiferromagnet (KHAF) model, the theory predicts a $1/3$ magnetization plateau for both spin $1/2$ and spin 1 systems [286]; however, experimentally, at least in one spin 1 KHAF, the magnetization plateaus appear at $1/2$ and $3/4$ of the saturation magnetization [144]. Presence of anomalies in the derivative plots above 7 T suggests the
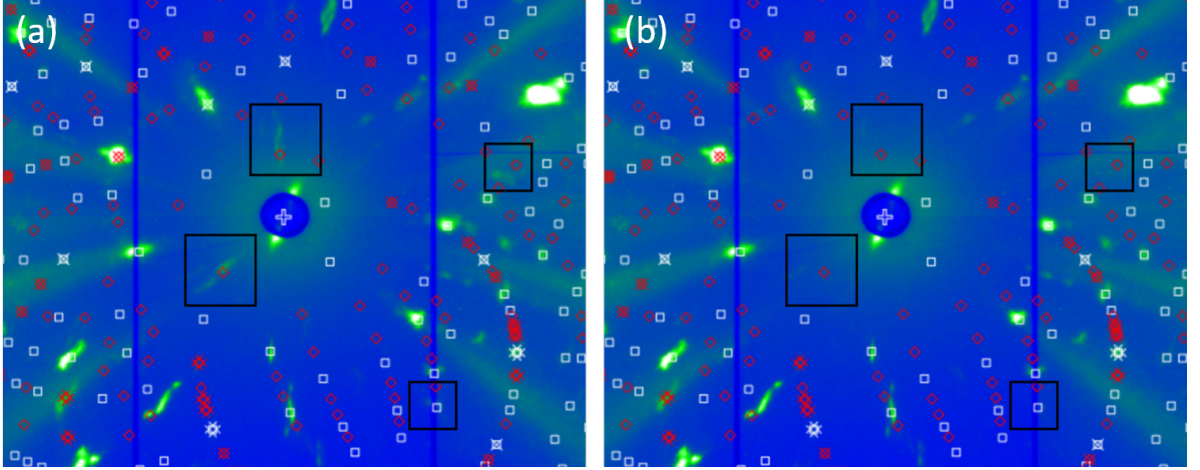
Figure 6.23: Laue diffraction patterns at $\omega = 0°$, zoomed-in at the center, at 1.5 K (left) and 10 K (right). The white boxes show the fitted nuclear peaks of the monoclinic space group $P12_1/c_1$ and the red ones show the magnetic fitting with $\vec{k} = (0.046, 0.34, 0)$. The black frames mark some of the new reflections at 1.5 K compared to 10 K.

occurrence of higher order plateaus. However, it is difficult to say with certainty whether the higher plateau is at $\sqrt{3}/3\mathrm{M}_s$ or $3/4\mathrm{M}_s$. In future, experiments at lower temperatures may help resolve the position of these plateaus more clearly. The theory for plateaus in spin 1 TLAFs (isosceles motif) also need further attention.

6.5.0.3 Neutron single-crystal diffraction

Various reciprocal lattice hkl-scans were carried out at D10 at T = 2 K for the AGT sample (from growth No.5 in Table 6.1). It was further examined by measuring Laue patterns at CY-CLOPS at T = 1.5 K and 10 K as shown in Fig. 6.23 (a) and (b) respectively. Compared to the paramagnetic phase at 10 K, new reflections appear at the base temperature T = 1.5 K, where the system is magnetically ordered. The Laue patterns could be fitted with the monoclinic space group $P12_1/c_1$ within the ESMERALDA software [287]. The magnetic fitting in ESMERALDA supports $\vec{k} \approx (0.046, 0.34, 0)$. However, the broad spots due to the crystal quality (presence of more than one grain or twin boundaries in the probed volume) does not allow us to rule out a simpler commensurate propagation vector of $\vec{k} = (0, 1/3, 0)$ (the 120° ordering), which is shown in Fig. 6.24(b). Further examination was performed by measuring different magnetic reflections based on $\vec{k} = (0.046, 0.34, 0)$ at the base temperature T = 2 K at D10. The ω-angle denoting sample rotation was scanned around the reflections, with two such representative scans shown in Fig. 6.25. As visible in the figure, these scans show

slightly different peak positions on the position-sensitive detector (± 0.05 for hkl in r.l.u.), for the above-mentioned reasons.
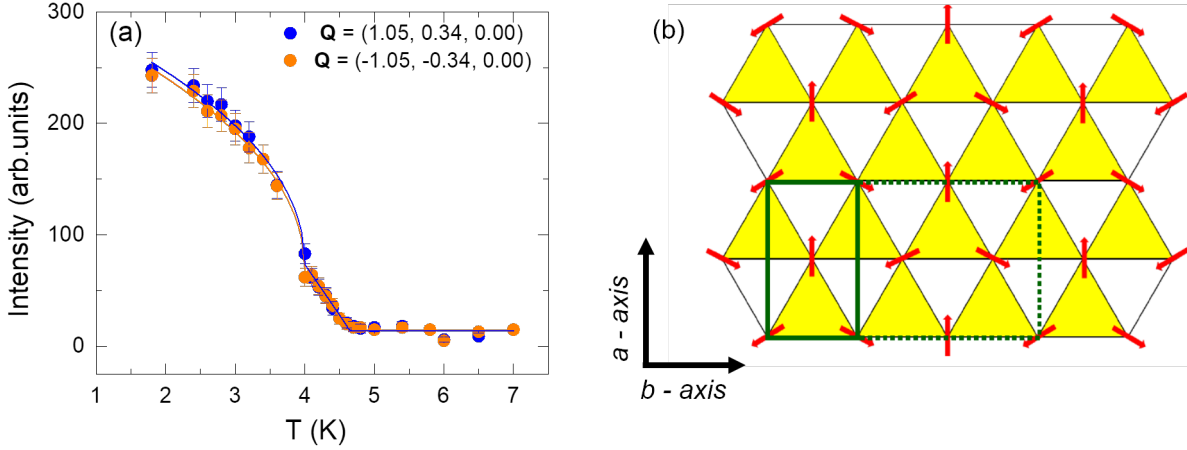
Figure 6.24: (a) Temperature-dependent scans fitted with a power law as described in Eq.6.1. The dots with the error bar show the measured data and the lines of the same color denote the corresponding fit. (b) The triangular lattice formed by Ni^{2+} ions in $Ca_3NiNb_2O_9$. This is the *ab*-plane in the structure with *a*-axis (vertical), and *b*-axis (horizontal) parallel to the sides of the unit cell shown in green. The solid lines show the nuclear unit cell, and the broken lines show the magnetic unit cell. The propagation vector $\vec{k}$ is given by $(0, 1/3, 0)$.

The temperature-dependence of the magnetic reflections based on $\vec{k} = (0.046, 0.34, 0)$ was measured at D10, which could be fitted to the power law [288] with a two-step transition:

$$
I = \begin{cases}
a_2 \left(T_{N_2} - T\right)^{2\beta_2} + a_1 \left(T_{N_1} - T_{N_2}\right)^{2\beta_1} + I_b, & T < T_{N_2} \\
a_1 \left(T_{N_1} - T\right)^{2\beta_1} + I_b, & T_{N_2} \leq T < T_{N_1} \\
I_b, & T \geq T_{N_1},
\end{cases} \tag{6.1}
$$

where a_1 and a_2 are scale prefactors, β_1 and β_2 the critical exponents, $T_{N_1} > T_{N_2}$ the transition temperatures, and I_b the background intensity. The least-square fit with this two-step transition gives a better result (χ^2) than with a single-step transition. Two representative scans are shown in Fig. 6.24(a), illustrating $T_{N_1} = 4.6(1)$ K and $T_{N_2} = 4.0(1)$ K. This agrees with the transition temperatures depicted by the measurement of specific heat and magnetic susceptibility as shown in Fig. 6.17.
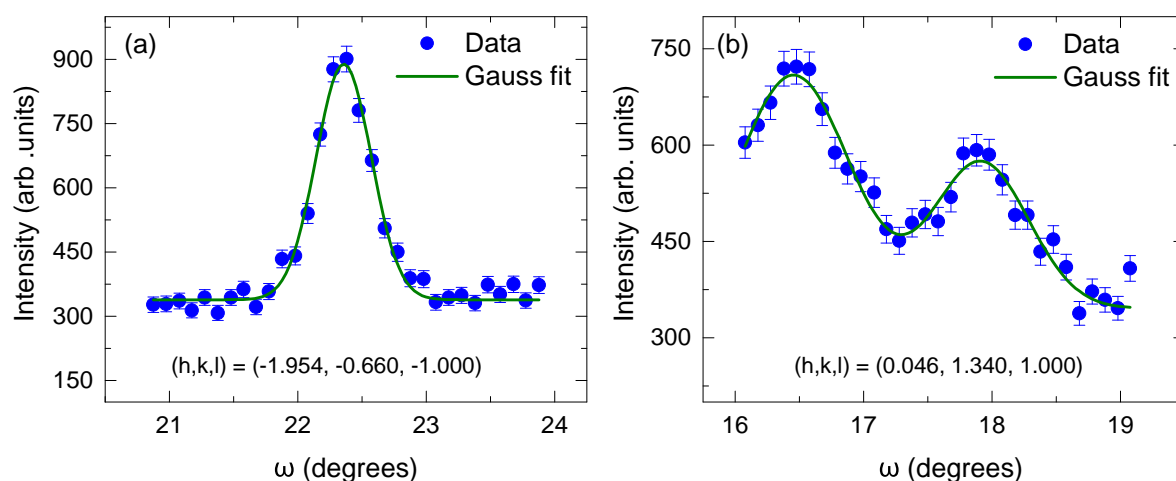
Figure 6.25: ω-scans around magnetic reflections. Fig. 6.25 (a) (no twinning visible) is fitted with one Gaussian function, whilst Fig. 6.25 (b) (with twinning) is fitted with two functions.

File	Scanned reflection			Peak intensity	Background	k-vector			Nuclear base			PSD peak		
	h	k	l			k_x	k_y	k_z	h	k	l	h	k	l
11458	1.046	0.340	-4.000	570.546	423.045	0.04	0.38	0.00	1	0	-4	1.04	0.38	-4.00
11463	0.954	-0.340	-4.000	736.940	343.784	-0.04	-0.29	0.02	1	0	-4	0.96	-0.29	-3.98
11476	-1.046	-0.340	-2.000	636.901	348.003	0.05	-0.29	-0.14	-1	0	-2	-0.95	-0.29	-2.14
11483	-0.954	0.340	-2.000	698.081	367.956	0.07	0.34	-0.03	-1	0	-2	-0.93	0.34	-2.03
11479	-1.046	-0.340	0.000	563.918	566.709	-0.02	-0.32	-0.14	-1	0	0	-1.02	-0.32	-0.14
11490	-0.954	0.340	0.000	1000.083	518.595	0.05	0.34	-0.01	-1	0	0	-0.95	0.34	-0.01
11501	-0.046	0.660	-1.000	387.317	699.203	0.00	-0.38	-0.03	0	1	-1	0.00	0.62	-1.03
11508	0.046	1.340	-1.000	465.076	392.536	0.05	0.34	0.03	0	1	-1	0.05	1.34	-0.97
11513	0.046	1.340	1.000	525.262	412.132	0.02	0.28	0.02	0	1	1	0.02	1.28	1.02
11514	-0.046	0.660	1.000	933.845	486.239	-0.02	-0.32	-0.11	0	1	1	-0.02	0.68	0.89
11455	0.954	-0.340	-2.000	943.550	498.694	-0.07	-0.31	0.01	1	0	-2	0.93	-0.31	-1.99
11464	0.046	-0.660	-1.000	976.398	466.820	0.04	0.35	-0.02	0	-1	-1	0.04	-0.65	-1.02
11467	0.046	-0.660	-3.000	329.027	406.387	0.06	0.34	-0.04	0	-1	-3	0.06	-0.66	-3.04
11477	-1.954	-0.660	-1.000	421.125	313.529	0.06	0.35	-0.09	-2	-1	-1	-1.94	-0.65	-1.09
11484	-0.046	0.660	-3.000	464.838	428.388	-0.02	-0.37	0.07	0	1	-3	-0.02	0.63	-2.93
11487	-2.954	0.340	2.000	364.142	331.927	0.05	0.35	-0.10	-3	0	2	-2.95	0.35	1.90
11491	-2.046	0.660	1.000	488.271	355.279	0.03	-0.32	-0.21	-2	1	1	-1.97	0.68	0.79
11496	-2.046	0.660	3.000	207.125	389.291	-0.05	-0.30	-0.08	-2	1	3	-2.05	0.70	2.92

Figure 6.26: Table of magnetic reflections, around which ω-scans were carried out.

6.6 Summary

We have successfully grown single crystals of the triple perovskite $Ca_3NiNb_2O_9$ and its non-magnetic analogue $Ca_3MgNb_2O_9$ using the four mirror optical float-zone furnace. In $Ca_3NiNb_2O_9$, depending on the growth conditions, the grown crystals either showed B-site 1:2 ordering of Ni and Nb ions with the ordered $Ca_3NiNb_2O_9$ structure or lacked the B-site ordering, resulting in a disordered $CaBO_3$-type structure with B-site randomly occupied by Ni and Nb. These crystals differed in their physical appearances: light-green, translucent for the B-site ordered

File	Scanned reflection			Nuclear base		
	h	k	l	h	k	l
11454	2.046	-0.660	-4.000	2	-1	-4
11456	1.046	-0.660	-2.000	1	-1	-2
11457	0.954	0.660	-4.000	1	1	-4
11459	1.046	-0.660	-3.000	1	-1	-3
11460	0.954	-1.340	-2.000	1	-1	-2
11461	0.954	-1.340	-3.000	1	-1	-3
11462	1.046	-0.660	-4.000	1	-1	-4
11465	-0.046	-1.340	-2.000	0	-1	-2
11466	0.046	-0.660	-2.000	0	-1	-2
11468	0.046	-0.660	-4.000	0	-1	-4
11469	-0.046	-0.340	-2.000	0	0	-2
11470	-0.046	-0.340	-4.000	0	0	-4
11471	-1.046	-1.340	-1.000	-1	-1	-1
11472	-0.954	-0.660	-2.000	-1	-1	-2
11473	-0.954	-0.660	-1.000	-1	-1	-1
11474	-0.954	-0.660	0.000	-1	-1	0
11475	0.046	0.340	-4.000	0	0	-4
11478	-1.954	-0.660	0.000	-2	-1	0
11480	0.046	0.340	-2.000	0	0	-2
11481	-0.046	0.660	-4.000	0	1	-4
11482	-2.046	-0.340	0.000	-2	0	0
11485	-1.046	0.660	-2.000	-1	1	-2
11486	-1.954	0.340	0.000	-2	0	0
11488	-2.046	0.660	0.000	-2	1	0
11489	-1.046	0.660	-1.000	-1	1	-1
11492	-0.046	0.660	-2.000	0	1	-2

File	Scanned reflection			Nuclear base		
	h	k	l	h	k	l
11493	-1.954	0.340	2.000	-2	0	2
11494	-1.046	0.660	0.000	-1	1	0
11495	-2.046	0.660	2.000	-2	1	2
11497	-0.954	1.340	-1.000	-1	1	-1
11498	-1.046	0.660	1.000	-1	1	1
11499	-1.954	1.340	2.000	-2	1	2
11500	-0.954	1.340	0.000	-1	1	0
11502	-1.046	0.660	2.000	-1	1	2
11503	-0.954	1.340	1.000	-1	1	1
11504	-1.046	1.660	1.000	-1	2	1
11505	0.046	1.340	-2.000	0	1	-2
11506	-0.954	1.340	2.000	-1	1	2
11507	-0.046	1.660	-1.000	0	2	-1
11509	-0.954	1.340	3.000	-1	1	3
11510	-0.046	1.660	0.000	0	2	0
11511	-0.046	1.660	1.000	0	2	1
11512	0.046	0.340	0.000	0	0	0
11515	0.046	1.340	2.000	0	1	2
11516	0.954	1.660	-1.000	1	2	-1
11517	1.046	1.340	-3.000	1	1	-3
11518	1.046	1.340	-2.000	1	1	-2
11519	1.046	1.340	-1.000	1	1	-1
11520	1.046	1.340	0.000	1	1	0
11521	1.046	1.340	1.000	1	1	1
11522	0.954	0.660	1.000	1	1	1

Figure 6.27: Table of ω-scans where no peaks were shown

crystals, and dark-green, opaque or black for the crystals lacking B-site ordering. Using synchrotron x-ray powder diffraction, the crystal structure of B-site disordered crystals is found to be orthorhombic ABO_3-type (space group $Pbnm$). On the other hand, the B-site ordered crystals consists of triangular layers of magnetic Ni-ions in the *ab*-plane of a monoclinic unit cell (space group $P12_1/c_1$). Low temperature characterization using specific heat and magnetization probes revealed contrasting magnetic ground states for the two types of crystals. The crystals lacking B-site order exhibits a glassy ground state, but the exact freezing temperature varied depending on the growth condition. On the other hand, the B-site ordered crystals undergo long-range antiferromagnetic ordering upon cooling, displaying two successive transitions in the specific heat at $T_{N_1} = 4.6$ K and $T_{N_2} = 4.2$ K. Low temperature single-crystal neutron diffraction clearly captures the magnetic transitions at T_{N_1} and T_{N_2}. The magnetic propagation vector in the ordered phase below T_{N_2} is found to be approximately $\vec{k} \sim (0, 1/3, 0)$ with a three-sublattice 120° spin structure.

Chapter 7

Summary and Outlook

The central objective of this thesis was to explore the intricate interplay between structure and property in three distinct classes of compounds. Specifically, we focused on the n = 3 members within both the Ruddlesden Popper nickelate and T' nickelate series, as well as the triangular lattice antiferromagnetic system, $Ca_3BNb_2O_9$ (B = Ni, Mg). In each of these families of low-dimensional nickelates, the magnetic Ni ion was stabilized on three unique lattice geometries, namely, octahedral, square planar, and triangular arrangements. Our research delved into the complex relationships between these different structural configurations and the resulting properties of these compounds. In the following segment, we present a summary of our findings organized by chapter, as well as potential encouraging prospects for the future.

In Chapter 4 we investigated in detail the low-temperature structural and physical properties of the trilayer nickelates $R_4Ni_3O_{10}$ (R= La, Pr, and Nd), which crystallized with a monoclinic symmetry (space group $P2_1/a, Z = 4$) and underwent a metal-to-metal transition (MMT) near T_{MMT} = 135 K (La), 156 K (Pr) and 160 K (Nd). Using high-resolution synchrotron powder x-ray diffraction technique, we not only solved the long-standing ambiguity related to the room temperature crystal structure of $La_4Ni_3O_{10}$ but also showed that the lattice parameters for all three samples exhibited an anomalous behaviour at T_{MMT}, without any sign of change in the lattice symmetry. Unambiguous signature of MMT was also observed in the magnetic and transport data, suggesting a strong coupling between the electronic, magnetic, and structural degrees of freedom. Analysis of thermal expansion yielded hydrostatic pressure dependence of MMT in close agreement with previous high-pressure experiments. From the

specific heat studies on $Pr_4Ni_3O_{10}$ and $Nd_4Ni_3O_{10}$ samples, we discovered some new anomalies associated with the rare-earth sublattice. In $Pr_4Ni_3O_{10}$, the Pr^{3+} ions located in the rocksalt (RS) layers ordered magnetically near 5 K, which was significantly suppressed compared to the Curie-Weiss temperature of $\theta_p \sim$ -36 K. In contrast, Pr^{3+} ions in the perovskite-block (PB) layers exhibited a crystal field (CF) induced nonmagnetic singlet ground state. In $Nd_4Ni_3O_{10}$, on the other hand, the CF ground state of Nd^{3+} ions in both RS and PB layers was a Kramers doublet. The heat capacity of $Nd_4Ni_3O_{10}$ showed a pronounced Schottky-like anomaly near 40 K, and a sharp upturn indicating short-range correlations between the Nd-moments below 10 K. However, no signs of long-range ordering of Nd-moments could be found down to 2 K despite a sizable value of $\theta_p \sim$ - 40K. The strongly suppressed magnetic long-range ordering in both R = Pr and Nd suggested the presence of strong magnetic frustration in these compounds. In the presence of an overwhelming Schottky contribution, the electronic term in the specific heat of $Pr_4Ni_3O_{10}$ and $Nd_4Ni_3O_{10}$ appeared highly inflated, which could be falsely interpreted as a sign of heavy fermion behaviour as was done in a recent study on $Nd_4Ni_3O_{10}$ by Li *et al.*. Accordingly, the low-temperature resistivity of these compounds was found to follow a $\sqrt{T}$ rather than a lnT dependence. With the advent of sophisticated crystal growth techniques (e.g., high-pressure floating zone technique), it should be possible to grow high-quality single crystals of these low dimensional nickelates. With the availability of large single crystals, more detailed measurements like angle-resolved photoemission spectroscopy (ARPES), Resonant Inelastic X-ray Scattering (RIXS), neutron scattering, etc can be carried out to study their similarities and dissimilarities with HTSC cuprates. The availability of single crystals will also open the avenue to probe for anisotropic properties in these nickelates.

Chapter 5 discusses the study of n = 3 members of the T' nickelate family, specifically $R_4Ni_3O_8$ compounds with R = La, Pr and Nd. The study aimed to understand the effect of chemical pressure on the concomitant charge/spin stripe ordering seen in the La compound at 105 K, and to investigate how the isovalent doping of Pr^{3+}/Nd^{3+} ion at La^{3+} site affects the MIT seen in the La sample. To begin with, the synthesis of the $R_4Ni_3O_8$ phase was highly tricky and multiple TGA experiments were carried out to realize the optimal reducing conditions to obtain the $R_4Ni_3O_8$ phase. From high-resolution low-temperature synchrotron xrd and transport measurements, we concluded that with increasing Pr/Nd content at the La site,

the MIT was suppressed to lower temperatures. No signatures of MIT were seen for the Pr series beyond 50% doping concentration. For both series, the CS stripe order was associated with a sudden drop in the c/a ratio. Future studies on single crystals of these layered materials, combined with sophisticated techniques like neutron and x-ray scattering, would help us better understand the crossover from the stripe-ordered phase to the metallic phase. Moreover, it would be worthwhile to explore the scenario of electron doping these systems, whereby they can be pushed into the superconducting dome, in analogy with the cuprate phase diagram.

In Chapter 6, we discuss the crystal growth and low-temperature properties of the triangular lattice antiferromagnet (TLAF) $Ca_3NiNb_2O_9$ and its non-magnetic analogue $Ca_3MgNb_2O_9$. The single crystals of these compounds were grown using the four-mirror optical float-zone furnace. During the growth of $Ca_3NiNb_2O_9$, the crystal boule tended to develop cracks upon cooling due to a high-temperature structural modification. Consequently, depending on the growth conditions, the crystal boules contained varying amounts of high and low-temperature modifications, present in the form of mm-sized grains distinguishable by their appearance: opaque, dark-green (AGO) and translucent, light-green (AGT) for the high and low-temperature modifications, respectively. Moreover, subjecting the as-grown AGO specimen to air annealing at 1200°C resulted in a change in its appearance from opaque to translucent green, without any noticeable change in weight. Low-temperature specific heat and low-field magnetization measurements were carried out on the AGO and AGT samples, revealing contrasting ground state properties. While AGO exhibited a spin-glass-like ground state, the AGT sample exhibited a two-step, long-range antiferromagnetic ordering of the Ni spins with transitions at $T_{N1} = 4.6$ K and $T_{N2} = 4.2$ K. Detailed structural analysis showed that AGO and AGT crystals crystallized in Pbnm (orthorhombic) and $P12_1/c_1$ (monoclinic) space groups, respectively. High-resolution TEM images confirmed the 1:2 ordering of Ni and Nb in the AGT sample. High-field magnetization up to 50 T in AGT revealed the presence of magnetization plateaus characteristic of TLAFs. The propagation vector in the ordered phase (2K) was inferred to be $\vec{k} \approx (0, 1/3, 0)$ based on magnetic neutron scattering. It would be interesting to attempt the crystal growth of these triangular lattice systems using the flux growth method. Using the flux growth method, one might be able to avoid the order-disorder transition temperature and hence prevent the structural transition happening in the crystal boule during the cooling process. The

availability of large, disorder-free single crystals would result in the possibility of solving the magnetic structure of these compounds using neutron scattering studies and having a quantitative measure of the exchange parameters. It would also be interesting to construct a H vs T phase diagram for this spin 1 system, which would add to the pre-existing knowledge of other spin 1 TLAFs and would aid in formulating a theory for the same.

Bibliography

[1] G. I. Kanel, S. V. Razorenov, K. Baumung, and J. Singer. Dynamic yield and tensile strength of aluminum single crystals at temperatures up to the melting point. *Journal of Applied Physics*, 90(1):136–143, 2001.

[2] Stephan Laube, Hans Chen, Alexander Kauffmann, Steven Schellert, Franz Müller, Bronislava Gorr, Julian Müller, Benjamin Butz, Hans-Juergen Christ, and Martin Heilmaier. Controlling crystallographic ordering in $Mo - Cr - Ti - Al$ high entropy alloys to enhance ductility. *Journal of Alloys and Compounds*, 823:153805, 2020.

[3] John E. Graebner. *Thermal Conductivity of Diamond*, pages 285–318. Springer US, Boston, MA, 1995.

[4] David G. Cahill, S. K. Watson, and R. O. Pohl. Lower limit to the thermal conductivity of disordered crystals. *Phys. Rev. B*, 46:6131–6140, Sep 1992.

[5] Catalin Chiritescu, David G. Cahill, Ngoc Nguyen, David Johnson, Arun Bodapati, Pawel Keblinski, and Paul Zschack. Ultralow thermal conductivity in disordered, layered WSe_2 crystals. *Science*, 315(5810):351–353, 2007.

[6] S. Jalili, M. Jafari, and J. Habibian. Effect of impurity on electronic properties of carbon nanotubes. *Journal of the Iranian Chemical Society*, 5(4):641–645, Dec 2008.

[7] Sergei V. Kalinin and Nicola A. Spaldin. Functional ion defects in transition metal oxides. *Science*, 341(6148):858–859, 2013.

[8] M. Veronica Ganduglia-Pirovano, Alexander Hofmann, and Joachim Sauer. Oxygen vacancies in transition metal and rare earth oxides: Current state of understanding and remaining challenges. *Surface Science Reports*, 62(6):219–270, 2007.

[9] Mark T. Greiner, Lily Chai, Michael G. Helander, Wing-Man Tang, and Zheng-Hong Lu. Transition metal oxide work functions: The influence of cation oxidation state and oxygen vacancies. *Advanced Functional Materials*, 22(21):4557–4568, 2012.

[10] Huicong Dong, Bin Wen, and Roderick Melnik. Relative importance of grain boundaries and size effects in thermal conductivity of nanocrystalline materials. *Scientific Reports*, 4(1):7037, Nov 2014.

[11] M.J. Verkerk, B.J. Middelhuis, and A.J. Burggraaf. Effect of grain boundaries on the conductivity of high-purity $ZrO_2Y_2O_3$ ceramics. *Solid State Ionics*, 6(2):159–170, 1982.

[12] Iu. I. Ukhanov. Optical properties of semiconductors. *Moscow Izdatel Nauka*, January 1977.

[13] Yanzhong Pei, Heng Wang, and G. J. Snyder. Band engineering of thermoelectric materials. *Advanced Materials*, 24(46):6125–6135, 2012.

[14] X. Obradors, L. M. Paulius, M. B. Maple, J. B. Torrance, A. I. Nazzal, J. Fontcuberta, and X. Granados. Pressure dependence of the metal-insulator transition in the charge-transfer oxides $RNiO_3$ (R = $Pr, Nd, Nd_{0.7}, La_{0.3}$). *Phys. Rev. B*, 47:12353–12356, May 1993.

[15] V. Laukhin, J. Fontcuberta, J. L. García-Muñoz, and X. Obradors. Pressure effects on the metal-insulator transition in magnetoresistive manganese perovskites. *Phys. Rev. B*, 56:R10009–R10012, Oct 1997.

[16] Bikash Padhi and Philip W. Phillips. Pressure-induced metal-insulator transition in twisted bilayer graphene. *Phys. Rev. B*, 99:205141, May 2019.

[17] L. H. Dawson. Piezoelectricity of crystal quartz. *Phys. Rev.*, 29:532–541, Apr 1927.

[18] Renee L. Bunde, Eric J. Jarvi, and Jeffrey J. Rosentreter. Piezoelectric quartz crystal biosensors. *Talanta*, 46(6):1223–1236, 1998.

[19] M. Acosta, N. Novak, V. Rojas, S. Patel, R. Vaish, J. Koruza, G. A. Rossetti, and J. Rödel. $BaTiO_3$-based piezoelectrics: Fundamentals, current status, and perspectives. *Applied Physics Reviews*, 4(4):041305, 2017.

[20] Min-Gyu Kang, Woo-Suk Jung, Chong-Yun Kang, and Seok-Jin Yoon. Recent progress on pzt based piezoelectric energy harvesting technologies. *Actuators*, 5(1), 2016.

[21] Hiroshi Kakiuchida, Edson. H. Sekiya, Noriaki Shimodaira, Kazuya Saito, and Akira. J. Ikushima. Refractive index and density changes in silica glass by halogen doping. *Journal of Non-Crystalline Solids*, 353(5):568–572, 2007. SiO2, Advanced Dielectrics and Related Devices 6.

[22] Yani Chen, Yong Sun, Jiajun Peng, Junhui Tang, Kaibo Zheng, and Ziqi Liang. 2d $Ruddlesden - Popper$ perovskites for optoelectronics. *Advanced Materials*, 30(2):1703487, 2018.

[23] Yixin Zhao and Kai Zhu. Organicâinorganic hybrid lead halide perovskites for optoelectronic and electronic applications. *Chem. Soc. Rev.*, 45:655–689, 2016.

[24] Ayesha Kausar, Irum Rafique, and Bakhtiar Muhammad. Aerospace application of polymer nanocomposite with carbon nanotube, graphite, graphene oxide, and nanoclay. *Polymer-Plastics Technology and Engineering*, 56(13):1438–1456, 2017.

[25] Colin J. Ingham, Jurjen ter Maat, and Willem M. de Vos. Where bio meets nano: The many uses for nanoporous aluminum oxide in biotechnology. *Biotechnology Advances*, 30(5):1089–1099, 2012.

[26] Ying Wang, Zhaohui Li, Jun Wang, Jinghong Li, and Yuehe Lin. Graphene and graphene oxide: biofunctionalization and applications in biotechnology. *Trends in Biotechnology*, 29(5):205–212, 2011.

[27] D.I. Khomskii and G.A. Sawatzky. Interplay between spin, charge and orbital degrees of freedom in magnetic oxides. *Solid State Communications*, 102(2):87–99, 1997. Highlights in Condensed Matter Physics and Materials Science.

[28] Shuhua Liang, Adriana Moreo, and Elbio Dagotto. Nematic state of pnictides stabilized by interplay between spin, orbital, and lattice degrees of freedom. *Phys. Rev. Lett.*, 111:047004, Jul 2013.

[29] Koushik Karmakar and Surjeet Singh. Finite-size effects in the quasi-one-dimensional quantum magnets $\mathrm{Sr_2CuO_3}$, $\mathrm{Sr_2Cu_{0.99}}M_{0.01}\mathrm{O_3}(\mathrm{M = Ni,\ Zn})$, and $\mathrm{SrCuO_2}$. *Phys. Rev. B*, 91:224401, Jun 2015.

[30] Koushik Karmakar, Rabindranath Bag, Markos Skoulatos, Christian Rüegg, and Surjeet Singh. Impurities in the weakly coupled quantum spin chains $\mathbf{Sr_2CuO_3}$ and $\mathbf{SrCuO_2}$. *Phys. Rev. B*, 95:235154, Jun 2017.

[31] Rabindranath Bag, Koushik Karmakar, Sudesh Dhar, Malvika Tripathi, R J Choudhary, and Surjeet Singh. Effect of impurities on the long-distance and $\mathrm{Zhang-Rice}$ dimers in the quantum magnet $\mathrm{Sr_{14}Cu_{24}O_{41}}$. *Journal of Physics: Condensed Matter*, 31(3):035801, Dec 2018.

[32] Kangwon Kim, Soo Yeon Lim, Jae-Ung Lee, Sungmin Lee, Tae Yun Kim, Kisoo Park, Gun Sang Jeon, Cheol-Hwan Park, Je-Geun Park, and Hyeonsik Cheong. Suppression of magnetic ordering in XXZ-type antiferromagnetic monolayer $\mathrm{NiPS_3}$. *Nature Communications*, 10(1):345, Jan 2019.

[33] Jae-Ung Lee, Sungmin Lee, Ji Hoon Ryoo, Soonmin Kang, Tae Yun Kim, Pilkwang Kim, Cheol-Hwan Park, Je-Geun Park, and Hyeonsik Cheong. Ising-type magnetic ordering in atomically thin $\mathrm{FePS_3}$. *Nano Letters*, 16(12):7433–7438, 2016. PMID: 27960508.

[34] Albert Fert, Nicolas Reyren, and Vincent Cros. Magnetic skyrmions: advances in physics and potential applications. *Nature Reviews Materials*, 2(7):17031, Jun 2017.

[35] Yoshinori Tokura and Naoya Kanazawa. Magnetic skyrmion materials. *Chemical Reviews*, 121(5):2857–2897, 2021. PMID: 33164494.

[36] U. K. Rößler, A. N. Bogdanov, and C. Pfleiderer. Spontaneous skyrmion ground states in magnetic metals. *Nature*, 442(7104):797–801, Aug 2006.

[37] C. N. R. Rao. Transition metal oxides. *Annual Review of Physical Chemistry*, 40(1):291–326, 1989.

[38] Masatoshi Imada, Atsushi Fujimori, and Yoshinori Tokura. Metal-insulator transitions. *Rev. Mod. Phys.*, 70:1039–1263, Oct 1998.

[39] D. B. McWhan and J. P. Remeika. Metal-insulator transition in $(V_{1-x}Cr_x)_2O_3$. *Phys. Rev. B*, 2:3734–3750, Nov 1970.

[40] Sang-Wook Cheong and Maxim Mostovoy. Multiferroics: a magnetic twist for ferroelectricity. *Nature Materials*, 6(1):13–20, Jan 2007.

[41] Shuai Dong, Jun-Ming Liu, Sang-Wook Cheong, and Zhifeng Ren. Multiferroic materials and magnetoelectric physics: symmetry, entanglement, excitation, and topology. *Advances in Physics*, 64(5-6):519–626, 2015.

[42] A P Ramirez. Colossal magnetoresistance. *Journal of Physics: Condensed Matter*, 9(39):8171, Sep 1997.

[43] P. FOURY and J.P. POUGET. Charge density wave transitions in two-dimensional transition metal bronzes and oxides. *International Journal of Modern Physics B*, 07(23n24):3973–4003, 1993.

[44] Schlenker, C., Hess, C., Le Touze, C., and Dumas, J. Charge density wave properties of quasi low-dimensional transition metal oxide bronzes. *J. Phys. I France*, 6(12):2061–2078, 1996.

[45] U. Staub, L. Rettig, E. M. Bothschafter, Y. W. Windsor, M. Ramakrishnan, S. R. V. Avula, J. Dreiser, C. Piamonteze, V. Scagnoli, S. Mukherjee, C. Niedermayer,

M. Medarde, and E. Pomjakushina. Interplay of Fe and Tm moments through the spin-reorientation transition in $TmFeO_3$. *Phys. Rev. B*, 96:174408, Nov 2017.

[46] S. J. Yuan, W. Ren, F. Hong, Y. B. Wang, J. C. Zhang, L. Bellaiche, S. X. Cao, and G. Cao. Spin switching and magnetization reversal in single-crystal $NdFeO_3$. *Phys. Rev. B*, 87:184405, May 2013.

[47] W. D. Wise, M. C. Boyer, Kamalesh Chatterjee, Takeshi Kondo, T. Takeuchi, H. Ikuta, Yayu Wang, and E. W. Hudson. Charge-density-wave origin of cuprate checkerboard visualized by scanning tunnelling microscopy. *Nature Physics*, 4(9):696–699, Sep 2008.

[48] E. J. W. VERWEY. Electronic conduction of magnetite (Fe_3O_4) and its transition point at low temperatures. *Nature*, 144:327–328, 1939.

[49] E.J.W. Verwey and P.W. Haayman. Electronic conductivity and transition point of magnetite (Fe_3O_4). *Physica*, 8(9):979–987, 1941.

[50] J. G. Bednorz and K. A. Müller. Possible high-Tc superconductivity in the Ba-La-Cu-O system. *Zeitschrift für Physik B Condensed Matter*, 64(2):189–193, Jun 1986.

[51] M. K. Wu, J. R. Ashburn, C. J. Torng, P. H. Hor, R. L. Meng, L. Gao, Z. J. Huang, Y. Q. Wang, and C. W. Chu. Superconductivity at 93 K in a new mixed-phase Y-Ba-Cu-O compound system at ambient pressure. *Phys. Rev. Lett.*, 58:908–910, Mar 1987.

[52] L. Gao, Y. Y. Xue, F. Chen, Q. Xiong, R. L. Meng, D. Ramirez, C. W. Chu, J. H. Eggert, and H. K. Mao. Superconductivity up to 164 K in $HgBa_2Ca_{m-1}Cu_mO_{2m+2+\delta}$ (m=1, 2, and 3) under quasihydrostatic pressures. *Phys. Rev. B*, 50:4260–4263, Aug 1994.

[53] J. H. Van Vleck. Theory of the variations in paramagnetic anisotropy among different salts of the iron group. *Phys. Rev.*, 41:208–215, Jul 1932.

[54] https: //2012books.lardbucket.org/books/principles-of-general-chemistry-v1.0/s27-05-crystal-field-theory.html.

[55] Aaron Christian. *Magnetic and Thermal Properties of Low-Dimensional Single-Crystalline Transition-Metal Antimonates and Tantalates*. PhD thesis, 04 2017.

[56] H. A. Jahn, E. Teller, and Frederick George Donnan. Stability of polyatomic molecules in degenerate electronic states - I - Orbital degeneracy. *Proceedings of the Royal Society of London. Series A - Mathematical and Physical Sciences*, 161(905):220–235, 1937.

[57] J. Hubbard and Brian Hilton Flowers. Electron correlations in narrow energy bands. *Proceedings of the Royal Society of London. Series A. Mathematical and Physical Sciences*, 276(1365):238–257, 1963.

[58] Martin C. Gutzwiller. Effect of correlation on the ferromagnetism of transition metals. *Phys. Rev.*, 134:A923–A941, May 1964.

[59] Junjiro Kanamori. Electron Correlation and Ferromagnetism of Transition Metals. *Progress of Theoretical Physics*, 30(3):275–289, 09 1963.

[60] Susumu Yamada, Toshiyuki Imamura, and Masahiko Machida. High performance lobpcg method for solving multiple eigenvalues of hubbard model: Efficiency of communication avoiding neumann expansion preconditioner. In Rio Yokota and Weigang Wu, editors, *Supercomputing Frontiers*, pages 243–256, Cham, 2018. Springer International Publishing.

[61] J. Zaanen, G. A. Sawatzky, and J. W. Allen. Band gaps and electronic structure of transition-metal compounds. *Phys. Rev. Lett.*, 55:418–421, Jul 1985.

[62] V. M. Goldschmidt. Die gesetze der krystallochemie. *Naturwissenschaften*, 14(21):477–485, May 1926.

[63] Marcel Risch. Perovskite electrocatalysts for the oxygen reduction reaction in alkaline media. *Catalysts*, 7(5), 2017.

[64] B. Frit and J.P. Mercurio. The crystal chemistry and dielectric properties of the aurivillius family of complex bismuth oxides with perovskite-like layered structures. *Journal of Alloys and Compounds*, 188:27–35, 1992.

[65] Lingling Mao, Weijun Ke, Laurent Pedesseau, Yilei Wu, Claudine Katan, Jacky Even, Michael R. Wasielewski, Constantinos C. Stoumpos, and Mercouri G. Kanatzidis. Hy-

brid Dion–Jacobson 2D lead iodide perovskites. *Journal of the American Chemical Society*, 140(10):3775–3783, Mar 2018.

[66] S. N. Ruddlesden and P. Popper. The compound $Sr_3Ti_2O_7$ and its structure. *Acta Crystallographica*, 11(1):54–55, Jan 1958.

[67] S. N. Ruddlesden and P. Popper. New compounds of the K_2NIF_4 type. *Acta Crystallographica*, 10(8):538–539, Aug 1957.

[68] Haoxiang Li, Xiaoqing Zhou, Thomas Nummy, Junjie Zhang, Victor Pardo, Warren E Pickett, J F Mitchell, and D S Dessau. Fermiology and electron dynamics of trilayer nickelate $La_4Ni_3O_{10}$. *Nature Communications*, 8(1):704, 2017.

[69] Junjie Zhang, A S Botana, J W Freeland, D Phelan, Hong Zheng, V Pardo, M R Norman, and J F Mitchell. Large orbital polarization in a metallic square-planar nickelate. *Nature Physics*, (June), 2017.

[70] S. N. Ruddlesden and P. Popper. The compound $Sr_3Ti_2O_7$ and its structure. *Acta Crystallographica*, 11(1):54–55, Jan 1958.

[71] Martha Greenblatt. Ruddlesden-popper $Ln_{n+1}Ni_nO_{3n+1}$ nickelates: structure and properties. *Current Opinion in Solid State and Materials Science*, 2(2):174 – 183, 1997.

[72] J.M. Bassat, F. Gervais, P. Odier, and J.P. Loup. Anisotropic transport properties of La_2NiO_4 single crystals. *Materials Science and Engineering: B*, 3(4):507–514, 1989.

[73] Shangxiong Huangfu, Gawryluk Dariusz Jakub, Xiaofu Zhang, Olivier Blacque, Pascal Puphal, Ekaterina Pomjakushina, Fabian O. von Rohr, and Andreas Schilling. Anisotropic character of the metal-to-metal transition in $Pr_4Ni_3o_{10}$. *Phys. Rev. B*, 101:104104, Mar 2020.

[74] Qing Li, Cheng Ping He, XiYu Zhu, Jin Si, XinWei Fan, and Hai-Hu Wen. Contrasting physical properties of the trilayer nickelates $Nd_4Ni_3O_{10}$ and $Nd_4Ni_3O_8$. *Science China Physics, Mechanics & Astronomy*, 64(2):227411, Dec 2020.

[75] Z. Zhang and M. Greenblatt. Synthesis, structure, and properties of $Ln_4Ni_3O_{10-\delta}$ (Ln = La, Pr, and Nd). *Journal of Solid State Chemistry*, 117(2):236 – 246, 1995.

[76] Z. Zhang, M. Greenblatt, and J.B. Goodenough. Synthesis, structure, and properties of the layered perovskite $La_3Ni_2O_{7-\delta}$. *Journal of Solid State Chemistry*, 108(2):402 – 409, 1994.

[77] Ph. Lacorre. Passage from t-type to t'-type arrangement by reducing $R_4Ni_3O_{10}$ to $R_4Ni_3O_8$ (R = La, Pr, Nd). *Journal of Solid State Chemistry*, 97(2):495–500, 1992.

[78] Colin K. Blakely, Shaun R. Bruno, and Viktor V. Poltavets. Low-temperature solvothermal approach to the synthesis of $La_4Ni_3O_8$ by topotactic oxygen deintercalation. *Inorganic Chemistry*, 50(14):6696–6700, 2011. PMID: 21696134.

[79] M. Crespin, O. Isnard, F. Dubois, J. Choisnet, and P. Odier. Lanio2: Synthesis and structural characterization. *Journal of Solid State Chemistry*, 178(4):1326–1334, 2005.

[80] https : //www.aps.org/publications/apsnews/updates/woodstock.cfm.

[81] Pia Jensen Ray. Master's thesis: Structural investigation of $La_{2-x}Sr_xCuO_{4+y}$ - Following staging as a function of temperature. 2 2016.

[82] V. I. Anisimov, D. Bukhvalov, and T. M. Rice. Electronic structure of possible nickelate analogs to the cuprates. *Phys. Rev. B*, 59:7901–7906, Mar 1999.

[83] K.-W. Lee and W. E. Pickett. Infinite-layer $LaNiO_2$: Ni^{1+} is not Cu^{2+}. *Phys. Rev. B*, 70:165109, Oct 2004.

[84] Danfeng Li, Kyuho Lee, Bai Yang Wang, Motoki Osada, Samuel Crossley, Hye Ryoung Lee, Yi Cui, Yasuyuki Hikita, and Harold Y Hwang. Superconductivity in an infinite-layer nickelate. *Nature Letter*, pages 7–11, 2019.

[85] Motoki Osada, Bai Yang Wang, Berit H. Goodge, Kyuho Lee, Hyeok Yoon, Keita Sakuma, Danfeng Li, Masashi Miura, Lena F. Kourkoutis, and Harold Y. Hwang. A superconducting praseodymium nickelate with infinite layer structure. *Nano Letters*, 20(8):5735–5740, Aug 2020.

[86] Shengwei Zeng, Changjian Li, Lin Er Chow, Yu Cao, Zhaoting Zhang, Chi Sin Tang, Xinmao Yin, Zhi Shiuh Lim, Junxiong Hu, Ping Yang, and Ariando Ariando. Superconductivity in infinite-layer nickelate $La_{1-x}Ca_xNiO_2$ thin films. *Science Advances*, 8(7):eabl9927, 2022.

[87] Grace A. Pan, Dan Ferenc Segedin, Harrison LaBollita, Qi Song, Emilian M. Nica, Berit H. Goodge, Andrew T. Pierce, Spencer Doyle, Steve Novakov, Denisse Córdova Carrizales, Alpha T. N'Diaye, Padraic Shafer, Hanjong Paik, John T. Heron, Jarad A. Mason, Amir Yacoby, Lena F. Kourkoutis, Onur Erten, Charles M. Brooks, Antia S. Botana, and Julia A. Mundy. Superconductivity in a quintuple-layer square-planar nickelate. *Nature Materials*, 21(2):160–164, Feb 2022.

[88] Antia S. Botana, Kwan-Woo Lee, Michael R. Norman, Victor Pardo, and Warren E. Pickett. Low valence nickelates: Launching the nickel age of superconductivity. *Frontiers in Physics*, 9, 2022.

[89] Junjie Zhang, A. S. Botana, J. W. Freeland, D. Phelan, Hong Zheng, V. Pardo, M. R. Norman, and J. F. Mitchell. Large orbital polarization in a metallic square-planar nickelate. *Nature Physics*, 13(9):864–869, Sep 2017.

[90] Antia S. Botana, Victor Pardo, and Michael R. Norman. Electron doped layered nickelates: Spanning the phase diagram of the cuprates. *Phys. Rev. Materials*, 1:021801, Jul 2017.

[91] Qing Li, Cheng Ping He, Jin Si, Xiyu Zhu, Yue Zhang, and Hai-Hu Wen. Absence of superconductivity in bulk $Nd_{1-x}Sr_xNiO_2$. *Communications Materials*, 1(1):16, Apr 2020.

[92] Antia S. Botana, Kwan-Woo Lee, Michael R. Norman, Victor Pardo, and Warren E. Pickett. Low valence nickelates: Launching the nickel age of superconductivity. *Frontiers in Physics*, 9, 2022.

[93] Warren E. Pickett. Author correction: The dawn of the nickel age of superconductivity. *Nature Reviews Physics*, 3(1):64–64, Jan 2021.

[94] Emilian M. Nica, Jyoti Krishna, Rong Yu, Qimiao Si, Antia S. Botana, and Onur Erten. Theoretical investigation of superconductivity in trilayer square-planar nickelates. *Phys. Rev. B*, 102:020504, Jul 2020.

[95] Y. Shen, J. Sears, G. Fabbris, J. Li, J. Pelliciari, I. Jarrige, Xi He, I. Božović, M. Mitrano, Junjie Zhang, J. F. Mitchell, A. S. Botana, V. Bisogni, M. R. Norman, S. Johnston, and M. P. M. Dean. Role of oxygen states in the low valence nickelate $La_4Ni_3O_8$. *Phys. Rev. X*, 12:011055, Mar 2022.

[96] M. P. Singh, K. D. Truong, S. Jandl, and P. Fournier. Stabilization and functional properties of $La_3NiAlMnO_9$ and $La_3CoAlMnO_9$ magnetoelectric triple perovskites. *Applied Physics Letters*, 94(17):171908, 2009.

[97] Q. Huang, M. Lee, E. S. Choi, J. Ma, C. Dela Cruz, and H. D. Zhou. Successive phase transitions and multiferroicity in deformed triangular-lattice antiferromagnets $Ca_3MNb_2O_9$ (M=Co, Ni) with spatial anisotropy. *ECS Journal of Solid State Science and Technology*, 11(6):063004, jun 2022.

[98] J. Hwang, E. S. Choi, F. Ye, C. R. Dela Cruz, Y. Xin, H. D. Zhou, and P. Schlottmann. Successive magnetic phase transitions and multiferroicity in the spin-one triangular-lattice antiferromagnet $Ba_3NiNb_2O_9$. *Phys. Rev. Lett.*, 109:257205, Dec 2012.

[99] B. Xu, W. F. Zhang, X.-Y. Liu, J. H. Ye, W. H. Zhang, L. Shi, X. G. Wan, J. Yin, and Z. G. Liu. Photophysical properties and electronic structures of the perovskite photocatalysts $Ba_3NiM_2O_9$ (M = Nb, Ta). *Phys. Rev. B*, 76:125109, Sep 2007.

[100] Meganathan Thirumal, Isuhak N. Jawahar, Kuzhichalil P. Surendiran, Pezholil Mohanan, and Ashok K. Ganguli. Synthesis and microwave dielectric properties of $Sr_3Zn_{1-x}Mg_xNb_2O_9$ phases. *Materials Research Bulletin*, 37(1):185–191, 2002.

[101] Jitender Kumar, Kaustav Dey, Soumendra Nath Panja, and Sunil Nair. Anomalous dielectric response in the triple perovskite ruthenate $Ba_3BiRu_2O_9$. *Journal of Physics: Condensed Matter*, 34(46):465401, Sep 2022.

[102] Guillaume F. Nataf, Qian Li, Yun Liu, Ray L. Withers, Sarah L. Driver, and Michael A. Carpenter. Ferroelastic aspects of relaxor ferroelectric behaviour in $Pb(In_{1/2}Nb_{1/2})O_3 - Pb(Mg_{1/3}Nb_{2/3})O_3 - PbTiO_3$ perovskite. *Journal of Applied Physics*, 113(12):124102, 2013.

[103] Job T. Rijssenbeek, Sylvie Malo, Vincent Caignaert, and Kenneth R. Poeppelmeier. Site and oxidation-state specificity yielding dimensional control in perovskite ruthenates. *Journal of the American Chemical Society*, 124(10):2090–2091, Mar 2002.

[104] G. Blasse. New compounds with perovskite-like structures. *Journal of Inorganic and Nuclear Chemistry*, 27(5):993–1003, 1965.

[105] S. Kundu, Aga Shahee, Atasi Chakraborty, K. M. Ranjith, B. Koo, Jörg Sichelschmidt, Mark T. F. Telling, P. K. Biswas, M. Baenitz, I. Dasgupta, Sumiran Pujari, and A. V. Mahajan. Gapless quantum spin liquid in the triangular system $Sr_3CuSb_2O_9$. *Phys. Rev. Lett.*, 125:267202, Dec 2020.

[106] V. Ting, Y. Liu, R.L. Withers, and L. Norén. An electron diffraction and bond valence sum study of the space group symmetries and structures of the photocatalytic 1:2 B site ordered $A_3CoNb_2O_9$ perovskites (A=Ca^{2+}, Sr^{2+}, Ba^{2+}). *Journal of Solid State Chemistry*, 177(7):2295–2304, 2004.

[107] A. Y. Borisevich and P. K. Davies. $La(Li_{1/3}Ti_{2/3})O_3$: a new 1:2 ordered perovskite. *Journal of Solid State Chemistry*, 170(1):198–201, 2003. INORGANIC, ORGANIC, PHYSICAL AND ANALYTICAL CHEMISTRY.

[108] Francis Galasso and Jane Pyle. Ordering in compounds of the $A(B'_{0.33}Ta_{0.67})O_3$ type. *Inorganic Chemistry*, 2(3):482–484, 1963.

[109] Francis. Galasso and Jane. Pyle. Preparation and study of ordering in $A(B_{0.33}Nb_{0.67})O_3$ perovskite-type compounds. *The Journal of Physical Chemistry*, 67(7):1561–1562, Jul 1963.

[110] S. Janaswamy, G. S. Murthy, E. D. Dias, and V. R. K. Murthy. Ordering in $BaMg_{1/3}Ta_{1/3}Nb_{1/3}O_3$ ceramics: An x-ray rietveld analysis. *Crystallography Reports*, 51(2):231–235, Mar 2006.

[111] J Vannimenus and G Toulouse. Theory of the frustration effect. ii. ising spins on a square lattice. *Journal of Physics C: Solid State Physics*, 10(18):L537, Sep 1977.

[112] A P Ramirez. Strongly geometrically frustrated magnets. *Annual Review of Materials Science*, 24(1):453–480, 1994.

[113] Lucile Savary and Leon Balents. Quantum spin liquids: a review. *Reports on Progress in Physics*, 80(1):016502, Nov 2016.

[114] C. Castelnovo, R. Moessner, and S.L. Sondhi. Spin ice, fractionalization, and topological order. *Annual Review of Condensed Matter Physics*, 3(1):35–55, 2012.

[115] C.Y. Huang. Some experimental aspects of spin glasses: A review. *Journal of Magnetism and Magnetic Materials*, 51(1):1–74, 1985.

[116] P. Fazekas and P. W. Anderson. On the ground state properties of the anisotropic triangular antiferromagnet. *The Philosophical Magazine: A Journal of Theoretical Experimental and Applied Physics*, 30(2):423–440, 1974.

[117] P. W. Anderson. The resonating valence bond state in La_2CuO_4 and superconductivity. *Science*, 235(4793):1196–1198, 1987.

[118] T. Dombre and N. Read. Absence of the hopf invariant in the long-wavelength action of two-dimensional quantum antiferromagnets. *Phys. Rev. B*, 38:7181–7183, Oct 1988.

[119] Yutaka Shirata, Hidekazu Tanaka, Toshio Ono, Akira Matsuo, Koichi Kindo, and Hiroki Nakano. Quantum magnetization plateau in spin-1 triangular-lattice antiferromagnet ba3nisb2o9. *Journal of the Physical Society of Japan*, 80(9):093702, 2011.

[120] T. Ono, H. Tanaka, H. Aruga Katori, F. Ishikawa, H. Mitamura, and T. Goto. Magnetization plateau in the frustrated quantum spin system Cs_2CuBr_4. *Phys. Rev. B*, 67:104431, Mar 2003.

[121] P.W. Anderson. Resonating valence bonds: A new kind of insulator? *Materials Research Bulletin*, 8(2):153–160, 1973.

[122] Leon Balents. Spin liquids in frustrated magnets. *Nature*, 464(7286):199–208, March 2010.

[123] M. Lee, J. Hwang, E. S. Choi, J. Ma, C. R. Dela Cruz, M. Zhu, X. Ke, Z. L. Dun, and H. D. Zhou. Series of phase transitions and multiferroicity in the quasi-two-dimensional spin-$\frac{1}{2}$ triangular-lattice antiferromagnet $Ba_3CoNb_2O_9$. *Phys. Rev. B*, 89:104420, Mar 2014.

[124] Takuya Susuki, Nobuyuki Kurita, Takuya Tanaka, Hiroyuki Nojiri, Akira Matsuo, Koichi Kindo, and Hidekazu Tanaka. Magnetization process and collective excitations in the $s=1/2$ triangular-lattice heisenberg antiferromagnet $Ba_3CoSb_2O_9$. *Phys. Rev. Lett.*, 110:267201, Jun 2013.

[125] Yutaka Shirata, Hidekazu Tanaka, Akira Matsuo, and Koichi Kindo. Experimental realization of a spin-1/2 triangular-lattice heisenberg antiferromagnet. *Phys. Rev. Lett.*, 108:057205, Jan 2012.

[126] J. G. Cheng, G. Li, L. Balicas, J. S. Zhou, J. B. Goodenough, Cenke Xu, and H. D. Zhou. High-pressure sequence of $Ba_3NiSb_2O_9$ structural phases: New $s = 1$ quantum spin liquids based on Ni^{2+}. *Phys. Rev. Lett.*, 107:197204, Nov 2011.

[127] Jason Alicea, Andrey V. Chubukov, and Oleg A. Starykh. Quantum stabilization of the 1/3-magnetization plateau in Cs_2CuBr_4. *Phys. Rev. Lett.*, 102:137201, Mar 2009.

[128] S. Miyahara, K. Ogino, and N. Furukawa. Magnetization plateaux of Cs_2CuBr_4. *Physica B: Condensed Matter*, 378-380:587–588, 2006. Proceedings of the International Conference on Strongly Correlated Electron Systems.

[129] Mitchell M. Bordelon, Eric Kenney, Chunxiao Liu, Tom Hogan, Lorenzo Posthuma, Marzieh Kavand, Yuanqi Lyu, Mark Sherwin, N. P. Butch, Craig Brown, M. J. Graf, Leon Balents, and Stephen D. Wilson. Field-tunable quantum disordered ground state

in the triangular-lattice antiferromagnet $NaYbO_2$. *Nature Physics*, 15(10):1058–1064, Oct 2019.

[130] N. A. Fortune, Q. Huang, T. Hong, J. Ma, E. S. Choi, S. T. Hannahs, Z. Y. Zhao, X. F. Sun, Y. Takano, and H. D. Zhou. Evolution of magnetic field induced ordering in the layered quantum heisenberg triangular-lattice antiferromagnet $Ba_3CoSb_2O_9$. *Phys. Rev. B*, 103:184425, May 2021.

[131] K M Ranjith, K Brinda, U Arjun, N G Hegde, and R Nath. Double phase transition in the triangular antiferromagnet $Ba_3CoTa_2O_9$. *Journal of Physics: Condensed Matter*, 29(11):115804, feb 2017.

[132] H. D. Zhou, E. S. Choi, G. Li, L. Balicas, C. R. Wiebe, Y. Qiu, J. R. D. Copley, and J. S. Gardner. Spin liquid state in the $s = 1/2$ triangular lattice $Ba_3CuSb_2O_9$. *Phys. Rev. Lett.*, 106:147204, Apr 2011.

[133] Siddharth Kumar, S. K. Panda, Manju Mishra Patidar, Shashank Kumar Ojha, Prithwijit Mandal, Gangadhar Das, J. W. Freeland, V. Ganesan, Peter J. Baker, and S. Middey. Spin-liquid behavior of the three-dimensional magnetic system $Ba_3NiIr_2O_9$ with $s = 1$. *Phys. Rev. B*, 103:184405, May 2021.

[134] A V Chubukov and D I Golosov. Quantum theory of an antiferromagnet on a triangular lattice in a magnetic field. *Journal of Physics: Condensed Matter*, 3(1):69–82, jan 1991.

[135] M. E. Zhitomirsky, A. Honecker, and O. A. Petrenko. Field induced ordering in highly frustrated antiferromagnets. *Phys. Rev. Lett.*, 85:3269–3272, Oct 2000.

[136] Kazuo Hida and Ian Affleck. Quantum vs classical magnetization plateaus of s=1/2 frustrated Heisenberg chains. *Journal of the Physical Society of Japan*, 74(6):1849–1857, 2005.

[137] Mengxing Ye and Andrey V. Chubukov. Half-magnetization plateau in a heisenberg antiferromagnet on a triangular lattice. *Phys. Rev. B*, 96:140406, Oct 2017.

[138] A V Chubukov and D I Golosov. Quantum theory of an antiferromagnet on a triangular lattice in a magnetic field. *Journal of Physics: Condensed Matter*, 3(1):69, Jan 1991.

[139] D. C. Cabra, A. Honecker, and P. Pujol. Magnetization curves of antiferromagnetic Heisenberg spin-$\frac{1}{2}$ ladders. *Phys. Rev. Lett.*, 79:5126–5129, Dec 1997.

[140] Masaki Oshikawa, Masanori Yamanaka, and Ian Affleck. Magnetization plateaus in spin chains: "haldane gap" for half-integer spins. *Phys. Rev. Lett.*, 78:1984–1987, Mar 1997.

[141] Keisuke Totsuka. Magnetization plateau in the $s = \frac{1}{2}$ heinsenberg spin chain with next-nearest-neighbor and alternating nearest-neighbor interactions. *Phys. Rev. B*, 57:3454–3465, Feb 1998.

[142] Mila, F. Ladders in a magnetic field: a strong coupling approach. *Eur. Phys. J. B*, 6(2):201–205, 1998.

[143] Shintaro Ishiwata, Dan Wang, Takashi Saito, and Mikio Takano. High-pressure synthesis and structure of $SrCo_6O_{11}$: Pillared Kagomé lattice system with a 1/3 magnetization plateau. *Chemistry of Materials*, 17(11):2789–2791, 2005.

[144] Taku Matsushita, Nobuko Hamaguchi, Kengo Shimizu, Nobuo Wada, Wataru Fujita, Kunio Awaga, Akira Yamaguchi, and Hidehiko Ishimoto. Quantum spin state and magnetization plateaus in an s=1 kagomé Heisenberg antiferromagnet. *Journal of the Physical Society of Japan*, 79(9):093701, 2010.

[145] Y. H. Matsuda, N. Abe, S. Takeyama, H. Kageyama, P. Corboz, A. Honecker, S. R. Manmana, G. R. Foltin, K. P. Schmidt, and F. Mila. Magnetization of $SrCu_2(BO_3)_2$ in ultrahigh magnetic fields up to 118 t. *Phys. Rev. Lett.*, 111:137204, Sep 2013.

[146] Zhenzhong Shi, Sachith Dissanayake, Philippe Corboz, William Steinhardt, David Graf, D. M. Silevitch, Hanna A. Dabkowska, T. F. Rosenbaum, Frédéric Mila, and Sara Haravifard. Discovery of quantum phases in the shastry-sutherland compound $SrCu_2(BO_3)_2$ under extreme conditions of field and pressure. *Nature Communications*, 13(1):2301, Apr 2022.

[147] Yoshihiko Okamoto, Daisuke Nakamura, Atsushi Miyake, Shojiro Takeyama, Masashi Tokunaga, Akira Matsuo, Koichi Kindo, and Zenji Hiroi. Magnetic transitions under

ultrahigh magnetic fields of up to 130 T in the breathing pyrochlore antiferromagnet **LiInCr$_4$O$_8$**. *Phys. Rev. B*, 95:134438, Apr 2017.

[148] W. H. Bragg and W. L. Bragg. The reflection of x-rays by crystals. *Proceedings of the Royal Society of London. Series A, Containing Papers of a Mathematical and Physical Character*, 88(605):428–438, 2023/01/02/ 1913. Full publication date: Jul. 1, 1913.

[149] R.A. Young and R.A. Young. *The Rietveld Method*. IUCr monographs on crystallography. Oxford University Press, 1995.

[150] H. M. Rietveld. A profile refinement method for nuclear and magnetic structures. *Journal of Applied Crystallography*, 2(2):65–71, Jun 1969.

[151] Juan Rodriguez-Carvajal. Recent advances in magnetic structure determination by neutron powder diffraction. *Physica B: Condensed Matter*, 192(1):55–69, 1993.

[152] Koichi Momma and Fujio Izumi. *VESTA3* for three-dimensional visualization of crystal, volumetric and morphology data. *Journal of Applied Crystallography*, 44(6):1272–1276, Dec 2011.

[153] https: //neutronoptics.com/OrientExpress.html.

[154] https: //en.wikipedia.org/wiki/Transmission$_electron_microscopy$.

[155] Amardeep Bharti and Navdeep Goyal. Fundamental of synchrotron radiations. In Daisy Joseph, editor, *Synchrotron Radiation*, chapter 2. IntechOpen, Rijeka, 2019.

[156] Donald H Bilderback, Pascal Elleaume, and Edgar Weckert. Review of third and next generation synchrotron light sources. *Journal of Physics B: Atomic, Molecular and Optical Physics*, 38(9):S773, apr 2005.

[157] https://analyzing-testing.netzsch.com/en/products/simultaneous-thermogravimetry-differential-scanning-calorimetry-sta-tg-dsc/sta-449-f1-jupiter.

[158] Frank Weimer. A method of measuring earth resistivity. 1916.

[159] L. J. van der PAUW. *A METHOD OF MEASURING SPECIFIC RESISTIVITY AND HALL EFFECT OF DISCS OF ARBITRARY SHAPE*, pages 174–182.

[160] https://www.ccmr.cornell.edu/wp-content/uploads/sites/2/2015/11/vsmappnote_5-09.pdf.

[161] https: //web.njit.edu/ tyson/PPMS_Documents/PPMS_Manual/1084-100%20c1%20acms%20manual.pdf.

[162] R Küchler, T Bauer, M Brando, and F Steglich. A compact and miniaturized high resolution capacitance dilatometer for measuring thermal expansion and magnetostriction. *Review of Scientific Instruments*, 83(9):095102, 2012.

[163] https: //www.ill.eu/users/instruments/instruments − list/d10/description/instrument-layout.

[164] Mercouri G. Kanatzidis, Rainer Pöttgen, and Wolfgang Jeitschko. The metal flux: A preparative tool for the exploration of intermetallic compounds. *Angewandte Chemie International Edition*, 44(43):6996–7023, 2005.

[165] Daniel E. Bugaris and Hans-Conrad zurâLoye. Materials discovery by flux crystal growth: Quaternary and higher order oxides. *Angewandte Chemie International Edition*, 51(16):3780–3811, 2012.

[166] J.P. Garandet and T. Alboussière. Bridgman growth: Modelling and experiments. *Progress in Crystal Growth and Characterization of Materials*, 38(1):133–159, 1999.

[167] J. Czochralski. Ein neues verfahren zur messung der kristallisationsgeschwindigkeit der metalle. *Zeitschrift für Physikalische Chemie*, 92U(1):219–221, 1918.

[168] S.M. Koohpayeh, D. Fort, and J.S. Abell. The optical floating zone technique: A review of experimental procedures with special reference to oxides. *Progress in Crystal Growth and Characterization of Materials*, 54(3):121–137, 2008.

[169] Nashra Pistawala, Dibyata Rout, Kumar Saurabh, Rabindranath Bag, Koushik Karmakar, Luminita Harnagea, and Surjeet Singh. Crystal growth of quantum materials: a review of selective materials and techniques. *Bulletin of Materials Science*, 45(1):10, Dec 2021.

[170] P.G. Harris. Zone refining and the origin of potassic basalts. *Geochimica et Cosmochimica Acta*, 12(3):195–208, 1957.

[171] H. C. Theurer. Method of processing semiconductive materials, US Patent Office, 1962.

[172] Paul H. Keck and Marcel J. E. Golay. Crystallization of silicon from a floating liquid zone. *Phys. Rev.*, 89:1297–1297, Mar 1953.

[173] R. Emeis. Notizen: Tiegelfreies ziehen von silicium-einkristallen. *Zeitschrift für Naturforschung A*, 9(1):67–68, 1954.

[174] A. Revcolevschi, A. Vietkine, and H. Moudden. Crystal growth and characterization of chain cuprates $SrCuO_2$, Sr2CuO3 and spin-ladder $Sr_{14}Cu_{24}O_{41}$. *Physica C: Superconductivity*, 282-287:493–494, 1997. Proceedings of the International Conference on Materials and Mechanisms of Superconductivity High Temperature Superconductors V Part II.

[175] A Revcolevschi, U Ammerahl, and G Dhalenne. Crystal growth of pure and substituted low-dimensionality cuprates $CuGeO_3$, La_2CuO_4, $SrCuO_2$, Sr_2CuO_3 and $Sr_{14}Cu_{24}O_{41}$ by the floating zone and travelling solvent zone methods. *Journal of Crystal Growth*, 198-199:593–599, 1999.

[176] Dibyata Rout, Sanchayeta Ranajit Mudi, Marco Hoffmann, Sven Spachmann, Rüdiger Klingeler, and Surjeet Singh. Structural and physical properties of trilayer nickelates $R_4Ni_3O_{10}$ (R = La, Pr, and Nd). *Phys. Rev. B*, 102:195144, Nov 2020.

[177] Sanchayeta Ranajit Mudi. Investigation of some metallic trilayer nickelates analogous to high Tc cuprates. 2019.

[178] Gianluca Giovannetti, Sanjeev Kumar, Daniel Khomskii, Silvia Picozzi, and Jeroen van den Brink. Multiferroicity in rare-earth nickelates $RNiO_3$. *Phys. Rev. Lett.*, 103:156401, Oct 2009.

[179] Hong Jian Zhao, Wei Ren, Yurong Yang, Jorge Íñiguez, Xiang Ming Chen, and L Bellaiche. Near room-temperature multiferroic materials with tunable ferromagnetic and electrical properties. *Nature Communications*, 5(1):4021, 2014.

[180] M. Hepting, M. Minola, A. Frano, G. Cristiani, G. Logvenov, E. Schierle, M. Wu, M. Bluschke, E. Weschke, H.-U. Habermeier, E. Benckiser, M. Le Tacon, and B. Keimer. Tunable charge and spin order in $\mathrm{PrNiO_3}$ thin films and superlattices. *Phys. Rev. Lett.*, 113:227206, Nov 2014.

[181] S Catalano, M Gibert, J Fowlie, J Íñiguez, J-M Triscone, and J Kreisel. Rare-earth nickelates $\mathrm{RNiO_3}$: thin films and heterostructures. *Reports on Progress in Physics*, 81(4):046501, feb 2018.

[182] J. M. D. Coey, M.Viret, and S.von Molnár. Mixed-valence manganites. *Advances in Physics*, 48(2):167–293, 1999.

[183] J. Zhang, D. Phelan, A. S. Botana, Y-S. Chen, H. Zheng, M. Krogstad, S. G. Wang, Y. Qiu, J. A. Rodriguez-Rivera, R. Osborn, S. Rosenkranz, M. R. Norman, and J. F. Mitchell. Intertwined density waves in a metallic nickelate, 2020.

[184] Danilo Puggioni and James M. Rondinelli. Crystal structure stability and electronic properties of the layered nickelate $\mathrm{La_4Ni_3O_{10}}$. *Phys. Rev. B*, 97:115116, Mar 2018.

[185] Bai-Zhuo Li, Cao Wang, P. T. Yang, J. P. Sun, Ya-Bin Liu, Jifeng Wu, Zhi Ren, J.-G. Cheng, Guang-Ming Zhang, and Guang-Han Cao. Metal-to-metal transition and heavy-electron state in $\mathrm{Nd_4Ni_3O_{10-\delta}}$. *Phys. Rev. B*, 101:195142, May 2020.

[186] Junjie Zhang, Hong Zheng, Yu-Sheng Chen, Yang Ren, Masao Yonemura, Ashfia Huq, and J. F. Mitchell. High oxygen pressure floating zone growth and crystal structure of the metallic nickelates $R_4\mathrm{Ni_3O_{10}}$ ($\mathrm{R = La, Pr}$). *Phys. Rev. Materials*, 4:083402, Aug 2020.

[187] Shangxiong Huangfu, Xiaofu Zhang, and Andreas Schilling. Correlation between the tolerance factor and phase transition in $A_{4-x}B_x\mathrm{Ni_3O_{10}}$ (A and $B = \mathrm{La, Pr},$ and $\mathrm{Nd}; x = 0, 1, 2,$ and 3). *Phys. Rev. Research*, 2:033247, Aug 2020.

[188] Maria Deus Carvalho, Fernanda Madalena A. Costa, Isabel da Silva Pereira, Alain Wattiaux, Jean Marc Bassat, Jean Claude Grenier, and Michel Pouchard. New prepara-

tion method of $La_{n+1}Ni_nO_{3n+1-\delta}$ (n=2,3. *Journal of Materials Chemistry*, 7(10):2107–2111, 1997.

[189] Z Zhang, Martha Greenblatt, and John B Goodenough. Synthesis, structure, and properties of the layered perovskite $La_3Ni_2O_{7-\delta}$. *Journal of Solid State Chemistry*, 108(2):402–409, 1994.

[190] Jia Song, De Ning, Bernard Boukamp, Jean-Marc Bassat, and Henny J. M. Bouwmeester. Structure, electrical conductivity and oxygen transport properties of Ruddlesden−Popper phases $Ln_{n+1}Ni_nO_{3n+1}$ (Ln = La, Pr and Nd; n = 1, 2 and 3). *J. Mater. Chem. A*, 8:22206–22221, 2020.

[191] François. Fauth, Roeland. Boer, Catalin. Gil-Ortiz, Fernando.and Popescu, Oriol. Vallcorba, Inma. Peral, Daniel. Fullà, Jordi. Benach, and Jordi Juanhuix. The crystallography stations at the alba synchrotron. *The European Physical Journal Plus*, 130:160, 2015.

[192] M Seppänen. Crystal-structure of $La_4Ni_3O_{10}$, 1979.

[193] AK Tkalich, VP Glazkov, VA Somenkov, SS Shil'shtein, AE Kar'kim, and AV Mirmel'shtein. Superconductivity: Physics. *Chemistry, Technology (USA)*, 4:2280–2286, 1991.

[194] V.I. Voronin, I.F. Berger, V.A. Cherepanov, L.Ya. Gavrilova, A.N. Petrov, A.I. Ancharov, B.P. Tolochko, and S.G. Nikitenko. Neutron diffraction, synchrotron radiation and exafs spectroscopy study of crystal structure peculiarities of the lanthanum nickelates $La_{n+1}Ni_nO_y$ (n=1,2,3). *Nuclear Instruments and Methods in Physics Research Section A: Accelerators, Spectrometers, Detectors and Associated Equipment*, 470(1):202 – 209, 2001. Proceedings of the 13th National Synchrotron Radiation Conference.

[195] Christopher D. Ling, Dimitri N. Argyriou, Guoqing Wu, and J.J. Neumeier. Neutron diffraction study of $La_3Ni_2O_7$: Structural relationships among n=1, 2, and 3 phases $La_{n+1}Ni_nO_{3n+1}$. *Journal of Solid State Chemistry*, 152(2):517 – 525, 2000.

[196] Junjie Zhang, Hong Zheng, Yu-Sheng Chen, Yang Ren, Masao Yonemura, Ashfia Huq, and J. F. Mitchell. High oxygen pressure floating zone growth and crystal structure of the metallic nickelates $R_4Ni_3O_{10}$ (R = La, Pr). *Phys. Rev. Mater.*, 4:083402, Aug 2020.

[197] Susmit Kumar, Oystein Fjellvag, Anja Olafsen Sjastad, and Helmer Fjellvag. Physical properties of ruddlesden-popper (n=3) nickelate: $La_4Ni_3O_{10}$. *Journal of Magnetism and Magnetic Materials*, 496:165915, 2020.

[198] Marius Uv Nagell, Wojciech Andrzej Sławiński, Ponniah Vajeeston, Helmer Fjellvåg, and Anja Olafsen Sjåstad. Temperature induced transitions in $La_4(Co_{1-x}Ni_x)_3O_{10+\delta}$; oxygen stoichiometry and mobility. *Solid State Ionics*, 305:7 – 15, 2017.

[199] J.M. Bassat, C. Allancon, P. Odier, J.P. Loup, M. Deus Carvalho, and A. Wattiaux. Electronic properties of $Pr_4Ni_3O_{10\pm\delta}$. *European Journal of Solid State and Inorganic Chemistry*, 35(2):173 – 188, 1998.

[200] Anja Olafsen, Helmer Fjellvåg, and Bjørn C. Hauback. Crystal structure and properties of $Nd_4Co_3O_{10+\delta}$ and $Nd_4Ni_3O_{10-\delta}$. *Journal of Solid State Chemistry*, 151(1):46 – 55, 2000.

[201] Grace A. Pan, Qi Song, Dan Ferenc Segedin, Myung-Chul Jung, Hesham El-Sherif, Erin E. Fleck, Berit H. Goodge, Spencer Doyle, Denisse Córdova Carrizales, Alpha T. N'Diaye, Padraic Shafer, Hanjong Paik, Lena F. Kourkoutis, Ismail El Baggari, Antia S. Botana, Charles M. Brooks, and Julia A. Mundy. Synthesis and electronic properties of $Nd_{n+1}Ni_nO_{3n+1}$ Ruddlesden-Popper nickelate thin films. *Phys. Rev. Mater.*, 6:055003, May 2022.

[202] Yoshiki Sakurai, Narihiko Chiba, Yoshihide Kimishima, and Masatomo Uehara. Electronic and magnetic properties of $La_4Ni_{3-x}Cu_xO_8$ and $Nd_{4-y}Sm_yNi_3O_8$. *Physica C: Superconductivity*, 487:27 – 30, 2013.

[203] Patrick A. Lee and T. V. Ramakrishnan. Disordered electronic systems. *Rev. Mod. Phys.*, 57:287–337, Apr 1985.

[204] K. Sreedhar, M. McElfresh, D. Perry, D. Kim, P. Metcalf, and J.M. Honig. Low-temperature electronic properties of the $La_{n+1}Ni_nO_{3n+1}(n = 2, 3, \text{ and } \infty)$ system: Evidence for a crossover from fluctuating-valence to fermi-liquid-like behavior. *Journal of Solid State Chemistry*, 110(2):208 – 215, 1994.

[205] Yoshiaki Kobayashi, Satoshi Taniguchi, Mayumi Kasai, Masatoshi Sato, Takashi Nishioka, and Masaaki Kontani. Transport and magnetic properties of $La_3Ni_2O_{7-\delta}$ and $La_4Ni_3O_{10-\delta}$. *Journal of the Physical Society of Japan*, 65(12):3978–3982, 1996.

[206] Guoqing Wu, J. J. Neumeier, and M. F. Hundley. Magnetic susceptibility, heat capacity, and pressure dependence of the electrical resistivity of $La_3Ni_2O_7$ and $La_4Ni_3O_{10}$. *Phys. Rev. B*, 63:245120, Jun 2001.

[207] G. Sala, M. B. Stone, B. K. Rai, A. F. May, C. R. Dela Cruz, H. Suriya Arachchige, G. Ehlers, V. R. Fanelli, V. O. Garlea, M. D. Lumsden, D. Mandrus, and A. D. Christianson. Physical properties of the trigonal binary compound nd_2o_3. *Phys. Rev. Mater.*, 2:114407, Nov 2018.

[208] S. Rosenkranz, M. Medarde, F. Fauth, J. Mesot, M. Zolliker, A. Furrer, U. Staub, P. Lacorre, R. Osborn, R. S. Eccleston, and V. Trounov. Crystalline electric field of the rare-earth nickelates $RNiO_3(R = Pr, Nd, Sm, Eu, , \text{ and } Pr_{1-x}La_x, 0 \leq x \leq 0.7)$ determined by inelastic neutron scattering. *Phys. Rev. B*, 60:14857–14867, Dec 1999.

[209] M. Freamat, X. N. Lin, V. Durairaj, S. Chikara, G. Cao, and J. W. Brill. Thermal and magnetic properties of the spin-chain material Pr_3RuO_7. *Phys. Rev. B*, 72:014458, Jul 2005.

[210] F Bartolomé, MD Kuz'min, J Bartolomé, J Blasco, J García, and F Sapina. Low-temperature specific heat of $NdMO_3$ (M = Co, Fe, Cr, Ni): magnetic ordering of Nd. *Solid state communications*, 91(3):177–182, 1994.

[211] Cho Yen Ho and Richard Erwin Taylor. *Thermal expansion of solids*, volume 4. ASM international, 1998.

[212] R. Klingeler, J. Geck, R. Gross, L. Pinsard-Gaudart, A. Revcolevschi, S. Uhlenbruck, and B. Büchner. Magnetism and the charge order transition in lightly doped $La_{1-x}Sr_xMnO_3$. *Phys. Rev. B*, 65:174404, Apr 2002.

[213] Philipp Gegenwart. Grüneisen parameter studies on heavy fermion quantum criticality. *Reports on Progress in Physics*, 79(11):114502, oct 2016.

[214] R. Klingeler, J. Geck, S. Arumugam, N. Tristan, P. Reutler, B. Büchner, L. Pinsard-Gaudart, and A. Revcolevschi. Pressure-induced melting of the orbital polaron lattice in $La_{1-x}Sr_xMnO_3$. *Phys. Rev. B*, 73:214432, Jun 2006.

[215] L. Wang, U. Köhler, N. Leps, A. Kondrat, M. Nale, A. Gasparini, A. de Visser, G. Behr, C. Hess, R. Klingeler, and B. Büchner. Thermal expansion of $LaFeAsO_{1-x}F_x$: Evidence for high-temperature fluctuations. *Phys. Rev. B*, 80:094512, Sep 2009.

[216] R. M. Fernandes, L. H. VanBebber, S. Bhattacharya, P. Chandra, V. Keppens, D. Mandrus, M. A. McGuire, B. C. Sales, A. S. Sefat, and J. Schmalian. Effects of nematic fluctuations on the elastic properties of iron arsenide superconductors. *Phys. Rev. Lett.*, 105:157003, Oct 2010.

[217] Motoki Osada, Bai Yang Wang, Berit H. Goodge, Shannon P. Harvey, Kyuho Lee, Danfeng Li, Lena F. Kourkoutis, and Harold Y. Hwang. Nickelate superconductivity without rare-earth magnetism: $(La, Sr)NiO_2$. *Advanced Materials*, 33(45):2104083, 2021.

[218] Motoki Osada, Bai Yang Wang, Kyuho Lee, Danfeng Li, and Harold Y. Hwang. Phase diagram of infinite layer praseodymium nickelate $Pr_{1-x}Sr_xNiO_2$ thin films. *Phys. Rev. Materials*, 4:121801, Dec 2020.

[219] B. Keimer, S. A. Kivelson, M. R. Norman, S. Uchida, and J. Zaanen. From quantum matter to high-temperature superconductivity in copper oxides. *Nature*, 518(7538):179–186, Feb 2015.

[220] J. Q. Lin, P. Villar Arribi, G. Fabbris, A. S. Botana, D. Meyers, H. Miao, Y. Shen, D. G. Mazzone, J. Feng, S. G. Chiuzbăian, A. Nag, A. C. Walters, M. García-Fernández, Ke-Jin Zhou, J. Pelliciari, I. Jarrige, J. W. Freeland, Junjie Zhang, J. F. Mitchell, V. Bisogni,

X. Liu, M. R. Norman, and M. P. M. Dean. Strong superexchange in a $d^{9-\delta}$ nickelate revealed by resonant inelastic x-ray scattering. *Phys. Rev. Lett.*, 126:087001, Feb 2021.

[221] Junjie Zhang, Yu-Sheng Chen, D. Phelan, Hong Zheng, M. R. Norman, and J. F. Mitchell. Stacked charge stripes in the quasi-2d trilayer nickelate $La_4Ni_3O_8$. *Proceedings of the National Academy of Sciences*, 113(32):8945–8950, 2016.

[222] Viktor V. Poltavets, Konstantin A. Lokshin, Andriy H. Nevidomskyy, Mark Croft, Trevor A. Tyson, Joke Hadermann, Gustaaf Van Tendeloo, Takeshi Egami, Gabriel Kotliar, Nicholas ApRoberts-Warren, Adam P. Dioguardi, Nicholas J. Curro, and Martha Greenblatt. Bulk magnetic order in a two-dimensional Ni^{1+}/Ni^{2+} (d^9/d^8) nickelate, isoelectronic with superconducting cuprates. *Phys. Rev. Lett.*, 104:206403, May 2010.

[223] J.G. Cheng, J.S. Zhou, J. B. Goodenough, H. D. Zhou, K. Matsubayashi, Y. Uwatoko, P. P. Kong, C. Q. Jin, W. G. Yang, and G. Y. Shen. Pressure effect on the structural transition and suppression of the high-spin state in the triple-layer $T^{'}La_4Ni_3O_8$. *Phys. Rev. Lett.*, 108:236403, Jun 2012.

[224] Junjie Zhang, D. M. Pajerowski, A. S. Botana, Hong Zheng, L. Harriger, J. Rodriguez-Rivera, J. P. C. Ruff, N. J. Schreiber, B. Wang, Yu-Sheng Chen, W. C. Chen, M. R. Norman, S. Rosenkranz, J. F. Mitchell, and D. Phelan. Spin stripe order in a square planar trilayer nickelate. *Phys. Rev. Lett.*, 122:247201, Jun 2019.

[225] Nicholas ApRoberts-Warren, Adam P. Dioguardi, Viktor V. Poltavets, Martha Greenblatt, Peter Klavins, and Nicholas J. Curro. Critical spin dynamics in the antiferromagnet $La_4Ni_3O_8$ from [139]La nuclear magnetic resonance. *Phys. Rev. B*, 83:014402, Jan 2011.

[226] Tomonori Miyatake, Yuki Wako, Satoru Tsukamoto, Izuru Umehara, and Masatomo Uehara. Chemical doping to Ni-sites in layered nickelate $Pr_4Ni_3O_8$ for high-tc superconductor candidate. *Social Science Research Network*, 2022.

[227] Akitoshi Nakata, Syunsuke Yano, Hiroki Yamamoto, Syunsuke Sakura, Yoshihide Kimishima, and Masatomo Uehara. The first observation of metallic behaviour in $Nd_{3.5}Sm_{0.5}Ni_3O_8$. *Advances in Condensed Matter Physics*, 2016:5808029, Feb 2016.

[228] R. Retoux, J. Rodriguez-Carvajal, and P. Lacorre. Neutron diffraction and tem studies of the crystal structure and defects of $Nd_4Ni_3O_8$. *Journal of Solid State Chemistry*, 140(2):307–315, 1998.

[229] Victor Pardo and Warren E. Pickett. Pressure-induced metal-insulator and spin-state transition in low-valence layered nickelates. *Phys. Rev. B*, 85:045111, Jan 2012.

[230] Xinglong Chen, Hong Zheng, Daniel P. Phelan, Hao Zheng, Saul H. Lapidus, Matthew J. Krogstad, Raymond Osborn, Stephan Rosenkranz, and J. F. Mitchell. Competing charge/spin-stripe and correlated metal phases in trilayer nickelates $(Pr_{1-x}La_x)_4Ni_3O_8$. *Chemistry of Materials*, 34(10):4560–4567, 2022.

[231] Shangxiong Huangfu, Zurab Guguchia, Denis Cheptiakov, Xiaofu Zhang, Hubertus Luetkens, Dariusz Jakub Gawryluk, Tian Shang, Fabian O. von Rohr, and Andreas Schilling. Short-range magnetic interactions and spin-glass behavior in the quasi-two-dimensional nickelate $Pr_4Ni_3O_8$. *Phys. Rev. B*, 102:054423, Aug 2020.

[232] Kai Kobayashi, Hiroki Yamamoto, Akitoshi Nakata, Izuru Umehara, Masatomo Uehara, Hiroki Yamamoto, Akitoshi Nakata, Izuru Umehara, and Masatomo Uehara. Electrical resistivity measurements under high pressure for $Nd_{3.5}Sm_{0.5}Ni_3O_8$. *JJAP Conference Proceedings*, 011106:6, 2017.

[233] Emilian M. Nica, Jyoti Krishna, Rong Yu, Qimiao Si, Antia S. Botana, and Onur Erten. Theoretical investigation of superconductivity in trilayer square-planar nickelates. *Phys. Rev. B*, 102:020504, Jul 2020.

[234] Jonathan Karp, Alexander Hampel, Manuel Zingl, Antia S. Botana, Hyowon Park, Michael R. Norman, and Andrew J. Millis. Comparative many-body study of $Pr_4Ni_3O_8$ and $NdNiO_2$. *Phys. Rev. B*, 102:245130, Dec 2020.

[235] E. Abrahams, P. W. Anderson, D. C. Licciardello, and T. V. Ramakrishnan. Scaling theory of localization: Absence of quantum diffusion in two dimensions. *Phys. Rev. Lett.*, 42:673–676, Mar 1979.

[236] Jun Kondo. Resistance Minimum in Dilute Magnetic Alloys. *Progress of Theoretical Physics*, 32(1):37–49, 07 1964.

[237] Shinobu Hikami, Anatoly I. Larkin, and Yosuke Nagaoka. Spin-Orbit Interaction and Magnetoresistance in the Two Dimensional Random System. *Progress of Theoretical Physics*, 63(2):707–710, 02 1980.

[238] Ying Xing, Yi Sun, Meenakshi Singh, Yan-Fei Zhao, Moses H. W. Chan, and Jian Wang. Electronic transport properties of topological insulator films and low dimensional superconductors. *Frontiers of Physics*, 8(5):491–508, Oct 2013.

[239] Antti Laitinen, Manohar Kumar, and Pertti J. Hakonen. Weak antilocalization of composite fermions in graphene. *Phys. Rev. B*, 97:075113, Feb 2018.

[240] Marcus Jenderka, José Barzola-Quiquia, Zhipeng Zhang, Heiko Frenzel, Marius Grundmann, and Michael Lorenz. Mott variable-range hopping and weak antilocalization effect in heteroepitaxial Na_2IrO_3 thin films. *Phys. Rev. B*, 88:045111, Jul 2013.

[241] C. Haas. Spin-disorder scattering and magnetoresistance of magnetic semiconductors. *Phys. Rev.*, 168:531–538, Apr 1968.

[242] Shengwei Zeng, Chi Sin Tang, Xinmao Yin, Changjian Li, Mengsha Li, Zhen Huang, Junxiong Hu, Wei Liu, Ganesh Ji Omar, Hariom Jani, Zhi Shiuh Lim, Kun Han, Dongyang Wan, Ping Yang, Stephen John Pennycook, Andrew T. S. Wee, and Ariando Ariando. Phase diagram and superconducting dome of infinite-layer $Nd_{1-x}Sr_xNiO_2$ thin films. *Phys. Rev. Lett.*, 125:147003, Oct 2020.

[243] Gerd Bergmann. Weak localization and its applications as an experimental tool. *International Journal of Modern Physics B*, 24(12n13):2015–2052, 2010.

[244] Dibyata Rout, Ran Tang, Markos Skoulatos, Bachir Ouladdiaf, Yuto Kinoshita, Atsushi Miyake, Masashi Tokunaga, Sagar Mahapatra, and Surjeet Singh. Ordered and disordered variants of the triangular lattice antiferromagnet $Ca_3NiNb_2O_9$: Crystal growth and magnetic properties. *Phys. Rev. Mater.*, 7:024419, Feb 2023.

[245] A V Chubukov, S Sachdev, and T Senthil. Large-s expansion for quantum antiferromagnets on a triangular lattice. *Journal of Physics: Condensed Matter*, 6(42):8891, oct 1994.

[246] Luca Capriotti, Adolfo E. Trumper, and Sandro Sorella. Long-range néel order in the triangular Heisenberg model. *Phys. Rev. Lett.*, 82:3899–3902, May 1999.

[247] R. Rawl, L. Ge, H. Agrawal, Y. Kamiya, C. R. Dela Cruz, N. P. Butch, X. F. Sun, M. Lee, E. S. Choi, J. Oitmaa, C. D. Batista, M. Mourigal, H. D. Zhou, and J. Ma. $Ba_8CoNb_6O_{24}$: A spin-$\frac{1}{2}$ triangular-lattice Heisenberg antiferromagnet in the two-dimensional limit. *Phys. Rev. B*, 95:060412, Feb 2017.

[248] R. Coldea, D. A. Tennant, R. A. Cowley, D. F. McMorrow, B. Dorner, and Z. Tylczynski. Quasi-1d $S = 1/2$ antiferromagnet Cs_2CuCl_4 in a magnetic field. *Phys. Rev. Lett.*, 79:151–154, Jul 1997.

[249] Yutaka Shirata, Hidekazu Tanaka, Akira Matsuo, and Koichi Kindo. Experimental realization of a spin-1/2 triangular-lattice heisenberg antiferromagnet. *Phys. Rev. Lett.*, 108:057205, Jan 2012.

[250] A. I. Smirnov, H. Yashiro, S. Kimura, M. Hagiwara, Y. Narumi, K. Kindo, A. Kikkawa, K. Katsumata, A. Ya. Shapiro, and L. N. Demianets. Triangular lattice antiferromagnet $RbFe(MoO_4)_2$ in high magnetic fields. *Phys. Rev. B*, 75:134412, Apr 2007.

[251] N. A. Fortune, Q. Huang, T. Hong, J. Ma, E. S. Choi, S. T. Hannahs, Z. Y. Zhao, X. F. Sun, Y. Takano, and H. D. Zhou. Evolution of magnetic field induced ordering in the layered quantum heisenberg triangular-lattice antiferromagnet $Ba_3CoSb_2O_9$. *Phys. Rev. B*, 103:184425, May 2021.

[252] Ryui Kaneko, Satoshi Morita, and Masatoshi Imada. Gapless spin-liquid phase in an extended spin 1/2 triangular Heisenberg model. *Journal of the Physical Society of Japan*, 83(9):093707, 2014.

[253] Zhenyue Zhu and Steven R. White. Spin liquid phase of the $s = \frac{1}{2}$ $J_1 - J_2$ Heisenberg model on the triangular lattice. *Phys. Rev. B*, 92:041105, Jul 2015.

[254] Yasir Iqbal, Wen-Jun Hu, Ronny Thomale, Didier Poilblanc, and Federico Becca. Spin liquid nature in the Heisenberg $J_1 - J_2$ triangular antiferromagnet. *Phys. Rev. B*, 93:144411, Apr 2016.

[255] N. D. Mermin and H. Wagner. Absence of ferromagnetism or antiferromagnetism in one- or two-dimensional isotropic Heisenberg models. *Phys. Rev. Lett.*, 17:1133–1136, Nov 1966.

[256] R. Ishii, S. Tanaka, K. Onuma, Y. Nambu, M. Tokunaga, T. Sakakibara, N. Kawashima, Y. Maeno, C. Broholm, D. P. Gautreaux, J. Y. Chan, and S. Nakatsuji. Successive phase transitions and phase diagrams $Rb_4Mn(MoO_4)_3$ for the quasi-two-dimensional easy-axis triangular antiferromagnet. *EPL (Europhysics Letters)*, 94(1):17001, mar 2011.

[257] M. Lee, E. S. Choi, X. Huang, J. Ma, C. R. Dela Cruz, M. Matsuda, W. Tian, Z. L. Dun, S. Dong, and H. D. Zhou. Magnetic phase diagram and multiferroicity of $Ba_3MnNb_2O_9$: A spin-$\frac{5}{2}$ triangular lattice antiferromagnet with weak easy-axis anisotropy. *Phys. Rev. B*, 90:224402, Dec 2014.

[258] Mutsuki Saito, Masari Watanabe, Nobuyuki Kurita, Akira Matsuo, Koichi Kindo, Maxim Avdeev, Harald O. Jeschke, and Hidekazu Tanaka. Successive phase transitions and magnetization plateau in the spin-1 triangular-lattice antiferromagnetic $ba_2la_2nite_2o_{12}$ with small easy-axis anisotropy. *Phys. Rev. B*, 100:064417, Aug 2019.

[259] N. Li, Q. Huang, A. Brassington, X. Y. Yue, W. J. Chu, S. K. Guang, X. H. Zhou, P. Gao, E. X. Feng, H. B. Cao, E. S. Choi, Y. Sun, Q. J. Li, X. Zhao, H. D. Zhou, and X. F. Sun. Quantum spin state transitions in the spin-1 equilateral triangular lattice antiferromagnet $Na_2BaNi(PO_4)_2$. *Phys. Rev. B*, 104:104403, Sep 2021.

[260] J. G. Cheng, G. Li, L. Balicas, J. S. Zhou, J. B. Goodenough, Cenke Xu, and H. D. Zhou. High-pressure sequence of $Ba_3NiSb_2O_9$ structural phases: New $s = 1$ quantum spin liquids based on Ni^{2+}. *Phys. Rev. Lett.*, 107:197204, Nov 2011.

[261] J. A. Quilliam, F. Bert, A. Manseau, C. Darie, C. Guillot-Deudon, C. Payen, C. Baines, A. Amato, and P. Mendels. Gapless quantum spin liquid ground state in the spin-1 antiferromagnet $6HB - Ba_3NiSb_2O_9$. *Phys. Rev. B*, 93:214432, Jun 2016.

[262] Maksym Serbyn, T. Senthil, and Patrick A. Lee. Exotic $s = 1$ spin-liquid state with fermionic excitations on the triangular lattice. *Phys. Rev. B*, 84:180403, Nov 2011.

[263] Cenke Xu, Fa Wang, Yang Qi, Leon Balents, and Matthew P. A. Fisher. Spin liquid phases for spin-1 systems on the triangular lattice. *Phys. Rev. Lett.*, 108:087204, Feb 2012.

[264] G. Chen, M. Hermele, and L. Radzihovsky. Frustrated quantum critical theory of putative spin-liquid phenomenology in $6h - B - Ba_3NiSb_2O_9$. *Phys. Rev. Lett.*, 109:016402, Jul 2012.

[265] M Lee, E S Choi, J Ma, R Sinclair, C R Dela Cruz, and H D Zhou. Magnetism and multiferroicity of an isosceles triangular lattice antiferromagnet $Sr_3NiNb_2O_9$. 28(47):476004, sep 2016.

[266] Mark T. Anderson, Kevin B. Greenwood, Gregg A. Taylor, and Kenneth R. Poeppelmeier. B-cation arrangements in double perovskites. *Progress in Solid State Chemistry*, 22(3):197–233, 1993.

[267] Albina Y. Borisevich and Peter K. Davies. La(li1/3ti2/3)o3: a new 1:2 ordered perovskite. *Journal of Solid State Chemistry*, 170(1):198–201, 2003.

[268] K.L. Holman, Q. Huang, T. Klimczuk, K. Trzebiatowski, J.W.G. Bos, E. Morosan, J.W. Lynn, and R.J. Cava. Synthesis and properties of the double perovskites La_2NiVO_6, La_2CoVO_6, and La_2CoTiO_6. *Journal of Solid State Chemistry*, 180(1):75–83, 2007.

[269] V.C. Fuertes, M.C. Blanco, D.G. Franco, J.M. De Paoli, R.D. Sánchez, and R.E. Carbonio. Influence of the B-site ordering on the magnetic properties of the new $La_3Co_2MO_9$ double perovskites with M=Nb or Ta. *Materials Research Bulletin*, 46(1):62–69, 2011.

[270] Z. Lu, L. Ge, G. Wang, M. Russina, G. Günther, C. R. dela Cruz, R. Sinclair, H. D. Zhou, and J. Ma. Lattice distortion effects on the frustrated spin-1 triangular-antiferromagnet $A_3NiNb_2O_9$ (A = Ba, Sr, and Ca). *Phys. Rev. B*, 98:094412, Sep 2018.

[271] Meifeng Liu, Huimin Zhang, Xin Huang, Chunyang Ma, Shuai Dong, and Jun-Ming Liu. Two-step antiferromagnetic transitions and ferroelectricity in spin-1 triangular-lattice antiferromagnetic $Sr_3NiTa_2O_9$. *Inorganic Chemistry*, 55(6):2709–2716, 2016. PMID: 26934503.

[272] V. Fratello, G. Berkstresser, C. Brandle, and A. J. V. Graitis. Nickel containing perovskites. *Journal of Crystal Growth*, 166:878–882, 1996.

[273] D. Prabhakaran and A.T. Boothroyd. Crystal growth of the triangular-lattice antiferromagnet $Ba_3CoSb_2O_9$. *Journal of Crystal Growth*, 468:345–348, 2017. The 18th International Conference on Crystal Growth and Epitaxy (ICCGE-18).

[274] Kenji Kitamura, Shigeyuki Kimura, and Kazushi Watanabe. Control of interface shape by using heat reservoir in FZ growth with infrared radiation convergence type heater. *Journal of Crystal Growth*, 57(3):475–481, 1982.

[275] Surjeet Singh, R. Suryanarayanan, Romuald S. Martin, G. Dhalenne, and A. Revcolevschi. Single-crystal growth and magnetic properties of the metallic molybdate pyrochlore $Sm_2Mo_2O_7$. *Journal of Crystal Growth*, 308(2):237–240, 2007.

[276] Liang Li, Defang Duan, Qiang Zhou, Dapeng Xu, Tian Cui, Bingbing Liu, and Hongming Yuan. Optical floating zone method growth and optical properties of corundum $Mg_4Nb_2O_9$ single crystal. *Journal of Crystal Growth*, 402:109–112, 2014.

[277] N. MIYAZAKI, A. HATTORI, and H. UCHIDA. Thermal shock cracking of lithium niobate single crystal. *Journal of Materials Science: Materials in Electronics*, 8(3):133–138, Jun 1997.

[278] Dongsheng Yuan, Federico Moretti, Didier Perrodin, Gregory Bizarri, Tetiana Shalap-ska, Christophe Dujardin, and Edith Bourret. Modified floating-zone crystal growth of $Mg_4Ta_2O_9$ and its scintillation performance. *CrystEngComm*, 22:3497–3504, 2020.

[279] Diana M. Arciniegas Jaimes, Juan M. De Paoli, Vivian Nassif, Paula G. Bercoff, Germán Tirao, Raúl E. Carbonio, and Fernando Pomiro. Effect of b-site orderâdisorder in the structure and magnetism of the new perovskite family $La_2MnB^{'}O_6$ with $B^{'} =$ $Ti, Zr,$ and Hf. *Inorganic Chemistry*, 60(7):4935–4944, 2021. PMID: 33705132.

[280] A. M. Glazer. The classification of tilted octahedra in perovskites. *Acta Crystallographica Section B*, 28(11):3384–3392, 1972.

[281] Naoto Nagaosa, Akira Furusaki, Manfred Sigrist, and Hidetoshi Fukuyama. Non-magnetic impurities in spin gap systems. *Journal of the Physical Society of Japan*, 65(12):3724–3727, 1996.

[282] Kazuya Yokota, Nobuyuki Kurita, and Hidekazu Tanaka. Magnetic phase diagram of the $s = \frac{1}{2}$ triangular-lattice heisenberg antiferromagnet $Ba_3CoNb_2O_9$. *Phys. Rev. B*, 90:014403, Jul 2014.

[283] J.A. Mydosh. *Spin Glasses: An Experimental Introduction (1st ed.)*. CRC Press, 1993.

[284] L.A. Bendersky, I. Levin, R.S. Roth, and A.J. Shapiro. $Ca_4Nb_2O_9 - CaTiO_3$: Phase equilibria and microstructures. *Journal of Solid State Chemistry*, 160(1):257–271, 2001.

[285] D.G. Franco, V.C. Fuertes, M.C. Blanco, M.T. Fernández-Díaz, R.D. Sánchez, and R.E. Carbonio. Synthesis, structure and magnetic properties of $La_3Co_2SbO_9$: A double perovskite with competing antiferromagnetic and ferromagnetic interactions. *Journal of Solid State Chemistry*, 194:385–391, 2012.

[286] Kazuo Hida. Magnetization process of the S=1 and 1/2 uniform and distorted kagomé Heisenberg antiferromagnets. *Journal of the Physical Society of Japan*, 70(12):3673–3677, 2001.

[287] Esmeralda Laue Suite.

[288] Malcolm F. Collins and Stephen M. Shapiro. Magnetic critical scattering. *Physics Today*, 43(10):97–98, 1990.